Transformations induites par la déformation dans les alliages métastables à base de Ti-Mo : étude des mécanismes de déformation et application d'un stent cardiovasculaire

Bingnan Qian

▶ **To cite this version:**

Bingnan Qian. Transformations induites par la déformation dans les alliages métastables à base de Ti-Mo : étude des mécanismes de déformation et application d'un stent cardiovasculaire. Chimie analytique. Université Paris sciences et lettres, 2021. Français. NNT : 2021UPSLC015 . tel-03956240

HAL Id: tel-03956240

https://pastel.hal.science/tel-03956240

Submitted on 25 Jan 2023

HAL is a multi-disciplinary open access archive for the deposit and dissemination of scientific research documents, whether they are published or not. The documents may come from teaching and research institutions in France or abroad, or from public or private research centers.

L'archive ouverte pluridisciplinaire **HAL**, est destinée au dépôt et à la diffusion de documents scientifiques de niveau recherche, publiés ou non, émanant des établissements d'enseignement et de recherche français ou étrangers, des laboratoires publics ou privés.

PSL UNIVERSITÉ PARIS

THÈSE DE DOCTORAT
DE L'UNIVERSITÉ PSL

Préparée à Chimie ParisTech / École Nationale Supérieure de Chimie de Paris (ENSCP)

Deformation induced transformations in Ti-Mo based metastable alloys: deformation mechanisms study and cardiovascular stent application

Soutenue par
Bingnan QIAN
Le 11 octobre 2021

Ecole doctorale n°388
Chimie Physique et Chimie Analytique de Paris Centre

Spécialité
Chimie Physique

Composition du jury :

Armelle RINGUEDE Directrice de Recherche CNRS, Chimie ParisTech	*Présidente*
Thierry GLORIANT Professeur des Universités, INSA de Rennes	*Rapporteur*
Rajarshi BANERJEE Professor, University of North Texas	*Rapporteur*
Mathilde LAURENT-BROCQ Chargée de recherche, Université Paris-Est Créteil	*Examinatrice*
Emmanuel BERTRAND Maître de Conférences, Université de Nantes	*Examinateur*
Frédéric PRIMA Professeur des Universités, Chimie ParisTech	*Examinateur*
Fan SUN Chercheur, Chimie ParisTech	*Co-encadrant de thèse*
Philippe VERMAUT Maître de Conférences, Chimie ParisTech	*Directeur de thèse*

Contents

General introduction

Titanium and its alloys have been extensively used in numerous application fields and keep growing due to their excellent combination of properties. Among these outstanding properties, one can cite their high strength, low density, high strength-to-weight ratio, good corrosion resistance, excellent biocompatibility, and non-ferromagnetic. Due to these properties, titanium and its alloys are attractive for biomedical applications, such as orthopedic and dental prostheses with a long clinical history and new applications in cardiovascular implants, e.x. Balloon-expandable coronary stents are still made of the same material as the first stent invented more than 40 years ago. The reason can be revealed when comparing the mechanical properties of Ti alloys to the stent alloys, i.e., stainless steel and CoCr alloys. Commercial pure (CP) titanium and commercial titanium alloys exhibit weaknesses of low uniform elongation and lack of work-hardening rate, which limited their applications in stents that need to be plastically expanded during implantation up to 40% elongation. However, the recent discovery in Ti-12Mo (wt. %), the first reported TRansformation Induced Plasticity (TRIP) and TWinning Induced Plasticity (TWIP) Ti alloy, raised our hopes again due to its unique combination of high strain-hardening rate and excellent uniform elongation. Therefore, the strategy of utilizing TRIP/TWIP effects, inspired by Ti-12Mo alloy, was applied to enhance metastable β titanium alloys to overcome the mechanical properties' limitations. As a proof-of-the-concept, Ti-12Mo has been used to fabricate real-size stent prototypes and confirmed that TRIP/TWIP Ti's mechanical properties could be compatible with stent application. It also found that controlling the TRIP/TWIP effect is of essential importance in tailoring the mechanical properties of TRIP/TWIP Ti for stent use. Therefore, this work continues to understand the transformation mechanisms in Ti-12Mo to control the TRIP/TWIP effect via thermomechanical treatment. In parallel, the knowledge is used to develop new TRIP/TWIP Ti alloys by optimizing the chemical compositions for stent applications. The Ph.D. works were accordingly planned in two research axes, the first of which is to investigate the deformation mechanisms of Ti-12Mo alloy at various thermomechanical states via comprehensive in-situ characterizations. Along this axis, understanding the corresponding changes between mechanical properties and the TRIP/TWIP mechanisms is the main objective. Along the second axis, partially based on the results of the first one, a new Ti-W-Mo system will be explored to combine enhanced

mechanical properties by activating TRIP/TWIP effects and optimized chemical compositions for stent application.

The supervisor specified the target application of the Ph.D. work to cardiovascular stents based on the knowledge and insights from more than one decade of continuous researches on commercial stents and their clinical outcomes. The work is a critical part of the solution to answer the urgent requirements for stent material innovation to improve the short- and long-term safeties of current balloon-expandable stents made of steels and Co-Cr alloys with cytotoxic drug coating. Indeed, to specify the best material specification for cardiovascular stents is a complex multi-constrain problem compared to other implants in the human body due to the severe plastic expansion during implantation then the lifetime service in a coronary artery. There are minimal mechanical requirements to be met with generally, yield strength of about 200MPa, high ultimate tensile strength (UTS) > 300MPa, and enough elongation (> 15%). A steep strain-hardening rate leads to a desirable rise in strength during expansion. Higher tensile properties also permit thinner stents for an overall lower profile, thus improving flexibility, deliverability, and access to smaller vessels. Besides the mechanical behavior, the performance of the stent material depends on the appropriate flexibility, radial force, resistance to fracture, radio-opacity, biocompatibility, and non-ferromagnetic for Magnetic Resonance Imaging (MRI) safe.

This dissertation will be organized into seven chapters.

Chapter 1 will provide the general concepts relative to titanium and its alloys. The deformation mechanism could be observed in metastable β titanium alloy. Then the requirements of material properties for cardiovascular stents were explained in this chapter. In addition, the limitation applications of the commercially pure Ti and traditional Ti alloys and the potential application of the metastable Ti-12Mo (wt. %) alloy in cardiovascular stents will be discussed in this chapter. Besides, the deformation mechanism of Ti-12Mo alloy, the strategies for improving the mechanical properties of the alloy, and the development of a new family of metastable titanium alloys will also be discussed in this chapter.

Chapter 2 will introduce the experimental techniques, analytical software, and calculations used for elaboration, manufacturing, heat treatment, and characterization of the designed alloys.

In **Chapter 3**, to build an in-depth understanding of the transformation mechanisms of Ti-12Mo alloy during the deformation process and thereby improve its mechanical behavior by heat treatment or optimizing the chemical composition, transformation pathways operating in the β

grains of a β-metastable Ti-alloy for different Schmid factor conditions were carefully investigated via Schmid factor calculation coupled with in-situ electron backscatter diffraction (EBSD) and ex-situ/in-situ transmission electron microscopy (TEM) observations.

In **chapter 4**, the SIM α″ transformation with twinning and detwinning evolution will be traced by in-situ investigations (EBSD and TEM) under tensile loading and unloading conditions.

In **Chapter 5**, the effects of grain size and ω_{iso} hardening treatment at low temperature (holding at 200℃) for a short time (60s~150s) on mechanical properties and the transformation mechanisms during the deformation process in TRIP/TWIP Ti-12Mo alloy will be well studied in the Chapter.

Chapter 6 will focus on the solution strengthening effect via adding Zr elements in Ti-12Mo to increase the yield strength while maintaining high plasticity. Based on the results, the deformation mechanisms involved in the macroscopic mechanical behavior are discussed by considering the heterogeneous nature of the microstructural evolution.

Chapter 7 will focus on designing new metastable Ti-W-Mo-Zr alloys with a combination of high yield strength and excellent ductility via adding W element to replace the Mo element in Ti-Mo-Zr based alloys. The added W element could increase its density and thereby increase its radio-opacity.

Finally, the main results obtained through this thesis will be summarized in the **general conclusions**, and prospects concerning the development and optimization of the metastable TRIP/TWIP titanium alloys will be given.

Chapter 1 Metallurgical and physical background of metastable β titanium alloys

1.1 Introduction

In recent several decades, titanium and its alloys are more and more commercially crucial for many application fields [1, 2], such as engineering applications in the aerospace industry [1, 3, 4], the biomedical and healthcare industry [5-11], and the energy and power generation industry [12], due to their combination of properties: their very high strength-to-weight ratio, low density, excellent corrosion resistance, and their biocompatibility. Despite their excellent properties, their price remains high, limiting their application to high value-added industries. In addition, titanium alloys present a large variety of phase transformations thanks to the allotropic transformation of titanium, and thus, a large variety of microstructure and mechanical properties can be obtained.

1.1.1 Classification of titanium alloys

In solid-state, there exist two allotropes in titanium alloys, namely hexagonal close-packed (hcp) α-phase and body-centered cubic (bcc) β-phase [1, 3]. Each allotrope is only stable within a particular temperature range. For pure titanium, the temperature at which the transformation hcp α ⇋ bcc β could be activated is called β-transus temperature [13]. The transformation offers the prospect of the alloys with α, β, or mixed α/β microstructures [13]. The β-transus mentioned above can be affected by the alloying elements. These alloying elements of titanium can be classified as α-stabilizers, β-stabilizers, and neutral, depending on their influence on the β-transus temperature [13]. The α-stabilizers can extend the α phase field to higher temperature including Al, Ga, B, Sc, La, Ce, C, O, and N. The elements such as V, Mo Nb, Hf, Ta, Mn, Cr, Cu, Ni, Fe, Co, Au, Ag, W and H able to lower the β-transus temperature causing stabilization of β phase down to low temperatures, are called β stabilizers. All these chemical elements change the β transus temperature with more or less efficiency. Generally, the Mo equivalent as an empirical expression is used to get a quantitative value for the β phase stabilization effect, taking into account the individual contributions of the different alloying elements [14]. The molybdenum equivalent (Mo_{eq}) can be expressed by the following equation [15]:

$[Mo]_{eq}$ = Mo (wt. %) + Nb (wt. %)/3.6 + Ta (wt. %)/4.5 + W (wt. %)/2.27 + Cr (wt. %)/0.63 + V (wt. %)/1.5 + Fe (wt. %)/0.35 + Ni (wt. %)/0.8 + Co (wt. %)/0.7 -Al (wt. %).

The elements like Zr, Sn, and Hf, which have negligible influence on the stability of α and β phases, are referred to as neutral elements [13]. However, recent studies have reported that these neutral alloying elements could be considered weak β-stabilizing elements when combined with other beta stabilizing elements.

Given the great variety of microstructures and properties that can be obtained for titanium alloys depending on their chemical composition and the heat treatments that can be applied, a classification has been proposed, based on the microstructure obtained either after quenching from the stability range of the beta phase, or after slow cooling (equilibrium microstructure) depending on the chemical composition. This attempt at classification is summarized graphically in figure 1.1 based on a pseudo-binary diagram [19], where the chemical composition is reduced to a single parameter: the equivalent Mo.

Based on the equilibrium microstructures, α, near-α, α+β, and β types of alloys can be distinguished [1, 2]. From the quenching microstructures, non-equilibrium phases have to be taken into account. Martensitic α', α"+β, β-metastable and beta-stable type alloys are distinguished [19].

The α Ti alloys, including commercially pure titanium and titanium alloys, are exclusively alloyed with α-stabilizers elements. They are generally used in non-structural applications requiring low strength and good corrosion resistance. When increasing the amount of the β stabilizers, an α+β structure develops. Dual-phase α+β alloys are generally used in applications where higher strength, good fatigue behavior, good toughness, and excellent corrosion resistance are required. The most well-known α+β alloy is Ti-6Al-4V (wt. %) [1, 2]. The final microstructure of α+β alloys is often controlled by using the solution and aging treatments. β alloys can be further divided into two sub-classes, stable β alloys and metastable β alloys, depending on their deformation behavior under applied stress. Stable β alloys exhibit superior reachable strength, formability, and corrosion resistance, while the lack of ductility under the high-strength conditions limited their applications. Compared to stable β alloys, the metastable β alloys seem to attract more attention these last decades due to specific properties such as superelasticity, shape memory effect, low Young's modulus, and better formability. Metastable β titanium alloys also possess excellent

mechanical properties, which completely depend on the final microstructure and transformations during the deformation process. These alloys are predominated by β phase upon the quenched state but can also contain a small volume fraction of martensitic phases or athermal ω phase depending on the composition [1]. The formation of the ω phase can greatly affect the mechanical properties [16-18]. This later point will be introduced in detail in the latter part of the chapter. Besides, the degree of meta-stability of the beta phase can also affect the mechanical properties, which will determine its deformation mechanism by offering new deformation modes such as stress-induced martensitic transformation, mechanical twinning, and dislocations glide. Stress-induced martensite as a deformation-induced transformation mechanism in the plastic range of deformation has been widely observed in metastable β titanium alloys and named TRansformation Induced Plasticity (TRIP) effect. Another important transformation mechanism during the plastic deformation process is the mechanical twinning named TWinning Induced Plasticity (TWIP) effect. These deformation mechanisms will be introduced in the following.

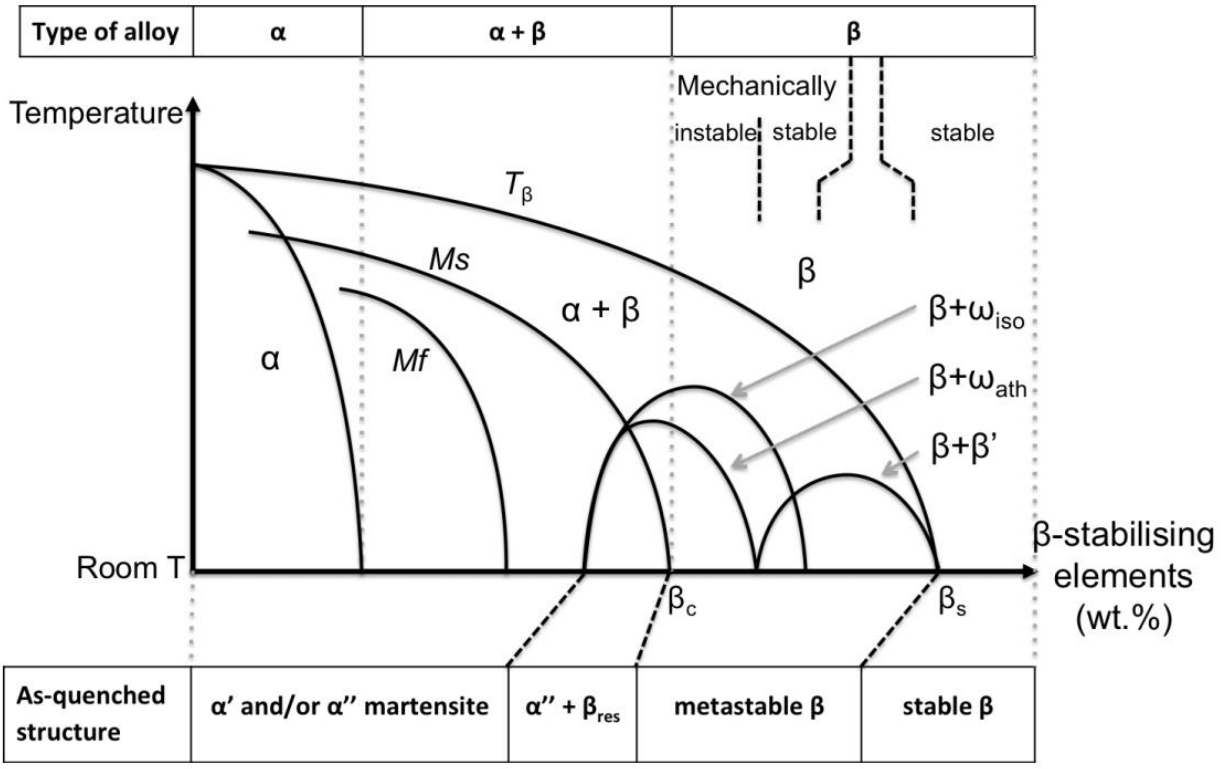

Figure 1.1 Pseudo-binary phase diagram of Ti-alloys with the decomposition products of the β-phase. Here, βc is the critical minimum β stabilizer amount for near β or metastable β alloys to retain β completely on quenching from β phase field, and βs is the minimum amount of β stabilizer for stable β alloys; T_β, RT, Ms, and Mf refer to the β-transus temperature, room temperature, martensite start and finish temperatures, respectively [19].

1.1.2 ω phase in metastable titanium alloys

ω phase is a metastable phase that could be formed in some metastable β Ti alloys on quenching from the temperatures above T_β. Generally, there exist two types of ω phase based on their formation condition, namely the athermal ω (ω_{ath}) phase and the isothermal ω phase (ω_{iso}). The mechanical properties of metastable β Ti alloys can be affected by the formation of the ω phase, as mentioned above [16-18]. $\omega_{ath,}$ which occurs upon quenching, is a diffusionless transformation, and its formation cannot be avoided regardless of the cooling rate is. The formation of ω_{ath} is due to the collapse of two successive {111} planes in the β phase, as illustrated in figure 1.2 [20]. ω_{ath} particles always have petite size, and the diameter is usually no more than 5 nanometers, as shown in figure 1.3 (a) [21]. The ω_{iso} precipitates from the β phase because β stabilizers diffuse out of the growing ω particles during aging at relatively low temperatures (below 300℃), resulting in a stabilization of the β matrix. ω_{iso} particles with a size range of 10-20 nm usually exhibit cuboidal or ellipsoidal (as shown in figures 1.3b and c) depending on the coherency with the surrounding β matrix [22]. The ω_{iso} formation usually causes severe embrittlement, i.e., increases the yield strength and reduces the ductility of Ti alloys [20, 22]. Plate-like ω phases have also been observed in some metastable Ti alloys at the early deformation stage at room temperature, as shown in figure 1.3 d [23]. In this case, the phase transformation is stress-induced, similarly to the stress-induced martensitic transformation.

The ω phase has a hexagonal (not close-packed) symmetry (space group P6/mmm) upon the complete transformation, or trigonal symmetry (space group P3m1) upon the incomplete transformation [20]. The orientation relationship between β matrix and ω can be described as $\{111\}_\beta // (0001)_\omega$; $<110>_\beta // <1120>_\omega$ [20].

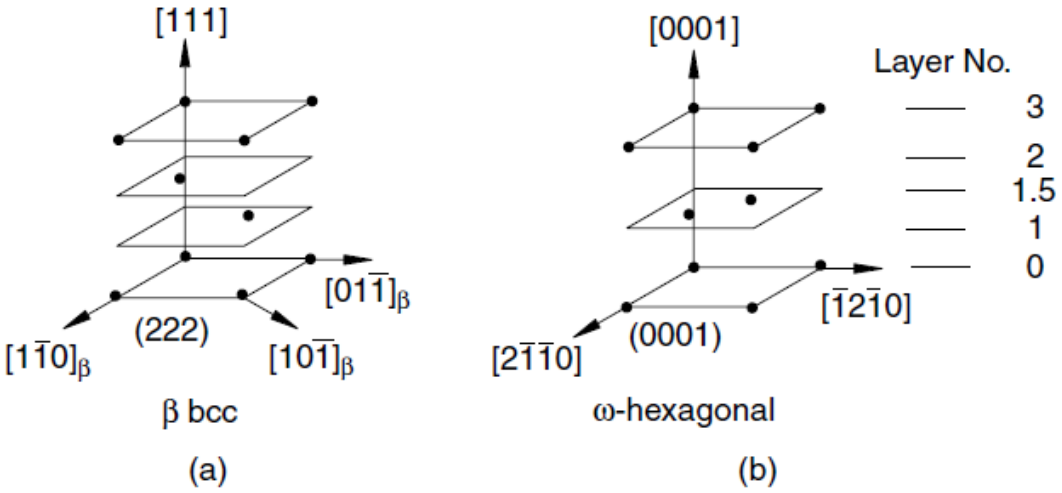

Figure 1.2 illustration of collapse of $\{111\}_\beta$ planes to form ω_{ath} phase [20].

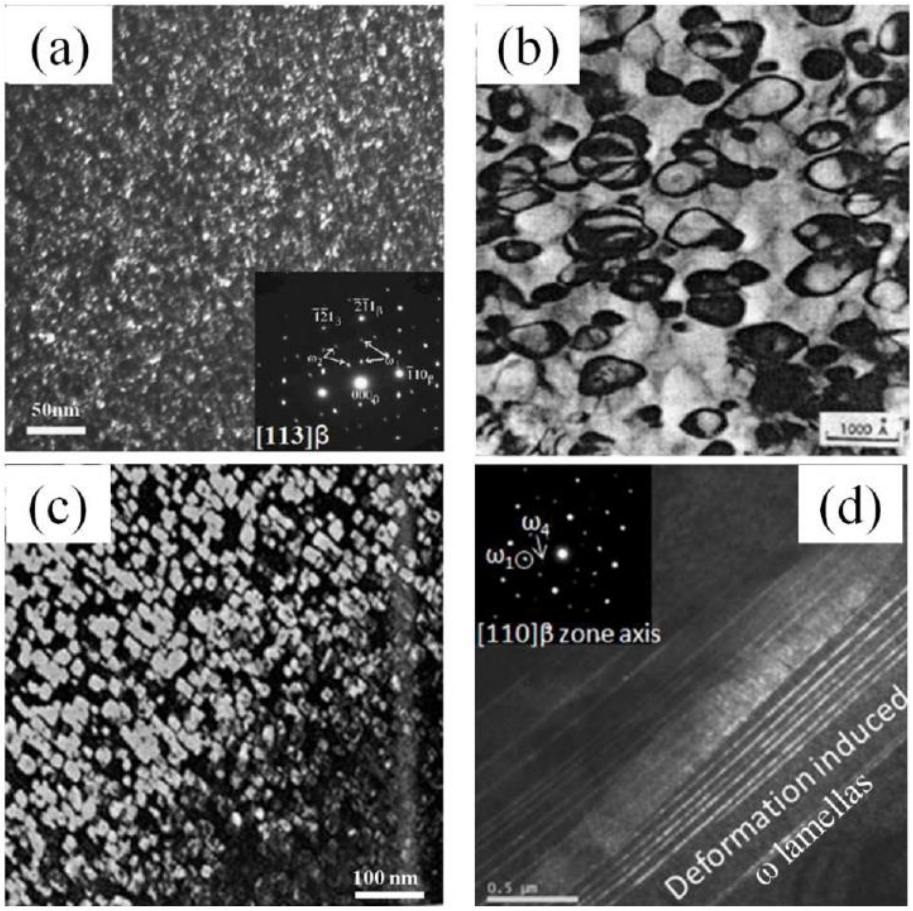

Figure 1.3 The typical TEM micrographs and corresponding diffraction patterns of three types ω phase. (a) nano-size athermal ω particles in quenched Ti-Mo alloys [23]; (b) ellipsoidal morphology isothermal ω phase in Ti-Mo system [22]; (c) cuboidal morphology isothermal ω phase in Ti-V alloys [22]; (d) plate-like deformation-induced ω phase in Ti-12Mo alloy upon strain[23].

1.2 Deformation mechanisms in metastable β titanium alloys

Metastable β titanium alloys exhibit excellent mechanical properties due to the variety of deformation mechanisms, including dislocation slips, deformation twinning ($\{332\}\langle 113\rangle_\beta$ twinning and $\{112\}\langle 111\rangle_\beta$ twinning) [27-29], and stress-induced martensite (SIM) formation [26] during the deformation process. Among these deformation mechanisms, SIM and deformation twinning, which result in TRIP and TWIP effect, respectively, has been reported to contribute to the high work hardening rate and uniform elongation. In addition, some hierarchical substructures such as secondary SIM and secondary/tertiary mechanical twinning are reported in metastable β titanium alloys as accommodation mechanisms [23, 25, 26]. These deformation mechanisms will be described in detail in the following.

1.2.1 Dislocation glide

Generally, dislocation slip is the most important deformation mode in metallic alloys, and even if they present other deformation mechanisms, this remains true in the BCC structure of the metastable β titanium alloys. Dislocations will glide on the most closely packed planes and along with the most closely packed directions of the crystal lattice. In the case of BCC structure, the most densely packed planes are the {110} planes, while dislocations slip could also be activated on the {112} and {123} planes. These three different families of planes have the same Burger vector along <111> direction, leading to 48 potential slip systems.

1.2.2 Deformation twinning

Mechanical twinning in the parent β phase plays a significant role in the mechanical properties of metastable Ti alloys as it results in the TWIP effect. The nucleation and growth of mechanical twinning under the loading process constitutes an alternative plastic deformation mode with the crystallographic dislocation slip in metastable Ti alloys.

A particular twinning mode can be identified by a set of four crystallographic parameters as illustrated in figure 1.4: the invariant plane of the shear K_1 and the shear direction (lying in K_1) η_1, as well as the conjugate plane K_2 and the conjugate shear direction η_2. The magnitude of shear is generally noted s.

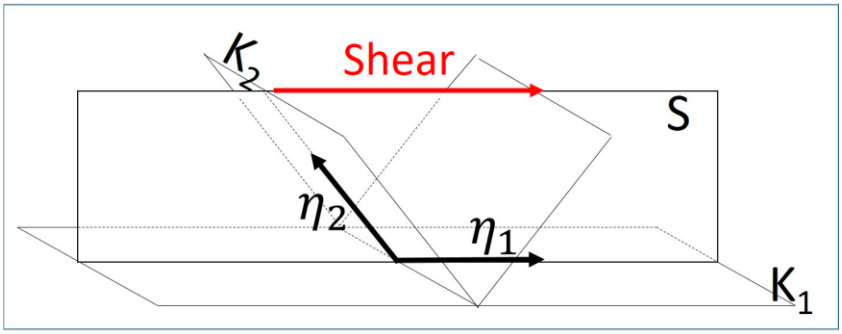

Figure 1.4 The twinning elements: K_1-twinning plane, η_1-twinning direction, K_2 – conjugate twinning plane, η_2-conjugate twinning direction [42].

Generally, in BCC structure, the {112}<111>$_\beta$-type is the most common twinning system [43, 44]. By contrast, {332}<113>$_\beta$-type twinning is unusual. It has long been known as a unique twinning mode for metastable β titanium alloys since its first identification in a Ti-Mo based alloy in 1971 [44]. Recently this mode of twinning has also been observed in iron based metastable alloys, such as Fe-Ni-C or Fe-Be alloys [42]. Today, both twinning systems {112}<111>$_\beta$ (hereafter called 112T) and {332}<113>$_\beta$ (hereafter called 332T) have been reported in the literature to occur in metastable β Ti alloys in correlation with the metastability of the alloys. The crystallographic parameters of 332T and 112T are tabulated in Table 1.1.

It is generally accepted that 112T forms by the collective glide of partial dislocations with the same burgers vector 1/6 <111> on successive {112} crystallographic planes. In the present work, this 112T is not the primary deformation mechanism in our metastable β Ti alloys, so it will not be discussed in detail here.

In contrast, 332T is generally considered to be one of the most important deformation mechanisms in metastable β Ti alloys. The 332T and its associated TWIP effect have attracted much attention due to the improvement of the strain-hardening rate it produces due to the dynamic Hall-Petch effect and the subsequent large uniform elongation obtained during tensile plastic flow before necking. The formation mechanism of 332T is still controversial. Different theories and models have been proposed to explain this particular twinning mode, but up to now, none of them have obtained a consensus in the community.

Croker proposed in 1962 a simple model, which combines shear and shuffle, to explain the formation of 332T [46]. The schematic of the model is shown in figure 1.5. In this model, the shear equals $n \cdot a/44$ $[113]_\beta$ (marked by the red arrow), where n denotes the number of atomic layers apart

from the interface. Then the half of the atoms undergo a shuffling of $a\sqrt{3}/4$ along with another $[113]_\beta$ direction.

This model is theoretically possible. However, a large amount of shuffle is needed, and the position of the atoms at the twin boundaries renders this mechanism unlikely in the present state. Compared to the normal BCC stacking, the atoms located on the first {332} layer on each side of the boundary are too close, which will result in huge repulsive energy. Therefore, the model is thus unlikely to occur.

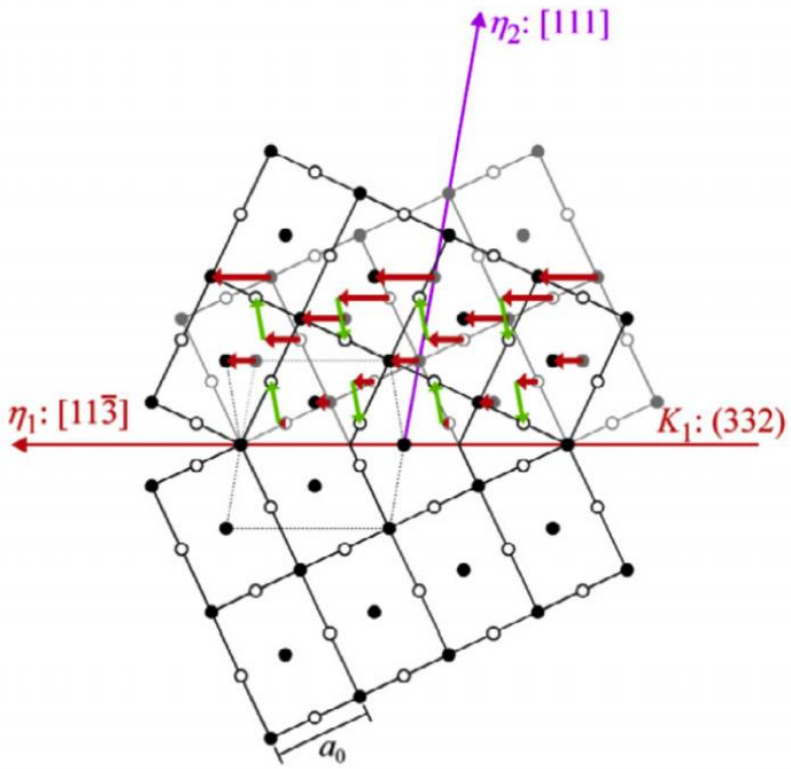

.

Figure 1.5 (1$\bar{1}$0) projection of (332)<11$\bar{3}$> twinning in BCC lattice. Red arrows represent shear direction and magnitude, while the green ones represent the shear direction and magnitude [46, 47].

In 1998, Kawabata et al. [48] proposed another model based on partial dislocations illustrated in figure 1.6. In their model, the twinning process is divided into three stages:

1. A shear resulted from the passage of the vector 1/22[$\bar{1}$1$\bar{3}$] (From L, M, and N to L', M' and N,' respectively) on S1 plane parallel to ($\bar{3}$32) plane (as shown in figure 1.6 a).
2. A shuffling of two third of the atoms (from L', M' and N' to L", M" and N", respectively) of magnitude 1/11{332}in opposite directions (as shown in figure 1.6b).
3. A secondary shear of 1/22[$\bar{1}$1$\bar{3}$] on S2 completing the elementary twin layer (as shown in

figure 1.6c).

However, this model still needs an additional shuffle.

Livinov and Rusakov proposed a similar partial dislocation mechanism by the glide of 5/22 <113> partial dislocation on a stack of {332} planes avoiding the additional atomic shuffle [49]. However, the plane and the direction are not close-packed, the question of why such partial dislocation mechanisms are energetically favorable remains open.

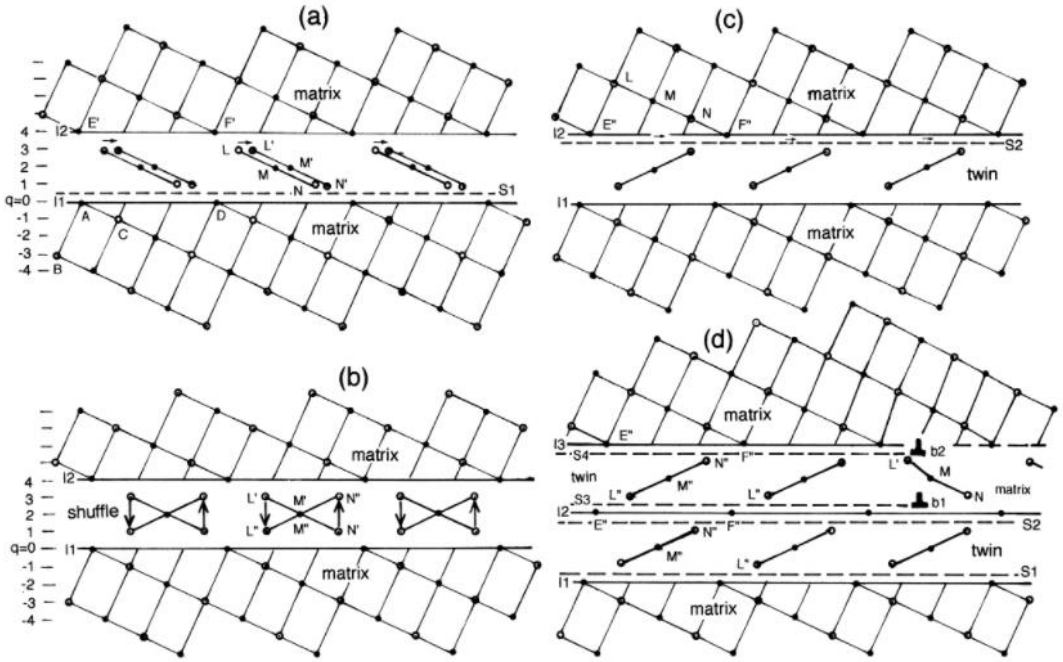

Figure 1.6 The proposed dislocation model for 332T on the (110) plane showing (a) a twinning shear of 1/22 [$\bar{1}1\bar{3}$] on the S1 plane, (b) shuffling of two-third of the atoms of magnitude 1/11{332}in opposite directions, (c) the completion of twinning for one elementary twinned layer by a secondary shear of magnitude 1/22 [$\bar{1}1\bar{3}$] on the S_2 plane, and (d) formation of a second twinned layer on the first one by the movement of a pair of stacked twinning dislocations which produces an equivalent structure to the sequence (a–c), and the ledge structure on the twin interface and a strain field around the ledge. [48].

Tobe et al. [47] proposed, in 2014, a new shear mechanism with a smaller shuffling magnitude compared to Croker's mechanism. The mechanism is illustrated in figure 1.7. The low shear modulus in β metastable Ti alloys causes lattice instabilities during straining, which bring small shifts in atomic positions in $\{110\}_\beta$ planes, leading to a pseudo tetragonal structure (t). Then, $(130)_t[\bar{3}10]_t$, which corresponds to 332T in the BCC β phase, occurs in the tetragonal lattice, where the shuffle magnitude is much decreased compared to the initial model of Croker [46].

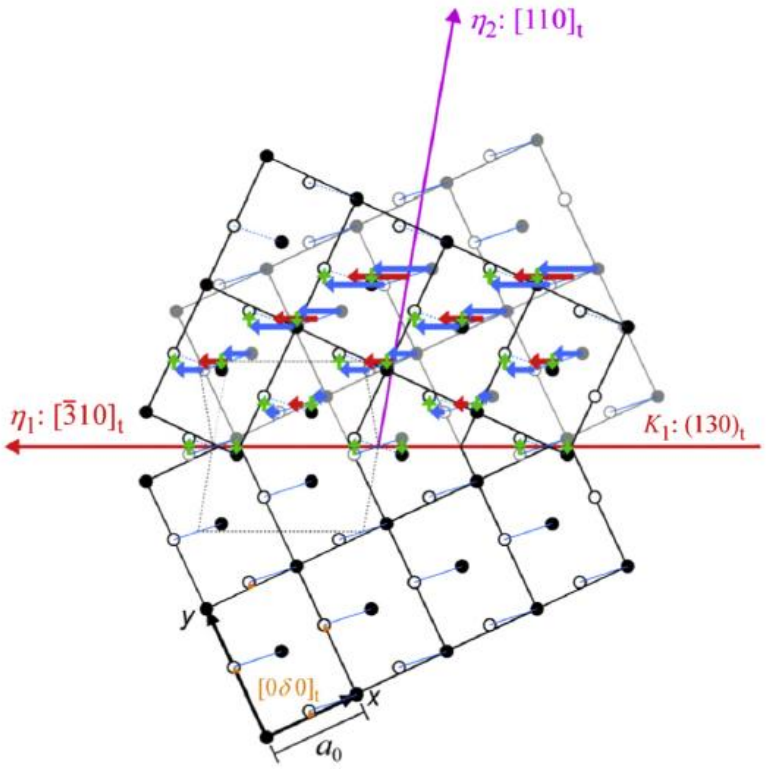

Figure 1.7 $(001)_t$ Projection of the $(130)_t[310]_t$ twinning in the tetragonal structure (d = 1/24). Closed circles represent atoms in the projection plane, and open circles are atoms $0.7071a_0$ above or below the projection. The red arrows indicate the shear of the lattice points. The blue lines and arrows indicate the motif units and the shear of the atoms comprising the units, respectively. The green arrows indicate the shuffle [47].

Recently, in 2016, a new twinning mechanism involving α″ martensitic transformation was proposed by Lai et al. and Castany et al. to occur during plastic deformation of metastable titanium alloys [50, 51]. It was found that the {130}<310>$_{α″}$ deformation twinning in α″ phase has a correspondence with 332T in BCC β phase and suggested that the α″ could activate 332T assisted twinning mechanism in metastable titanium alloys with low β stability. However, no direct evidence of this mechanism has been reported.

Currently, among all the possible mechanisms of 332T, no consensus has been achieved since no mechanism has been proved experimentally.

The schematic diagram of the selected area electron diffraction pattern of 112T and 332T twinning modes recorded along $[110]_β$ direction are illustrated in Figure 1.8.

Table 1.1 Twining modes observed in metastable β alloys. *s* denotes the magnitude of shear, K_1-twinning plane, η_1-twinning direction, K_2 – conjugate twinning plane, η_2-conjugate twinning direction, and *q* corresponds to the smallest number of lattice planes parallel to the twinning plane for reproducing the lattice in the twin [42].

Twinning Modes	Elements corresponding to twinning					
	s	***K*₁**	***K*₂**	***η*₁**	***η*₂**	***q***
112T	$2^{-0.5}$	{112}	$\{\bar{1}\bar{1}2\}$	$<\bar{1}\bar{1}1>$	<111>	2
332T	$2^{-0.5}/2$	{332}	$\{11\bar{2}\}$	$<11\bar{3}>$	<111>	4

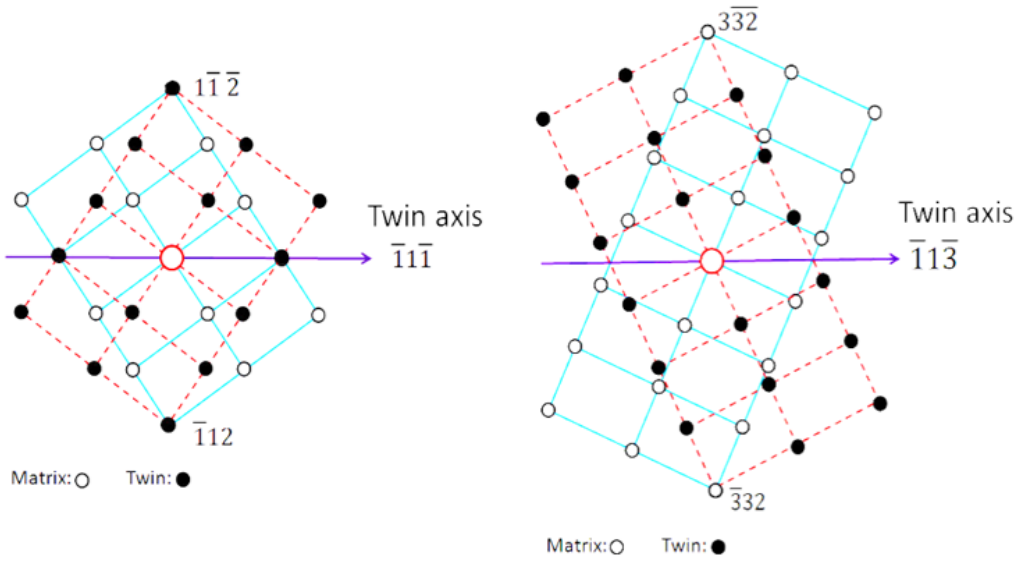

Figure 1.8 the schematic diagram of 112T and 332T diffraction spots with $[110]_\beta$ zone, respectively [52].

1.2.3 Martensitic transformation

Martensitic transformation is a kind of diffusionless, displacive solid-state structural transformation where a shear dominates the lattice change. Depending on their formation, martensite can be classified into thermally induced martensite, when a shift in temperature drives its formation, and stress-induced martensite (SIM), when the deformation causes its formation imposed to the alloy. In titanium alloys, two types of martensite can be found depending on the amount and nature of alloying elements it contains: α' with hcp structure [27], and α″ with orthorhombic structure [28], and both of them can be suppressed by adding β stabilizers elements above a critical value [27, 28]. In this study, metastable β titanium alloys are designed and heat-treated so that they only retain the β phase and slightly ω phase when quenched from the high-

temperature single β phase-field down to room temperature. Therefore, the thermally induced martensite will not be discussed in detail in this manuscript.

SIM α″ phase (orthorhombic) transformation is one of the most important features in metastable β-Ti alloys. This phase presents the smallest Young modulus among the phases in Ti alloys. Some metastable β-Ti alloys show a reversible martensitic transformation between a low-temperature phase, α″ martensite, and a high-temperature phase, β, resulting in shape memory effect or pseudo-elasticity with strain recovery while unloading [28]. Recently, extensive investigations have been carried out on the SIM α″ during plastic deformation resulting in the TRIP effect. Then the TRIP effect leads to a higher strain-hardening rate than in the case of simple dislocation glide leading to a large ductility in metastable β titanium alloys.

A more global theory called Phenomenological Theory of Martensite Crystallography (PTMC) was proposed and successfully applied in metastable β titanium alloys. Bowles and Mackenzie suggested that the martensitic transformation requires the transformation of one phase to the other one to be an invariant plane strain [30], meaning that the habit plane needs to be the invariant plane. However, in most cases, such a condition is not fulfilled if unit cell shape change between both phases, also called Bain strain, is considered alone. A rigid body rotation and a second strain have to be applied to respect this condition. This second strain has to keep invariant the lattice. It is called Lattice Invariant Shear (LIS) and can be produced by twinning or dislocation glide. The shear direction of this LIS will be determined by the mode of deformation (twins or dislocations). The magnitude of the LIS will determine the volume fraction of the twinned martensite or the density of dislocation lines at the habit plane. Inamura et al. [31] also showed that the types of martensitic twining inside martensite plates depend on the mismatch between the β matrix and the martensite due to the change of the unit cell of two phases.

Details of the crystallography of SIM α″ in metastable Ti-alloys, such as the habit planes and directions [13, 32], and the dependence of the crystal structure to the composition have been well characterized by experimental observations in good agreement with theoretical predictions. Several {hkk} types of habit planes have been reported such as $\{433\}_\beta$ habit plane in Ti-11Mo (wt. %) [32] and close to $\{755\}_\beta$ $\{111\}_\beta$ habit plane in Ti-23Nb-3Al (at. %) [31] and in Ti-53Ta (wt. %) [24]. According to these studies, the habit plane shows a dependence on lattice misfit (η_3), which can be calculated using *Eq* 1.3, between parent β phase and α″ martensite lattice parameters. When the η_3 becomes zero at a certain alloy composition, no LIS is necessary for the martensitic

transformation except a rigid body rotation [31]. Required LIS mode and magnitude, and thus the mean orientation of the final habit plane depends on the value of η_3. Experimental characterization revealed that the habit plane was $(7\bar{5}\bar{5})_\beta$ when $\eta_3 = 0$, and the planes moved to $(1\bar{1}\bar{1})_\beta$ when η_3 = 0.0055 or -0.0018 [31].

In the present work, we are interested in the stress-induced martensite in the Ti-12Mo alloy during tensile deformation. The PTMC will be used here to predict the potential deformation that SIM can produce. These predictions are calculated with the lattice parameters of both phases for Ti-12Mo alloy measured under tensile load by in-situ synchrotron X-ray diffraction [23], and using $\{111\}_{\alpha''}$ (type I) twinning as the lattice invariant shear (LIS) [31], and the following orientation relationships illustrated in figure 1.9 [34]:

$<110>_\beta // [001]_{\alpha''}$, $\{110\}_\beta // (001)_{\alpha''}$, and $\{112\}_\beta // (110)_{\alpha''}$

According to these relationships, six lattice correspondence variants (CVs) of α″can be defined and are designated as CV1 to CV6, and listed in Table 1.2. The principal strains during the β to α″ transformation are calculated as:

$\eta_1 = (a_{\alpha''} - a_\beta)/a_\beta$ (*Eq*. 1.1)

$\eta_2 = (b_{\alpha''} - \sqrt{2}\, a_\beta)/\sqrt{2}\, a_\beta$ (*Eq*. 1.2)

$\eta_3 = (c_{\alpha''} - \sqrt{2}\, a_\beta)/\sqrt{2}\, a_\beta$ (*Eq*. 1.3)

Where the lattice parameter of the β phase is a_β, and those of SIM α″ are $a_{\alpha''}$, $b_{\alpha''}$ and $c_{\alpha''}$ (table 2.1).

In the normalized basis β, the transformation strain, s_i, resolved on the tensile direction, $[_\beta\ ;\ u]$, resulted from the transformation of β phase to each potential SIM α″ CV_i (i = 1 - 6) can be calculated as:

$s_i = (u\ ;_\beta)(_\beta\ \varepsilon_i\ _\beta)[_\beta\ ;\ u]$. (*Eq*. 1.4)

where ($_{\beta}\,\varepsilon_{i}\,_{\beta}$) *is* the transformation tensor for each CV given in ref. [35]. The notation scheme is adopted from the crystallography of martensite transformations introduced by Bowles and Mackenzie [30].

Table 1.2 Six lattice correspondence variants (CV) derived from β to α″ crystals.

Variant	$[100]_{\alpha''}$	$[010]_{\alpha''}$	$[001]_{\alpha''}$
CV1	$[100]_{\beta}$	$[011]_{\beta}$	$[0\bar{1}1]_{\beta}$
CV2	$[100]_{\beta}$	$[0\bar{1}1]_{\beta}$	$[0\bar{1}\bar{1}]_{\beta}$
CV3	$[010]_{\beta}$	$[101]_{\beta}$	$[10\bar{1}]_{\beta}$
CV4	$[010]_{\beta}$	$[10\bar{1}]_{\beta}$	$[\bar{1}0\bar{1}]_{\beta}$
CV5	$[001]_{\beta}$	$[110]_{\beta}$	$[\bar{1}10]_{\beta}$
CV6	$[001]_{\beta}$	$[\bar{1}10]_{\beta}$	$[\bar{1}\bar{1}0]_{\beta}$

The prediction for one variant of α″ (CV1) is shown in table 1.3 as an example. Two habit plane variants, namely CV1 (+) and CV1 (-), were predicted for CV1, which are near to $\{755\}_{\beta}$ plane. The magnitude of the LIS for both habit plane variants are very small, implying that almost no twinning is needed as LIS.

Table 1.3 Prediction based on the invariant plane strain theory for the α" martensite crystallography in a Ti-12Mo alloy (Lattice parameters were measured under tensile loading at ε = 0.024[23]).

lattice parameter (Å)	β	α″		
	a_{β}	$a_{\alpha''}$	$b_{\alpha''}$	$c_{\alpha''}$
	3.27924	3.07871	4.91978	4.63289
Transformation strain of CV1, e_1	$\begin{pmatrix} -0.06188 & 0 & 0 \\ 0 & 0.03272 & 0.03177 \\ 0 & 0.03177 & 0.03272 \end{pmatrix}$b			
	Solution 1		Solution 2	
variant	CV1(+)		CV1(-)	
Habit plane	(0.6875 0.5212 0.5057) $_{\beta}$		(0.6976 -0.5218 -0.4910) $_{\beta}$	
Transformation strain direction	$\begin{pmatrix} -0.7409 \\ 0.4896 \\ 0.4597 \end{pmatrix}$		$\begin{pmatrix} -0.7315 \\ -0.4889 \\ -0.4753 \end{pmatrix}$	
LIS magnitude	0.0058		0.0058	

The amount of SIM α″ phase occurred during the deformation process depends on several parameters like chemical composition [38], grain size [39, 40], initial texture [41], the presence of ω phase [16], etc.

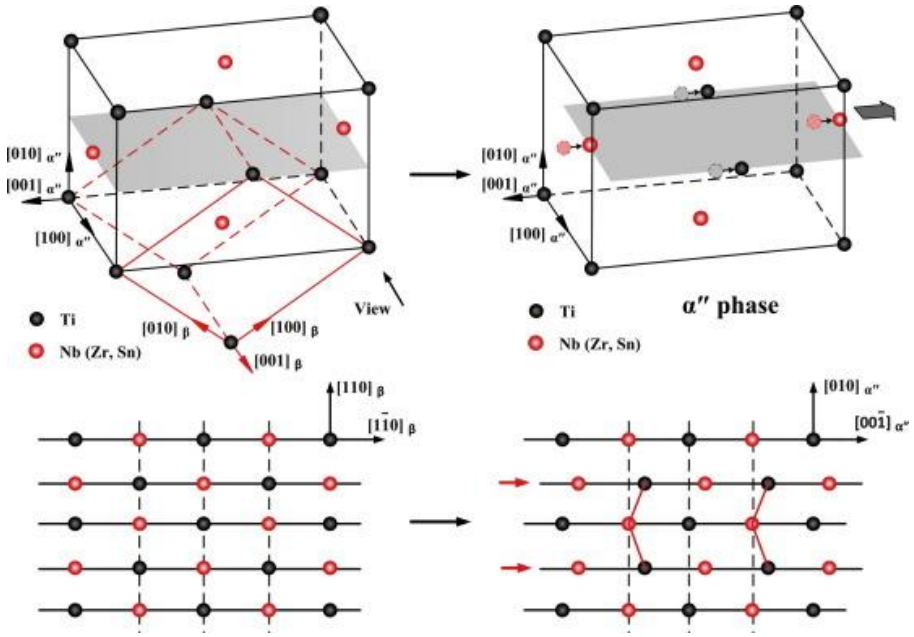

Figure 1.9 Illustration of lattice correspondence between β and α″ [34].

Recent investigations have confirmed the occurrence of mechanical twinning in α″ during a plastic tensile process in metastable β Ti alloys, which could provide more strain along the tensile direction. Two mechanical twinning modes for martensite α″, have been reported in the literature [37] in metastable β alloy, i.e. {130}<310>$_{α″}$ and {110}<110>$_{α″}$.

The crystallographic parameters of {130}<310>$_{α″}$ and {110}<110>$_{α″}$. Twinning are tabulated in Table 1.4, and according to these data, the {130}<310>$_{α″}$ and {110}<110> $_{α″}$ mechanical twinning are reciprocal i.e. $K_1(130) = K_2(110)$, $K_2(130) = K_1(110)$. $\eta_1(130) = \eta_2(110)$, and $\eta_2(130) = \eta_1(110)$, which means they are practically identical, except for the atomic shuffle required in each case. The {130}<310>$_{α″}$ martensitic mechanical twinning (hereafter called 130 α″ DT) system formed in martensite in the plastic stage during tensile stress has been widely observed in superelastic Ti-Nb [51, 64, 66] and TRIP/TWIP Ti-Mo based alloys [38, 63]. Due to the crystallographic equivalences of the twinning elements between {130}<310>$_{α″}$ twinning in α″ and {332}<113> $_{β}$ in the parent β phase, the reversed transformation from 130 α″ DT to β matrix has been proposed to be the origin of {332}<113>$_{β}$ twining (will be described in chapter 1.2.2) in β metastable alloys[50-51]. Otherwise, in-situ observations in TRIP/TWIP Ti alloys have shown a

detwinning process from 130 α″ DT to its parent SIM α″ during tensile unloading [38]. About the twinning activation, Yang et al. reported that the selected variant of 130 α″ DT activated in primary SIM α″ obey the Schmid law in Ti2448 alloy [64], and similar phenomena were observed by Bertrand et al. in Ti-25Ta-20Nb alloy [35]. Besides 130 α″ DT mode, the {110}<110>$_{\alpha''}$ mode (hereafter called 110 α″ DT), with twinning elements equivalent to {112}<111>$_{\beta}$ mode (will be described in chapter 1.2.2) in the parent α″ phase, has also been reported to be operational in plastic deformation stage near the surface of TRIP/TWIP Ti alloys [65, 66].

Table 1.4 Two possible α″ twinning modes in metastable β Ti alloys.

Twinning mode	K_1	K_2	η_1	η_2
{130}<310>$_{\alpha''}$	{1$\bar{3}$0}	{110}	<310>	<1$\bar{1}$0>
{110}<110>$_{\alpha''}$	{110}	{1$\bar{3}$0}	<1$\bar{1}$0>	<310>

The transformation strains, s_i, of variant i of the two modes of mechanical martensitic twinning resolved on any tensile direction n, can be calculated in the normalized α″ basis as:

$$S_i = \frac{\left|\left[I+S(\tilde{d}\cdot\tilde{p}^t)\right]\cdot n\right|}{|n|} - 1 \qquad (Eq.\ 1.5)\ [36]$$

Where, $\tilde{d}$ is twinning direction, $\tilde{p}$ is twinning plane, the shear magnitude S is 0.1872 for both {130}<310>$_{\alpha''}$ and {110}<110>$_{\alpha''}$ mechanical twinning [37].

1.3 Prospects of metastable β titanium alloys in the application of cardiovascular stents

As a kind of life-saving device to treat coronary artery disease, Cardiovascular stents are one of the most significant medical breakthroughs in the 21st century. Since 1994 [53], when the bare metal stent was introduced into the clinical arena, several alloys have been developed as material for metallic stents. The working mechanism of these stents is shown in figure 1.10. These stents are used for dilation to counteract the decrease in the stenotic vessel's diameter and maintain sufficient blood flow. Therefore, minimal mechanical requirements must be met to support the

vessel while preventing elastic recoil during balloon expansion. The material selection for the stent is a multiple performance indexes problem involving multiple constraints and compound objectives—some of the limitations conflict, resulting in one property's harmful effects on other performances. Therefore, the standard procedure for dealing with multiple constraints [54] has been performed in the previous stent R&D. The brief description of the selection strategy and the quantitative material specifications are provided in the manuscript. The strategy to select correct materials from existing ones or to develop new materials for stent requires to achieve the subtle balance between yielding stress, ultimate tensile stress, ductility, elastic modulus, and hardening rate to satisfy in priority the structural function, then the optimizations on radio-opacity, biocompatibility, magnetic resonance imaging (MRI) compatibility and other properties can be considered for the selection among the candidate materials approved with mechanical balance, or as the pre-considerations since the design of new materials. In literature, a yield strength (YS) of about 200MPa, an ultimate tensile strength (UTS) above 300MPa, and enough elongation before fracture (>15%) are usually adopted as mechanical requirements for stent in material researches. A steep strain-hardening rate leads to a desirable rise in strength during expansion. However, the above specifications are oversimplified and misleading for practical stent applications as guiding specifications for new material development. The reason is that the performance of the stent following those requirements will not only be essentially inferior to the conventional CoCr stent in terms of mechanical strength (YS:600MPa, UTS:1100MPa) and ductility (> 40%) but could also aggravate the recoil problem of CoCr stent (about 5%) by looking for high strain-hardening rate. Recently, Foin et al. suggested that the thickness of stents strut has an important impact on injury and inflammation: a thicker stent could lead to a higher degree of inflammation and neointimal hyperplasia than a thinner stent [55]. These alloys for stents also need to process high Young's modulus and suitable strain-hardening rate, which are required in order to minimize elastic recoil (< 4%). Besides the mechanical behavior, the performance of the stent material depends on the appropriate flexibility, radial force, resistance to fracture, radio-opacity, biocompatibility, and non-ferromagnetic for safe MRI [56]. CoCr alloys such as the L605 (Co-20Cr-15W-10Ni, wt. %) and the MP35N (Co-Cr-35Ni-10Mo, wt. %) were qualified mechanically in stent applications to meet these requirements [56]. However, Co metal is considered a new carcinogenic, mutagenic and toxic to reproduction (CMR). It will be banned in the EU as material for implantations for the human body after 2025 [57]. Reducing the strut thickness and using

biocompatible alloying elements for the next-generation stent are the overall critical objectives for the new stent material research.

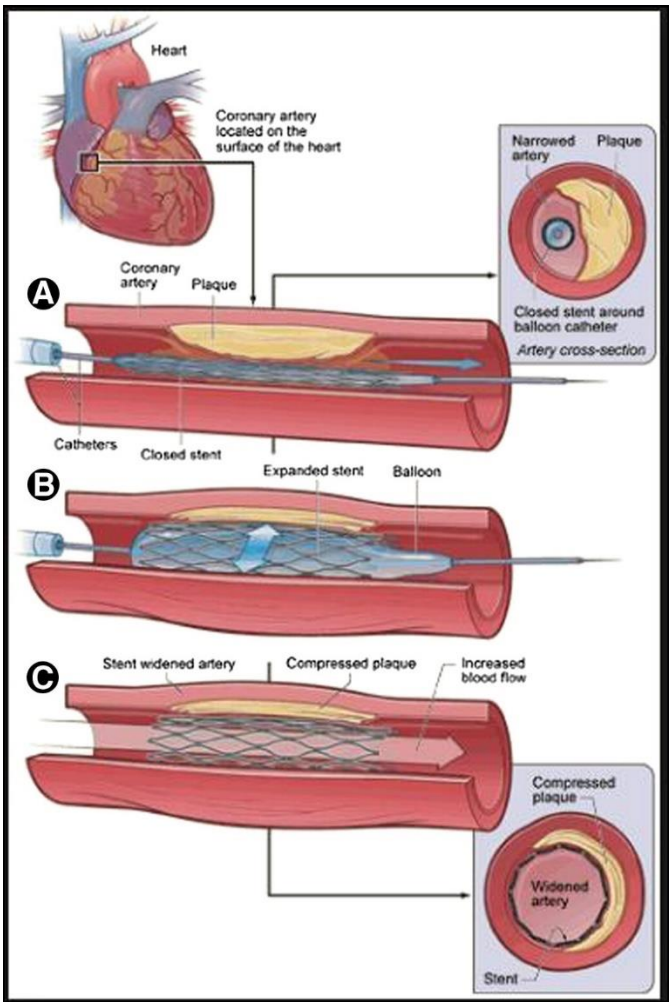

Figure 1.10 The working mechanism of balloon-expandable stent [58].

Ti and some Ti alloys show good biocompatibility and corrosion resistance, which lead to their use in implantations in the human body. At the same time, commercially pure Ti (CP Ti) and traditional Ti alloys are not used for stents for several reasons. Firstly, the mechanical properties of CP Ti and conventional Ti alloys hardly meet the requirement of stents [59]. As shown in figure 1.11, the tensile strength of CP Ti is much lower than that of Co-Cr alloys and stainless steel. Thus, the rigidity of the CP Ti stent is challenging to resist the elastic recoil pressure of blood vessels. In addition, the plasticity of CP Ti and traditional Ti alloys (Ti-6Al-4V) is low compared to Co-Cr alloys, which may lead to fracturing occurring during service, and the alloys may not follow plastic

deformation during balloon expansion [59]. In addition, as light metals, the CP and Ti6Al4V are unsuitable for X-ray imaging due to their low radio-opacity [59].

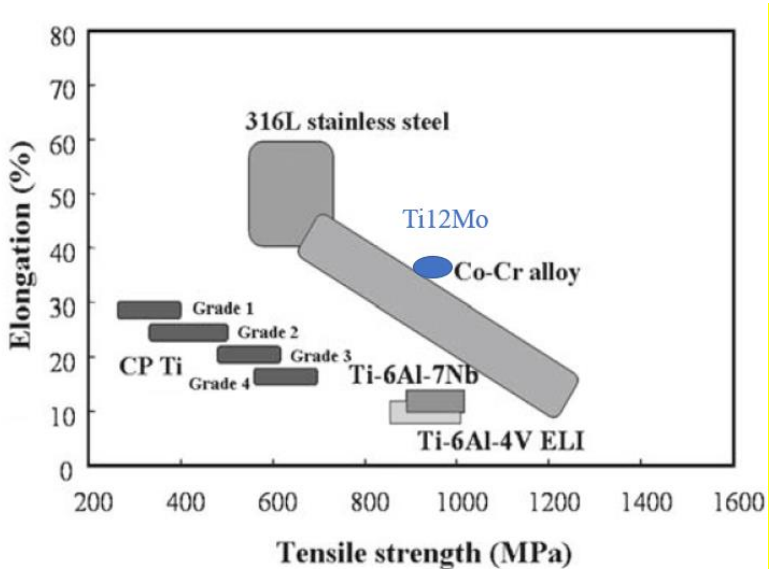

Figure 1.11 Tensile strength and elongation balance of various metals for medical use made based on the ref [59].

Recently, a new generation of TRIP/TWIP metastable titanium alloys dedicated to biomedical applications has been developed. As mentioned above, in these alloys, SIM transformation (orthorhombic α"), deformation twinning, and precipitation hardening (ω or α phase) can be observed, which leads to a combination of high strength and high ductility. Besides, the addition of β stabilizers such as Mo, Nb, and W could increase the density of titanium alloys. Therefore, these TRIP/TWIP alloys can be attractive with improved density, high strain-hardening rate, ductility, and strength. Some studies focus on the Ti-Mo based TRIP/TWIP alloys due to their excellent mechanical behavior (as shown in figure. 1.11 and Table 1.5) [33, 60]. Table 1.5 lists relevant properties for the Ti-Mo alloys, CP Ti, traditional alpha/beta Ti alloys, and primary alloys used in permanent implants. As shown in Table 1.5, Ti-12Mo has the potential to be an alternative alloy for stent application due to its combination of high strength, high strain-hardening rate, and excellent elongation.

Table 1.5 Physical and mechanical properties of selected materials made based on ref [33, 56, 60].

	Density (g/cm^3)	Elastic Modulus (GPa)	UTS (MPa)	Yield Strength (MPa)	UTS-Yield (MPa)	Elong. (%)	Elastic Range (%)
Stainless steels							
Fe-18Cr-14Ni-2.5Mo "316LVM"	7.95	193	670	340	330	48	0.17
Fe-21Cr-10Ni-3.5Mn-2.5Mo	7.90	195	740	430	310	35	0.22
Fe-22Cr-13Ni-5Mn	7.88	193	827	448	379	45	0.23
Fe-23Mn-21Cr-1Mo-1N	7.63	190	931	607	324	49	0.32
Cobalt alloys							
Co-20Cr-15W-10Ni "L605"	9.10	243	820-1200	380-780	420-600	35-55	0.16-0.32
Co-20Cr-35Ni-10Mo "MP35N"	8.43	233	930	414	516	45	0.18
Co-20Cr-16Ni-16Fe-7Mo "Pynox"	8.30	221	950	450	500	45	0.20
Titanium alloys							
CP Ti Grade 1	4.50	107	300	200	100	30	0.19
Ti-6Al-4V (alpha/beta)	4.43	105	860	795	65	10	0.72
Ti-6Al-7Nb (alpha/beta)	4.74	106	1000	900	100	12	0.85
Ti-15Mo (beta)	4.95	83	793	655	168	22	0.79
Ti-12Mo (beta)	4.84	82	974	480	494	45	0.50

The quantitative specifications of ideal stent material rationalized from previous studies for industrial product R&D are presented in table 1.6 for the thin-strut stent. The specifications are used as a reference in this study as design objectives and evaluation references for TRIP/TWIP Ti alloys. For the thin-strut stent material, to adapt to its working condition, these materials are required to process good mechanical properties (high yield stress, high ultimate tensile stress, and high ductility), Low recoil (require high strain hardening rate and high elastic modulus), high X-

ray visibility (require high mass attenuation coefficient, *Mc*, and high mass magnetic susceptibility, c_{alloy}.), low MRI artefact, and high corrosion resistance.

Table 1.6 Specifications for L605 stent alloy [59].

Stent performance	Properties associated	L605
Stent strut thickness < 100μm	High yielding stress	600 MPa
High fracture resistance during expansion	High ultimate tensile stress	1100 MPa
	High ductility	50%
Low recoil after expansion	Reasonable strain hardening rate	2000~2300 MPa
	High elastic modulus	233 GPa
High X-ray visibility	mass attenuation coefficient, Mc_{alloy}*	0.99 cm^2/g
	Density, ρ_{alloy}	9.1 g/cm3
High MRI compatibility **	Low magnetic susceptibility	9.71 x 10^{-6} cm^3g^{-1}
High corrosion resistance	High corrosion breakdown potential, *Eb* ***	819 mV
	Biocompatibility	Conform to ISO 10993 and ASTM standards

* $Mc = \sum_{i=1}^{n} c_i \times \frac{u_i}{\rho_i}$ *(Eq. 1.6)*

Mc is the mass attenuation coefficient of alloy; m_i: linear attenuation coefficient of element *i*; c_i is the mass fraction of alloying element *i*; r_i is the density of part *i* [61]. Eq calculates the mass attenuation coefficient of L605 alloy and other metastable Ti alloy. 1.6 under the medical X-ray with the energy of 100keV.

** c_{alloy}: $c_{alloy} = x_{alloy} \times \rho_{alloy} = \sum_{i}^{phase\ (\alpha,\ \beta,\omega\ldots)} V_i \times x_i \times \rho_i$ *(Eq. 1.7)*

Where v_i is the volume fraction, c_i is the mass magnetic susceptibility, and ((i) density of phase *i* [62].

*** *Eb*: breakdown potential defined in ASTM F2129.

Figure 1.11 shows the results of MRI compatibility of L605 alloy and metastable Ti alloys (beta phase and ω phase), calculated according to *Eq*. 1.7. The metastable titanium alloy (β + ω) process has lower MRI compatibility than the L605 alloy.

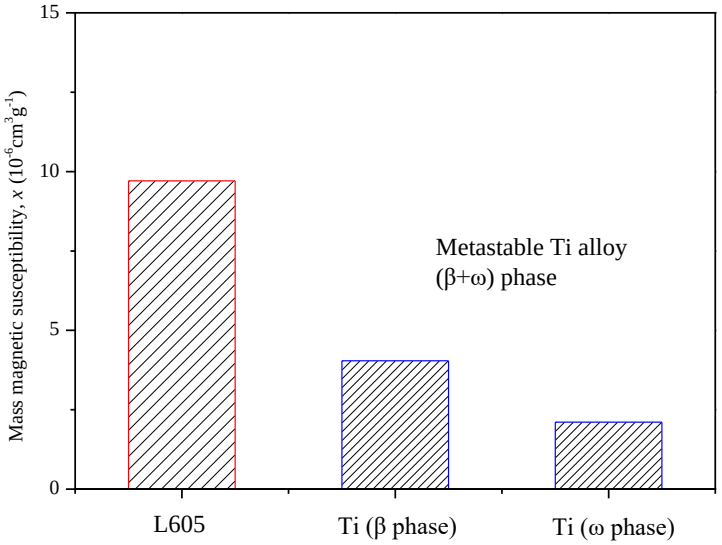

Figure 1.12 mass magnetic susceptibility of L605 alloy and metastable Ti alloy (β and ω).

1.4 The mechanical behavior and deformation mechanism of Ti-12Mo

Ti-12Mo, as a metastable TRIP/TWIP β titanium alloy, was reported to exhibit excellent mechanical performance (as shown in figure 1.13): large strength, large ductility, and a significant work-hardening effect close to the theoretical limit [23]. As shown in figure 1.13, the corresponding strain-hardening rate (dσ/dε) and true strain curve are similar to those for some TRIP/TWIP steels and could be divided into three stages. Stage I corresponds to the conventional transition between the elastic and the onset of plastic range; The strain-hardening rate increases monotonically from the onset of plastic range to ε = 0.1 at Stage II (the early deformation stage); And then the strain-hardening rate decreases in stage III (the late deformation stage). The transformation pathways and combined TRIP/TWIP effects have been carefully investigated in every evolution stage, especially the early stage.

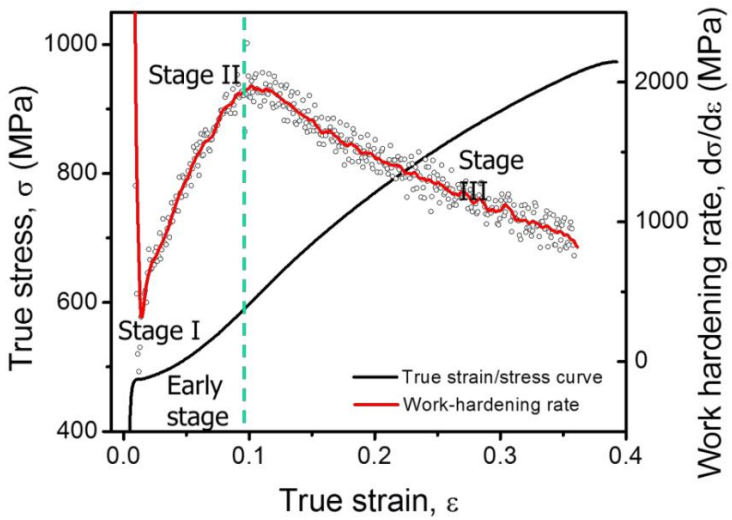

Figure. 1.13 Tensile true strain/true stress curve of solution treated Ti-12Mo alloy is shown in black line. The corresponding work-hardening rate, dσ/dε, is plotted in black cycles, and the soothed curve is shown in red [23].

The deformation mechanism and microstructure evolution of Ti-12Mo in the early stage have been reported by Sun et al. [23]. Figure 1.14 illustrates the microstructure evolution during tensile deformation. According to their observation, the stress-induced ω phase appears at stage I and gradually disappears during subsequent straining. With the increase of the strain, depending on the local Schmid factor (SF) concerning the external stress, the primary 332T and primary SIM α″ are activated simultaneously in the early plastic deformation stage (stage II). In the meantime, the secondary twinning and secondary SIM α″ occur in the primary 332T and continue to form in stage III. Focusing on the model TRIP/TWIP Ti-12Mo alloy, Cho et al. [63] proposed another hypothesis (illustrated in figure 1.15) on the deformation mechanisms: SIM α″ can act as a nucleation site for 332T, and then the SIM α″ could be progressively replaced by 332T with further loading [63]. According to their hypothesis, the nano-sized SIM α″ is firstly activated from β matrix at the initial plastic stage. SIM α″ will be orientated and/or twinned in 130 α″ mode with the increase of stress. In the meantime, 332T could be nucleated within reoriented and/twinned α″. Thus, the 332T could grow and replace the SIM α″. Therefore, different transformation mechanisms and sequences have been observed and proposed in the Ti-12Mo alloy. Lilensten et al. have reported dependence of the deformation mechanism on the orientation of the grain with the tensile direction, which plays a role in the selection of the primary deformation mechanism, SIM α″ or deformation twinning in a TRIP/TWIP alloy, strongly suggesting that all grain do not undergo the same deformation path

[41]. Despite numerous attempts, the interplay of the two deformation mechanisms and the transformation pathways occurring in metastable Ti-alloys remain only partially understood, making these materials' mechanical behavior difficult to predict. Thus, the transformation pathways operating in the β grains of a β-metastable Ti-12Mo alloy for different orientation conditions were carefully investigated via Schmid Factor calculations coupled with in-situ SEM and ex-situ TEM observations in Chapter 3.

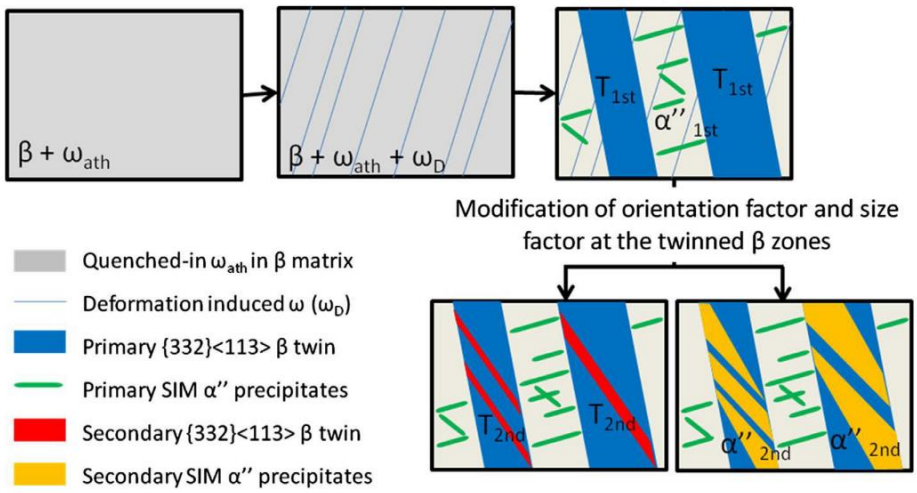

Figure 1.14 Schematic illustration of the evolution of the microstructure of the Ti-12Mo alloy when deformed in tension. The activation sequence of different deformation mechanisms is shown from the ST state to the early deformation stages (Stage I and stage II) [23].

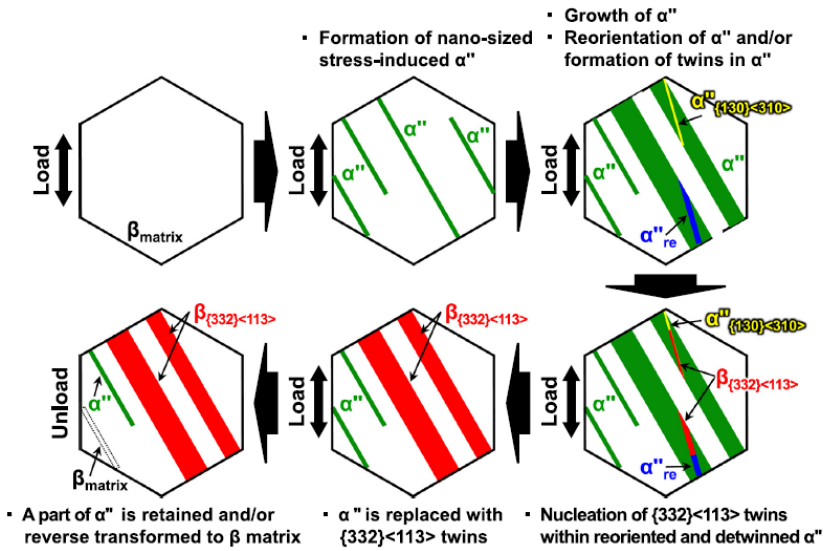

Figure 1.15 Schematic drawing for the formation behavior of the 332T nucleated within the nano-sized SIM α″ phase [63].

SIM α″ plays a vital role in improving the strain-hardening rate and the subsequent significant uniform elongation during tensile plastic flow [33, 38, 63]. As accommodation mechanisms, secondary martensite deformation twinning as hierarchical substructures has been reported in TRIP/TWIP Ti alloys [38]. The 130 α″ DT system formed in martensite in the plastic stage during tensile stress has been widely observed in metastable β titanium alloys [35, 51, 63]. Due to the crystallographic equivalences of the twinning elements between 130 α″ DT in α″ and 332T in the parent β phase, the reverse transformation from 130 α″ DT to β has been proposed to be the origin of 332T in β metastable alloys [35, 50, 51, 63]. Otherwise, *in-situ* observations in TRIP/TWIP Ti alloys have shown a detwinning process from 130 α″ DT to its parent SIM α″ during tensile unloading [38]. About the twinning activation, Yang et al. reported that the selected variant of 130 α″ DT activated in primary SIM α″ obey the Schmid law in Ti2448 alloy [64], and similar phenomena were observed by Bertrand et al. in Ti-25Ta-20Nb alloy [35]. Besides 130 α″ DT and 110 α″ DT, with twinning elements equivalent to 112T mode in the parent β phase, have also been reported to be operational in the plastic deformation stage near the surface of TRIP/TWIP Ti alloys [64, 65]. Yang. et al. [66] suggested that the reversion of 110 α″ DT was one of the origins of 112T in β metastable alloys.

Deformation products have been observed to detain into the parent SIM α″ or revert to the mother β phase during stress release [35, 38, 50, 51, 63]. However, the twinning mode selection, the twinning process, and the detwinning mechanisms are still unclear since the SIM α″ twinning products can be mechanically unstable. Therefore, the instability of α″ twinning products results in difficulties and uncertainties to interpret the results of ex-situ studies (EBSD and TEM [67]). To study the operative mechanisms, the martensitic mechanical twinning of this material at the micrometric length scale has to be investigated under *in-situ* conditions. The operative mechanisms of martensitic twinning will be examined in Chapter 4.

Chapter 3 and chapter 4 continue to understand in depth the transformation mechanisms in Ti-12Mo. This knowledge could be used to control the TRIP/TWIP effect via thermomechanical treatment and develop new TRIP/TWIP Ti alloys by optimizing the chemical compositions for stent applications.

Thermomechanical treatment is a universal method to modify the mechanical properties and microstructure of alloys. Chen et al. [17] suggested that the structural evolution of the ω phase during aging at 300℃ controls the deformation mechanism transition from a twinning-to-dislocation slip in Ti-Mo alloy, such a transition being the origin of ductile-to-brittle transition of this alloy. Sun et al. [18] reported that low temperature aging treatments for a short time could enhance the yield strength while preserving the ductility in ω containing Ti-12Mo alloy, as shown in figure 1.16. In addition, Lai et al. also reported that the mechanical behavior could be significantly affected by ω_{iso} phase precipitation due to the suppression of TRIP and TWIP effects [16]. These results open a new strategy for aging at ω_{iso} transformation temperature to nucleate ω_{iso} in titanium, strengthening the alloy while retaining substantial ductility. The mechanical behavior and deformation mechanism of metastable β-Ti alloys are also dependent on the grain size of the alloy. Wang et al. [68] observed that the 332T becomes more difficult as the average grain size decreases. However, Bhattacharjee et al. [39] suggested that the triggering stress of SIM α″ increase with the increasing β grain size in the solution treated Ti-10V-2Fe-xAl (wt. %) with grain size ranging from 100μm to 475μm. A similar phenomenon also has been reported in Ti-16V-3.5Al-3Sn (wt. %) alloy with grain sizes in the range 1.3μm~30μm [40]. The grain size of the Ti-12Mo alloy could be controlled by the solution treatment time, i.e., the grain size will increase with the increase of solution treatment time. As mentioned above, the transformation pathways are not unique and are dependent on the orientation of grains. The effect of grain size and ω_{iso} on the mechanical behavior and TRIP-TWIP effects as well as the orientation-dependent transformation pathways, will be carefully investigated in Chapter 5.

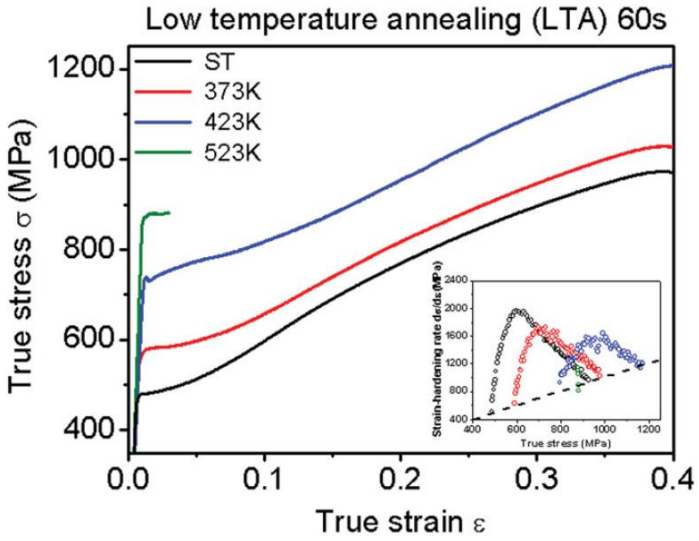

Figure 1.16 True strain-true stress tensile curves of the ST specimen and low temperature aging specimens. The corresponding strain-hardening rates are shown in the inset figure [18].

Optimizing the chemical compositions is another universal way to change the mechanical properties and microstructure of alloys in metallurgy. As well-known, the TRIP and TWIP effects and their influence on mechanical properties are highly dependent on the stability of the β phase in Ti-alloys. Martensitic transformation (β → α″) can be favorably activated by applying external stress or strain in the β-metastable Ti-alloys when the stability of β phase retained by water quench (usually estimated by Mo-equivalent content, Mo_{eq} wt. %) is relatively low at a rough range of 10.0% ≤ alloy Mo_{eq} ≤ 13% [69, 70]. Mechanical twinning can be mainly activated when the β stability increases (Mo_{eq} roughly between 12% and 15%) [33, 60, 71]. For alloys displaying intermediate β stability (the overlapping zone between the two ranges), the simultaneous occurrence of TRIP/TWIP effects has been observed [33, 72, 73]. Therefore, a continuous transition of deformation mechanisms, from near-TRIP to near-TWIP, can be expected by increasing the chemical stability of a TRIP/TWIP alloy progressively. The Zr element is a neutral element (in the Ti-Zr system) or a weak β-stabilizing element (in the Ti-Nb-Zr system) [74, 75]. Previous studies have reported that the nature of Zr in a Ti-M-Zr system (M = β-stabilizer alloying element) strongly depends on the β-stability and concentration of M [74-78]. A theoretical equivalence factor of Zr in the Mo_{eq} estimation has been proposed to be +0.47 by Wang et al. [79], showing that the β stabilizing effect of Zr is about half of that of Mo. Therefore, using Zr could be two-fold advantageous since a wide composition range (up to tens of weight percent) can be added

into the master alloy: (1) to achieve better tolerance of alloys composition for TRIP/TWIP fine-tuning; (2) to obtain the solid solution strengthening effect. The effect of Zr addition on the mechanical behavior and the TRIP to TWIP transition in Ti-12Mo alloys will be studied and discussed in Chapter 6.

Radio-opacity is an important criterion for permanent implants to facilitate the surgeon's work during their placement by improving their visibility under X-rays. The addition of tungsten in proper amounts could improve the Ti-based implants' radio-opacity due to the high density of this element. Tungsten can be regarded as a β-stabilizing element, which is weaker than Mo element. Therefore, a series of novel quaternary Ti-W-Mo-Zr alloys was developed by replacing Mo with W in the Ti-Mo-Zr based alloys to get higher density and maintain excellent mechanical properties. Ti-Mo-Zr-based alloys possessing high strength, excellent ductility, and good industrial potential are reported in Chapter III. Among these alloys, a metastable β Ti-W-Mo-Zr with a combination of high strength, high ductility, excellent strain-hardening rate, and improved density ($5.7 g/cm^3$) was designed and fabricated. Its mechanical behavior, microstructure evolution, biocompatibility evaluation, and finite element analysis of cardiovascular stents made from the alloy will be carefully investigated in Chapter 7.

Hence to solve the limitations of Ti-12Mo alloys on the application of cardiovascular stent, my thesis focus on the following points:

1. In order to build an in-depth understanding of Ti-12Mo alloy and thereby improve its mechanical behavior by thermomechanical treatment, transformation pathways operating in the β grains of a β-metastable Ti-alloy for different orientation conditions were carefully investigated via SF calculation coupled with in-situ SEM and ex-situ TEM observations.
2. The effects of grain size and ω_{iso} hardening treatment at low temperature (holding at 200℃) for a short time (60s~150s) on mechanical properties and the transformation mechanisms during the deformation process in TRIP/TWIP Ti-12Mo alloy will also be well studied in the thesis.
3. To further clarify the role of martensitic transformation and its twinning in the deformation process of Ti-12Mo, the SIM α″ transformation with twinning and detwinning evolution was traced by in-situ investigations (EBSD and TEM) under tensile loading and unloading conditions.
4. By adding Zr to Ti-12Mo, an increase in yield strength was obtained while maintaining high plasticity. Based on the results, the deformation mechanisms involved in the macroscopic mechanical behavior are discussed by considering the heterogeneous nature of the microstructural

evolution.

5. The substitution of Mo by W in Ti-Mo-Zr-based alloys increased its density and radio-opacity while maintaining relevant mechanical properties.

Chapter 2 Experimental procedure

2.1 Introduction

The experimental technique, fabrication, manufacturing, heat-treatment, and characterization of designed alloys are introduced in this chapter. The research route is summarized in figure 2.1: after fabrication of the alloy by arc melting, the homogenization treatment, cold-rolling, and recrystallization heat treatments are applied. Then, tensile tests samples are taken from the heat-treated samples. Finally, the deformation mechanism, the transformation mechanisms, the microstructural observation are traced and observed by these in-situ and ex-situ investigations. Meanwhile, different thermal treatments were designed and applied to the alloys to improve mechanical behaviors. All these steps are described in detail in the following.

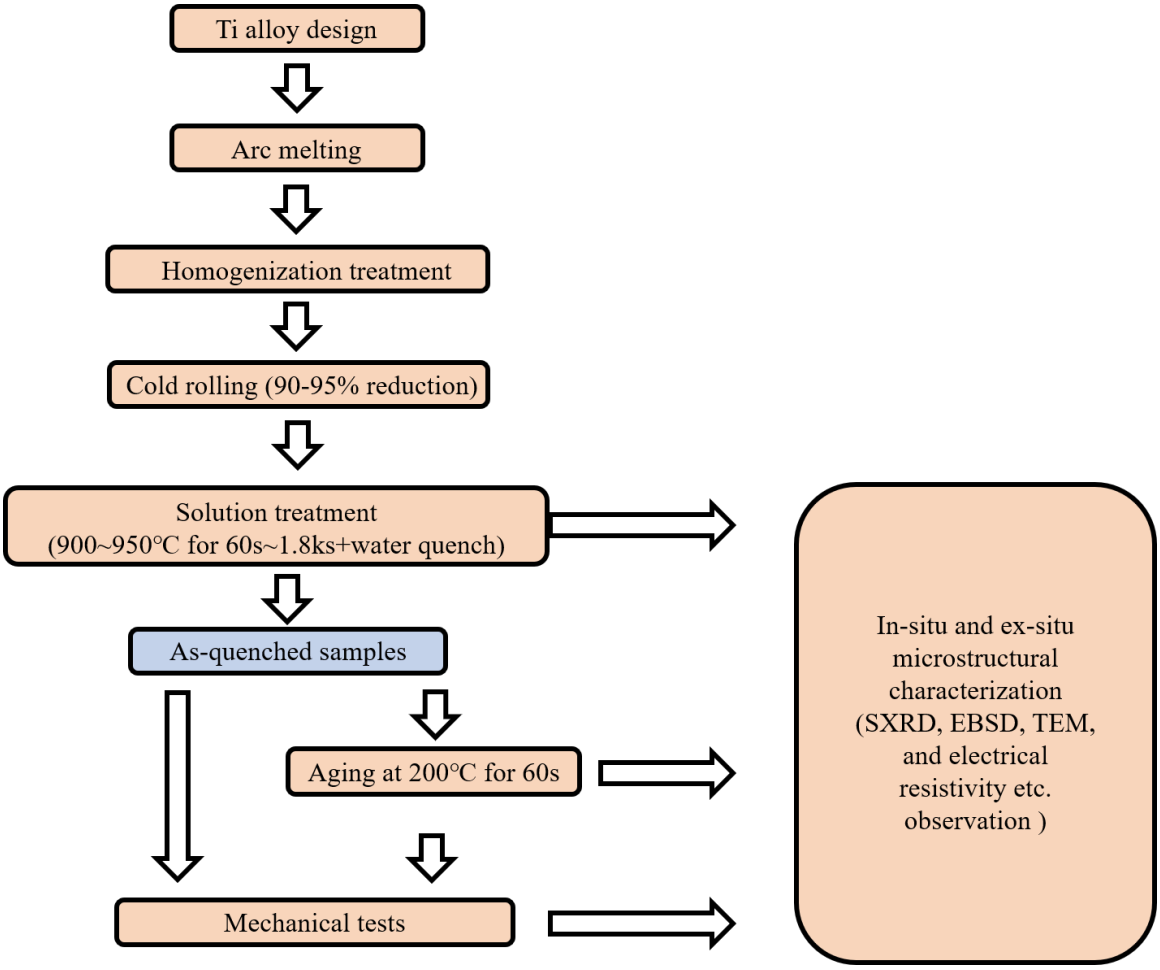

Figure 2.1 The simple procedure diagram of the research route for investigated alloys.

2.2 Fabrication and cold-rolling process

20g ingots of Ti-12Mo (wt. %), Ti-12Mo-xZr (x = 3, 6, 10) (wt. %), and Ti-W-Mo-Zr were fabricated by vacuum arc-melting using high purity Ti (99.6%), Mo (99.98%), Zr (99.2%) and W (99.95%) metals. A picture of the vacuum arc melting system (Buhler AM500) is shown in figure 2.2. It consists of a high vacuum chamber with a viewing window, a water-cooled tungsten electrode, a water-cooled copper crucible, and the operating handle. The mixtures of raw materials were subsequently melted using a tungsten electrode. During the melting process, the alloy was melted at least five times under a high purity argon atmosphere, flipped over each time before melting, and finally formed into a cylinder shape. After melting, the ingots were homogenized at 900℃ for 30min under a high vacuum of 10^{-5} Pa using a vacuum quenched furnace and then water quenched.

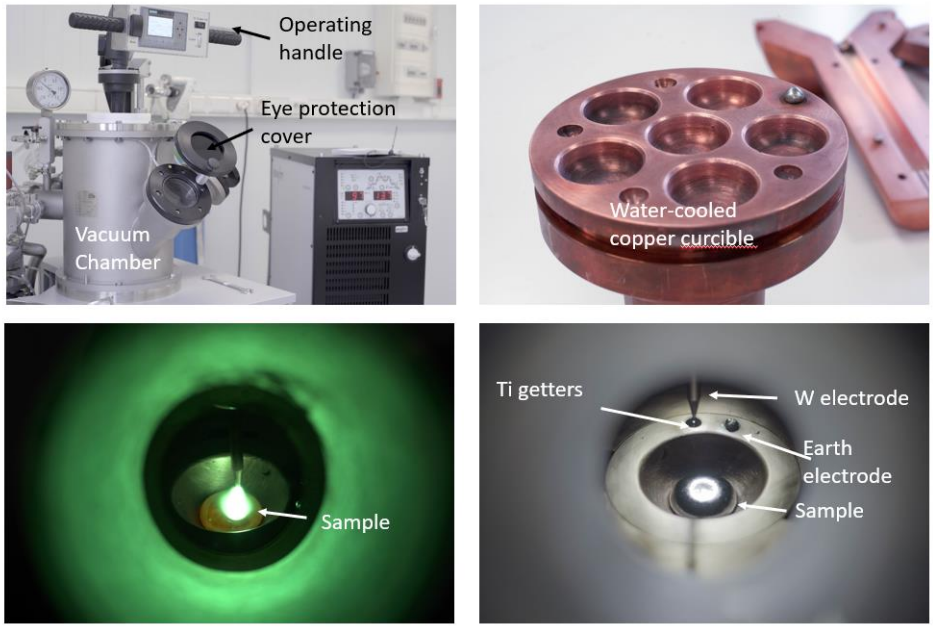

Figure 2.2 The photograph of the vacuum arc melting furnace and melted sample.

The as-quenched ingots were cold-rolled by the rolling machine (figure 2.3a) at room temperature. The deformation rate, R, achieved in a flat rolling operation (thickness reduction) is calculated using equation 2.1:

$$R = (H_o - H)/H_o \quad (Eq.\ 2.1)$$

Where H_o is the initial thickness of samples before rolling, and H is the thickness of sheet samples after rolling, as shown in figure 2.3b. Generally, high cold rolling rates can be applied to metastable TRIP/TWIP β titanium alloys as they possess excellent workability. As shown in figure 2.3c, the initial thickness of the sample was 8~12mm, and the final thickness of the sheet sample is about 0.5mm with over 95% reduction.

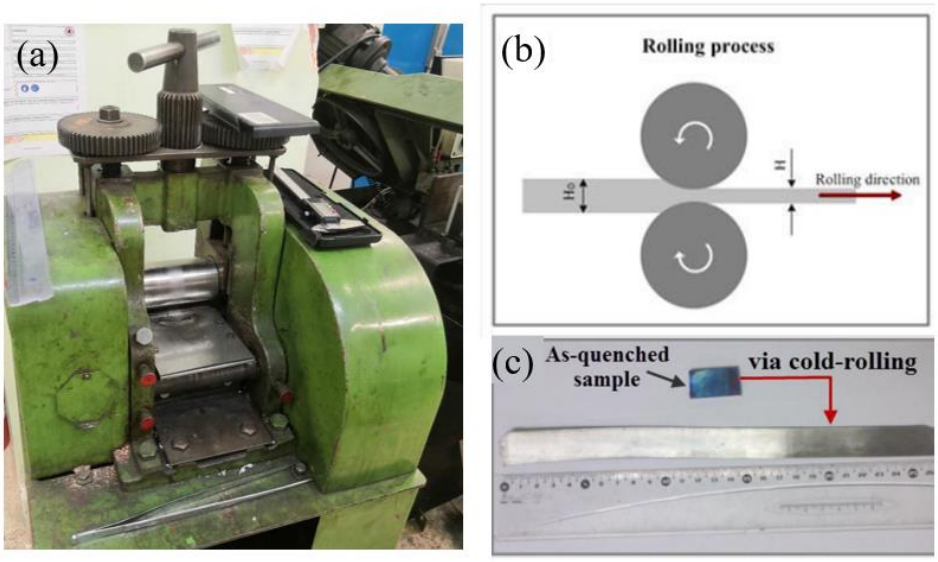

Figure 2.3 (a) the photograph of rolling machine; (b) the scheme of rolling process; (c) as rolled sheet of titanium alloys.

2.3 Thermo-mechanical treatment procedure

The schematic illustration of the thermo-mechanical process for ST samples (The samples via solution treatment were called ST samples.) and low temperature aging samples (the ST samples via aging treatment at 200℃) are shown in figure 2.4. There are two kinds of heating treatment in this work, i.e., the high-temperature treatment above T_β temperature and the low temperature aging at 200℃.

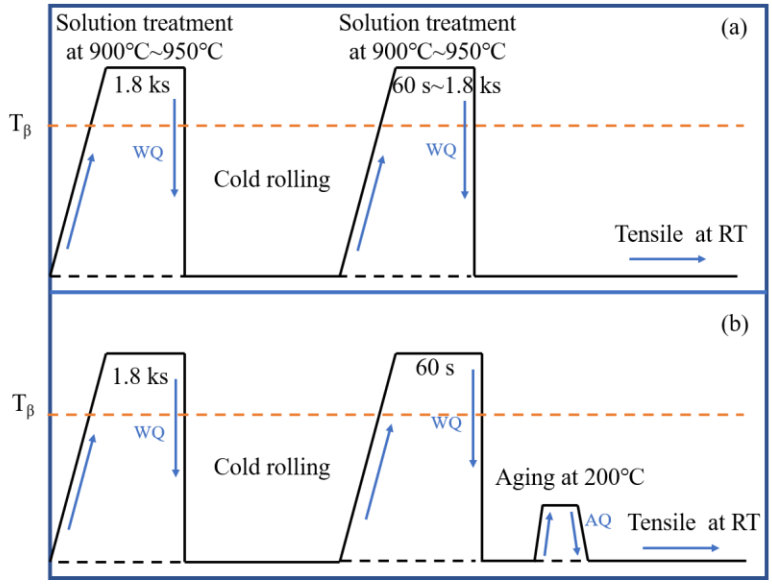

Figure 2.4 Schematic illustration of the thermo-mechanical process of (a) solution treatment state (ST) and (b) aging state Ti alloys.

When Ti-alloys are treated at high temperatures, and oxidation layer, which could significantly affect the mechanical behavior, is easy to be formed at the surface of the samples. In order to reduce the oxidation, a vacuum tube furnace (as shown in figure 2.5) with water quenched accessory was often used in thermal treatment. After the high deformation rate, the β grain of as-quenched ingots was completely dislocated. Thus, the as-rolled sample display very low ductility and extremely high strength. A second solution treatment was then applied to recrystallize the alloy. For the Ti-12Mo and Ti-12Mo-xZr (x = 3, 6, and 10) alloys. In order to obtain different grain sizes, the solution treatments with different times from the 60s to 1.8ks were applied. Rolled sheets were heat-treated at 900°C (over their β transus temperature) for the 60s and 1.8ks and then quenched to retain the fully recrystallized β grains with diameters of 20 μm (fine grain, solution treatment for 60s) and 100μm (coarse grain, solution treatment for 1.8ks). The Ti-W-Mo-Zr alloys were treated at 950°C for 1.8ks due to their higher β transus temperature compared to Ti-12Mo. The ST Ti-12Mo alloy was aged at 200°C to precipitate ω_{iso} phase resulting in a strengthening effect.

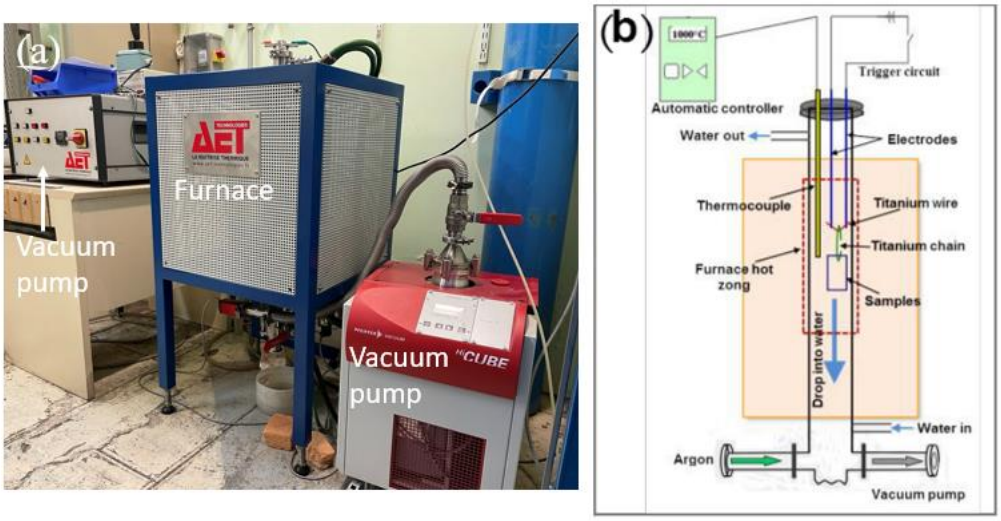

Figure 2.5 (a) the photograph of the tubular water-quenched furnace; (b) the corresponding schematic diagram.

In order to stabilize the temperature at 200℃ and control the aging time accurately, a thermostatic heating oil bath ((Silicon Oil with 300℃ boiling point, heated in Huber CC 304 heater as shown in the figure. 2.6) was used for the low-temperature aging and isothermal resistivity runs at 200℃ (as shown in figure 2.6 b).

Figure 2.6 is the photograph of the thermostatic heating oil bath.

2.4 Microstructural characterization methods

2.4.1 Electrical resistivity measurement

The electrical resistivity is very sensitive to the defect density, solute content, and phase transformation in metallic materials. In this work, the phase transformations of Ti-12Mo in low-temperature aging were characterized by using isochronal or isothermal electrical resistivity measurement (ERM). Specimens for electrical resistivity measurements were cut into thin 30 mm × 1mm × 0.5mm bar from ST sheets. A constant heating rate of 1℃/min was applied in the vacuum tube furnace (as shown in figure 2.7a). The samples were placed in the oil bath for the isothermal ERM and held at 200℃ (as shown in figure 2.7b). The ERMs were performed by using the four-probe method with a serial electrical circuit set-up. The circuit diagram of the four-probe method measurements device is shown in figure 2.7c.

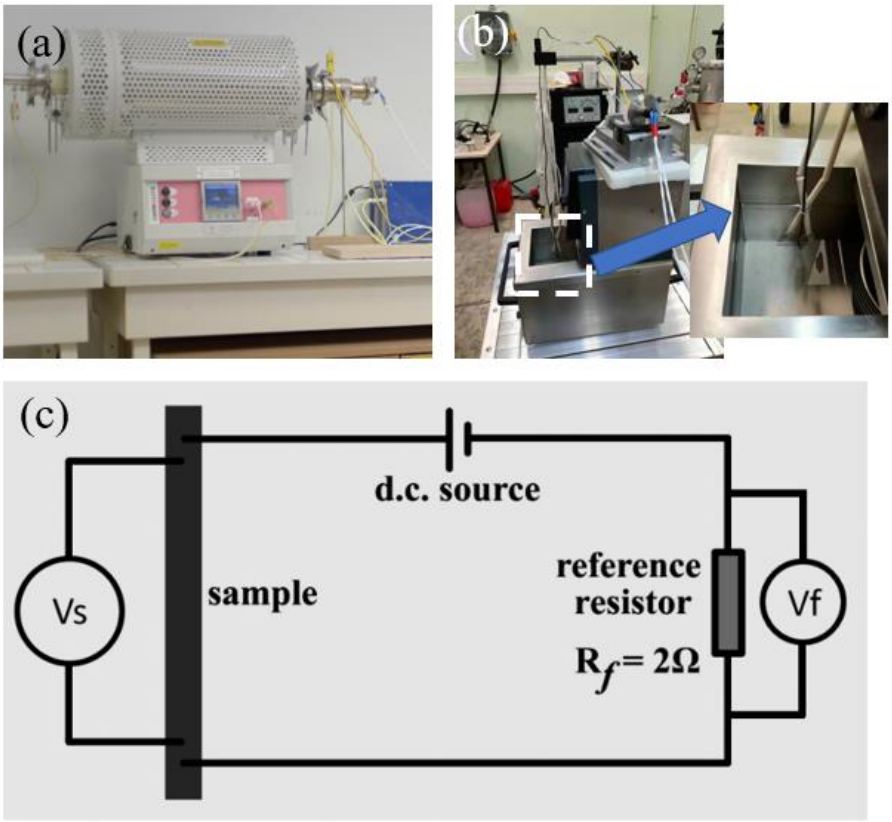

Figure 2.7 electrical resistivity measurement (EMR): (a) phothography of isochronal ERM measured in vacuum tube furance, (b) isothermal ERM measured in oil bath, and (c) circuit diagram of the enperimental set-up for 4-point resistivity measurements.

2.4.2 In-situ electron backscattered diffraction (EBSD)

Samples for EBSD measurements, with dimensions 40mm × 3mm × 0.5mm, were mechanically polished and then electrochemically polished in 4% perchloric acid in methanol, held at about 10 ℃ for 1min to get mirror surface and reduce specimen section locally to localize the plastic deformation. Usually, it is difficult to get specimens with perfectly flat surfaces after electrochemical polishing, but the dimple curvature formed does not prevent the collection of diffraction patterns. Before analysis, ultrasonic cleaning was performed in methanol for the 60s.

A tensile test specimen stage, Micromecha Proxima 100 machine (shown in figure 2.8), in a field emission gun scanning electron microscope (FEG-SEM ZEISS LEO1530) was used for the combination straining and EBSD analysis. The stage has an externally controlled electromotor exerting the tensile force on the sample. The elongation was measured by a sensor counting revolution within the straining mechanism. It should be noted that orthorhombic martensite α″ could be observed in deformed Ti-12Mo alloy. The lattice parameters of orthorhombic martensite α″ were measured under tensile loading at ε = 0.024 [27]: $a_{\alpha''}$ = 3.07871, $b_{\alpha''}$ = 4.91978, and $c_{\alpha''}$ = 4.63289.

Figure 2.8 the photography of the Proxima 100-Micromecha machine

Deformation is followed by secondary electron imaging during the loading state, and deformation microstructures were analyzed using in-situ tensile tests coupled with EBSD scans at different strains. Typical parameters applied during the combined EBSD, and in-situ tensile tests are shown in table 2.1. The raw EBSD data was indexed by TSL OIM Data Collection 7 software then analyzed by TSL OIM Analysis 7 × 64 software. The pixels with a confidence index higher than 0.08 were selected to analyze using the orientation imaging microscopy (OIM) software. The

pixels with a confidence index lower than 0.08 were removed from the dataset, and no image cleaning was conducted.

Table 2.1 Parameters applied during EBSD combined with in-situ straining.

Parameter	Value
Acceleration voltage/kV	20
Apeture/μm	240
Probe current/nA	37
Working distance/mm	22-24
Specimen tilt angle/(°)	70
Magnification	100-1000
Vacuum/Pa	~2×10^{-5}
EBSD scan step size/μm	0.02~0.4
Strain rate of tensile specimen/μm·s^{-1}	2

2.4.3 Ex-situ and in-situ transmission electron microscopy (TEM)

A JEOL 2100plus transmission electron microscope (TEM) operating at 200kV was used to characterize microstructural details beyond EBSD resolution. In-situ heating and straining tests in TEM were conducted by using a Gatan 672single tilt heating-straining holder. The observations were recorded as short videos with Gatan Rio camera with resolution 4096 × 4096 pixels. The dimensions of the in-situ TEM specimens are 11 mm × 2.4 mm × 0.2 mm, as shown in figure 2.9. Samples for ex-situ TEM observations were cut from the deformed samples after in-situ EBSD tests. All the specimens for TEM observations were thinned by twin-jet electropolishing, using a solution of 4% perchloric acid in methanol, held at about -15 ℃.

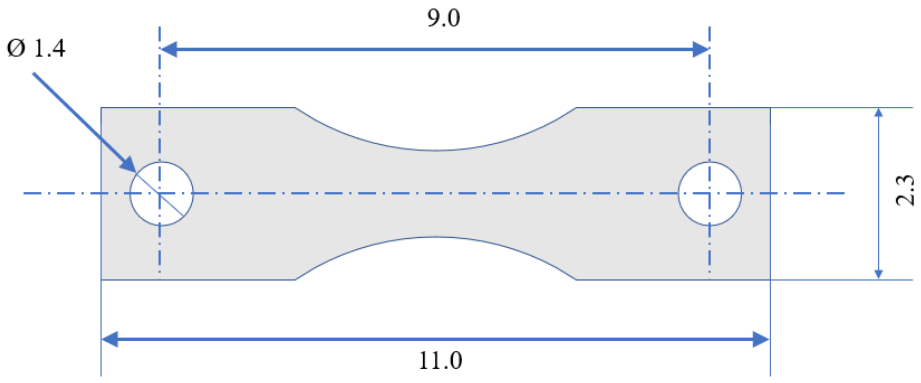

Figure 2.9 Dimensions of micro-tensile specimens for in-situ TEM experiments.

2.4.4 X-ray diffraction (XRD)

Conventional XRD

In this work, the conventional X-ray diffraction (XRD) was carried out by Bruker D8 ADVANCE with CuKα radiation operating at 40 kV and 40 mA. The wavelength of the produced photons was 1.5406 Å. The 2θ range was 30~90° with an angular step of 0.02°.

Synchrotron-based high energy XRD

The high-energy synchrotron X-ray measurements were carried out on the beamline 11-ID-C at the Advanced Photon Source, Argonne National Laboratory. High-energy X-rays with a beam size of 0.5 mm × 0.5 mm and wavelength of 0.1173 Å were used in transmission geometry for data collection. The measurement was conducted in a high-purity argon atmosphere. Two-dimensional diffraction patterns were obtained using a Perkin-Elmer large area detector. Fit2D software was used to analyze the 2D data and convert the patterns into diffraction spectra.

Synchrotron-based in-situ tensile XRD

The experiments were performed on the DIFFABS beamline with 8keV energy and 1.55 Å wavelength at the synchrotron Soleil. The data were collected using a CriPad curved hybrid pixel array detector with a -2.2° angle at different strain levels on a Proxima 100-Micromecha machine (as shown in figure 2.8).

2.5 Tensile testing and Vickers hardness testing

Mechanical properties were characterized by uniaxial tensile tests using an INSTRON 5966 machine with a constrained strain rate of $10^{-3}s^{-1}$ at room temperature. Figure 2.10a shows the photograph of the tensile test machine. The dimension of the tensile specimen was also presented in figure 3.7b. All tensile tests were performed along the rolling direction of the tensile sample.

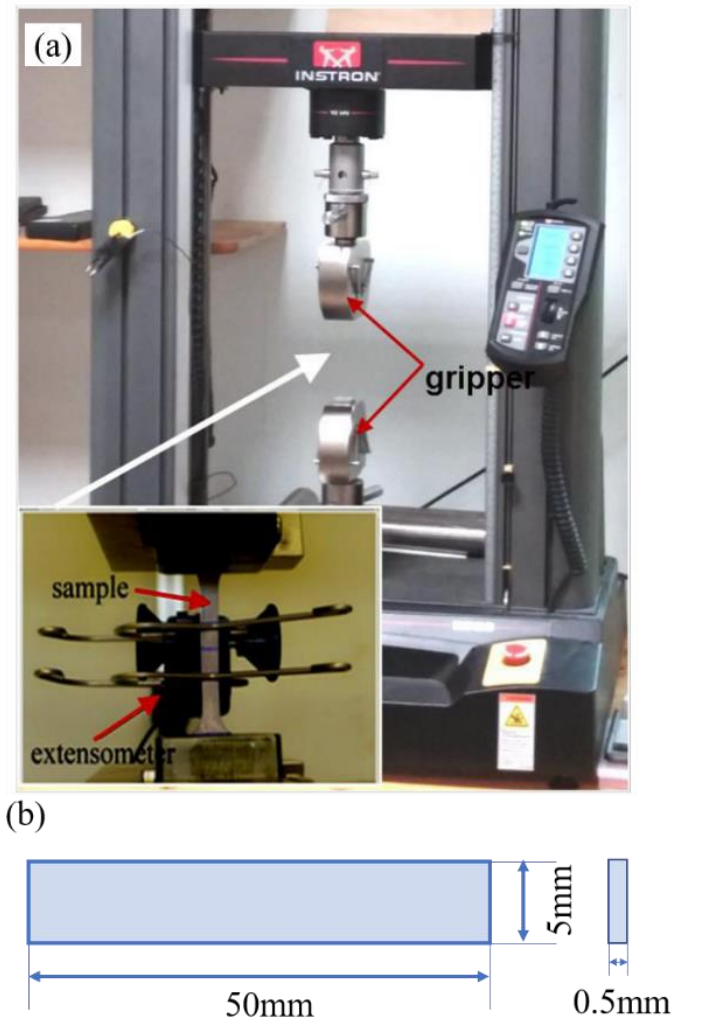

Figure 2.10 (a) the tensile test device and (b) the dimension of the sample for testing.

The Vickers hardness measurements of alloys specimens with polished surface were carried out on a Diamond Vickers Hardness tester (MHT-200), at an indentation load of 500g and a dwell time of 5s. At least 20 indentations were taken for each specimen, and the average values were calculated.

2.7 The calculation of Schmid Factor (SF) and lattice correspondence variants (CV) derived from β to α″ crystals

As shown in figure 2.11, the Schmid factor (SF) is defined as: SF = cos λ cos φ, where λ and φ are the angles between the tensile direction and the normal to martensite habit plane (or the

twinning plane) and the associate invariant strain direction (or the twinning direction), respectively. The values of λ and φ in each grain were obtained from the EBSD data.

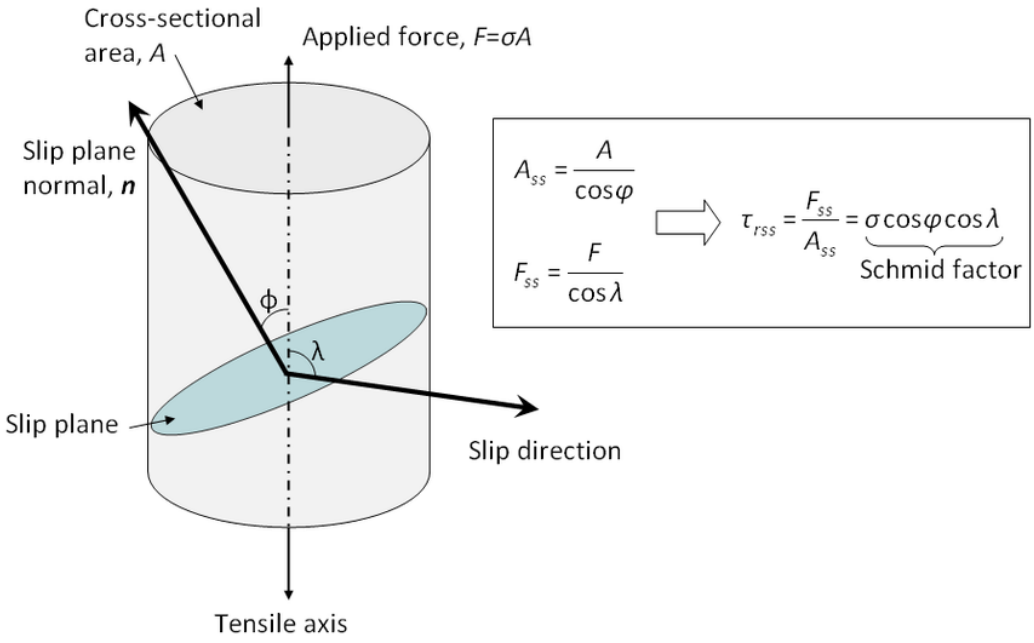

Figure 2.11 Derivation of Schmid factor for a single slip system [80].

2.8 Finite element analysis (FEA) of the plastic deformation during the expansion of a cardiovascular stent

Figure 2.12 shows the geometry of the Palmaz-Schatz stent model, represented with the meshed domain. It is possible to model only one of the twenty-fourth geometries due to the stent's circumferential and longitudinal symmetry. The main focus of the study consists of the local stress evaluation in the stent. The model has a length of 10mm, an inner diameter of 0.74mm, and a thickness of 0.1mm. The angioplasty balloon is assumed to stretch a maximum expansion radius of 2mm. The material parameters required for simulations include density, Young's modulus, Poisson's ratio, initial yield stress, and isotropic tangent modulus, obtained from tensile curves or material standard databases.

The recoil of the stent also could be obtained by the FEA simulation of the Palmaz-Schatz stent model. The percentage by which the diameter of a stent decreases from its expanded diameter (when the balloon is inflated at the nominal pressure) to its relaxed diameter (when the balloon is retrieved from the stent) is called recoil.

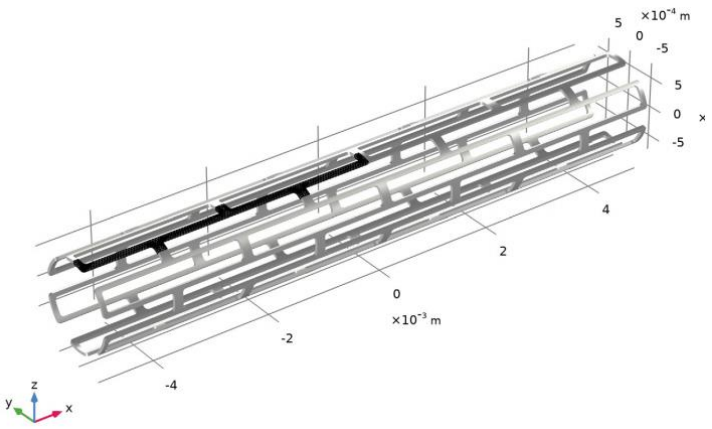

Figure. 2.12 The reduced geometry used in the study (meshed) and the full stent geometry.

Chapter 3 Studies of transformation pathways in TRIP/TWIP Ti-12Mo alloy.

Introduction

In this chapter, Ti-12Mo coarse grain (with average grain diameters of 100 μm) is selected as a model TRIP/TWIP alloy to understand the relationships between TRIP/TWIP effects and its excellent mechanical performance in Chapter 1. This excellent mechanical performance could be attributed to $\{332\}\langle 113\rangle_{\beta}$ twinning and SIM α″ due to their effects on the improvement of strain-hardening rate, mainly as a result of dynamic Hall-Petch development and the subsequent significant uniform elongation during tensile plastic flow. Therefore, further clarification of their transformation mechanism during the deformation process could help us improve the mechanical behavior of Ti-12Mo to meet the requirement of the cardiovascular stents. This chapter aims to understand better the transformation pathways operating in the β grains of a β-metastable Ti-alloy for different orientations of the BCC structure regarding the tensile load direction via Schmid factor calculation coupled with in-situ SEM and ex-situ TEM observations.

3.1 The Schmid factor-dependent selection of primary deformation mechanism

About 600 grains of various orientations are analyzed during in-situ tensile tests, and EBSD characterizes their primary deformation mechanism at yielding. Figure 3.1a shows the EBSD statistical analysis of the primary transformation products in the grains originating from the same sample. In this chapter, the term “primary” refers to the transformation products directly formed from β matrix at yielding (ε ~ 0.02), and “secondary” refers to the products formed within a primary product. Besides, some special cases observed in this study, such as transformation products that nucleate at the boundary of primary products but grow into the β matrix, are considered secondary products since their formation depends on the primary products. The orientations of the analyzed β grains are plotted in the inverse pole figure of figure 3.1a concerning the tensile axis. The color code corresponding to different deformation products is adopted. The blue color is attributed to the grains where the primary deformation products are 332T. The red color highlights the grains showing both 332T and SIM α″ as primary deformation products. The yellow color is used for grains with only primary SIM α″ transformation. Interestingly, distinct regions appear on the inverse pole figure triangle, suggesting that the transformation products distribution is drastically grain-orientation dependent. The colors are roughly partitioned into three

domains, corresponding to their associated deformation mechanism, which indicates that the deformation mechanisms are not unique even in the same alloy.

To interpret the orientation dependence characterized above in terms of criteria for selection of the deformation mechanism, statistical calculation of Schmid factor for random grain orientations is performed for a body-centered cubic (BCC) structure under tensile conditions. The {755}<10 7 7>$_\beta$ habit plane and the associated invariant strain direction [82] are used for Schmid factor calculation according to the agreement between theoretical prediction and EBSD measurement. For the 332T, the habit plane and twin direction {332}<113>$_\beta$ are used for calculation. For each random grain orientation, the Schmid factor values for every 332T variant and every SIM α″ variant are calculated and ranked. The highest values of Schmid factor for each grain orientation among all variants of the two transformation products, 332T and SIM α″, are drawn in figure 3.1b and c, respectively.

Three poles corresponding to the maximum value of the Schmid factor (SF=0.5) are identified by red dots in the inverse pole figure (Figure 3.1b and c); one corresponds to 332T (figure 3.1b), and the other two (Fig. 3.1c and d) correspond to SIM α″ without or with applying transformation strain criterion ($s_i \geq 0$, *Eq.* 1.4), respectively. The criterion requires that the transformation strain of the SIM α″ variant should be non-negative under applied strain together with the non-negative Schmid factor. The lattice strain along the tensile direction, s_i, for each potential SIM α″ variant thus needs to be considered. Therefore, the variant is favorable for activation under tension when both of its Schmid factor and s_i are positive and preferably high [35]. Thus, the Schmid factor inverse pole figure of the variants of SIM α″ with a positive value of s_i is shown in figure 3.1d. There is only one Schmid factor pole of 0.5 corresponding to SIM α″ with a positive value of s_i in the inverse pole figure marked red pot in figure 3.1d.

Empirically, the variants with Schmid factor higher than a material-specific threshold value can be considered to be active in metastable Ti alloys where only one transformation mechanism, either 332T or SIM α″, is operative over the whole material [134]. However, in the TRIP/TWIP Ti alloys, with both mechanisms possibly activated, the Schmid factor threshold of the single transformation mechanism proposed above is insufficient to determine the selected mechanism. The activation of twinning or SIM α″ in a specific grain will thus depend on both the Schmid factor threshold for 332T and the Schmid factor threshold for SIM α″, that have not been reported in the

literature previously. In this study, we propose a novel method to assess the Schmid factor thresholds of each transformation.

The proposed method is based on the computation of a series of theoretical transformation partition maps for different combinations of Schmid factor thresholds for 332T and SIM α″. A laboratory-made computer program calculates the Schmid factor of all variants of 332T and those of SIM α″ at a given grain orientation concerning tensile direction and s_i. Then, the program compares each Schmid factor of 332T with an arbitrary Schmid factor threshold for 332T: the mechanical twinning mechanism is validated or rejected in the grain with the considered orientation, depending on the comparison of its Schmid factor and the defined threshold. The same approach is performed for SIM α″ with $s_i \geq 0$ consideration, and a corresponding theoretical transformation partition map is then produced, describing the expected deformation mechanism for each orientation. Comparison of the academic transformation partition maps and the experimental one finally allows finding the best match, ultimately providing the Schmid factor threshold for both deformation mechanisms. Practically, the computation takes thresholds varying between 0.3 and 0.5, with 0.01 steps. For the sake of clarity, only selected cases, for Schmid factor thresholds of 0.35, 0.4, and 0.45 for 332T and Schmid factor thresholds of 0.3, 0.35, and 0.4 for SIM α″ compiled into inverse pole figure maps are provided in Figure 3.1e. Each transformation partition map's red domain (332T+ SIM α″), corresponding to a pair of specific Schmid factor thresholds, is unique regarding the size and position. Such unicity allows us to study, as suggested above, the Schmid factor thresholds in the TRIP/TWIP situation by fitting the given experimental transformation partition maps to the computational ones. For the present Ti-12Mo studied alloy, the situation where the Schmid factor threshold of 332T equals 0.4, and the Schmid factor threshold of SIM α″ equals to 0.35, framed in figure 3.1e, shows the best agreement between calculated and experimental transformation partition maps (figure 3.1a).

By experimental examination of grains with various orientations, therefore belonging to distinct domains (figure 3.1a), the various deformed microstructures resulting from different deformation mechanisms and evolution sequence of 332T and SIM α″ are observed. This results in a large diversity and complexity of the deformation microstructures over the whole sample. Therefore, the transformation partition maps can be used as a guide to select grains of interest for further investigation on their transformation pathways. For instance, the microstructure of the grains located in the blue and yellow domains (deformation dominated by primary 332T or SIM

α") has been well investigated in many previous types of research [1, 2, 33]. These results presented that the selections of primary deformation mechanisms in these grains are heterogeneously dominated either by twinning or by SIM α" [41], resulting in the missing key information whether the formation of 332T can be mediated from SIM α". For this reason, two special grain orientations, I and II marked in figure 3.1, are investigated to complete the transformation pathway study between the two mechanisms, where both mechanisms are superior to their Schmid factor thresholds (at Orientation. I) and both of them are inferior to the thresholds (at Orientation. II).

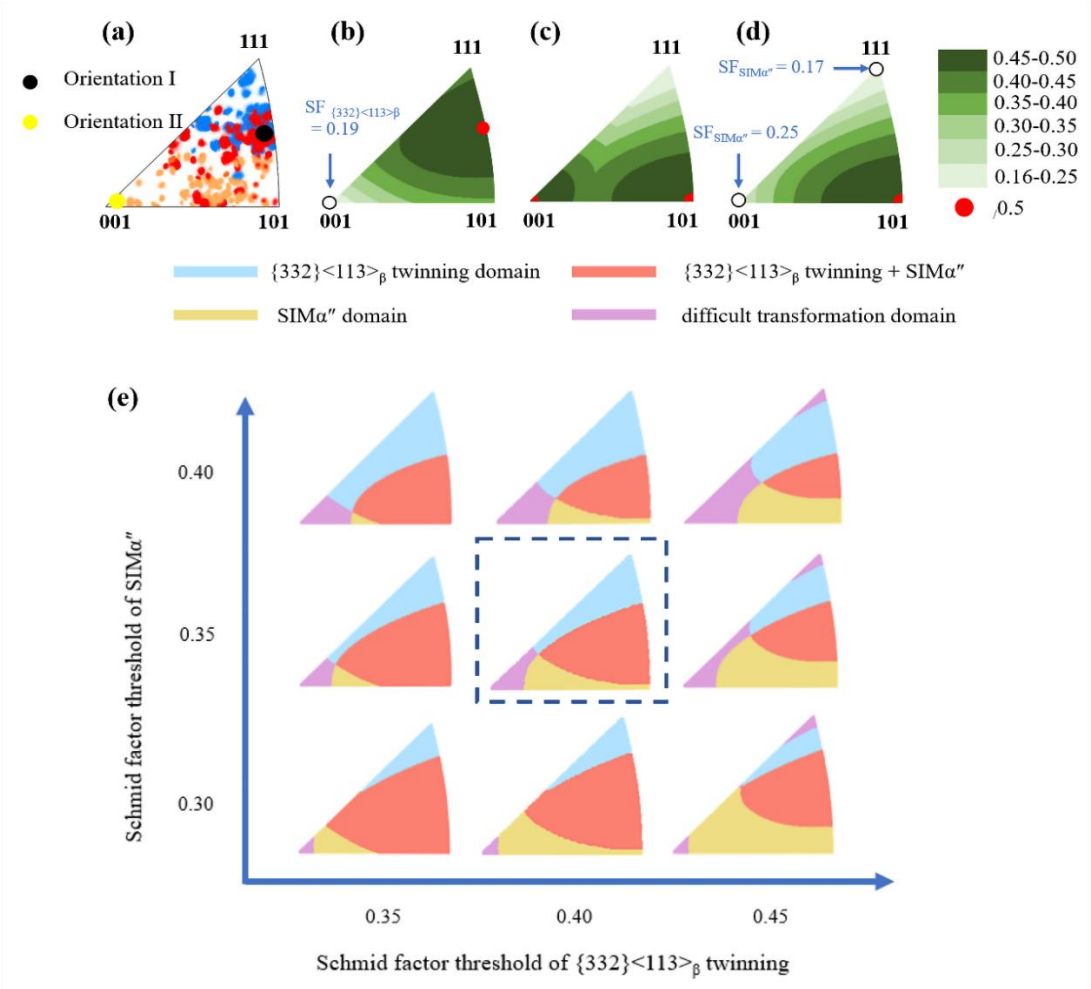

Figure 3.1: (a) Experimental transformation partition map: Experimental Inverse pole figure of the statistic of the primary deformation products in different Ti-12Mo grains by in-situ EBSD under tensile strain (ε = 0.02); (b~d) inverse pole figure showing the distribution of the highest SF of 332T(b), all variant of SIM α″(c), and the variant of SIM α″ with a positive value of ε_i under tensile deformation; (e) theoretical transformation partition maps: inverse pole figures of the calculation of the orientation domains as a function of the

combinations of threshold SFs. The one marked by a dashed square confirms the domain distribution observed experimentally in (a). The normal direction of inverse pole figures is along the tensile direction.

3.2 The grain orientation dependent pathways to activate {332}<113>$_\beta$ mechanical twinning

At orientation I, the Inverse pole figure and phase maps from a specimen under loading are shown in figure 3.2 (EBSD scan with the tensile force). Two primary deformation bands form independently: a 332T (labeled by A in figure 3.2) and a SIM α″ band (labeled by B). The traces of the $(3\bar{2}3)_\beta$ and $(575)_\beta$ planes are drawn in figure 3.2 (white dashed line and black dashed line, respectively), corresponding to the habit plane of each observed band. It is the first time that independent formation of primary 332T and primary SIM α″ is observed simultaneously in the exact grain. This can be rationalized because orientation I is located at the border between the blue region (332T dominated) and the red one (combination of 332T and SIM α″).

Besides, it can be noticed from figure 3.2 that a thin layer of α″ is formed during loading at one of the 332T interface. A similar phenomenon has been reported in previous studies [50], in which focused ion beam (FIB) sampling clarified that it was a superficial α″ layer near the twin interface. It has been proposed to be the evidence of α″-assisted 332T mechanism [50]. However, another hypothesis on the origin of this layer could be suggested, such as SIM α″ formed to accommodate the mechanical contrast between the twin and the matrix, similar to what happens with the omega phase [66, 81]. As an extension, in this study, TEM thin foils are prepared at the core portion of the sample to investigate such interfacial microstructure.

TEM observations were performed on grain with orientation I to confirm the formation of interfacial α″ and reveal the microstructural details. The bright-field image in figure 3.3a shows a deformation band in the matrix. The upper region of the band is bordered by another band. The diffraction pattern (DP) acquired at the upper interface, pertaining to the primary deformation band, the matrix, and the interface allows identifying the primary deformation band as a 332T. However, additional diffraction spots that do not belong to the matrix (a purple legend in figure 3.3b) or the twin (a blue code in figure3.3a) are also visualized. A dark field (DF) on one of the spots (red circle (d) in figure 3.3a) is provided in figure 3.3d and shows that the interfacial band is made of α″, composed by fine parallel α″ lamellae at 332T boundary. The parallel α″ lamellae are separated by the matrix, as highlighted by the DF of the matrix given in figure 3.3e (from the spot (e) shown by a red circle in figure 3.3c). The SAED patterns (figure 3.3b and figure 3.3c) taken at the

boundary between the 332T, α″ and the β matrix and in the β matrix (c and d in figure 3.3a), suggest that these α″ lamellae fulfill the classic $(211)_{\beta}$ // $\{110\}_{\alpha''}$ orientation relationship (OR) with the β matrix (illustrated in the key diagram in figure 3.3f). The trace of the habit plane of SIM α″, highlighted by the yellow dotted line in figure 3.3d, corresponds to the $(\bar{7}55)_{\beta}$ trace of β matrix. Due to the low resolution of in-situ EBSD mapping, it is difficult to conclude if the interfacial α″ observed by TEM and EBSD are the same in the microstructure. But the highly organized interfacial α″ lamellae (TEM images in figure 3.3) are very different in microstructure than those reported in the literature.

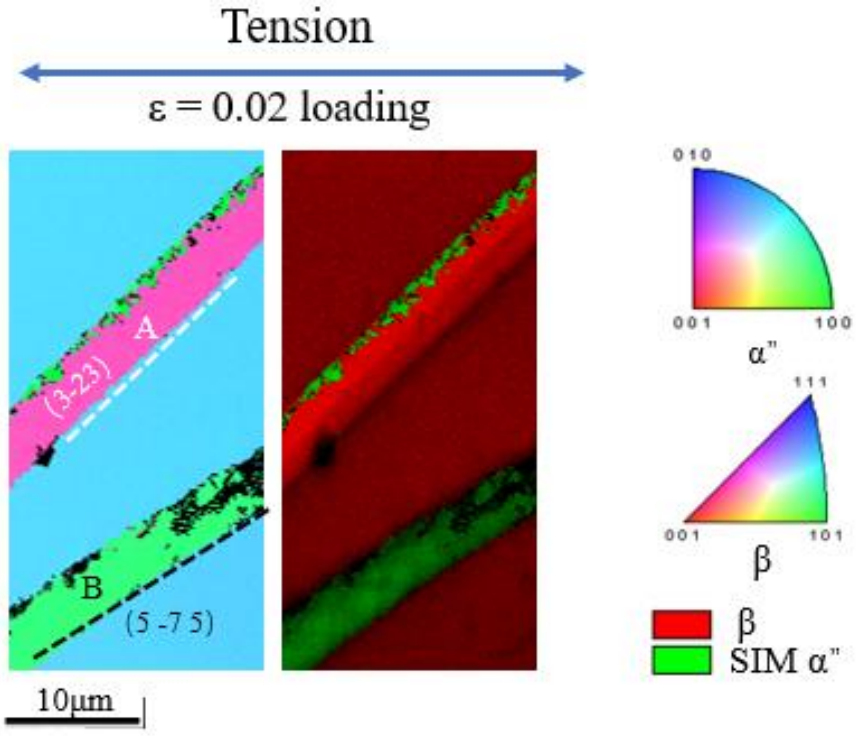

Figure 3.2. EBSD investigations at the grain with orientation I: IPF maps and phase + IQ maps of the deformed sample taken at ε = 0.02 (holding tensile stress).

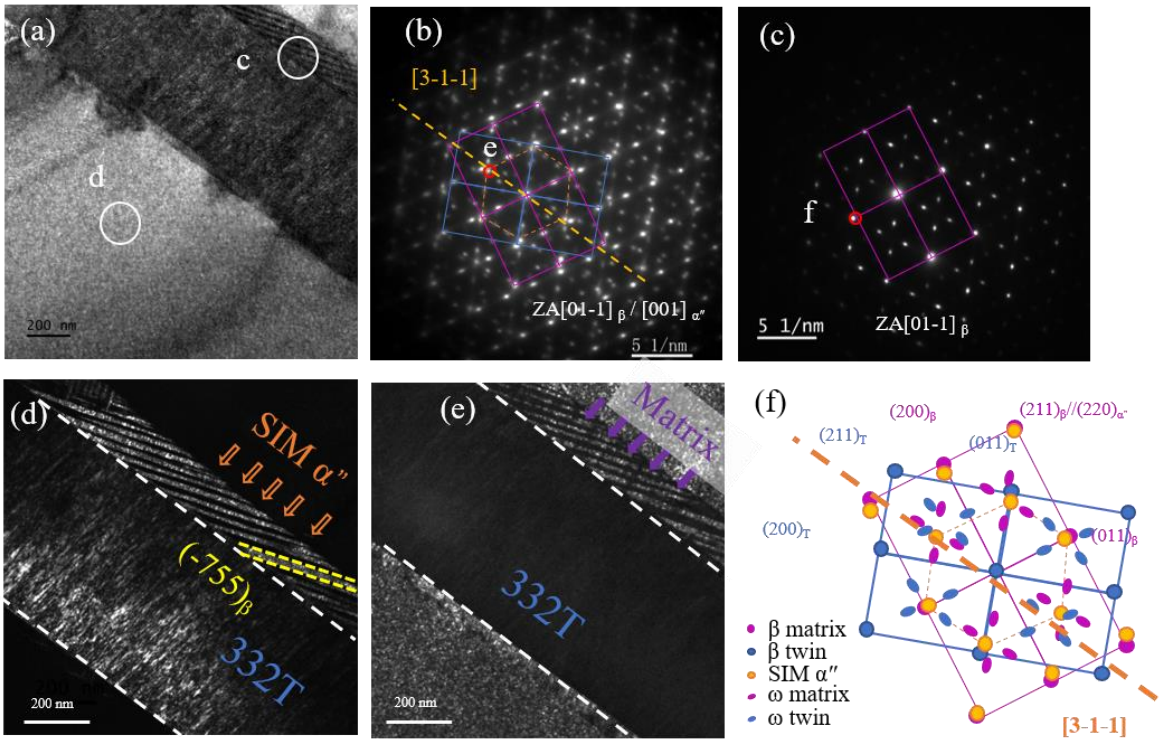

Figure 3.3 TEM investigations at the grain with orientation I: (a) bright-field (BF) image of a {332}<113> with interfacial SIM α″ in a sample taken at ε = 0.05 (unloading), (b-c) SAED pattern taken from the region indicated by a circle in (a), (d) and (e) corresponding dark-field (DF) images of one variant of SIM α″and of the β matrix, respectively, and (f) essential diagrams corresponding to the SAED pattern in (b).

Table 3.2 Transformation lattice strain for each CV along the tensile direction.

Variant	SF	s_i
CV1	0.27	3.53%
CV2	-0.23	2.98%
CV3	0.27	3.53%
CV4	-0.23	2.98%
CV5	-0.50	-6.14%
CV6	0.50	-6.16%

A similar analysis is performed into grains with orientation II (SF_{332T} = 0.23, $SF_{SIM\ \alpha''}$ = 0.27), located in the difficult transformation domain (near [001]) of figures 3.1a (yellow dot in figure 3.1a). Deformation microstructure is once again monitored during in-situ tensile tests with EBSD scans at ε = 0.02 and ε = 0.05 (under loading) and after unloading from ε = 0.05. Two SIM α″ bands appear first from the β matrix in the position (marked by the green arrows in figure 3.4a) where the grain boundary intersects the martensite in adjacent grains at ε = 0.02 (figure 3.4a). The

trace of the habit plane of SIM α″ is parallel to $(755)_{\beta}$ trace (marked by orange line in figure 3.4a), which can be identified as CV1 [82]. The SF of the six potential SIM α″ in the orientation II and the corresponding lattice strain along tensile direction (si) are listed in table 3.2. The first feature to notice that the CV6 process the highest SF of SIM α″among the six variants of SIM α″ (0.50), however, it is hard to be activated during the tensile process since the s_i value of CV6 is negative. At ε = 0.05, it is observed that the α″ bands have thickened. The α″ color on the IPF changes from purple to yellow in figure 3.4b, and crystallographic analysis identifies that these yellow products are secondary 130α″ DT of the primary α″. It should be noticed that two 332T bands (marked by the gray arrow in figure 3.4b) form during the deformation, after the transformation of primary α″, as branches that extend from the main martensite bands into the matrix. The habit plane traces of this 332 T lie along $(233)_{\beta}$, see black dashed line in figure 3.4b, which is about 23° off the habit plane of the primary α″ bands but parallel to the $(130)_{\alpha''}$ twinning plane of the internal 130 α″ DT (see purple dashed line in figure 3.4b). After unloading from ε = 0.5 (figure 3.4c), it can be seen that most of the 130 α″ DT are reversed to primary α″, strongly suggesting a detwinning phenomenon. However, part of 130 α″ DT is still preserved after unloading, including those which are aligned with the 332T (marked by black and yellow arrows in figure 3.4c) and some others (marked by blue arrows in figure 3.4c) located at the boundaries between the primary α″ bands and the matrix.

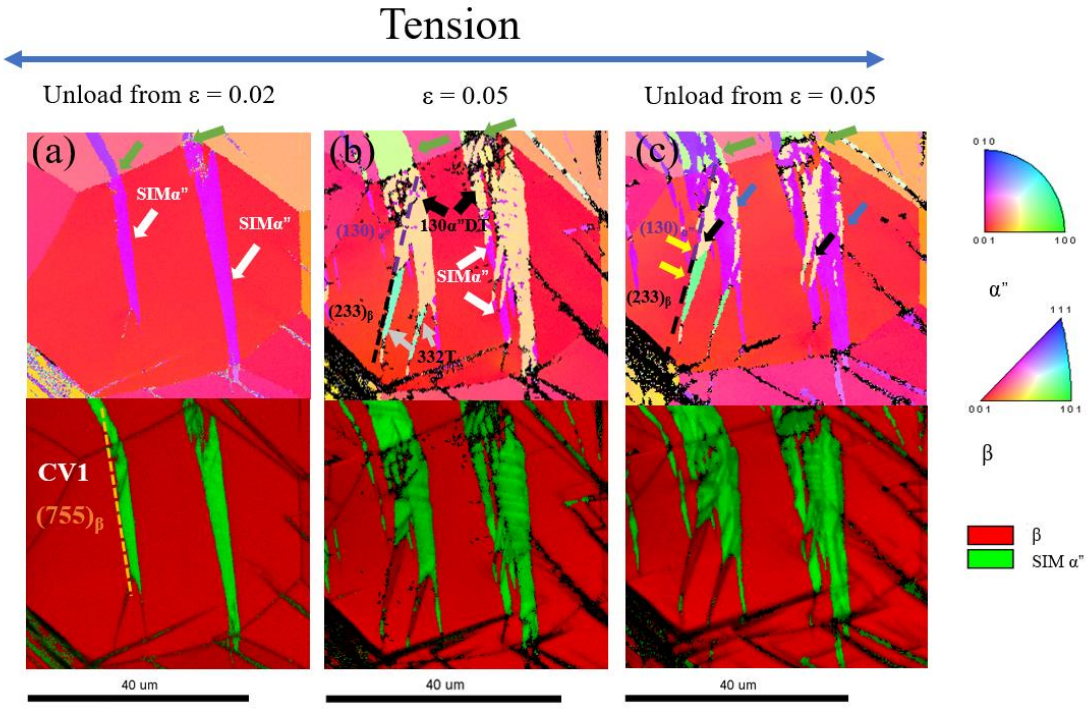

Figure 3.4. IPF maps and phase + IQ maps of grain with orientation II taken from the same region at strain steps of (a) ε = 0.02, (b) 0.05 (holding tensile stress), and (c) 0.05 (stress released).

In order to study the residual 130 α″ DT at the primary SIM α″ boundary, as shown in figure 3.4c with blue arrows, TEM investigations are performed in grain with orientation II, and the results are shown in figure 3.5. The bright-field (BF) image in figure 3.5a provides an overview of the internal microstructure. A large deformation band is identified as orthorhombic SIM α″. The trace of the interface between β matrix and the SIM α″ band (represented in blue in figure 3.5) is measured close to $(\bar{1}1\bar{1})_{\beta}$ // $(\bar{1}20)_{\alpha''}$ trace, which is one of the classic $\{hkk\}_{\beta}$ habit plane but is different from the $\{755\}_{\beta}$ habit plane observed at the EBSD scale [31]. The DP and DF about this interface are shown in figure 4b. From the DP, it can be seen that the α″ orientation does not conform to the classical orientation relationship, $\{211\}_{\beta}$ //$\{110\}_{\alpha''}$, with the β matrix [83].

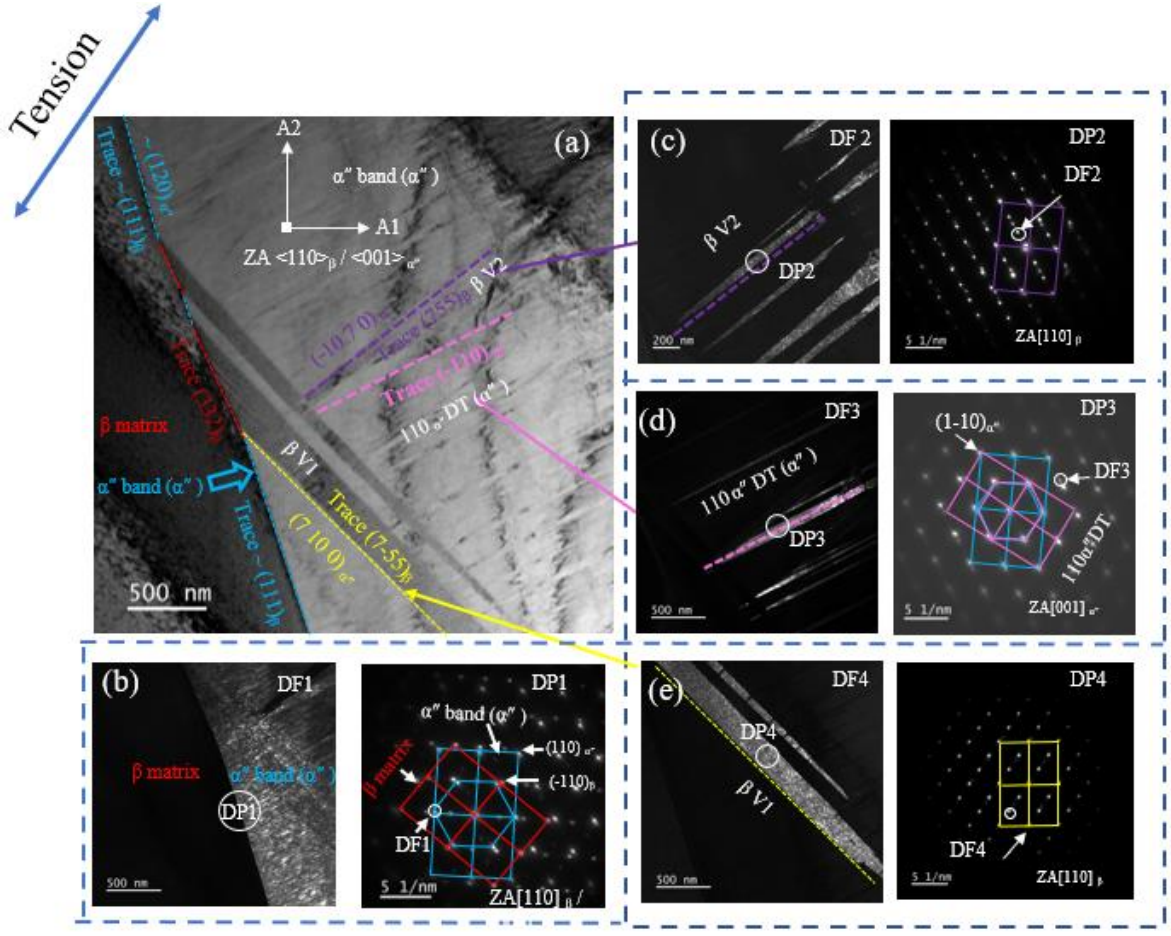

Figure 3.5 TEM observations of a grain with orientation II in a specimen strained to 0.05 and unloaded. Micrographs of (a) BF image, (b-e) DF images and their corresponding DPs associated by arrows to the locations of the interfaces.

The BF image in figure3.5a also shows that the martensite band contains internal secondary features. DF imaging and analysis of the diffraction patterns provided in figures 3.5c to figure 3.5e allow identifying three different features types. DF2 and DP2 in figure 3.5c show the presence of thin β platelets (variant 2 represented by purple color), with habit plane in the α″ martensite identified as $(7\ 10\ 0)_{\alpha''}$ and $(755)_{\beta}$. Secondary $\{110\}\langle 110\rangle_{\alpha''}$ orthorhombic deformation twins are also observed in the martensite, as evidenced in DF3 and DP3 in figure 3.5d (represented by pink color). Finally, a second β variant with a different orientation from the first ones (yellow color) is found, as illustrated in DF4 and DP4 in figure 3.5e. As shown in figure 3.5, the three DFs and their corresponding DPs demonstrate the morphologies and ORs of three different subproducts transformed from the large SIM band (represented by blue color).

3.3 Discussions

3.3.1 Schmid factor-controlled selection of the deformation mechanisms

The computation of TPM revealed that the IPF triangle is partitioned into three transformation zones and a domain unfavorable for both transformations, each of which corresponds to a deformation mode (figure 3.1g). This partitioning of deformation-induced transformations in Ti-12Mo is originated from the differences of habit planes and shear directions between the 332T and SIM α″. The minimal angle is 9.71° between the habit planes of twinning ($\{332\}_{\beta}$) and SIM α″ ($\{755\}_{\beta}$), and the minimal angle between the two shear directions is 19.47°. These geometrical differences result in the polarized distribution of effective SF (two poles of effective SF = 0.5) (figure 3.1b and d). In the experimental IPF (figure 3.1a), three distinct domains can be identified based on the type of activated transformations. This leads to a 332T domain, a SIM α″ domain, and a 332T + SIM α″domain. As a fact, the TPM is related to the SF, the threshold of SF for the activation of each transformation, and the transformation strain of the corresponding martensite variant. For example, in a grain belonging to the 332T domain at yielding point, the SF of at least one 332T variant is sufficiently high so that reaching a high enough resolved shear stress initiates the nucleation of such variant to accommodate the local tensile strain. Additionally, in the same grain, the SF of any variant of SIM α″ is insufficient to reach enough shear stress to activate martensitic transformation. A similar situation happens in the α″ domain, where the grains have at least one operative SIM α″ variant but no operative 332T variant. Both transformations may become operative, with at least one variant of each, inside the 332T + SIM α″ domain. In addition,

the primary deformation products can actually be observed in the unfavorable domain (near [001] pole) where grains possess both lower SF of 332T and SIM α″ than each threshold. The reason could probably be the stress concentrations due to the deformation incompatibility between the unfavorable grain and its neighbor grains, especially when the neighbors are favorable grains for transformations. Orientation II is of such situation (α″ transmission from neighbor grain marked by green arrows in figure 3.4) among several similar cases examined in this study (not shown in the thesis).

3.3.2 Pathways of twinning and martensitic transformations to accommodate the external and internal stresses

In the view of local microstructure evolution, the deformation starts, in the grains dominated by twinning, with the formation of band-like variants of primary 332T. The secondary products, SIM α″ and 332T, occur due to the change of the β orientation by primary twinning operation and also possibly due to the stress concentrations at primary 332T boundaries [33, 38, 84]. In the grains governed by twinning and SIM α″, both 332T and primary SIM α″ can nucleate and grow independently in the same grain to accommodate the external stresses. This is exemplified by the analysis of a grain with orientation I: for this orientation, $SF_{332T} = 0.50$ and $SF_{SIM\ \alpha''} = 0.41$, therefore both SF are above their threshold defined. Indeed, the experimental investigation of figure 3.2a shows that at the onset of the plastic regime, both mechanisms are triggered in this grain. In the domain theoretically unfavorable for transformations, i.e., near [001] pole, the SF of the positive SIM α″ variant is always higher than SF of 332T. Therefore, when stress concentration occurs at grain boundary due to the deformation incompatibility concerning neighbor grains, SIM α″ could be activated as the primary deformation prior to 332T. Nevertheless, 332T could be activated as secondary deformation mechanism as shown in figure 3.3 and figure 3.4. Such 2nd 332T in 1st martensite mechanism has not been reported in the previous studies of primary SIM α" behaviors in TRIP/TWIP alloys [41], which are usually attributed by reversibility of martensite to β matrix [41] or massive detwinning of the martensite [38].

Secondary transformations are observed in the primary products or at their interfaces to accommodate local stress. The peculiar α″ martensite at the 332T boundary (orientation I) exhibits a highly organized structure, in which alternate α″ lamellae of fixed thickness form a regular array. The structure is similar to the well-known transformation twinning microstructure in martensite.

In such a case, the twinning array is the LIS of the martensitic transformation to obtain an invariant plane strain to accommodate the transformation misfit at martensite/austenite boundary as required by the crystallographic theory of martensite [1]. Analogously, the α″ array at the 332T could probably fulfill a similar function to accommodate the stress concentration at the twin boundary by highly organized martensitic transformations. It has been well documented that very high stresses are generated in the boundary area of a deformation twin which is confined within an externally stressed parent crystal [42].

In the case of TWIP/TRIP Ti, the highly stressed areas would be at vicinities of grain boundary, 332T, and 130 α″ deformation twinning boundaries. The high-stress concentration could be related to the primary and secondary transformations. In the case of orientation II, the transformation is very hard to be activated due to its low SF for both 332T and SIM α″. As shown in table 3.2 the activated SIM α″ variant is CV1, and the SF of CV1 is only 0.27, which is less than the SF threshold of SIM α″ (0.35). Even though the resolved shear stress is insufficient to activate this variant of SIM α″ operation according to SF calculation, the primary α″ band seems to be nucleated at the grain boundary to accommodate the stress concentration caused by the intersection of grain boundary and SIM α″ (marked by green arrows in figure 3.2a) in adjacent grain. The SF of the variant SIM α″ activated in adjacent grain can be calculated as 0.36, which is higher than the SF threshold of SIM α″. Similar cases also be observed in other grains in the difficult transformation domain (near [001] pole) in Ti-12Mo alloy. Additionally, the secondary 130 α″ twinning in the primary α″ band (see figure 3.3) is believed to provide extra shear strain along the tensile direction, resulting in the almost fully reorientated parent α″. As observed in fully martensitic Ti alloy under tensile deformation, the reorientation of primary α″ variants are controlled by the local SF and deformation strain it provides along the tensile direction [35]. Regarding the detwinning phenomenon observed at Orientation II (figure 3.3), the detwinning process is triggered immediately after the unloading, meaning that enough driving force has been stored in the material during the loading step. The driving force could be the stress concentration at the primary α″ interface. At this boundary, the secondary 130 α″ DT shears are stopped by the primary α″ habit plane. The two shear planes $(7\ 10\ 0)_{\alpha''}$ for primary SIM α″ transformation and $(130)_{\alpha''}$ for secondary twinning intersect each other, leading to strain misfit, between the two variant martensite on each side of the boundary. These stresses arise from the resistance of the β matrix and α″ martensite to the macroscopic change of shape in the twinned volumes [85]. In

orientation II of Ti-12Mo, the accommodation phenomenon of this interfacial stress, thought to be operative during tensile loading, is the 332T branch nucleating at the primary α″ boundary after the 130 α″ DT, that then grows into the parent β matrix along a $\{332\}_\beta$ plane (please note the portions marked by green arrows in figure 3.3b). It is considered a secondary deformation mechanism related to the primary formation of martensite because the 332T observed here has a SF ($SF_{332T} = 0.23$) below the SF for SIM α″ ($SF_{SIM\ \alpha''} = 0.27$), and the SF threshold of 332T (0.4) is higher than that of SIM α″ (0.35). Correspondingly, the portion of 130 α″ DT aligned with this $\{332\}_\beta$ plane is preserved after the unloading (note the portions marked by black arrows in figure 3.3b). Regarding the portion of 130 α″ DT misaligned to accommodative 332T branch, the detwinning probably happens due to the release of stored backward stress. This leads to the hypothesis that the driving force might be weakened (accommodated) by the formation of the 332T branch, and therefore stabilize the 130 α″ DT from detwinning after unloading the external tensile stress. Indeed, the β grain choosing the 332T to accommodate the backward stress is reasonable, because the shear planes and directions are perfectly parallel between the equivalent 130 α″ DT system and 332T system operating in the same β matrix. On the other part, the 332T contributes to the overall shear strain for the tensile deformation of the grain, even though the resolved shear stress is insufficient to activate such twinning operation according to SF calculation ($SF_{332T} = 0.23 < 0.4$). Nevertheless, the formation of the 332T branches as an extension of 130 α″ DT into β matrix (marked by the yellow arrow in figure 3.3c), or similar cases, to the best of our knowledge, has never been reported in the literature.

3.3.3 Pathways of 332T formation via {130} <310>$_{\alpha''}$ twinning in martensite

The situation of accommodation is more complicated in the preserved 130 α″ DT without 332T accommodation (see the portions marked by blue arrows in figure 3.3c) in Orientation II. TEM observations reveal a complex secondary microstructure in one of this 130 α″ DT that remains after unloading (figure 3.4). The origin of these secondary features was rationalized by reconstructing their orientation relationships and habit planes in a stereographic projection given in figure 3.5a along the zone axis and directions A1 and A2 of figure 3.4a.

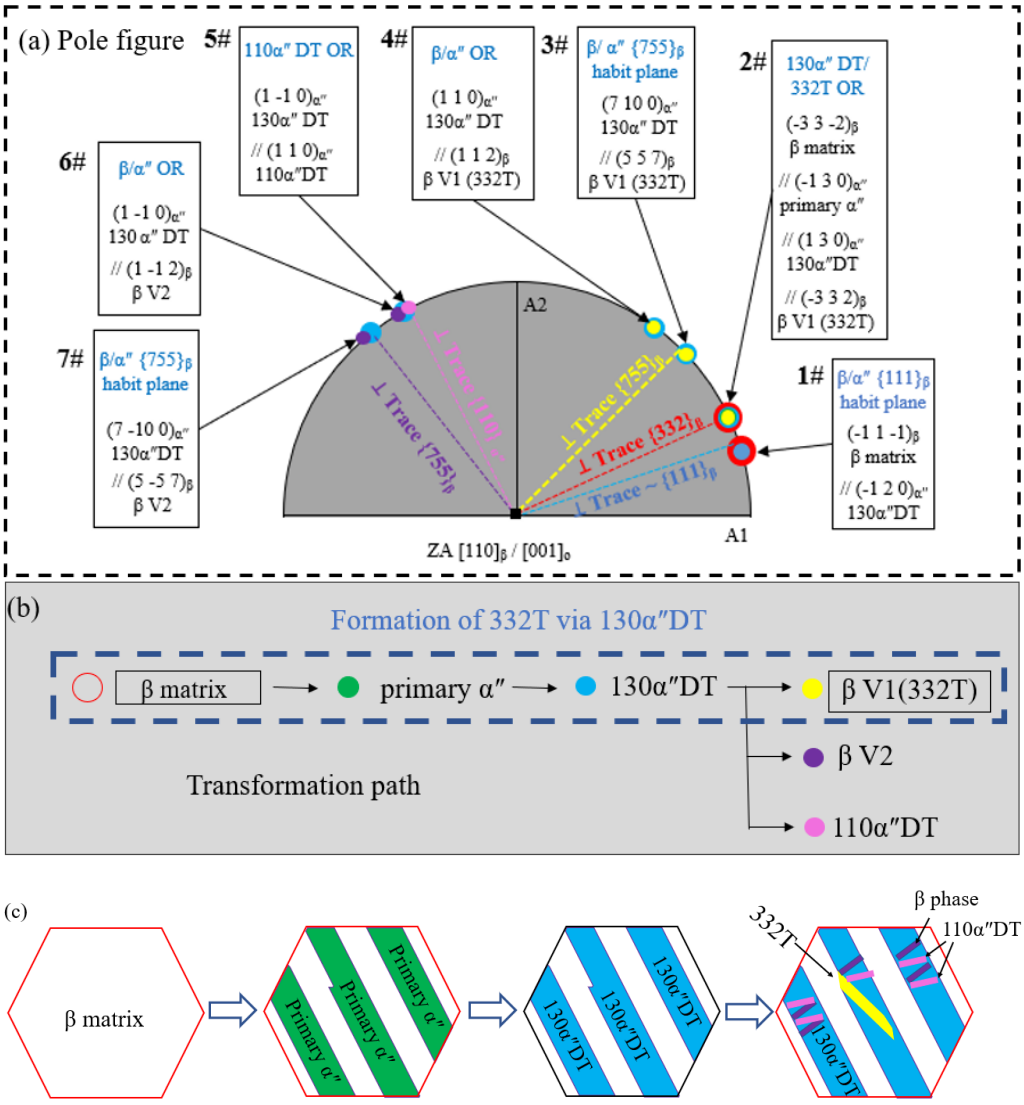

Figure 3.6 (a) The stereographic projections of the poles for all the deformation variants, identified in Figure 4 (orientation II) at the observation area along ZA $[110]_{\beta}$ / $[001]_{\alpha''}$. The OR and habit planes are indexed in the text blocks around the pole figure. The normal of the observed traces are plotted in the pole figure by dash lines; (b) and (c) transformation path under tensile stress. The 332T relationship is identified between β matrix and β V1. The color code used in the figure is the same one as in figure 3.5.

The interface of the observed main α″ band (marked by blue color in figure 3.4) and β matrix is measured as $(\bar{1}1\bar{1})_{\beta}/(\bar{1}20)_{\alpha''}$..(as shown in figure 5.10a box 1#). From the DP (figure 5.4b) it can be seen the main α″ band has an orientation relationship of $(130)_{\alpha''}$// $(\bar{3}3\bar{2})_{\beta}$ with β matrix (box 2#), which does not conform to the classic orientation relationship with β matrix. This unexpected orientation relationship, compared to the one observed at the mesoscale by EBSD, was interpreted

as the following: the β matrix (in red in figure 3.5a) first formed primary martensite (marked by the green dot in figure 3.5), with the conventional habit plane $\{557\}_{\beta}$. The whole martensitic band was then deformed by a 130 α″ DT operation, which resulted in an unexpected habit plane and transformed orientation relationship. This band, being then fully a 130 α″ DT, is somehow preserved after unloading, probably due to the internal microstructure. In it, two variants of β phase and one variant of α″ phase are recorded. The two variants of β phase in the 130 α″ DT band, β V1 marked by yellow dots and β V2 marked by purple dots, conform with the classical orientation relationship (box 4# and 6#), $\{211\}_{\beta}$ //$\{110\}_{\alpha''}$, and conventional $\{557\}_{\beta}$ habit plane (box 3# and 7#) with 130 α″ DT. Besides, the one variant of α″ conforms a $\{110\}<1\bar{1}0>_{\alpha''}$ DT relationship with 130 α″ DT (box 5#).

Based on the TEM observations in figure 3.5, figure 3.6b, and figure 3.6c show a schematic illustration of the transformation pathway in the grain with orientation II. Primary SIM α″ appeared first in the deformation process and then 130 α″ DT forms inside the SIM α″ until filling the whole martensitic volume, generating a new variant of α″. Part of it is then transformed via 110 α″ DT mode. Additionally, two variants of the β phase are formed in the 130 α″ martensite needles. Among them, one variant (β V1) shows a 332T orientation relationship with the β matrix while the other variant (β V2) does not conform to any known orientation relationship to the β matrix. It should be noticed that the 332T (β V1) exhibits a much longer interface trace with the 130 α″martensite than with the β matrix, suggesting that the 332T (β V1) should form from the reverse martensitic transformation from α″ to β phase. This is the first experimental observation that the formation of 332T can be induced by the reverse transformation from 130 α″ DT in Ti-12Mo alloy. Thanks to the formation of 332T (β V1), the habit plane between 332T (β V1) and 130 α″ DT becomes the normal 332T interface (marked by red dashed line in figure 3.5a), showing deflections along the original trace $(7\bar{5}5)_{\beta}$ habit plane (marked by yellow dashed line in figure 3.5a). However, the rest (marked by blue dashed line in figure 3.5a) of the interface between the primary twinned α″ needle and the matrix can be identified as $(111)_{\beta}$, which are still far from the ideal lattice invariant configuration ($\{755\}_{\beta}$ habit plane) between the α″ and β matrix, since the 130 α″ DT is directly in contact with the β matrix without the parent primary α″ as an intermediate layer (can be seen in figure 3.5b and outlined in figure 3.6c). Based on the observation that the 130 α″ is actually preserved with such microstructure, it is thought that all these internal transformations may be

responsible for stabilizing the non-lattice-invariant interface, thus inhibiting the detwinning of the 130 α″ DT otherwise observed in EBSD.

3.4 Summary

In this chapter, we proposed a method to describe and predict the distribution of the primary deformation mechanisms for all the grain orientations in TRIP/TWIP Ti alloys. This method is based on the experimental transformation partition maps and the computation of a series of theoretical transformation partition maps for different combinations of SF thresholds for 332T and SIM α″. The following main results are obtained.

1. The transformation pathway in Ti-12Mo depends on the grain orientation. The transformation pathways could be partitioned into four orientation domains in the stereographic triangle based on the Schmid factor simulation, leading to "transformation partition maps". They correspond to twin-dominated- or martensite-dominated-deformation or a combination of both or the domain unfavorable for both transformations.

2. The transformation pathways are highly diversified in TRIP/TWIP alloys due to the operations of the two transformations in a cascade manner with respect to the external tensile stress resolved in each grain; to the deformation incompatibility between neighbor grains belonging to different orientation domains; and to the strain-stress misfits at newly formed interfaces by $\{332\}\langle 113\rangle_{\beta}$ twinning and SIM α″. The transformations are adaptive to the local deformation condition at each grain without a unique pathway.

3. Experimental evidences are highlighted on the unprecedented formation mechanisms of $\{332\}\langle 113\rangle_{\beta}$ twins assisted by martensite $\{130\}\langle 310\rangle_{\alpha''}$ twinning via two different ways.

The stress-induced martensite and its twinning in Ti-12Mo alloy was investigated carefully in chapter 3. The SIM α″ transformation and its twinning play an important role in the high strain-hardening rate and the subsequent large uniform elongation during tensile plastic flow in TRIP/TWIP Ti-12Mo alloys. Therefore, the works on Ti-12Mo continue to further clarify the transformation mechanism of the martensitic mechanical twinning in Ti-12Mo alloy and the effect of the martensitic mechanical twinning on the mechanical properties of Ti-12Mo alloy.

Chapter 4 Studies of mechanical twinning and detwinning in stress-induced α″ martensite of TRIP/TWIP Ti-12Mo alloy.

Introduction

As mentioned in Chapter 3, the SIM transformation and its twinning play an important role in the mechanical properties of Ti-12Mo alloy. The chapter aims to clarify the evolution of the two modes of martensitic mechanical twinning in Ti-12Mo alloy with *in-situ* SEM and *in-situ* TEM observation. The selection criteria between the two mechanical twinning modes are quantitatively characterized by crystallographical transformation strain analysis. Then chapter 4 extends to clarify the twinning/detwinning process via in-situ electron microcopies under tensile deformation. Regarding the macroscopic tensile behavior, the pseudo-elasticity observed in the cyclic unloading test can be related to the detwinning of SIM α″. The samples of Ti-12Mo alloy with two different average diameters of grains, 20 μm (fine grain) and 100 μm (coarse grain), are studied in chapter 4. The in-situ investigations of this chapter are mainly carried out on the Ti-12Mo coarse grain and repeated on the Ti-12Mo fine grain. There is no descriptive effect of grain size on the selection mechanism of martensitic twinning modes and the twinning-detwinning process. The investigations carried out on Ti-12Mo fine grain will be marked in this chapter, otherwise carried out on Ti-12Mo coarse grain. The effects of grain size on the mechanical properties and transformation mechanism during the deformation process will be discussed in Chapter 5.

4.1 Cyclic loading-unloading tensile behavior of Ti-12Mo

The cyclic loading-unloading tensile tests at room temperature are carried out until fracture with the increments of 5% strain, and the first cycle is presented in figure 4.1. A pseudo-elastic behavior is observed in the unloading curve with a 0.006 strain of pseudo-elastic (ε_p). The pseudo-elastic phenomena have been reported related to reversion of twinned α″ in Ti-Nb alloy [51]. And the apparent Young's modulus in the second loading cycle id lower than that in the first loading. Since residual SIM α″ remains in the β matrix after the unloading process, and the shear modulus of SIM α″ is lower than the β phase.

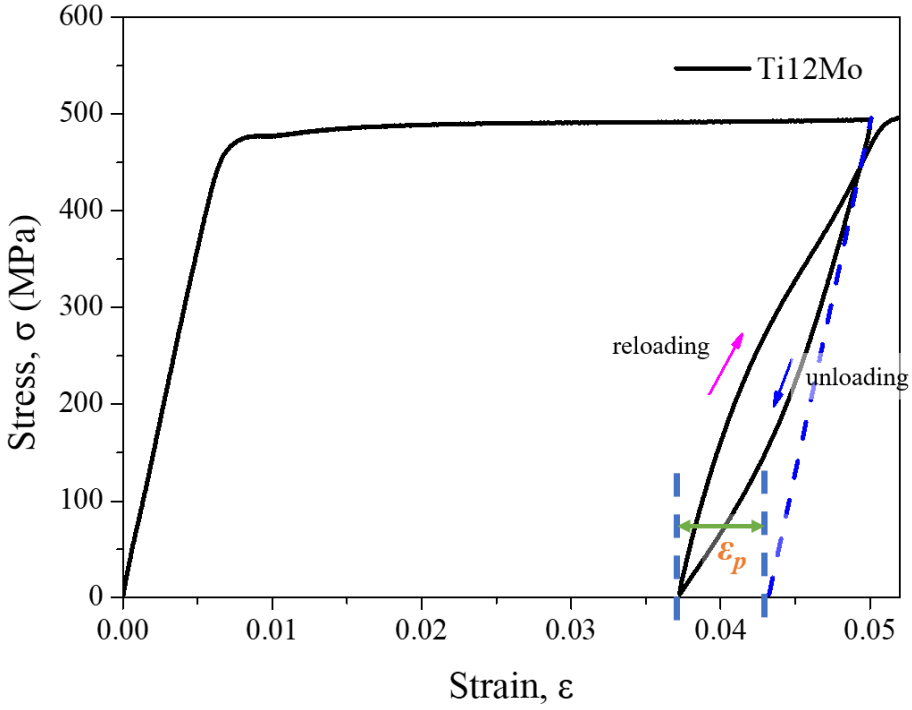

Figure 4.1 The stress-strain curve of first cyclic loading-unloading test is presented, ε_p: pseudo-elastic strain at room temperature after unloading.

4.2 Hierarchical mechanical twinning in SIM α″ during the loading process

In order to clarify the activation and evolution of the SIM α″ and its twinning process, more than 1000 grains in solution-treated Ti-12Mo alloy (same initial microstructure as in Chapter 3) are analyzed by *in-situ* EBSD mapping under tension. Five cases with different orientations and their associated Schmid factors all possible twinning variants are selected and listed in table 4.1 to analyze the martensitic twinning selection mechanism. The activated variant among the two systems of 130α″ DT and 110α″ DT is marked by blue color. Two representative cases of martensitic twinning, orientation I (130α″ DT dominant) and orientation II (110α″ DT dominant), are shown in details in the following, to investigate further the microstructural characteristics of 130α″ DT and 110α″ DT formation, respectively.

Table 4.1 Schmid factor for each martensitic mechanical twinning according to the primary SIMα″.

Orientation	Variant of $\{130\}_{\alpha''}$ twinning	SF of $\{130\}_{\alpha''}$ twinning	Variant of $\{110\}_{\alpha''}$ twinning	SF of $\{110\}_{\alpha''}$ twinning
I [3 9 1]	(130) $[\bar{3}10]$	0.26	(110) $[\bar{1}10]$	0.49
	$(1\bar{3}0)$ $[\bar{3}\bar{1}0]$	0.49	$(1\bar{1}0)$ $[\bar{1}\bar{1}0]$	0.32
II [3 25 7]	(130) $[\bar{3}10]$	0.32	(110) $[\bar{1}10]$	0.45
	$(1\bar{3}0)$ $[\bar{3}\bar{1}0]$	0.43	$(1\bar{1}0)$ $[\bar{1}\bar{1}0]$	0.36
III [7 21 5]	(130) $[\bar{3}10]$	0.26	(110) $[\bar{1}10]$	0.48
	$(1\bar{3}0)$ $[\bar{3}\bar{1}0]$	0.47	$(1\bar{1}0)$ $[\bar{1}\bar{1}0]$	0.31
IV [3 28 8]	(130) $[\bar{3}10]$	0.35	(110) $[\bar{1}10]$	0.44
	$(1\bar{3}0)$ $[\bar{3}\bar{1}0]$	0.42	$(1\bar{1}0)$ $[\bar{1}\bar{1}0]$	0.39
V [4 15 0]	(130) $[\bar{3}10]$	0.30	(110) $[\bar{1}10]$	0.50
	$(1\bar{3}0)$ $[\bar{3}\bar{1}0]$	0.48	$(1\bar{1}0)$ $[\bar{1}\bar{1}0]$	0.35

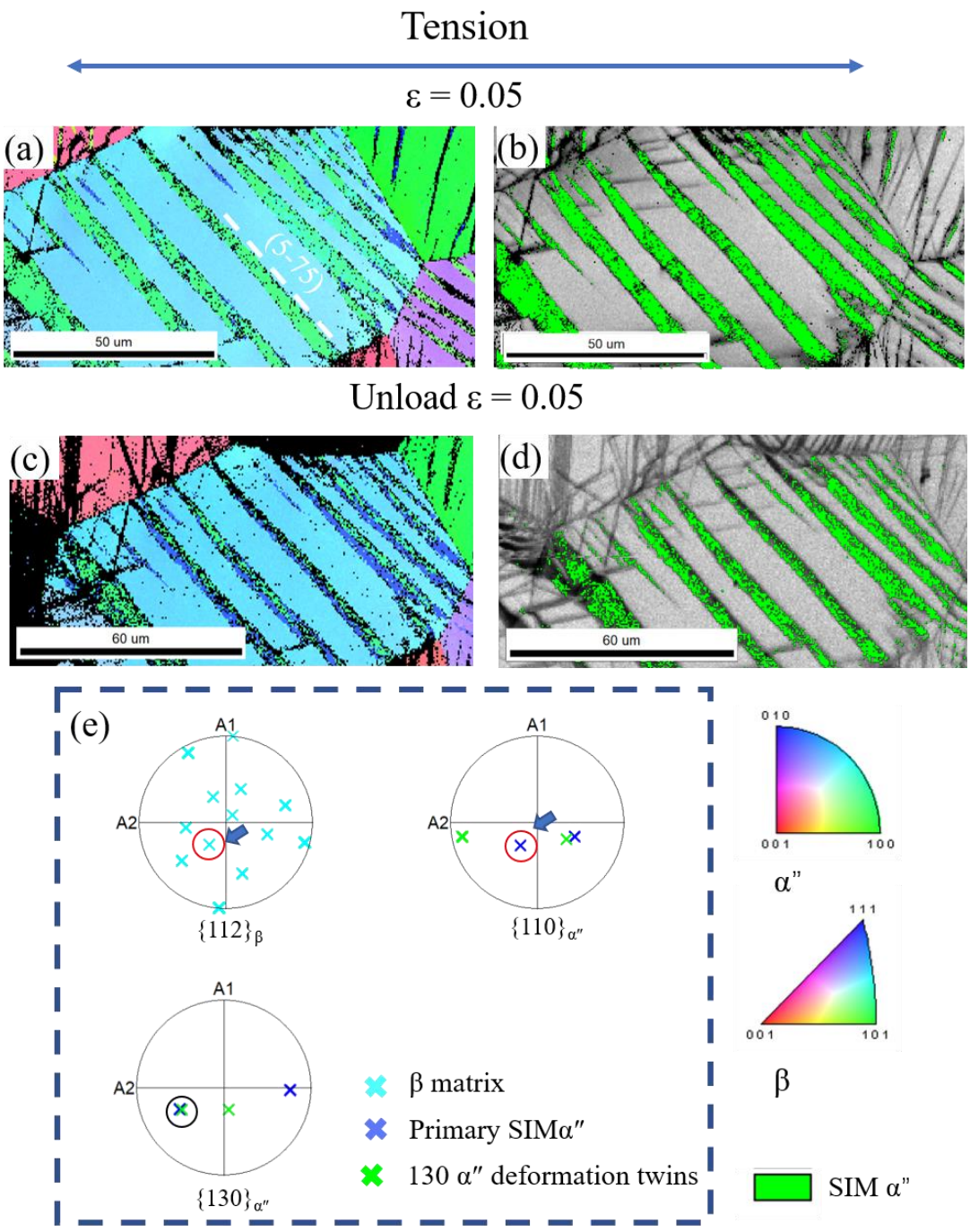

Figure 4.2 EBSD analysis of the Orientation II taken from the same region at strain ε = 0.05 (loading): (a) IPF maps (tensile direction) and (b)orientation maps for SIM α″ phase, and 0.05 (unloading): (c) IPF maps and (d) orientation maps for SIM α″ phase, respectively; (e) pole figures of β matrix and SIM α″. (A1 – rolling direction, A2 – transverse direction).

Figure 4.2 shows *in-situ* EBSD mapping of orientation I. Plate-like deformation bands with two different color contrasts (blue and green) appear in the β matrix at ε = 0.05 (figure 4.2a). These deformation bands are identified to be SIM α″, shown in the corresponding α″ phase maps (Fig. 4.2b). According to the crystallography analysis (common poles marked by red cycles in the pole figures in Fig. 4.2e), the blue SIM α″ is the primary phase directly transformed from β matrix following the classic orientation relationship $\{211\}_{\beta}$ //$\{110\}_{\alpha''}$ [86]. The green SIM α″, although presented in important fraction among the total SIM α″ volume, does not orientate in classic relationship to the β matrix. The orientation relationship analysis (Fig. 4.2e) shows that the green variant yields 130 α″ DT relationship with primary blue variant. Therefore, the results suggest that a mechanical twinning transformation could have probably occurred before ε = 0.05 in the primary SIM α″. The sample is unloaded from ε = 0.05 by fully releasing the tensile stress to study the detwinning process of the130 α″ DT during unloading. The EBSD scan at the same zone is shown in Fig. 4.2c and d at the unloaded state. It can be noticed that some of the 130 α″ DT (the green variant) detwinning to a primary blue variant, suggesting a detwinning process due to the releasing of tensile stress.

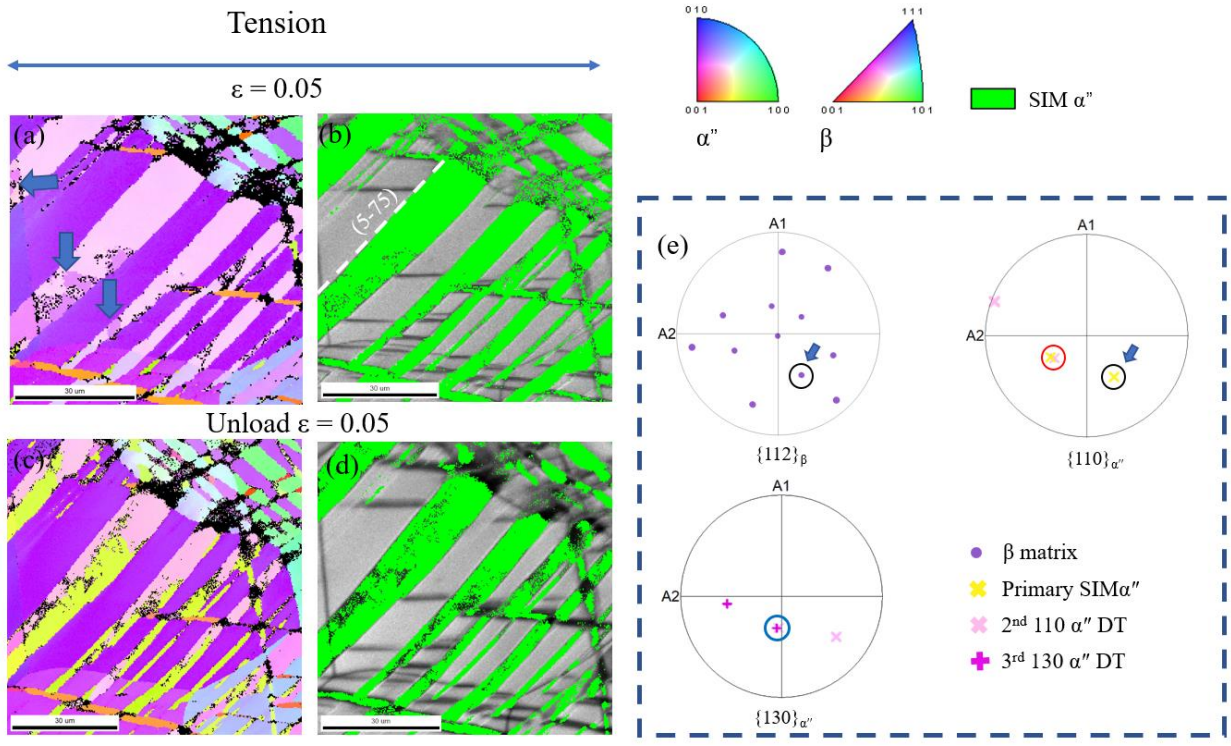

Figure 4.3 EBSD analysis of the Orientation II taken from the same region at strain ε = 0.05 (loading): (a) IPF maps (normal direction) and (b)orientation maps for SIM α″ phase, and 0.05 (unloading): (c) IPF maps and (d) orientation maps for SIM α″ phase, respectively.; (e) pole figures of β matrix and SIM α″. (A1 – rolling direction, A2 – transverse direction).

The other representative case is shown in figure 4.3, where a transformation cascade of β → α″ → 110 α″ DT→130 α″ DT and its reversion are captured by *in-situ* EBSD mapping. At ε = 0.05, SIM α″ (phase map in Fig. 4.3b) bands can be observed in the IPF map (Fig. 4.3a), in which some of the bands are composed of two variants differ in color (the pink ones are in the majority, and arrows indicate the purple ones in Fig. 4.3a). By performing the same crystallography analysis (Fig. 4.3e) shown in the previous case, it is found that neither of the two α″ variants at loading state (pink and purple in Fig. 4.3a) orientates in a classic relationship with respect to the β matrix. The pink orientation can be explained by the 110 α″ DT twinning of a primary SIM α″ precursor. However, no residual precursor SIM α″ is observed in these SIM α″ bands at loading state. The purple variant matches the orientation relationship of the 130 α″ DT product transformed from the pink variant. By unloading the sample, the EBSD scan at the same zone (Fig. 4.3c and d) identify the missing primary SIM α″ precursor, the yellow variant orientated in classic $\{211\}_{\beta}$// $\{110\}_{\alpha''}$ relationship [86] (by black cycle and blue arrows in figure 4.3e). The classic orientation relationship suggests that the yellow variant SIM α″ could probably transform directly from the β matrix. The crystallographic relationship between the pink variant and yellow variant (note the common $\{110\}_{\alpha''}$ plane marked by red cycle in Fig. 4.3e) indicates the 110 α″ DT relationship between the two variants. The finding corroborates the assumption that the pink variant could probably be secondary 110 α″ DT from the primary SIM α″ (yellow variant), revealed after a detwinning process after unloading. In fact, the detwinning effect is also observed in the 130 α″ DT couple between the pink and purple variants. It can be noticed that the purple variants (marked by blue arrows in Fig. 4.3a) disappear completely in Fig. 4.3c after unloading. Regarding the entire transformation pathway in a loading/unloading cycle, these results suggest that primary SIM α″ occurred during the loading and could be fully transformed to 110 α″ DT. The 2^{nd} 110 α″ DT could partly transform to 3^{rd} 130 α″ DT. During unloading, the detwinning process could occur in reversion of the twinning sequence, which is 3^{rd} 130 α″ DT → 2^{nd} 110 α″ DT → 1^{st} SIM α″.

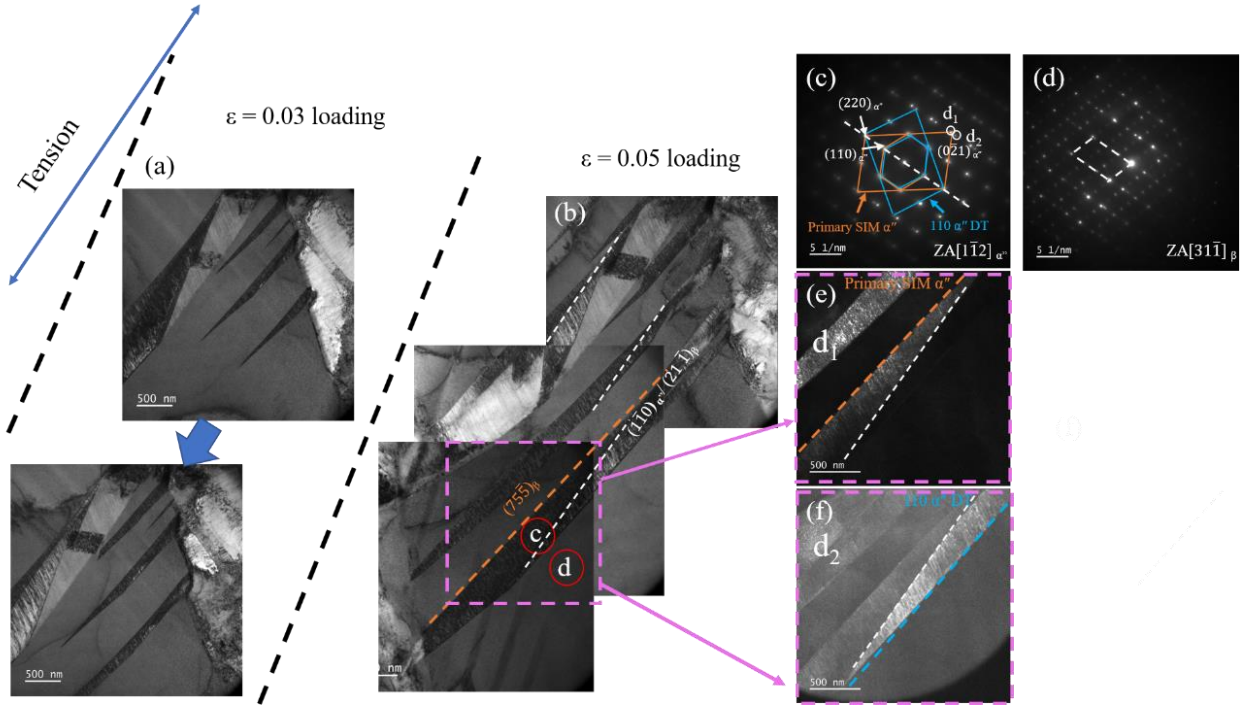

Figure 4.4 *In-situ* tensile TEM investigations of SIM α″ at Ti-12Mo fine grain: (a-b) bright field image: at (a) ε = 0.03, (b)ε = 0.05; (c and d) SAED pattern taken from region indicated by circle in (b), and corresponding dark-field images of (e) primary SIM α″and (f) 110 α″ DT, respectively.

Figure 4.4 (a and b) shows the bright-filed images under loading. A set of 1st SIM α″ bands about 100 μm in width, identified by diffraction patterns and dark-field imaging, are observed during their initial nucleation and growth processes from a pre-existing boundary under tensile loading. Since the very early stage of the 1st α″ formation, as shown in Fig. 4.4a, the 110 α″ DT is found to be activated immediately after the nucleation of the primary α″ band. The habit plane $(75\bar{5})$ of 1st SIM α″ is marked in Fig. 4.4 by the orange dash line. The twinning plane is 110 α″ marked by white dash lines in Fig. 4.4. The *in-situ* TEM observations confirm the transformation pathway proposed based on the EBSD studies that the 1st SIM α″ is activated firstly from β matrix then almost immediately twinned in forming a deformation band composed by 1st and 2nd α″. The volume fraction of 110 α″ DT increases along with the formation of 1st α″. It can be seen from Fig. 4.4b that one extremity of the SIM α″ band (marked by white arrows in Fig. 4.4b) has already fully twinned, presumably because the twinning is favorable to provide efficiently extra shear strain to accommodate the local deformation.

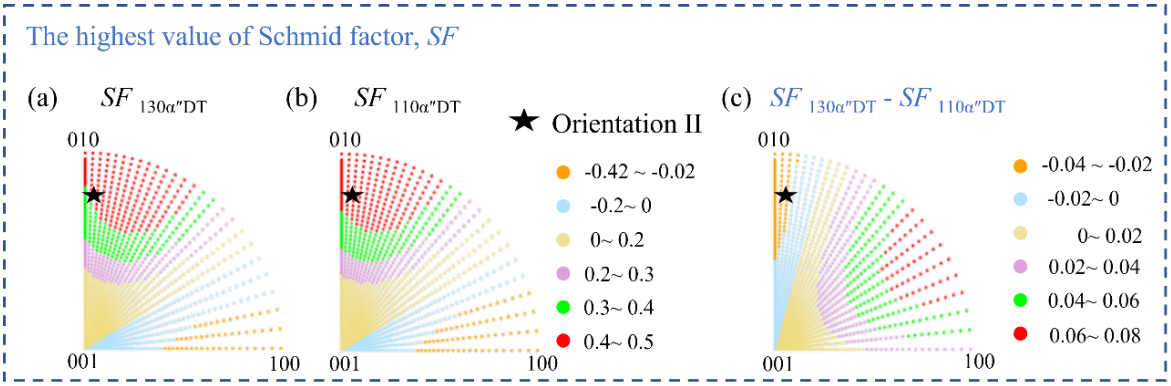

Figure 4.5 Inverse pole figure showing the distribution of the highest Schmid factor, *SF*, of (a) 130α″ DT, (b) 110α″ DT and (c)the values of $SF_{130\alpha''DT}$ minus $SF_{110\alpha''DT}$.

In order to rationalize the DT mode selection in α″ in terms of orientation dependence criteria, calculations of the Schmid factor for random grain orientations are performed for an orthorhombic α″ structure (Lattice parameters were measured under tensile loading at ε=0.04 [23]). The 130α″ DT and 110α″ DT plane and the associated invariant strain direction [37] are used for Schmid factor calculation. For each random grain orientation, the Schmid factor values for every 130α″ DT variants and every 110α″ DT variants are calculated and ranked, respectively. The highest values of Schmid factor for each grain orientation among all variants of the two twinning modes, 130α″ DT and 110α″ DT, are drawn in figure 5a and b respectively. It can be seen from these figures that the distributions of the highest values of the Schmid factor are similar. To further see the difference between the Schmid factor of 130α″ DT and 110α″ DT, the differences of Schmid factor ($SF_{130\alpha''\,DT}$ - $SF_{110\alpha''\,DT}$) for random grain orientations are shown in figure 4.5c.

4.3 Discussions

According to Chen et al. [37], 130 α″ DT and its reciprocal mode 110 α″ DT process comparatively smaller shear (0.1872) and the simplest shuffle (q = 2) of all the possible deformation twinning modes for SIM α″ (listed in table 4.4). Therefore, the 130 α″ DT and its

reciprocal mode, 110 α″ DT should be predominated during the loading process. However, according to our results, 130 α″ DT can be activated much more usually than its reciprocal mode, 110 α″ DT, which should be equally favored. These phenomena require a further explanation.

According to our experimental statistics (Table 4.1) of the secondary DT selection in α″ at random grains, the 130α″ DT is more likely to be occurred compared to 110α″ DT. The twin variant selection could be dominated by the Schmid factor of the variant and the critical resolved shear stress (CRSS) of the twinning modes. Under the same twinning mode (130α″ DT or 110α″ DT), the mechanical twinning activated obey the Schmid law as shown in Table 1, which consist with the results reported by Yang et al. in Ti2448 [64]. Regarding 110α″ DT, the associated Schmid factor can be superior to that of 130α″ DT in a narrow orientation range near to $[010]_{\alpha''}$ (see orange and light blue in figure 5c). The orientation II investigated experimentally is in this range, marked by the star in Figure 4.5. However, it also should be noticed that 130α″ DT is favorable even for the orientations where $SF_{130\alpha'' DT} < SF_{110\alpha'' DT}$ or $SF_{130\alpha'' DT} = SF_{110\alpha'' DT}$ (e.x. Orientation I, III, IV, and V). Tobe et al. [47] reported that $\{130\}_t\langle\bar{3}10\rangle_t$ is expected to occur more easily compared to $\{110\}_t\langle\bar{1}10\rangle_t$ due to the smaller magnitude of shuffle in tetragonal structure. A similar result was also reported by Chen et al. in the orthorhombic martensite α″ phase [13]. The smaller magnitude leads to a lower CRSS of 130α″ DT compared to 110α″ DT, which could explain the prevalence of 130α″ DT twinning over than 110α″ DT in metastable titanium alloy.

It is worth noting that the calculation presents nearly one-third of the standard triangle is of negative range (-0.42, 0) on the SF in both DT modes (figure 4.5a and 4.5b). The fact suggests that both mechanical twinning modes are unfavorable for activation under tensile deformation. In this range, the reorientation of SIMα″, i.e., the transformation among correspondence α″ variants, could be preferentially operational to provide positive transformation strain, as reported in [35].

The mechanical twinning products in 1st α″ exhibit reverse transformation during tensile unloading via a detwinning process. A similar process has been reported in chapter 3. The spontaneous detwinning results in pseudo-elastic recovery at room temperature during unloading (Fig. 4.1). Moreover, the detwinning process is found to be the major contributor to the pseudo-elastic recovery since the SIM α″ volume fraction is almost unchanged before and after unloading (phase maps in Fig. 4.2 and 4.3). Such detwinning-induced pseudo-elasticity has not been reported. In the SIM α″ containing Ti alloys, it has been reported in a full α″ Ti-Nb-Ta alloy that shape memory effect can be achieved by the reverse transformation of the deformation-induced

reorientation of α″ martensites after heating to more than 200°C [35]. On the other hand, in a pseudo-elastic Ti-Nb alloy, the product of unloading-induced reverse transformation from a twinned α″ has been reported to be a new β variant exhibiting {332}<113>$_\beta$ twinning relationship with β matrix. This pathway is proposed to be the origin of {332}<113>$_\beta$ twinning formation in Ti alloys [51]. However, the detwinning process identified in this study suggests again that the mechanism of 332T formation is non-unique (in chapter 3).

4.4 Summary

This chapter clarifies the evolution of the two modes of martensitic mechanical twinning in Ti-12Mo alloy with *in-situ* SEM and *in-situ* TEM observation. The selection criteria between the two mechanical twinning modes are quantitatively characterized by crystallographical transformation strain analysis. The following main results can be obtained.

2. The experiment in this work confirmed that 130 α″ DT is much easier activated in bulk Ti-12Mo sample than 110 α″ DT in Ti-12Mo alloy.

3. The mechanical twinning products in 1st α″ exhibit reverse transformation during tensile unloading via a detwinning process. The spontaneous detwinning results in pseudo-elastic recovery at room temperature during unloading.

As shown in chapters 3 and 4, the TRIP and TWIP effects play an important role in mechanical behavior. It has been reported that the mechanical behavior could be significantly affected by ω phase precipitation due to the suppression of TRIP and TWIP effects by ω particles [16]. The effects of ω particles in mechanical behavior and deformation mechanism will be studied in Chapter 5.

Chapter 5 Mechanism studies of isothermal omega hardening in metastable TRIP/TWIP Ti-12Mo alloy

Introduction

In order to study the effect of grain size on the mechanical properties and transformation mechanism of Ti-12Mo, the samples of Ti-12Mo with two different average grain diameters, 20 μm (fine grain) and 100 μm (coarse grain), are studied in this chapter. The average grain size is controlled by the time of solution treatment time at 900℃, 60s (20 μm) and 1.8ks (100 μm), respectively. This chapter also clarifies the ω_{ath}−ω_{iso} transition mechanism as well as its effects on mechanical properties and the transformation pathways in metastable Ti alloy. The same Ti-12Mo alloy and a fixed hardening temperature at 200℃ are selected to realize two objectives: a) to clarify the ω_{ath}−ω_{iso} transition by electrical resistivity measurement, synchrotron X-ray diffraction, and in-situ TEM under heating; b) to understand and to control the effects of the ω_{iso} at different maturity stages to the deformation mechanisms selection then the overall tensile properties via EBSD statistics and TEM studies under in-situ traction conditions.

5.1 Mechanical properties and characterization of solution treated states.

Figure 5.1 shows the true strain-true stress curves of Ti-12Mo alloys at different states. The alloys alloy states and the corresponding thermal treatment histories are listed in Table 5.1. In the table, the mechanical properties, the average grain sizes, and the plastic deformation mechanisms observed in the experiments are also summarized in comparison to the coarse grain Ti-12Mo. It can be seen from Fig. 5.1a that the yield and flow stresses of the fine-grain Ti-12Mo are higher than the coarse grain alloy. The grain morphology and orientation distribution of the fine-grain alloy are shown in Fig. 5.2a. After being hardened at 200℃ for 60s (ω_{iso} hardened 60s), another considerable increment of yield strength from 659MPa to 865MPa is observed, still retaining the large uniform elongation close to that of the coarse grain alloy. After increasing the omega ω_{iso} hardening duration, the uniform elongation dramatically decreases to 3.3% after 150s of ω_{iso} hardening and is completely inhibited after a 300s ω_{iso} hardening (Fig. 5.1a). For the sample after 150s ω_{iso} hardening, the yield stress reaches about 1GPa with visual plasticity during the tensile test. However, the uniform elongation is limited due to the low strain hardening rate (Fig. 5.1b),

leading to immediate necking after the yield point. After further prolonging the ω_{iso} hardening treatment to 300s, the sample exhibits high strength (1048 MPa) but brittleness. The elastic moduli (figure 5.1 and table 5.1) of ω_{iso} hardened samples increase proportionally to the increments of the ω_{iso} hardening duration. It is worth noting that the plateau-like stress flow can be observed at the beginning of the plastic deformation in the Ti-12Mo fine-grain alloy and disappeared in ω_{iso} hardened samples. Sun et al. [23] suggested the appearance of the plateau is related to the SIM α″ transformation. To clarify the evolution of strain-hardening behavior, the corresponding strain-hardening rate ($d\sigma/d\varepsilon$) curves of the alloys at three treatment states are shown in inset of figure 5.1. The strain-hardening rate curves are non-monotonic, similar to those observed in TRIP/TWIP β Ti-alloys [23, 72]. Among the three states, the strain-hardening curves of the coarse and fine grain Ti-12Mo are similar. Their hardening rate reach respectively the maximum values, of 1975MPa and 2685MPa, at $\varepsilon = 0.1$. After 60s ω_{iso} hardening, an essential reduction of the strain-hardening rate curve can be noticed. However, the hardening rate is still above the Consider Criterion line ($d\sigma/d\varepsilon = \sigma$, the dashed line shown in Fig. 5.1b) to maintain the large uniform elongation. However, the strain-hardening rate drops rapidly below the Consider Criterion line in the 150s ω_{iso} hardened sample (Fig. 5.1b).

Table 5.1 Mechanical properties of Ti-12Mo after different strengthening treatments from as-cold-rolled state.

Alloy states	Ti-12Mo coarse grain	Ti-12Mo fine grain	ω_{iso} hardened 60s	ω_{iso} hardened 150s	ω_{iso} hardened 300s
Thermal treatment history	900℃/1.8ks WQ (water quenching)	900℃/60s WQ	Ti-12Mo fine grain + 200℃/60s air-cooling	Ti-12Mo fine grain + 200℃/150s air-cooling	Ti-12Mo fine grain + 200℃/300s air-cooling
Yielding strength, σ_s (MPa)	478±24	659±33	865±43	990±48	1048±52
Young's modulus, *E (GPa)*	82±4	76±4	110±6	115±6	140±7
Ultimate strength σ_{UTS} (MPa)	975±4	1093±55	1141±57	990±48	1048±52

Uniform elongation	39±5%	29±5%	33±5%	3.3±1%	< 1%
Average Grain size (μm)	100±5	20±2	20±2	20±2	20±2
Deformation mechanism in plastic regime	TRIP/TWIP/slip	TRIP/TWIP/slip	TRIP/TWIP/slip	TWIP	No plasticity

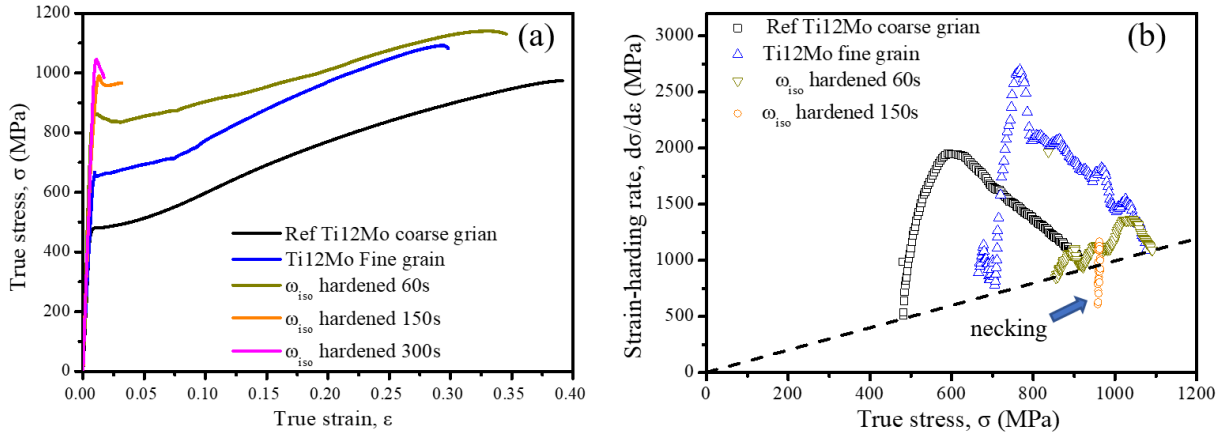

Figure. 5.1 (a)The true strain-stress curves of the Ti-12Mo at different states. (b) The corresponding strain-hardening rate curves of Ti-12Mo sample as function of true stress.

5.2 In-situ investigations of ω phase transformation during ω_{iso} hardened treatment

Figure 5.2 shows the comparisons of the initial microstructure and cell parameters before and after 60s ω_{iso} hardening. According to the EBSD results, there is not any change in average grain size and texture between the two states. In order to study the omega phase, high-energy synchrotron X-ray measurements before and after the hardening treatment under transmission mode over an area 500 mm × 500 mm, similar to the size of the EBSD maps shown in Fig. 5.2a and b. After ω_{iso} hardening for 60s, the lattice parameter of β phase decreases slightly from 0.3276 nm to 0.3263 nm. Similarly, the peaks of ω phase shifts to higher angles (marked by orange dash line in figure 5.2), caused by reduction of the *c* in ω phase from 0.2883 nm to 0.2817 nm. These results indicate a lattice contraction in ω phase along c axis as well as the slight decrease of cell parameters of β phase.

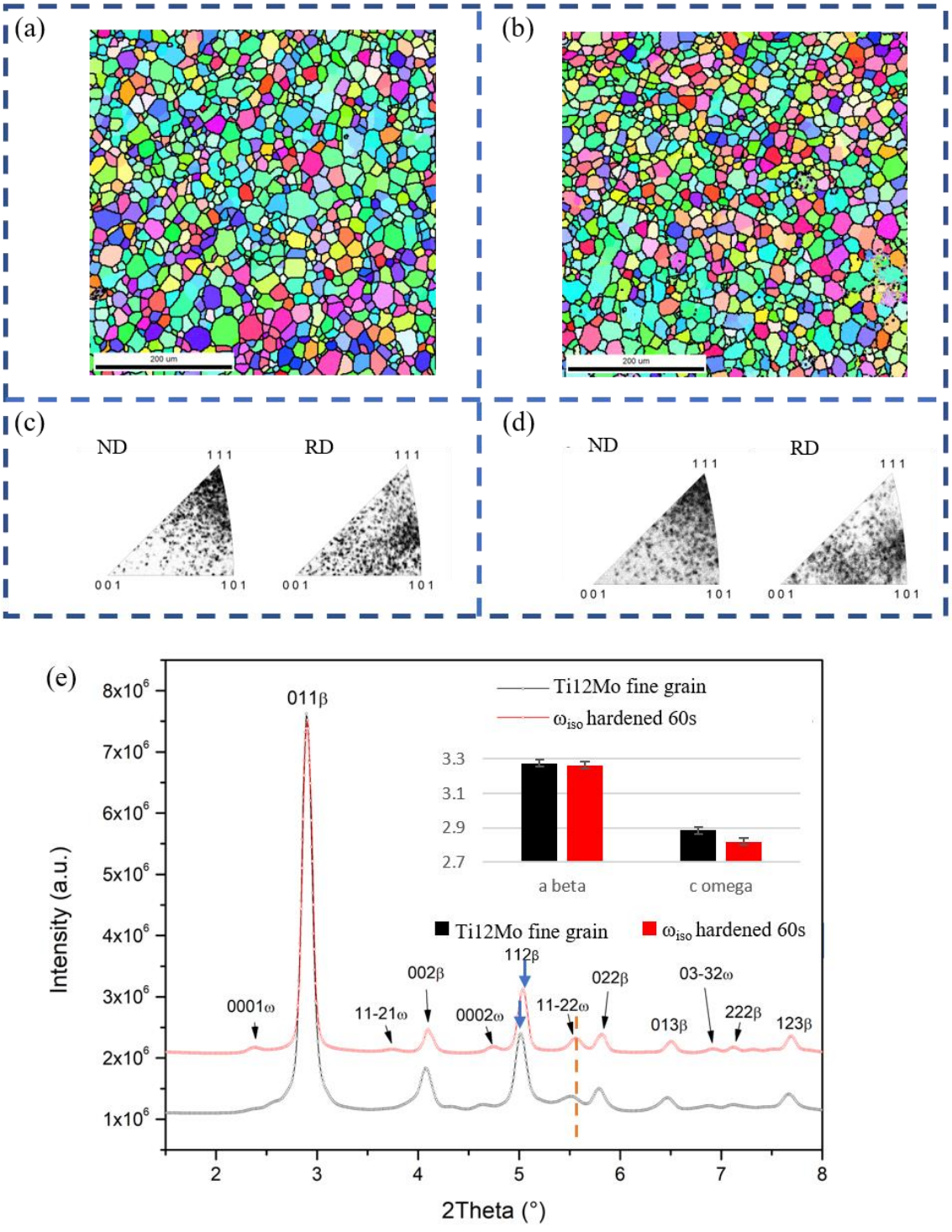

Figure 5.2 Initial microstructure of Ti-12Mo fine grain and ω_{iso} hardened 60s sample: Inverse pole figure maps of (a) Ti-12Mo fine grain and (b) ω_{iso} hardened 60s samples; inverse pole figure of the grain orientations at ND and RD directions of (c) Ti-12Mo fine grain and (d) ω_{iso} hardened 60s samples; (e) ex-situ Synchrotron X-ray

diffraction of Ti-12Mo fine grain and ω_{iso} hardened 60s samples. The comparison between the cell paraments of the β phase and ω phase is shown in the inset of (e). ND: normal direction, RD: rolling direction.

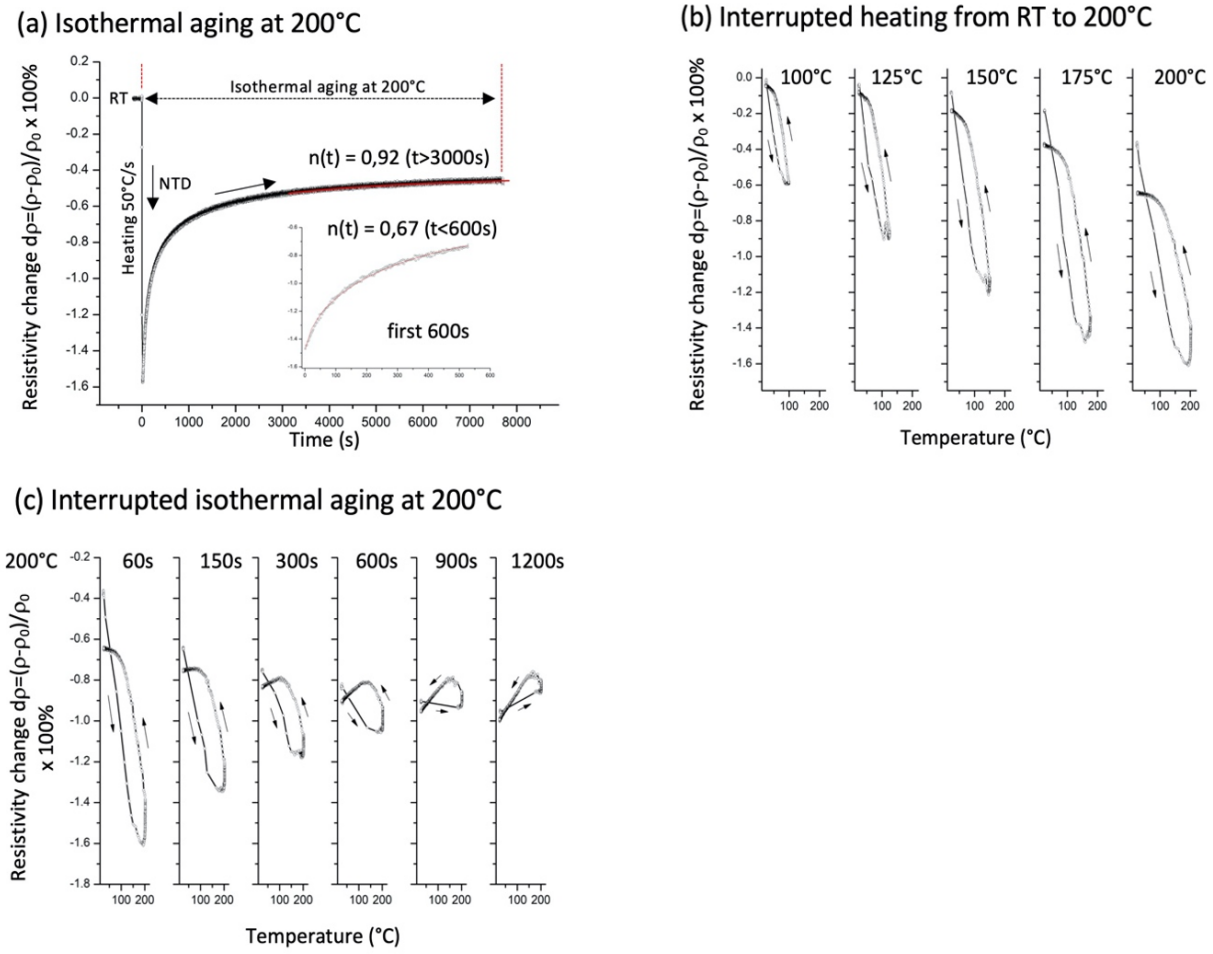

Figure 5.3 In-situ electrical resistivity measurement of fine-grain Ti-12Mo alloy: (a) ω_{iso} hardening treatment at 200°C, (b) interrupted heating from room temperature to 200°C (heating in 50°C/s rate and holding at the target temperature for the 60s then cooling at the air to room temperature), (c) interrupted isothermal up-quenched at 200°C (heating in 50°C/s rate and holding at 200°C for target time then cooling at air to room temperature).

In order to analysis of the ω_{iso} hardening process during 200°C, isothermal electrical resistivity measurements of Ti-12Mo fine-grain alloy at 200°C were performed. Figure 5.3a shows isothermal electrical resistivity variation $(\rho)/\rho_o$ of the ST alloy during the process of heating from room temperature to 200°C in a fast heating-rate (50°C/s) and then holding at 200°C. With the

increase of temperature from room temperature to 200°C, a negative temperature dependence (NTD) effect can be observed, i.e., the electrical resistivity decreased with the increasing temperature.

The isothermal resistivity change caused by phase transformation can usually be described by the classic Kinetic Law (inset the figure 5.3e) [85]:

$$\xi = 1-\exp(-kt^n) \qquad (Eq\ 5.1)$$

where the ξ is the fraction of transformation, t is transformed time, n is Avrami exponent and the constant k is called rate constant. It is defined as:

$$V^\beta / V = 1-exp\ (-kt) \qquad (Eq\ 5.2)$$

where V is the total transforming volume during isothermal, and the volume which has transformed from one phase to another phase at any time is V^β.

The non-linear fitting based on the kinetic law returns different n values at different stages of the transformation. At the very early stage (t < 600s), n yields to 0.67, which is in the typical kinetic found in diffusive precipitations from pre-existing sites, such as dislocations [85] and Guinier-Preston zones [87]. At the later stage (t> 3000s), n increased to 0.92, which is also similar to the growth kinetic (n near 1) reported in diffusion-controlled precipitation from dislocations [85].

It is well-known that the NTD in many Ti and Zr systems is reversible, cyclic resistivity measurements were performed at different temperatures and time points during the ω_{iso} hardening treatment. The results are shown in Fig. 5.3b, in which the rapid heating process from RT to 200°C was interrupted by progressive heating-cooling cycles. When reaching 200°C, the target temperature is maintained during which the cycles are repeated at different time points to track the NTD evolution during the isothermal aging (Fig. 5.3c). The sample was held in the bath for 60s after reaching the target temperatures in every cycle before cooling. The NTD is fully reversible at 100°C. The reversibility reduces since 125°C and the differences increase progressively between the initial resistivity of fine-grain Ti-12Mo and the resistivity after each heating-cooling cycle (Fig. 5.3b). The fine-grain Ti-12Mo loses permanently about 0.6% of its original resistivity after the cycles till 200°C. It should be reminded that the lattice contractions along an of β matrix and c of

ω phase are observed after 200°C/60s treatment. The evolution of the NTD effect is tracked by repeating the heat-cooling cycles at 200°C. It can be seen from Fig. 5.3c that the NTD effect becomes weak and finally disappears when the total aging duration reaches 1200s.

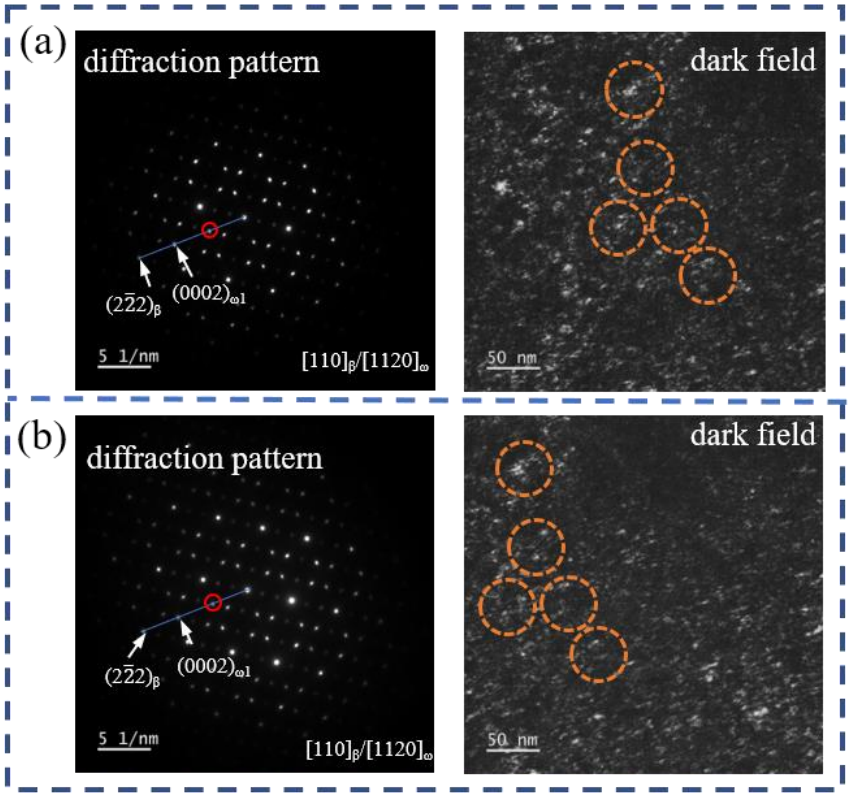

Figure 5.4 In-situ heating TEM observations of Ti-12Mo fine-grain recorded during the heating process: (a) before heating and (b) heating from room temperature to 200℃ with a heating rate of 5℃/s, then holding for 60 s.

The ω morphology and electron diffraction are traced by in-situ heating in TEM. figure 5.4 (a and b) shows the images of Ti-12Mo fine grain, which recorded at room temperature and 200°C, respectively. Prior to heating, the β matrix zone along $[110]_\beta$ axis was imaged in figure 5.4 a, diffraction and corresponding dark-field modes for both visible ω variants. The sample was then heated to 200°C at a rating rate of 5°C/s under surveillance by switching among the imaging modes. The second set of images (Fig. 5.4b) were taken at the same zone 60s after reaching 200°C when the sample stopped drifting. By comparing the two groups of the images, some original ω_{ath} particles dissolved at 200°C and some changed morphology (examples are marked by orange

cycles in dark-field images in figure 5.4 a and b). It has to be noted that this change observed in the dark-field image may also be due to the tilting and rotation of the sample caused by the heating.

5.3 Deformation mechanism

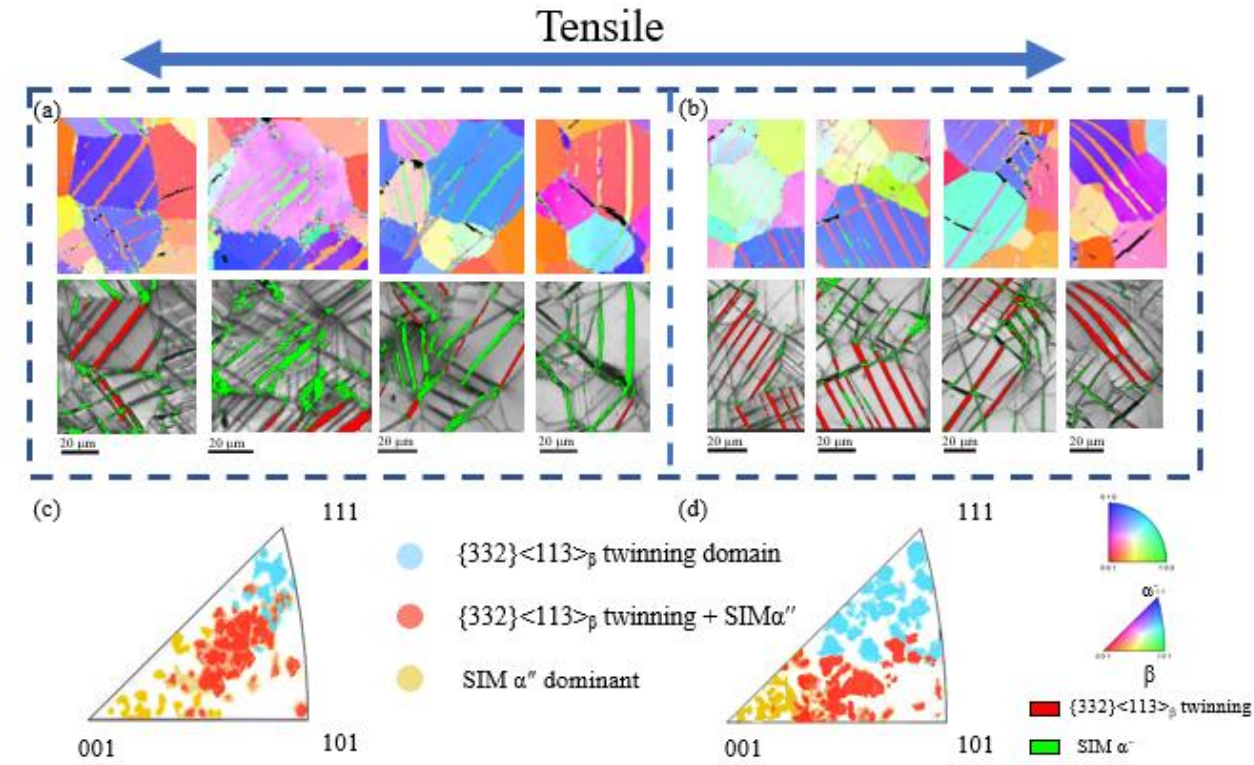

Figure 5.5 Experimental of the EBSD statistic of the primary deformation products in different grains in Ti-12Mo fine grain and ω_{iso} hardened 60s samples by in-situ EBSD under tensile strain (ε = 0.02): several cases inverse pole figure maps and phase+ IQ maps of Ti-12Mo fine grain (a) and ω_{iso} hardened 60s (b) alloys; Experimental Invers pole figure (IPF) of the statistic of the primary deformation products in Ti-12Mo fine grain (c) and ω_{iso} hardening 60s (d) alloy.

About 1000 grains in of various orientation in Ti-12Mo fine grain (c) and ω_{iso} hardened 60s alloys were analyzed during in-situ tensile test and their primary deformation mechanism at yielding was characterized by EBSD. Some cases of each state alloy are shown in figure 5.5 (a and b), both SIM α″ and 332T can be activated as the dominant deformation products in grains at each state depending on the orientation of these grains. Figure 5.5 (c and d) shows the EBSD statistical analysis of the primary transformation products in all these grains, originating from the same sample in each state alloy. In this chapter, the term "primary" refers to the transformation products directly formed from β matrix at yielding (ε = 0.02). As shown in figure 5.5 c and d, the orientations

of the analyzed β grains of Ti-12Mo fine grain and ω_{iso} hardened 60s alloys, respectively, are plotted in the inverse pole figure with respect to the tensile axis. This kind of inverse pole figure is named experimental transformation partition maps in this study. The different deformation products observed are represented by different color codes. The grains, where the primary deformation products are 332T, are represented by blue color. The grains with only primary SIM α″ transformation use for yellow color. And the grains showing both 332T and SIM α″ as primary deformation products are highlighted by red color. Distinct regions appear on the experimental transformation partition maps suggesting that the transformation products distribution is grain-orientation dependent. The colors are roughly partitioned into three domains, corresponding to their associated deformation mechanism. A similar phenomenon has been observed by our previous works in deformed Ti-12Mo coarse grain in chapter 3—the distributions directly from the Schmid factor of the two transformations and the corresponding threshold of Schmid factor. Interestingly, the distributions of deformation products of the experimental transformation partition maps in the three states alloys, Ti-12Mo coarse grain (figure 3.1 in chapter 3), Ti-12Mo fine grain (figure 5.5c), and ω_{iso} hardened 60s (figure 5.5d) alloys, with the same chemical composition shows a significant difference. Compared to Ti-12Mo coarse grain, a smaller $\{332\}\langle 113\rangle_{\beta}$ dominant area and a larger SIM α″ dominant area are presented in Ti-12Mo fine grain, while a larger 332T dominant area and a smaller SIM α″ dominant area are presented in ω_{iso} hardened 60s alloy (fig. 5.5d), which should be attributed to their different Schmid factor threshold of the two transformation products.

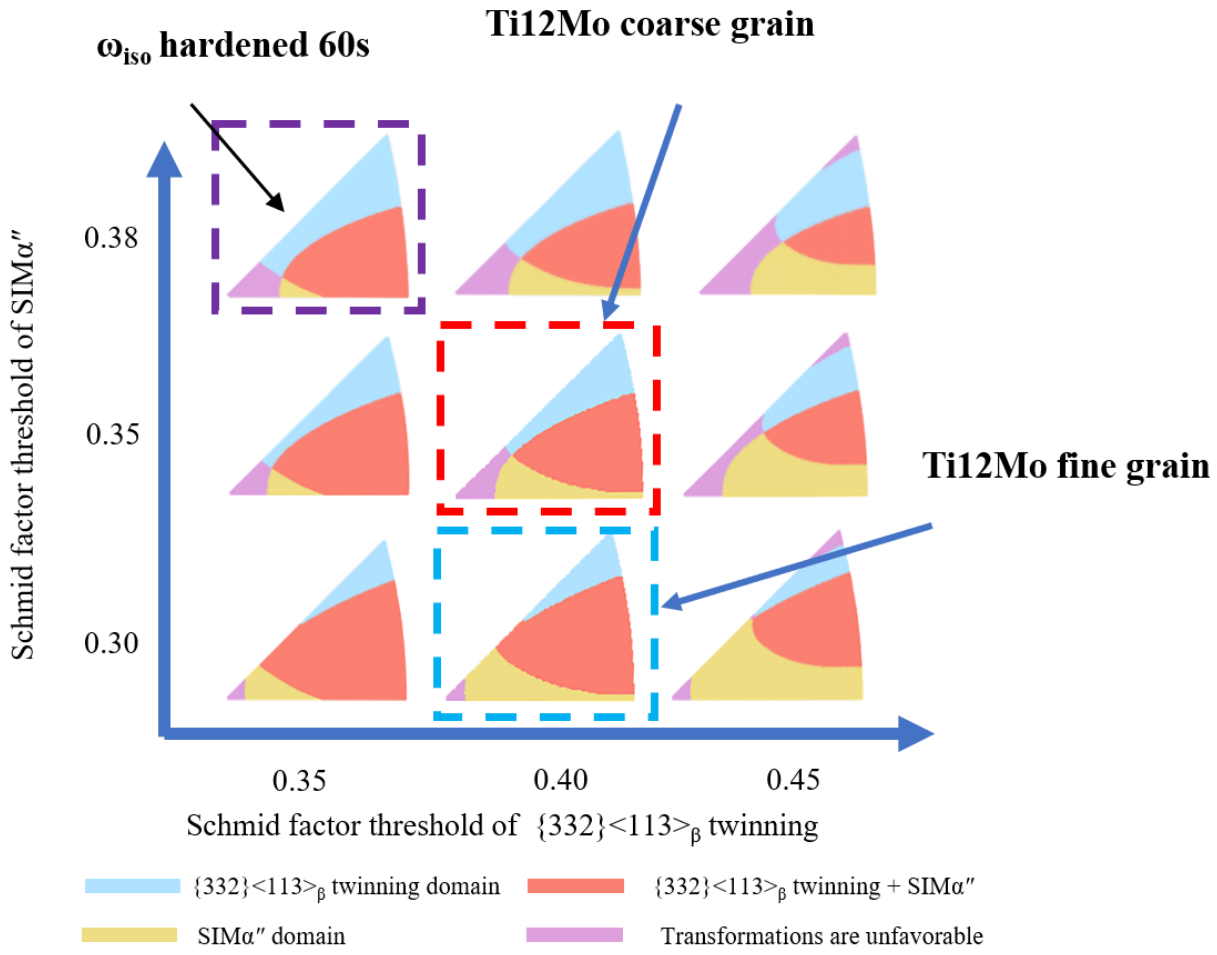

Figure 5.6 Inverse pole figures of the calculation of the orientation domains as a function of the combinations of threshold Schmid factors. The cases marked by dash square conforms the domain distribution observed experimentally in Ti-12Mo coarse grain (red), Ti-12Mo fine grain (blue), and ω_{iso} hardened 60s (purple) alloys.

In order to fit the three domains of product distribution observed in EBSD statistic of the two states alloys (Ti-12Mo fine grain and ω_{iso} hardened 60s), a laboratory-made computer program calculates a set of theoretical transformation partition maps for different combinations of Schmid factors threshold for 332T and SIM α″. The computation takes thresholds varying between 0.3 and 0.5, with 0.01 steps. Selected cases, for Schmid factor thresholds of 0.3, 0.35, and 0.38 for SIM α″ and 0.35, 0.40, and 0.45 for 332T, are compiled into inverse pole figure maps in figure 5.5. The cases framed by blue color and purple color in figure 5.6 present the best agreement of transformation partition maps between calculation and experiment of Ti-12Mo fine grain and ω_{iso} hardened 60s, respectively, illuminating the Schmid factor threshold of SIM α″ equals to 0.3 and Schmid factor threshold of 332T equals to 0.4 in Ti-12Mo fine grain; and Schmid factor threshold

of SIM α″ equals to 0.38 and Schmid factor threshold of 332T equals to 0.35 in ω_{iso} hardened 60s alloy.

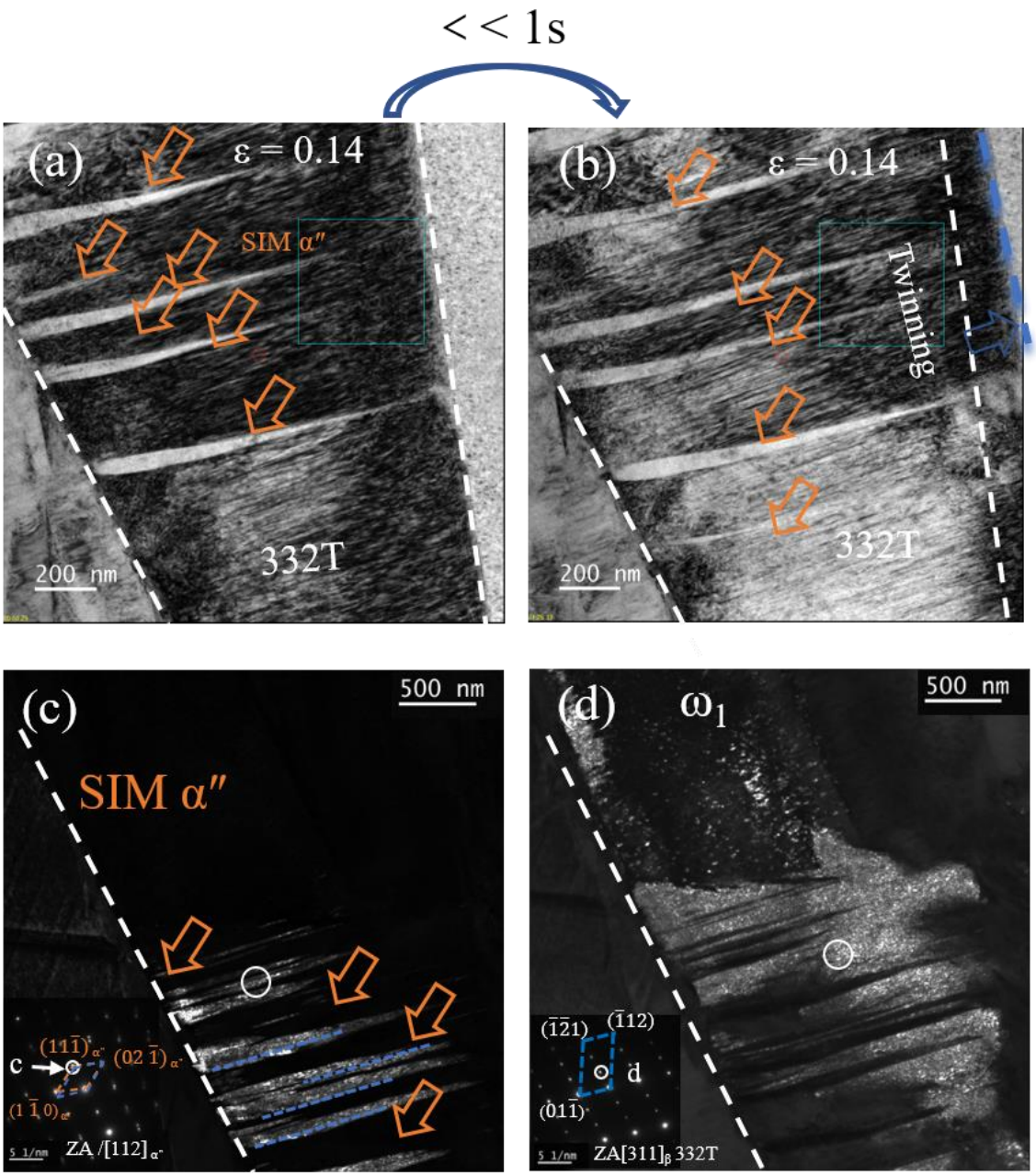

Figure 5.7 In-situ tensile TEM investigations of 332T at aging Ti-12Mo: (a-c) bright field image: (a) at ε = 0, (b-d) at ε = 0.14; (e-g) SAED pattern taken from region indicated by circle in (d); (h) and (i) corresponding dark-field images of one variant of SIM α″and of the ω phase, respectively.

Table 5.2 Crystallography characteristics of the grain observed in the in-situ tensile TEM in figure 5.7.

	Grain in figure 7		
Zone axis $(ZA)_\beta$	$[1\bar{3}5]$		
Highest Schmid factor (SF) 332T	0.46		
Highest SF SIM α″	0.34		
Primary deformation products	$(33\bar{2})$ [113] twinning		
Transformation strain of primary deformation products along Tensile direction (T)	+4.5%		
Transformation strain of primary deformation products along ZA	-4.4%		
Transformation strain of primary deformation products along ZA×T	+5.5%		
Secondary deformation products	SIM α″ CV1	SIM α″ CV4 ($\{11\bar{1}\}$ type I twin of CV1)	CV1 to CV4
SF of secondary deformation products	0.21	-0.40	0.21
Transformation strain of secondary deformation products along Tensile direction (T)	+2.8%	~	+5.2%
Transformation strain of secondary deformation products along ZA	-3.9%	~	+0.7%
Transformation strain of secondary deformation products along ZA×T	+1.4%	~	-4.9%

`` To clearly the effects of ω phase on the formation of 332T during the tensile process, carefully in-situ tensile TEM investigations were applied (figure 5.7) on a 60s ω_{iso} hardened sample. A 332T band with a width of 900 nm was captured during the tensile process. In the twin band, 2nd SIM α″ bands were identified by the diffraction pattern and the corresponding dark-field image (Figures 5.7c and d). Upon further traction, the 2nd SIM α″ bands grew in response to the strain increment at ε = 0.14 until they reached the boundary of the 332T band (figure 5.7a and b, and supplemental material). At this moment, the 332T band expanded abruptly by transforming a volume of the matrix into a twin. The dark-field imaging of ω in the twin band demonstrates a heterogenous distribution of the ω phase near the 2nd α″ (Fig. 5.7d). Only one single ω variant is detected (insert in Fig. 5.7d) by diffraction. It should be noticed that ω density in the α″-free zone is remarkably

low in the twin band, witnessing the destruction of the matrix ω phase in the matrix by twinning. The uneven distribution suggests that the new ω phase formed directly from the 332T332T rather than from the ω phase in the β matrix. The details of the crystallographic characteristics of the scene are summarized in Table 5.2. The calculations show that the 2nd α″ provides a positive contribution (+5.2%) to the micro-strain in the tensile direction and the twinning contribution (+4.5%). Moreover, the 2nd α″ provides strain (-4.9%) in the opposite direction to the twinning (+5.5%) in the normal direction of the sample. The twinning strain at sample normal direction is locally relaxed in the vicinity of 2nd α″ phase. These phenomena hint that a transformation ω→β matrix could be activated during the twinning process, and the stress inside the 332T could induce a new ω phase. A similar mechanism has been proposed by Xiao et al.[88].

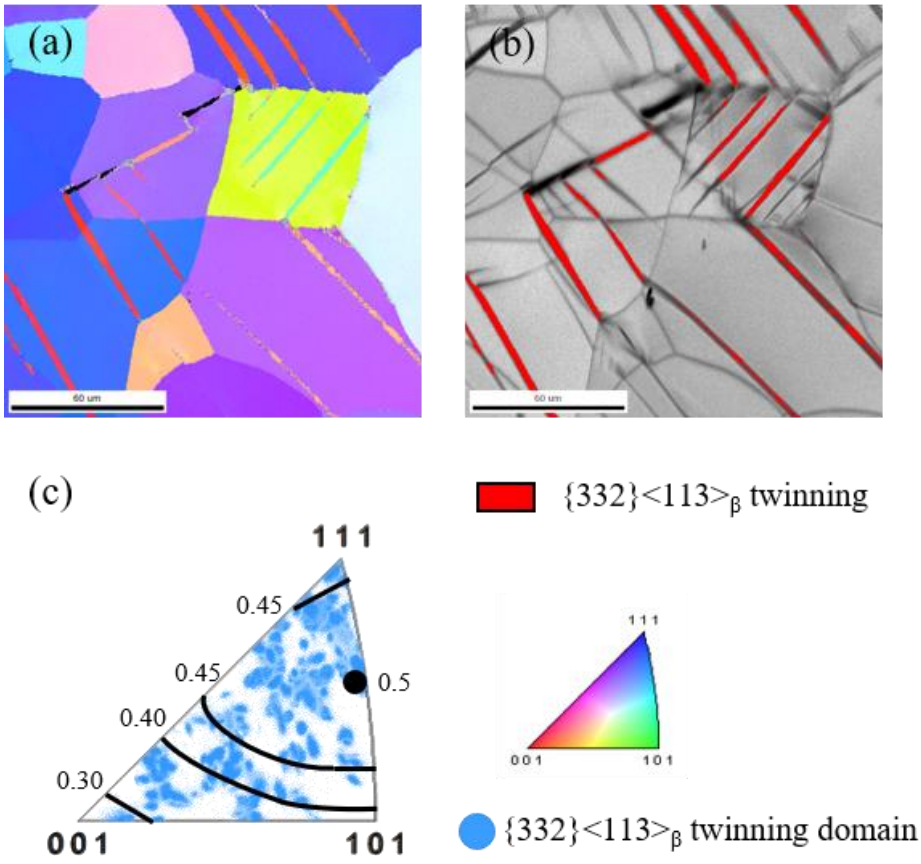

Figure 5.8 Experimental of the EBSD statistic of the primary deformation product in ω_{iso} hardened 150s samples by in-situ EBSD under tensile strain (ε = 0.02): (a) cases inverse pole figure maps, (b) phase+ IQ maps

of ω_{iso} hardened 150s, alloys, (c) experimental Inverse pole figure of the statistic of the primary deformation products in ω_{iso} hardened 150s as well as the distribution of the highest Schmid factor of 332T.

To further study the effect of ω_{iso} on the deformation mechanism of Ti-12Mo alloys, more than 1000 grains of various orientations in 150s ω_{iso} hardened samples were analyzed using in-situ EBSD study under traction. It is observed that the SIM α″ is completely inhibited, and only 332T can be observed as primary deformation mode as shown in Figures 5.8a and b. The grains with twinning activated at ε = 0,02 are plotted in inverse pole figure in figure 5.8c. The Schmid factor threshold for 332T is about 0.3 in the 150s ω_{iso} hardened sample, which allows massive twinning activation in most grains to accommodate the tensile strain. However, drastic differences in strain-hardening rates were seen between the 150s and 60s ωiso hardened samples (Fig. 5.1). The 150s one exhibits highly localized plastic deformation, not brittleness but important necking since yielding, leading to limited uniform elongation. In order to clarify such particular deformation behavior in the 150s sample, carefully TEM observations of the deformed ω_{iso} hardened 60s and 150s samples are performed.

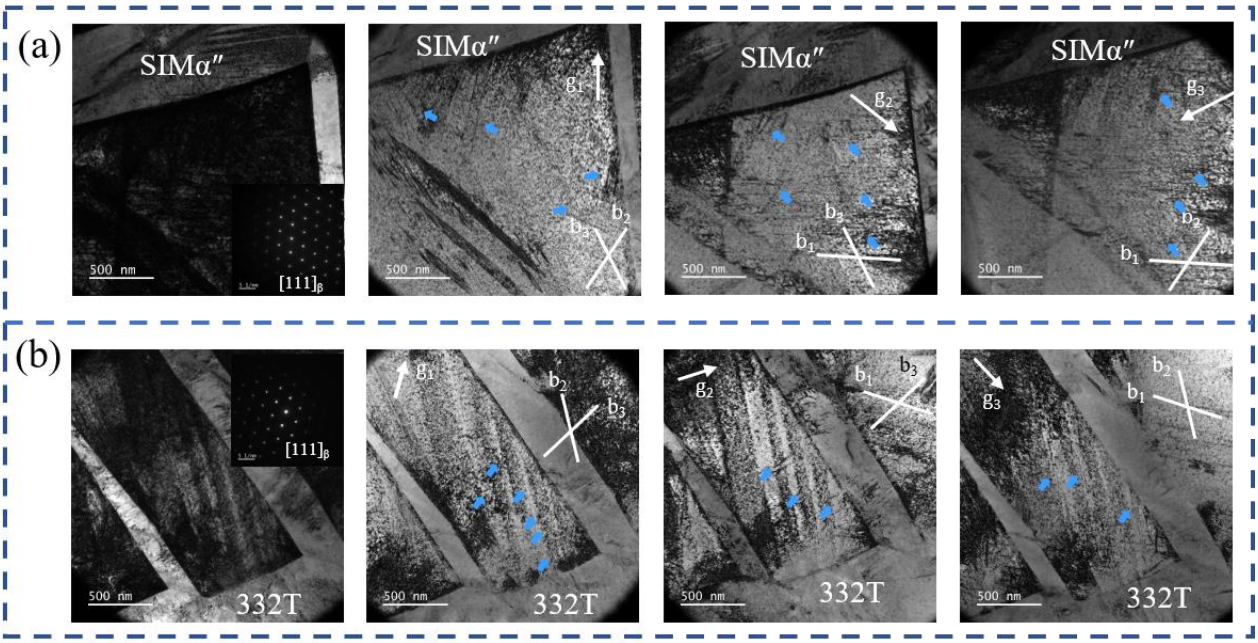

Figure 5.9 Ex-situ TEM micrographs of ω_{iso} hardened 60s alloy at ε = 0.02: (a) bright field images of an array of dislocations piled up to the SIM α″ and bright field images of the three *g* conditions around [111] $_{\beta}$ zone axis; (b) bright field images of an array of dislocations piled up to the 332T and bright field images of the three *g* conditions around [111] $_{\beta}$ zone axis.

As shown in figure 5.9, the β matrix zones isolated by 332T bands and SIM α″ bands are examined to reveal the dislocation activities after deformation. Individual dislocations and dislocation pile-ups near the boundaries of SIM α″ and 332T are observed in ω_{iso} hardened 60s alloy (marked by blue arrows in Fig. 5.9). The Burgers vectors of the dislocation lines is analyzed by using the three $g.b = 0$ extinction conditions around $[111]_\beta$ zone axis (Fig. 5.9b-d). It can be seen a set of dislocation lines is composed by a group of screw dislocations attributed to three Burgers vectors $b = a/2<111>$ (labeled by b_1, b_2, and b_3 in Fig. 5.9). The dislocations are in limited contrasts due to the particle-like ω contrast in the background under every g condition. Some ω-free channels can be seen in Fig.5.9b, probably due to the dislocation glide; the same phenomenon has been reported by Lai et al. [89].

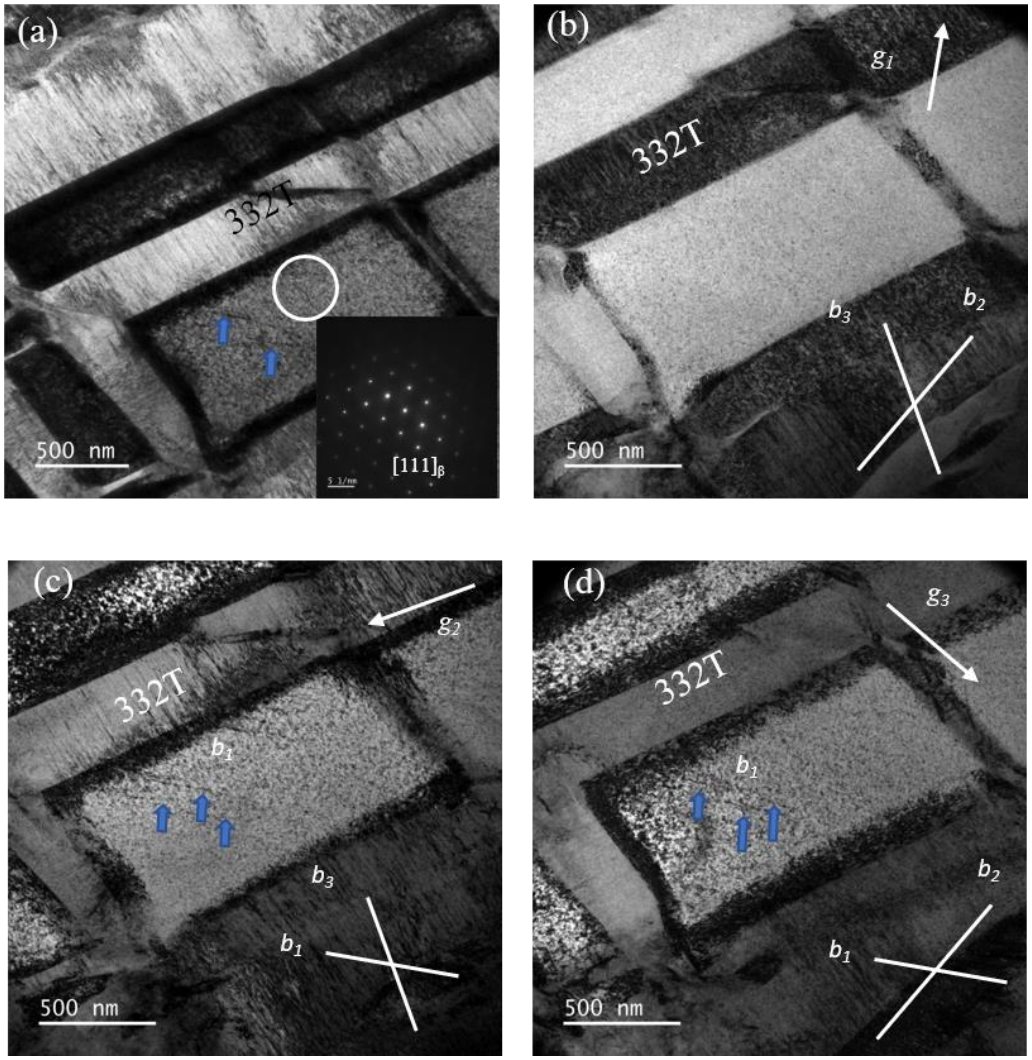

Figure 5.10 Ex-situ TEM micrographs of ω_{iso} hardened 150s alloy at ε = 0.02: (a) bright-field images and diffraction patterns of dislocations around the boundary of 332T; (b-d) bright-field images of the three *g* conditions around [111] $_{\beta}$ zone axis of the matrix.

Same TEM observations are performed in 150s ω_{iso} hardened alloy after deformation (figure 5.10 a-d). As shown in figure 10 a, the β matrix is divided into segments by the twin network. The sizes of the isolated β segments are similar to those in 60s hardened alloy (Fig. 5.9). A few individual dislocations (marked by blue arrows in Fig. 5.10c and d) could be observed in the isolated β with burgers vector along with b_1 under g_2 and g_3 conditions. It can be noticed that, when comparing to the 60s sample, the density of the dislocations is sharply less important in the 150s sample, and only b_1 dislocations are observed. Besides, strong contrasts along the twin boundaries (Fig. 10a, c and d) are observed in every *g* condition except $g1$ (Fig. 10b). Geometrically necessary dislocations and elastic lattice distortion can be the two possible reasons resulting in such a phenomenon. They operate as accommodation mechanisms to the strain-stress misfit between twin and matrix. However, the low dislocation density and the absence of ω-free channel could indicate that the dislocation glide is strongly suppressed in the 150s hardened alloy.

5.4. Discussions

5.4.1 The early-stage transformations of ω_{ath} and ω_{iso} in TRIP/TWIP Ti alloy

The reversible NTD effect could be observed during the in-situ electrical resistivity measurement of fine-grain Ti-12Mo alloy, which is related to the dissolution of ω_{ath} phase via displacive atom shuffle to β phase. The negative resistivity change is no longer fully reversible since 125°C as shown in figure 5.3, could probably result from the diffusive ω_{iso} nucleation. With the increase of the applied temperature and the heating time of the resistivity measurement, the differences increase progressively between the initial resistivity of fine-grain Ti-12Mo and the resistivity after each heating-cooling cycle (fig. 5.3b and c), until it completely disappears. The NTD effect completely disappears after 1200s aging at 200°C, probably due to that all original ω_{ath} sites (the quenched-in Mo-lean nanodomains), which has been observed in Ti-Mo based metastable β Ti alloys [90], have been occupied by ω_{iso}. The NTD effect has been long observed and interpreted by several assumptions. The dissolution of the ωath phase into β matrix is well accepted [91-96], but has not been observed in microscopic studies. Despite the differences on different assumptions, the proposed mechanisms agree that the NTD should relate to the relaxation

of the elastic strain field around the ω_{ath} particle, which could be realized by ω_{ath} dissolution [93] or by thermoelastic relaxation between two phases. About the increasing of the resistivity following the NTD stage at a higher temperature, agreement with proofs [91, 93, 96] is drawn on the diffusion-controlled ω_{iso} precipitation by isothermal thermodynamic studies.

During heating at 200℃, there is a monotonic increase of electrical resistivity as the increasing heating time until converge but still lower than the resistivity at room temperature. The transformation rate of ω_{ath} phase to ω_{iso} phase could be estimated by the difference of the real-time resistivity and the converge value of resistivity. In this case, about 40% ω_{ath} phase transformed to ω_{iso} phase at t = 60s; about 55% ω_{ath} phase transformed to ω_{iso} phase at t = 150s; and ω_{ath} phase almost completely transformed to ω_{iso} phase at t = 900~1200s. The nucleation of ω_{iso} precipitates in the first 600s exhibits typical kinetic (Avrami exponent n = 2/3) for precipitation from pre-existing sites. At the later stage (t > 3000s), n increased to 0.92, which is also similar to the growth kinetic (n near 1) reported in diffusion-controlled precipitation from dislocations [85]. Therefore, according to the resistivity results, most ω_{iso} will precipitate in the first stage (t < 600s), which exhibits typical kinetic for precipitation from pre-existing sites. According to De Fontaine et al. [97] proposed, the ω phase transformation can be viewed as a result of two-dimensional ordering of one-dimensional linear displacive defects along $[111]_{\beta}$ closed packed direction in the β phase alloys. Kuan et al. [98] also proposed a similar linear defect model. ω_{ath} was observed as linear structural in BCC Ti-Mo based alloys [99-101]. The electrical resistivity seems to suggest that the precipitation of ω_{iso} might be related to the ω_{ath} phase. However, this hypothesis needs to be confirmed by more experimental evidence.

5.4.2 Effect of ω_{iso} precipitation on the deformation mechanism

According to Schmid's Law, the resolved shear stress applied on the habit plane is equal to the stress applied to the material multiplied by its SF. And the SF threshold of each transformation is obtained by statistical EBSD mapping during the in-situ tensile test at yielding as shown in figure 5.5, figure 5.6, and figure 5.8. Thus, it should be reasonable to estimate the CRSS values via yield stress multiplying the SF threshold of each transformation. Figure 5.11 shows the estimated CRSS values of SIM α″ and 332T in the Ti-12Mo at various states. Compared to the Ti-12Mo coarse grain, both the values of $CRSS_{SIM\ \alpha''}$ and $CRSS_{332T}$ values of Ti-12Mo fine-grain increased, and a lower value of CRSS radio of SIM α″ and 332T (= 0.75) in Ti-12Mo fine-grain

than that value (= 0.875) in Ti-12Mo coarse grain was gotten. It suggested that the decreasing grain size of Ti-12Mo leads to the phenomenon that the SIM α″ could be activated in more orientations of grains in Ti-12Mo fine grain. It seems to suggest a smaller grain size caused suppression of both TRIP and TWIP effect in Ti-12Mo. Other reports have reported similar phenomena. In the coarse-grain size range, deformation twinning becomes more difficult with the increasing grain size for fcc, bcc, and hcp metals [102, 103]. And a "stimulated slip" model was developed to explain the strong size dependence of deformation twinning [103]. Wang et al. [68] also observed the 332T becomes more difficult as the average grain size decreases Ti-20V-2Nb-2Zr alloy. Cai et al [40]. suggested that the triggering stress of SIM α″ decrease with the increasing β grain size and then increased again in Ti-16V-3.5Al-3Sn (wt. %), which has been explained in terms of two factor of martensitic transformation, i.e. the internal frictional resistance and internal elastic energy, related to grain size.

After ω_{iso} hardening treatment for 60s, both the CRSS of SIM α″ and 332T increased (fig. 5.11), exhibiting suppression in both TWIP and TRIP effect compared to Ti-12Mo fine-grain alloy. The CRSS ratio of SIM α″ and 332T increased from 0.75 in Ti-12Mo fine-grain alloy to 1.09 in ω_{iso} hardened 60s alloy. The CRSS of 332T increases slightly, and the SIM α″ is completely inhibited after ω_{iso} hardening treatment for 150s (figure 5.8). For the dislocation slip, even though its CRSS is difficult to be evaluated by statistical methods by in-situ investigations, we can observe that the slip is strongly suppressed in ω_{iso} hardening 150s alloys (figure 5.10). All of the three mechanisms, SIM, 332T, and dislocations, can be observed suppressed in ω_{iso} hardening treatment. These results hint that the tree mechanism's suppressed effect should be attributed to the precipitations of ω_{iso} phase.

Kim et al. [104] suggested that the SIM α″ transformation from β matrix is mediated by the shuffling of $\{110\}_\beta$ planes along with <110> directions. Lai et al. [16] implied that ω phase is a solid obstacle to the collective $\{110\}\langle 110\rangle_\beta$ atomic movements involved in the martensitic transformation. They also implied that the degree of the obstacle effect in ω phase is related to the shear modulus on the $\{1120\}_\omega$, which is parallel to $\{110\}_\beta$ according to the orientation relationship between ω and β. Lai et al. [16] suggest that the shear modulus on the $\{1120\}_\omega$ of ω_{iso} is higher than that of ω_{ath}, which means that ω_{iso} precipitations have a more substantial obstacle to the martensitic transformation comparing to ω_{ath}. Therefore, the ω_{iso} precipitations during ω_{iso} hardening treatment process result in a stronger hindrance to the martensitic transformation

resulting in a higher CRSS $_{SIM\ \alpha''}$ in Ti-12Mo ω_{iso} hardening 60s and 150s alloys. A transformation $\omega \rightarrow \beta$ matrix could be activated during the twinning process, and the stress inside the 332T could induce the new ω phase. A similar mechanism has been proposed by Xiao et al.[88]. A similar mechanism has also been reported in alloys with hcp structure. It is thought to arise either due to boundary pinning by another deformation twinning [105] or by dislocation content [106] at the twin boundary. $\omega_{iso} \rightarrow \beta$ transformation is activated more difficult than $\omega_{ath} \rightarrow \beta$ transformation resulting in a higher CRSS 332T in ω_{iso} hardened 60s than that in Ti-12Mo fine grain (figure 5.11). Interestingly, with the increasing density of ω_{iso} precipitates, the CRSS of 332T remained stable, which might be related to reducing dislocation content (figure 5.10).

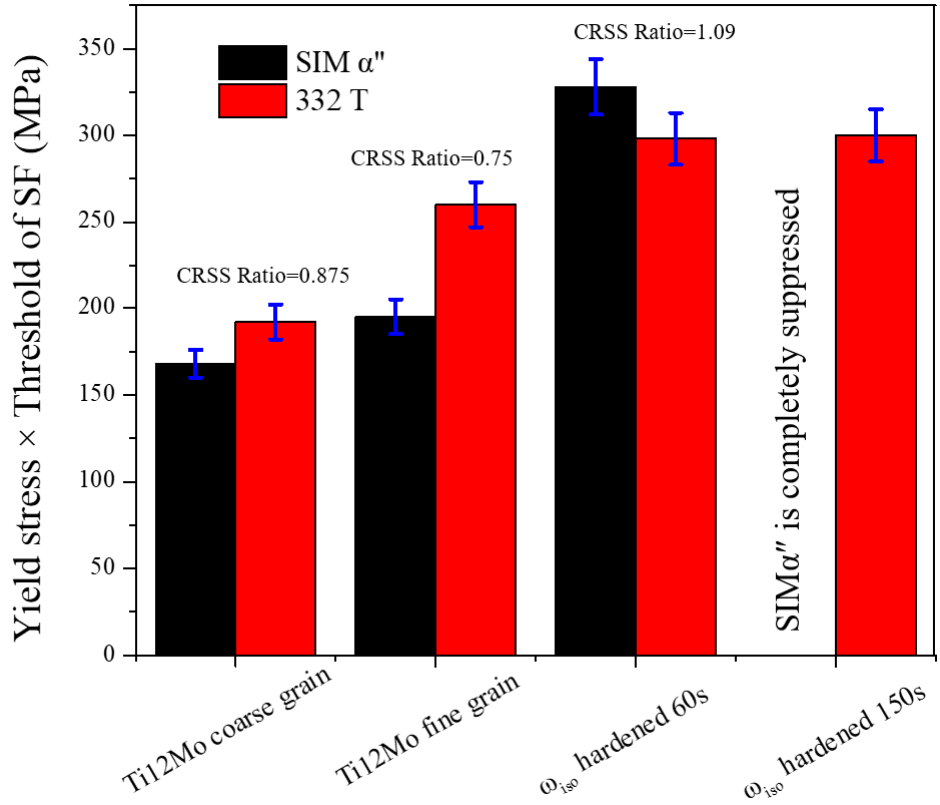

Figure 5.11 Apparent CRSS of SIM α″ and 332T in Ti-12Mo alloys at various states. (Apparent CRSS = YS × SF threshold)

The strengthening effect of the yield strength and the drop of plasticity contributed by the ω precipitations: The strengthening effect is due to the increasing CRSS of both SIM α″, 332T, and dislocations with the nucleation and growth of ω_{iso}; the drop of uniform elongation is due to the

suppression of SIM α″ and dislocations leading to a decrease of strain-hardening rate; with the ω_{iso} further growth, the alloys process brittleness due to the suppression of TRIP/TWIP and dislocations. 200°C/60s can deliver the best balance between yield strength and ductility by pushing the apparent CRSSs to the limit, at which the strain-hardening rate drops to the level slightly over consider line. The drop of the hardening rate could probably be due to the suppression of dislocation glide by ω_{iso} precipitates, because the hardening mechanisms, SIM α″, and 332T, are both still operative. By further suppressing dislocation glide as seen in the ω_{iso} hardened 150s sample, the twinning operates alone to induce plasticity, i.e. the pure TWIP effect. However, without dislocation glide, the dynamic Hall-Petch effect cannot be effective under such circumstances where the dislocation mean free path is reduced without mobile dislocations. The ω_{iso} hardening mechanism offers an appropriate strengthening strategy for TRIP/TWIP Ti to achieve significant tensile strength enhancement (+81% of YS in case of Ti-12Mo) without ductility trade-off. Meantime, the particular mechanical behavior in the hardened materials shows the origin of strain-hardening in TWIP Ti and the non-conventional origin of 332T.

5.5. Summary

Different states of metastable β TRIP/TWIP Ti-12Mo: Ti-12Mo coarse grain, Ti-12Mo fine grain, ω_{iso} hardened 60s, and ω_{iso} hardened 150s, were generated by different heat treatments. Tensile texts investigated the corresponding mechanical behavior in the four states. The effect of ω_{iso} hardening treatment (holding at 200°C for a short time) on the microstructures before and after tensile deformation was studied by in-situ tensile EBSD, SXRD, in-situ tensile and heating TEM, and in-situ electrical resistive measurement. Based on these investigations, the following main results are obtained.

1. The yield strength of Ti-12Mo could be further strengthened after the ω_{iso} hardening treatment. After being hardened at 200°C for the 60s, the alloy retains substantial ductility, and with the increasing the omega ω_{iso} hardening duration, the uniform elongation dramatically decreases to 3.3% after 150s of ω_{iso} hardening and completely inhibited after a 300s ω_{iso} hardening.

2. All of the three mechanisms, SIM α″, 332T and dislocations, are being suppressed in ω_{iso} hardening treatment. Among these, the SIM is completely inhibited, slip is strongly suppressed in ω_{iso} hardening 150s.

This chapter confirmed that the TRIP and TWIP effects in Ti-12Mo alloy could be tuning by

ω_{iso} hardening treatment. After ω_{iso} hardening treatment for 60s at 200°C, Ti-12Mo alloy could improve yield stress, which is higher than L605 alloy and retains substantial ductility. Optimization of the alloy composition in another strategy to improve the mechanical properties. The Zr element is a neutral element (in the Ti-Zr system) or weak β-stabilizing element (in the Ti-Nb-Zr system) [74, 75]. Adding Zr could be two-fold advantageous since a wide composition range (up to tens of weight percent) can be added into the Ti-12Mo alloy: (1) to achieve better tolerance of alloys composition for TRIP/TWIP fine-tuning; (2) to obtain the solution strengthening effect. Chapter 5 aims to study the effect of Zr addition on the mechanical properties and the TRIP to TWIP transition in Ti-12Mo alloy.

Chapter 6 Investigations of Zr additions in Ti-12Mo alloy

Introduction

In order to study the effect of Zr addition on the TRIP to TWIP transition in Ti-Mo system, a comparative investigation is performed between the TRIP/TWIP Ti-12Mo-xZr (x = 3, 6, 10, wt. %) alloys. This work focuses on *in-situ* investigations of the deformation mechanisms in β phase with different stability levels. The investigation is performed at various length scales using the Ti-12Mo-xZr system. The deformation sequence, orientation relationships, and the volume fraction of SIM α″ at different strain levels are traced by *in-situ* EBSD analysis during tensile loading and after unloading. The *in-situ* observations reveal the details of the formation, development, and transformation of the complex martensite/twin structure. Based on the results, the deformation mechanisms involved in the macroscopic mechanical behavior are discussed by considering the heterogeneous nature of the microstructural evolution.

6.1 Effect of Zr on the Tensile properties of Ti-12Mo-xZr alloys

Figure 6.1 shows the true strain - true stress curves of the present alloys at ST state. The stress level of the plastic flow curves increases with the Zr content, highlighting the notable solid solution strengthening contribution of Zr element in the Ti-12Mo-Zr system. In particular, the yield stress of Ti-12Mo-10Zr alloy approaches 740 MPa, which is notably high for a strain-transformable Ti alloy. Likewise, the uniform elongation of all three alloys is higher than ε = 0.24, displaying good ductility. It is worth noting that the plateau-like stress flow can be observed at the very beginning of plastic deformation in Ti-12Mo-3Zr alloy (marked in the figure. 6.1). Sun et al. [23] suggested previously that the appearance of the plateau is related to the strain-induced martensitic transformation. Aiming at clarifying the evolution of strain-hardening behavior, the corresponding strain-hardening rate (dσ/dε) curves of the three alloys are shown in the inset of figure 6.1. The three alloys exhibit different types of the evolution of the strain-hardening rate. The strain-hardening rate curves are non-monotonic, similar to those observed in TRIP/TWIP β Ti-alloys [33, 72, 77, 107-110]. It can be observed that Ti-12Mo-6Zr displays a noticeable difference concerning the other two alloys, regarding the presence of a stable strain-hardening rate at about 1750MPa in the range of ε = 0.05-0.13. The underlying mechanisms are investigated in detail by *in-situ* EBSD and TEM techniques.

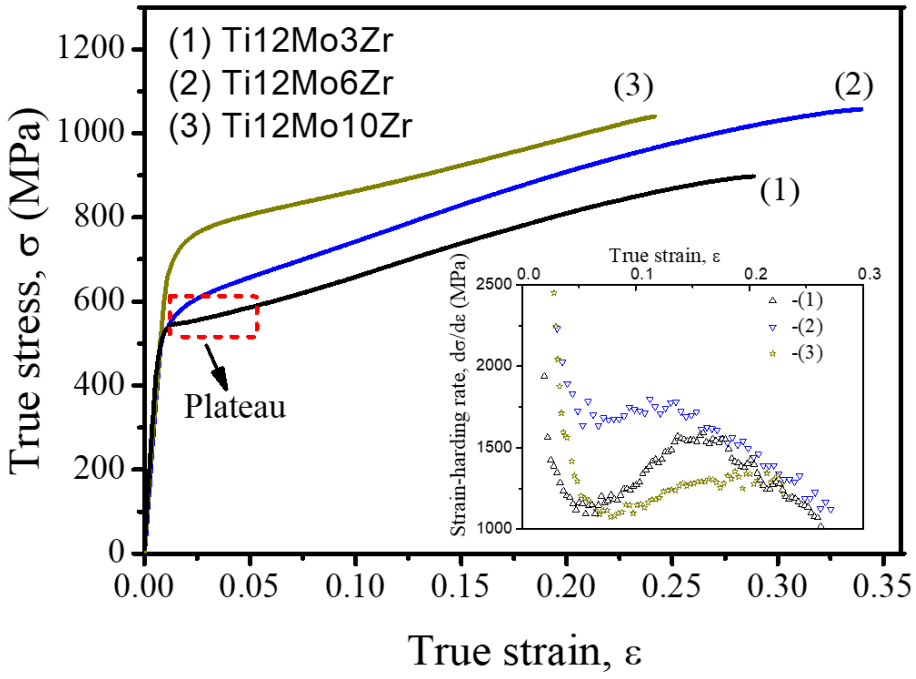

Figure 6.1. The true strain-stress curves of the ST Ti-12Mo-xZr (x = 3, 6, 10) samples, and the corresponding strain-hardening rate curves as function of true strain also shown in inset.

6.2 Effect of Zr on deformation induced transformation evolutions of Ti-12Mo-xZr alloys

6.2.1 Characterization of solution treated (ST) states

Figure 6.2 shows the XRD profiles, optical micrographs, and selected area electron diffraction (SAED) patterns of the ST samples of Ti-12Mo-3Zr, Ti-12Mo-6Zr, and Ti-12Mo-10Zr alloys, respectively. As shown in figure 6.2a, the presence of the β phase is confirmed in the three alloys without other additional diffraction peaks. It can be noticed that the peak position of the β phase (2θ: degree) slightly shifts towards lower angles with the increasing of Zr content, suggesting a small expansion of the β phase lattice parameter consistent with the bigger size of Zr atoms. Figure 6.2b displays that ST samples' microstructure consists of typical recrystallized β grains (with a grain size in the range 50-80 μm). Moreover, besides the β phase, the nanometer ω_{ath} phase present in the quenched β matrix is detected by TEM technique, as displayed in figure 6.2c. It can be observed that the reflections of ω_{ath} phase become weaker and more diffuse with the increased Zr content when normalized to the β matrix reflection intensities, suggesting that the ω_{ath} precipitation could probably be lower in volume fraction. Pang et al. [111] have observed that Zr addition in Ti-

24Nb-(0~8)Zr (at. %) alloys could suppress the formation of ω phase. In contrast to the results of Pang et al, the reflections of ω_{ath} phase is still visible in Ti-12Mo10Zr.

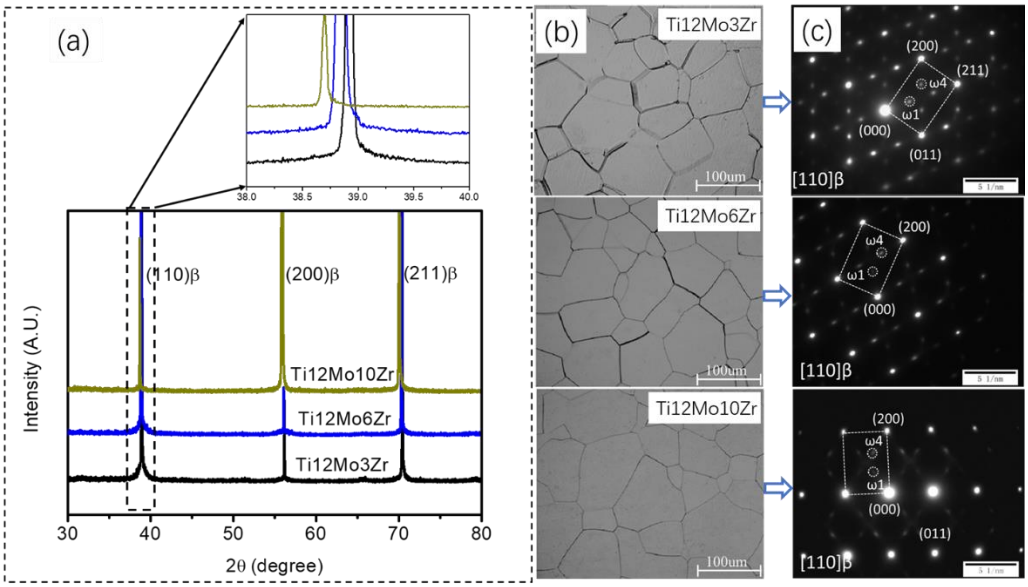

Figure 6.2. The characterizations of the Ti-12Mo-xZr (x = 3, 6, 10) alloys at ST state. (a) XRD profiles; (b) Optical images; (c) SAED patterns along the [110]$_\beta$ zone axis. The peak position of (110)$_\beta$ of the three alloys is magnified in the inset of (a). Two of the four ω-variants, labeled ω_1 and ω_4, are also discriminated on the basis of the reflections in (c).

6.2.2 Deformed microstructure characterization

The phase transformation between β and SIM α″ is known to be reversible during loading and unloading in the metastable β Ti alloys. Partial reversion is usually observed in the TRIP/TWIP Ti alloys after unloading from the tensile stress, with a residual volume of SIM α″ trapped by interfacial dislocations in the unloaded state. Figure 6.3 shows the XRD profile of Ti-12Mo-xZr (x = 3, 6, 10) fractured samples after tensile tests. The residual SIM α″ phase can be detected in the Ti-12Mo-3Zr and Ti-12Mo-6Zr alloys. The appearance of residual α″ is related to the occurrence of SIM in the plastic deformation stage in Ti-12Mo-3Zr and Ti-12Mo-6Zr alloys, partially preserved in the alloys after unloading. Such similar phenomenon is also observed in TRIP/TWIP Ti-12Mo alloy [33, 112] and Ti-9Mo-6W alloy [72]. In contrast, only β phase is detected in Ti-12Mo-10Zr alloy without SIM α″ phase, suggesting either SIM did not occur or has completely reversed to β phase during unloading [113].

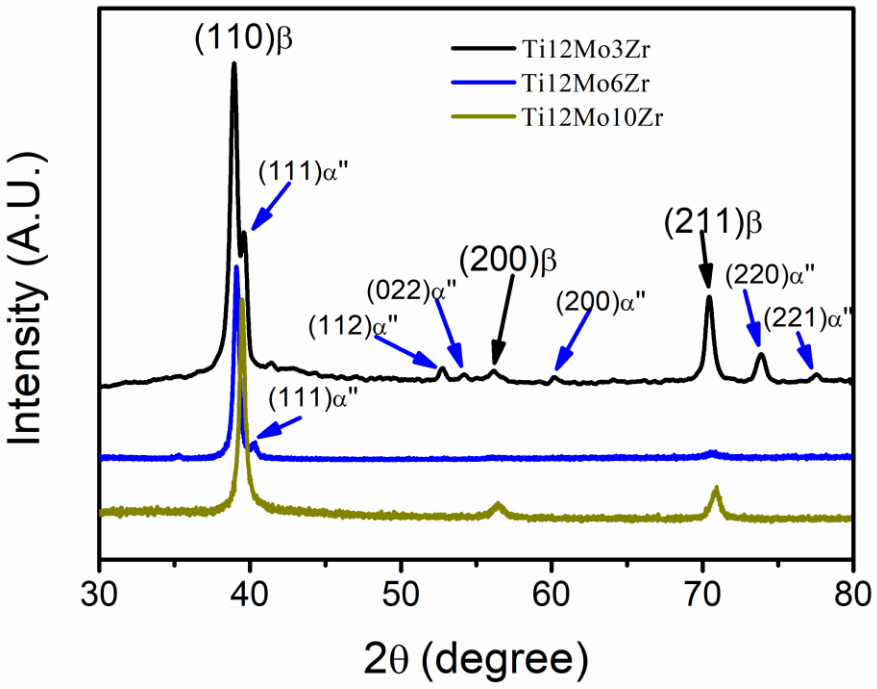

Figure 6.3. The XRD profiles of the ST sample of Ti-12Mo-xZr (x = 3, 6, 10) alloys after deformation until fracture.

6.2.3 *In-situ* EBSD analysis of activation and the evolution of microstructure of the Ti-12Mo-xZr (x = 3, 6, 10) alloys

In order to clarify the activation and the evolution of the TRIP/TWIP microstructure of the present alloys, *in-situ* EBSD mapping under tension is performed in the early deformation stage. Figure 6.4 shows the EBSD analysis of Ti-12Mo-3Zr sample taken from the same region at different strain. The inverse pole figure (IPF) map at ε = 0.02 in figure 6.4a shows that plate-like deformation bands with different orientations (coded by color contrast) appear in the β grain, upon loading. The green plate-like deformation bands are identified to be SIM α″, as indicated in the corresponding α″ phase maps (Figure 6.4b). For further clarifications, as shown in figure 6.4c, the orientation relationship between green SIM α″ deformation bands and β matrix has been analyzed and found to be in agreement with the classic crystallographic orientation relationship $\{211\}_{\beta}$ //$\{110\}_{\alpha''}$ [86], suggesting that SIM α″ could likely originate directly from the β matrix. It can be seen from figure 6.4b that the quantity and thickness of SIM α″ bands (inside Grain A) increase upon loading from ε = 0.02 to 0.04. After unloading from ε = 0.04, most of the SIM α″ bands are

preserved in β matrix. Similar to the observations reported in superelastic Ti-27at. %Nb [114] and TRIP/TWIP Ti-V-Cr-Al [109], internal twinning of SIM α″ as it is observed that the color contrast of some α″ bands become blue upon loading (ε = 0.04 loading) and then transformed back to green during unload (ε = 0.04 unloading). The α″ twinning mode is identified as {130} <310>$_{α″}$ martensite twinning by crystallographic stereo projection analysis in figure 6.4c.

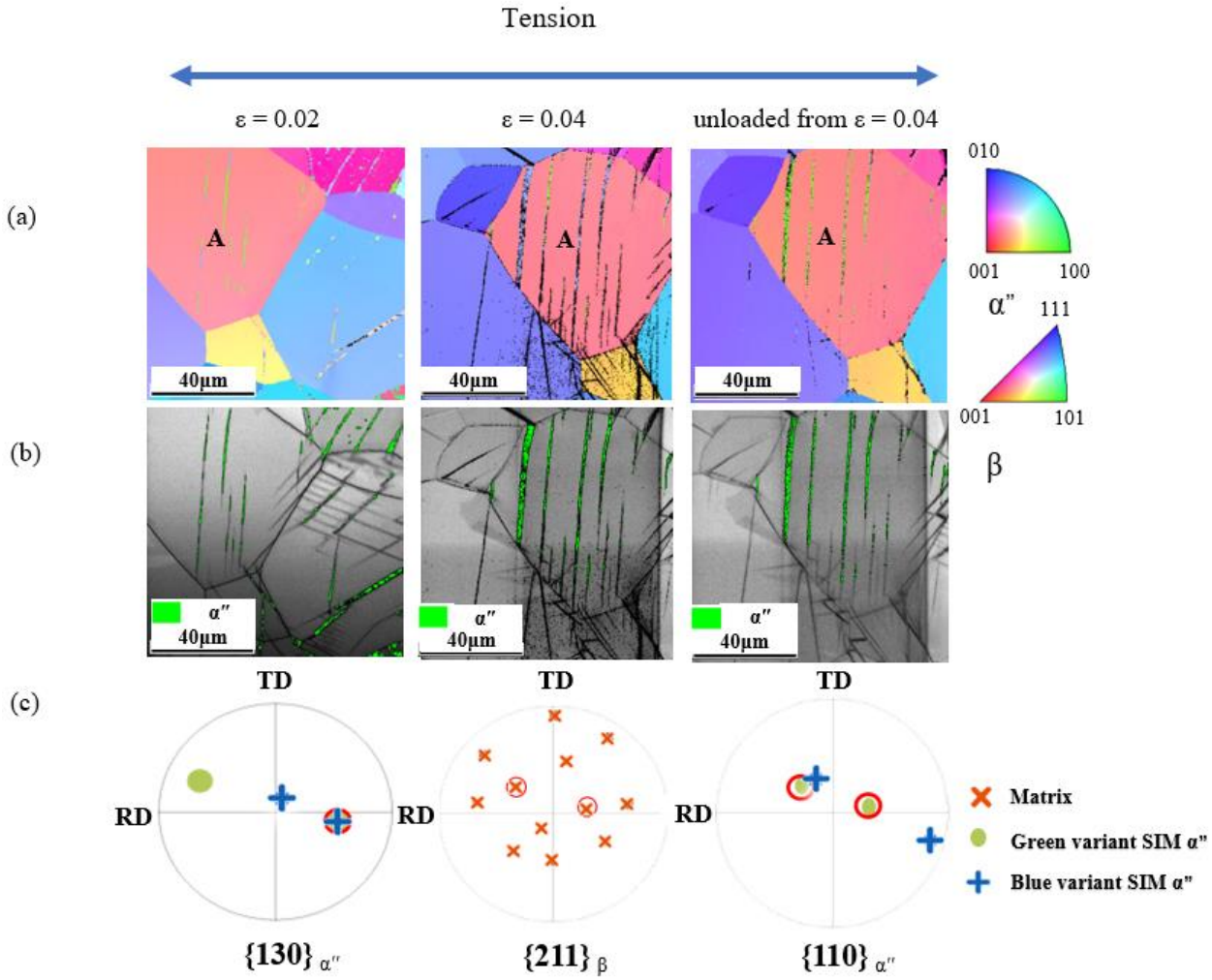

Figure 6.4 EBSD analysis of the Ti-12Mo-3Zr deformed sample taken from the same region at strain ε = 0.02 (loading), 0.04 (loading), and 0.04 (unloading), respectively. (a) IPF maps; (b) orientation maps for SIM α″ phase; (c) pole figures of β matrix and SIM α″. (RD – rolling direction, TD – transverse direction).

Figure 6.5 shows *in-situ* EBSD mapping of Ti-12Mo-6Zr sample. Both 332T and SIM α″ can be observed in the deforming sample. The IPF maps in figure 6.5a show that plate-like deformation bands with two different color contrasts (purple and blue) appear in the β matrix. It can be seen

from figure 6.5c that the first deformation band appears at loading to ε = 0.02. A quick multiplication of the bands happens when increasing the tensile strain to ε = 0.04. Most of the bands can be indexed as β phase respecting strictly the 332T relationship with respect to the β matrix, confirmed by the stereo projection analysis (figure 6.5c). Two variants of 332T can be observed in the grain traced by in-situ EBSD, belonging to two different 332 planes of the matrix (the two common poles circled in figure 6.5c). As shown in figure 6.5a, the two variants of 332T keep unchanged in their crystal orientations and thicknesses after unloading (ε = 0.04 unloading), which suggests that the mechanical twinning between the β matrix and 332T is irreversible. In addition, SIM α″ is also formed in the untwinned area of the β matrix, shown in green in the Image Quality (IQ) map in figure 6.5b. The orientation relationship of SIM α″ with β matrix is $\{211\}_{\beta}$ //$\{110\}_{\alpha''}$ according to the analysis of stereographic projection pole in figure 6.5c, indicating that SIM α″ should originate directly from the β matrix. Similar to the observation in unloaded Ti-12Mo-3Zr alloy, the length and thickness of the SIM α″ decrease after unloading from ε = 0.04, meaning that the martensitic transformation β → α″ should be partially reversible.

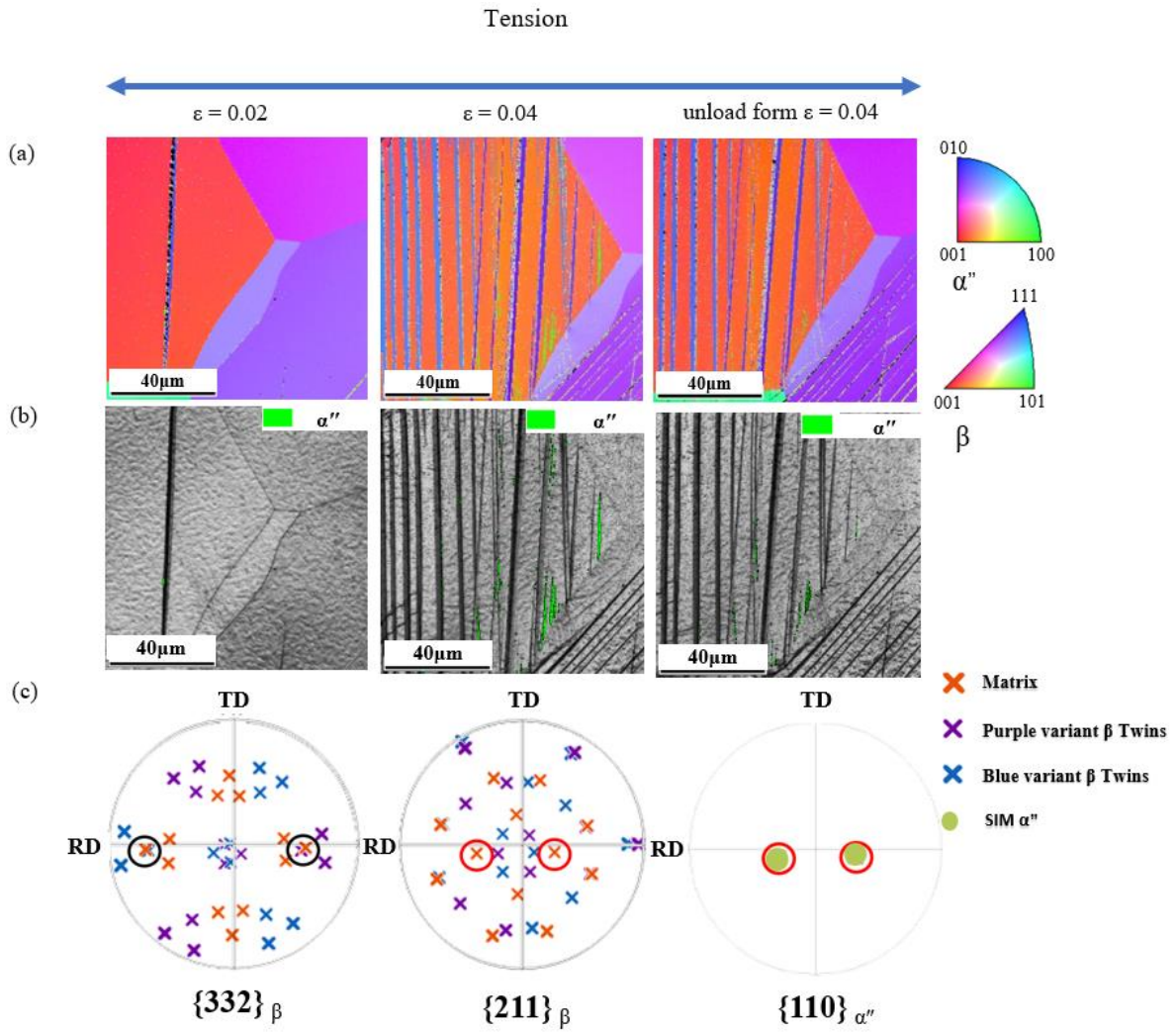

Figure 6.5. EBSD analysis of the Ti-12Mo-6Zr (Type A) deformed sample taken from the same region at strain ε = 0.02 (loading), ε = 0.04 (loading), and 0.04 (unloading), respectively. (a) IPF maps; (b) orientation maps for α″ phase; (c) pole figures of β matrix, {332}<113> twinning and SIM α″. (RD – rolling direction, TD – transverse direction).

Similarly, *in-situ* EBSD observations are also performed in the Ti-12Mo-10Zr sample, as shown in figure 6.6. The multiplication of deformation bands, identified as 332T by stereographic projection (figure 6.6c), can be observed in the β matrix in the IPF map (figure 6.6a) during tensile loading. The SIM α″ is not detected in the in-situ loading and unloading process (figure 6.6b), corroborating to the absence of SIM α″ in the post-mortem XRD characterization (figure 6.3). It suggests that 10wt. % Zr addition in Ti-12Mo suppresses the activation of SIM α″ under tension at room temperature.

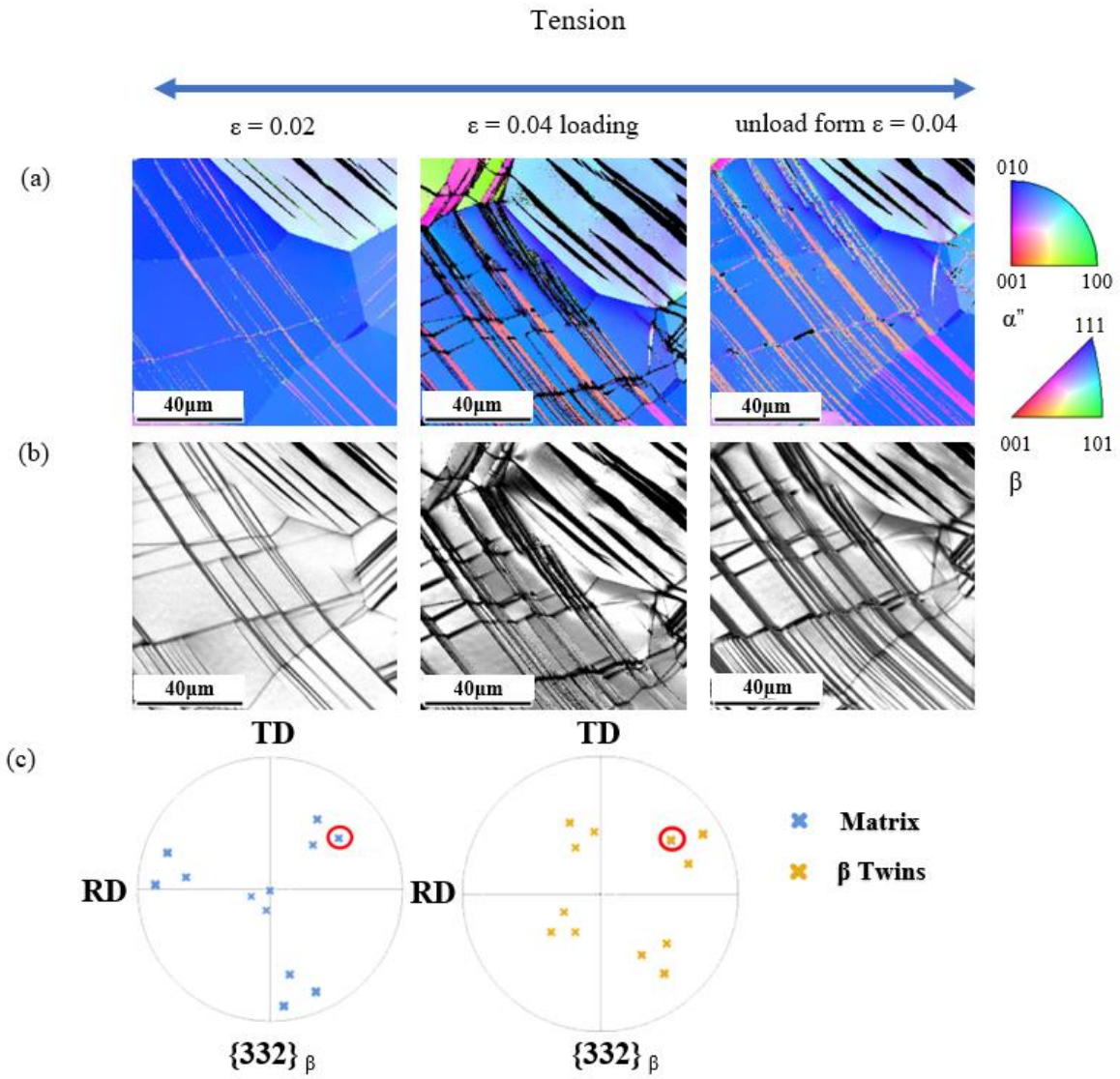

Figure 6.6. EBSD analysis of the Ti-12Mo-10Zr deformed sample taken from the same region at strain ε = 0.02 (loading), 0.04 (loading), and 0.04 (unloading), respectively. (a) IPF maps; (b) orientation maps for α″ phase; (c) pole figures of β matrix, {332}<113> twinning. (RD – rolling direction, TD – transverse direction).

6.2.4 TEM observations of deformed microstructure in the Ti-12Mo-xZr (x = 3, 6, 10) alloys

TEM observations are performed to investigate the deformation microstructures in the samples after ε = 0.05 tensile strain. Figures 6.7a and 6.7b show the morphology of SIM α″ in the deformed Ti-12Mo-3Zr sample by bright-field and dark-field imaging, respectively. It can be seen that a set of SIM α″ plates are formed along different orientations in this sample. The SIM α″ plates are, as well, observed in the Ti-12Mo-6Zr sample. Figure 6.7c and 6.7d shows a set of parallel

SIM α″ plates (width < 100 nm) occur in the β matrix between two 332T bands. This is consistent with the in-situ EBSD observations (figure 6.5), in which the SIM α″ plates form in the β matrix between the 332T bands during tensile loading. Some of the residual SIM α″ are preserved after the external stress is removed due to some local residual stresses. In contrast, no SIM α″ is observed at TEM length scale in Ti-12Mo-10Zr sample, complementary to the EBSD mapping resolution limited at the micrometric scale. The dislocation slip bands are also observed in the BF images of 6Zr and 10Zr, which can be seen as band-like contrasts in the untwinned β matrix (marked in figure 6.7c and figure 6.7e, respectively). The contrast is due to the inclination of the thin slip bands with respect to the imaging zone axis, resulting in parallel bands cut by the TEM foil surfaces. It is noted in figure 6.7e that secondary deformation bands take place inside the primary 332T bands, which is identified by SAED (inset of figure 6.7f) as secondary twinning bands in the mode of {332}<113> (2^{nd} 332T). The trace of the 2^{nd} 332T plane is almost parallel to the slip band contrast of the matrix. It is thought that such coincidence could be related to the accommodation needed to the stress-strain concentration at the primary 332T boundary when assuming that this twin boundary acts as a solid barrier to the intersecting dislocation slip. To prove that, the Ti-12Mo-6Zr and Ti-12Mo-10Zr foils are re-tilted to <111> zone axis to study the dislocation pile-ups in the β matrix near 332T boundary.

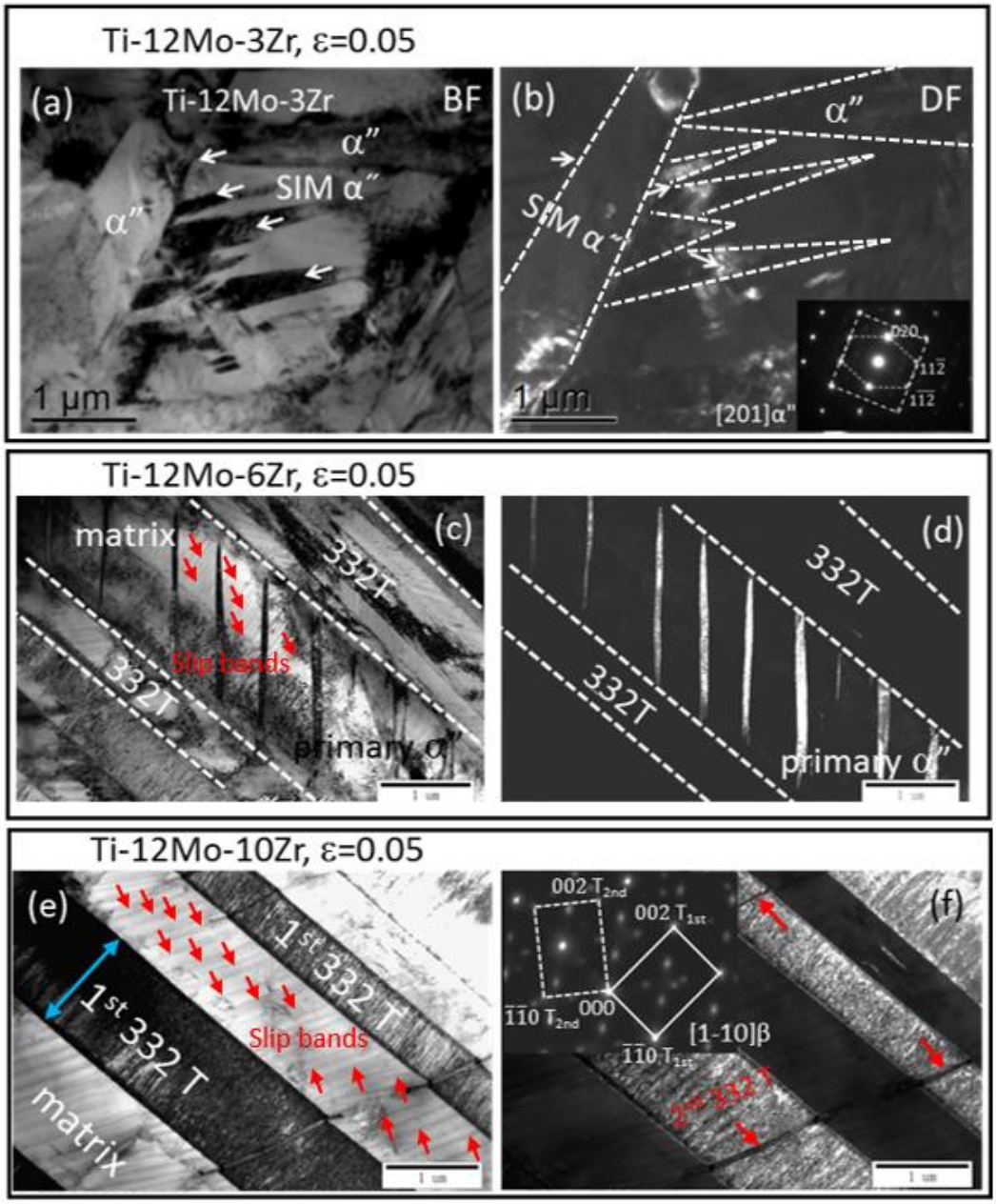

Figure 6.7. TEM micrographs of Ti-Mo-Zr samples after tensile deformation to ε = 0.05: (a) bright-field (BF) image of the Ti-12Mo-3Zr showing SIM α" bands; (b) dark-field (DF) image of one variant of the SIM α" in (a); (c) BF image of the Ti-12Mo-6Zr showing primary 332T bands and the primary SIM α"; (d) DF image of the primary SIM α" in (c); (e) BF image of the Ti-12Mo-10Zr showing primary 332T bands with secondary 332T bands; (f) DF image of (e) with the corresponding SAED pattern along [1-10]$_\beta$ zone axis.

Evidence is presented in figure 6.8, displaying the situation of the dislocation pile-up at a 332T twin boundary in an intersecting slip band. An array of different sets of dislocation lines is observed aligned towards the 332T interface. A gradient of the inter-distance between every two

lines can be seen decreasing when approaching the twin boundary. The dislocation lines' burgers vectors are analyzed using the three $g.b = 0$ extinction conditions around $[111]_\beta$ zone axis (figure 6.8b-d). It can be seen a set of dislocation lines is composed of a group of screw dislocations attributed to three Burgers vectors labeled by b_1, b_2, and b_3 in figure 6.8a. The b_1 dislocations are aligned and piled up well against the 332T interface (figure 6.8c), tangled by the dislocations of the other two burgers vectors, showing complex interactions between piled-up dislocation lines the gliding dislocations on other slip planes. Another observation is also performed at a SIM α" boundary in the Ti-12Mo6Zr foil. it seems that a dislocation transmission from the incoming slip band to the interior of SIM α" occurs at the intersection of the two bands. (figure 6.9).

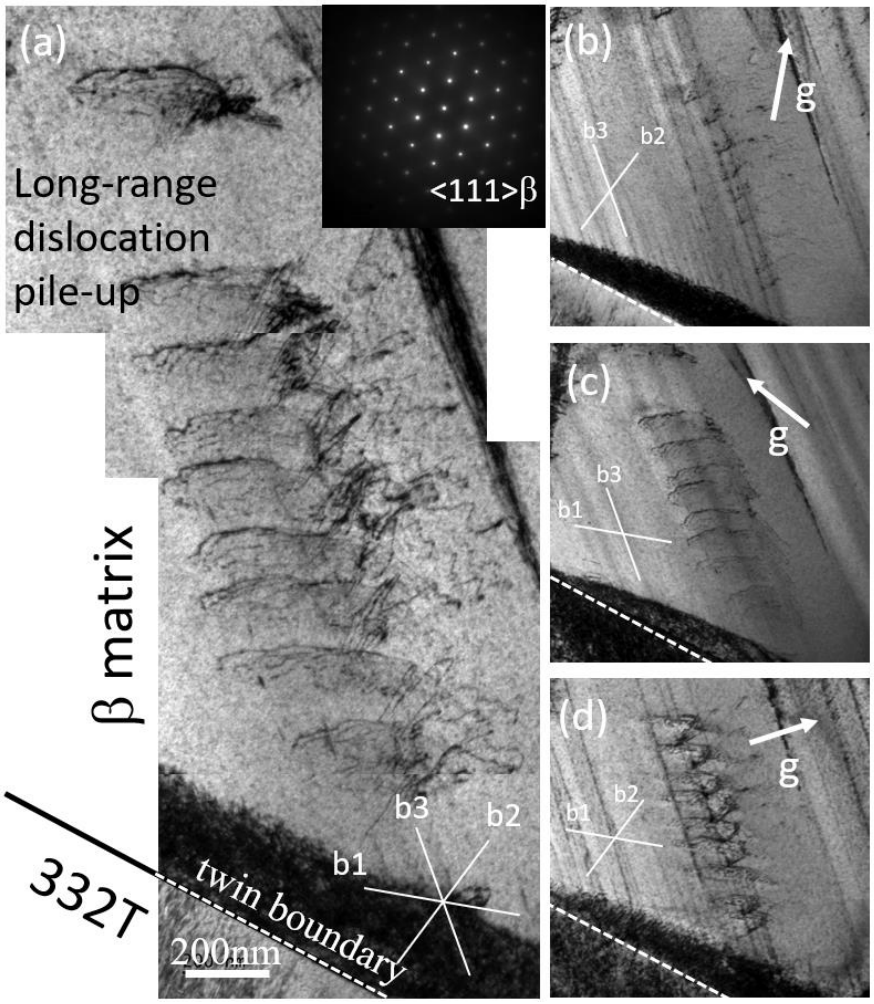

Figure 6.8. TEM micrographs of Ti-12Mo-6Zr at ε = 0.05: (a) BF image of an array of dislocations piled up to the 332T interface; (b-d) BF images of the three g conditions around $[111]_\beta$ zone axis.

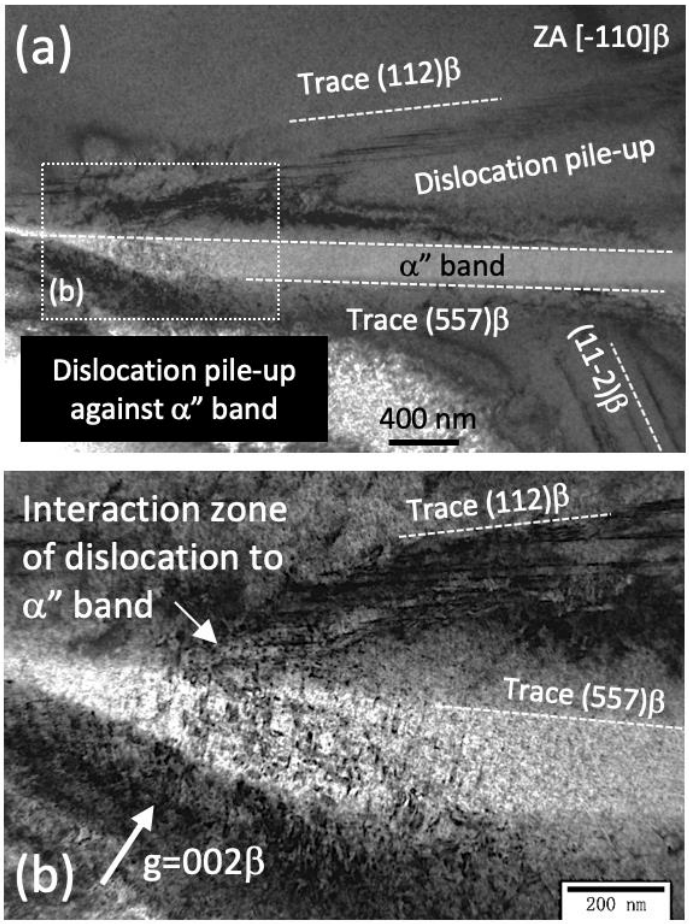

Figure 6.9. TEM micrographs of Ti-12Mo-6Zr sample at ε = 0.05: (a) BF image of a SIM α" band and the dislocation pile-up in the vicinity of the band; (b) zoomed image at the intersection of the SIM α" band and the dislocation array.

6.3 Finite element analysis simulation and prototype stent of Ti-12Mo-10Zr alloy.

Among these Ti-12Mo-xZr (x = 3, 6, 10) alloys, Ti-12Mo-10Zr has the highest yield strength and non-martensitic transformation, which could decrease the recoil of the stent after expansion caused by the reversion of martensitic transformation. Therefore, the Ti12-Mo-10Zr can be applied in the cardiovascular stent compared to other Ti-12Mo-xZr alloys. In order to study the potential of Ti-12Mo-10Zr as a stent material, the specifications of the alloy are carefully analyzed compared to the traditional stent alloy, L605 alloy, and these specifications are listed in table 6.1. They compared to L605 alloy, Ti-12Mo-10Zr alloy process a lower ultimate tensile stress, ductility, work hardening rate, and elastic modulus. These results suggest that as a stent material, the

mechanical properties of Ti-12Mo-10Zr alloys are inferior to L605 alloy. In addition, both the density and the mass attenuation coefficient of Ti-12Mo-10Zr are lower than the L605 alloy, which could limit the X-ray visibility of Ti-12Mo-10Zr alloy. In order to further verify the feasibility of Ti-12Mo-10Zr as a stent material, Ti-12Mo-10Zr alloy was processed into a prototype of a cardiovascular stent. Figure 6.10 shows the photographs of the prototype of the cardiovascular stent made by Ti-12Mo-10Zr. In order to study the fracture resistance of the Ti-12Mo-10Zr prototype stent during expansion, this prototype was inflated to the required expansion by the stent during balloon inflation. It can be seen that the Ti-12Mo-10Zr prototype stent could be inflation without fracture during growth. FEA simulations are conducted by applying Ti-12Mo-10Zr to analyze fracture resistance by quantifying the maximum stress during the balloon inflation of the stent. Figure 6.11a shows that the maximum stress in the stent during balloon inflation. The maximum stress value is 943MPa, which is much higher than the ultimate tensile stress of Ti-12Mo-10Zr (engineering stress 819MPa), which suggests that the fracture could be activated during the inflation. In terms of recoil simulation results of the stent, the properties of Ti-12Mo-10Zr alloy is better than L605 alloy. The central and the distal recoil rate of Ti-12Mo-10Zr is much lower than those values of traditional stent material L605 alloy, as shown in figure 6.11b.

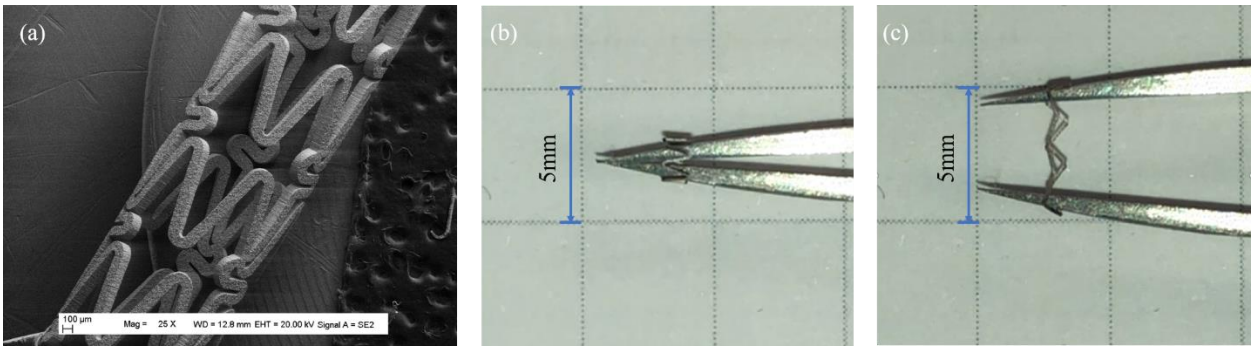

Figure 6.10 The photograph of the prototype of cardiovascular stent made by Ti-12Mo-10Zr: (a-b) before deformation and (b) expansion.

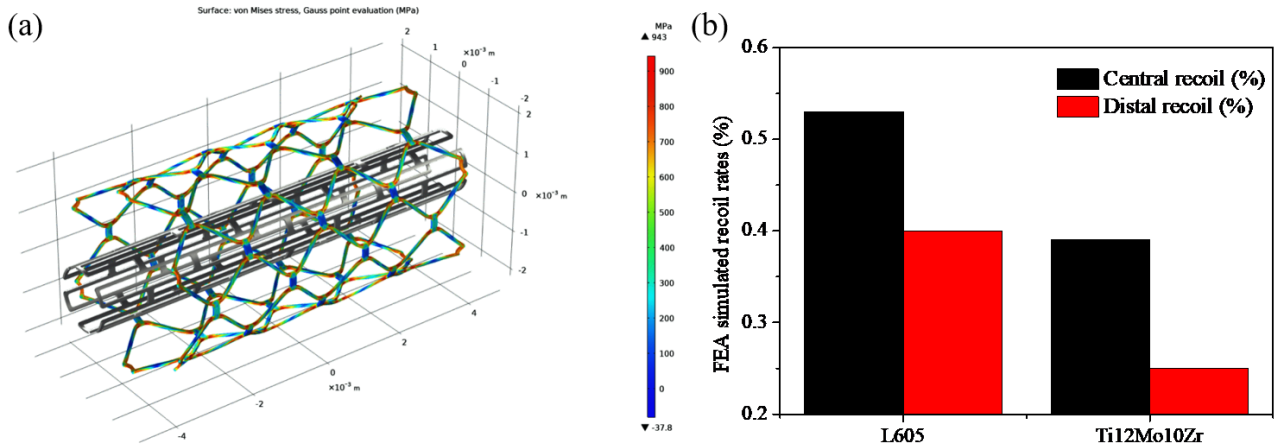

Figure 6.11 FEA simulation on expansion and recoil of Ti-12Mo-10Zr alloy: (a) maximum stress in stent during the balloon inflation. (b) the simulated recoil rates of Ti-12Mo-10Zr alloy and L605 alloy.

Table 6.1 Specifications for Ti-12Mo10Zr (obtained from engineering stress-strain curve) and L605 alloy (advantages of mechanical properties between the two alloys are marked in color blue)

Stent performance	Properties	L605	Ti-12Mo10Zr	Remarks
stent strut < 100mm	High yielding stress (YS)	600 MPa	740 MPa	The YS of Ti-12Mo-10Zr is higher than that of L605 alloy
High fracture resistance during expansion	High ultimate tensile stress (UTS)	1100 MPa	819MPa	The UTS of Ti-12Mo-10Zr is lower than that of L605 alloy
	High ductility	50%	27%	The ductility of Ti-12Mo-10Zr is lower than that of L605 alloy
Low recoil	Reasonable strain hardening rate	2000~2300 MPa	1358MPa	FEA simulations results show that the recoil of Ti-12Mo-10Zr is lower than that of L605 alloy
	High elastic modulus	233 GPa	71GPa	
High X-ray visibility	density	9.1 g/cm^3	5.0 g/cm^3	The X-ray visibility (proportional to $\rho \times Mc$) of Ti-12Mo-10Zr is much worse than that of L605 alloy
	Mass attenuation coefficient	0.99 cm^2/g	0.44 cm^2/g	

6.4 Discussions

Based on the *in-situ* EBSD analysis and TEM observations, figure 6.10 shows a global schematic illustration of the different evolutions of the deformation microstructure as a function

of Zr concentrations. The initial microstructures of the three alloys at ST state are the equiaxed β grains. The deformation modes of SIM and/or DTs could be activated after the yielding of the three alloys. As described in figure 6.10a, the SIM α″ appears just after yielding in Ti-12Mo-3Zr sample, and then {130}<310>$_{\alpha''}$ mode twinning forms inside the SIM α″. However, the 332T is not activated all along the loading and unloading process. The mechanical stability of the metastable β Ti alloy can be reflected by the deformation products since the required fault energy to activate the different deformation modes follows the order: SIM α″ < 332T < 112T < dislocation slip [115]. Therefore, the absence of 332T suggests that the critical stress (CRSS) is lower for SIM than for 332T as a result of the "low" beta stability of Ti-12Mo-3Zr at room temperature. By increasing Zr addition to 6%, the deformation twinning {332}<113> mode is activated prior to SIM α″, presenting a combined TWIP+TRIP deformation mechanism. Further increasing of Zr addition to 10%, the SIM α″ is fully suppressed during the loading-unloading process. It can be seen that the fine-tuning of deformation mechanism, from single TRIP via combined TRIP+TWIP to single TWIP, is achieved by progressively increasing the Zr addition in the range of 3% to 10% in Ti-12Mo. Nevertheless, it has to be noted that the current Mo_{eq} estimation of Zr fails to predict the mechanical stability of Ti-12Mo-xZr. According to the activation of deformation mechanisms at room temperature, the mechanical stability order of these alloys at comparable solution-treated states should be proposed as Ti-12Mo-3Zr < Ti-12Mo ≈ Ti-12Mo-6Zr < Ti-12Mo-10Zr. The finding suggests that the Zr effect on the chemical stability of metastable Ti alloys is not linear as proposed in the Mo_{eq} estimation, especially at the low concentration range Zr % < 6%. It has been reported that the addition of Zr can achieve dual effects in Ti-Nb based alloys: on the one hand, Zr suppresses the martensitic transformation from the β phase to SIM α″ [116, 117], implying the addition of Zr could decrease M_s temperature, on the other hand, it suppresses ω formation [111]. Al-Zain et al. [118, 119] have observed that the ω_{ath} phases suppress the martensitic transformation in Ti-Nb-Mo alloys, implying that the weaker ω precipitation could increase M_s temperature. Therefore, the mechanical stability of Ti-12Mo-xZr alloys could depend on the dual effects of Zr addition. Zr content up to 3% in Ti-12Mo-xZr suggests that the effect of Zr on the suppression of ω_{ath} phase is stronger than the compositional effect resulting in lower mechanical stability in Ti-12Mo-3Zr than that in Ti-12Mo. With the increase of Zr content (from 3% to 10%), the suppressing ω phase becomes weaker, and the compositional effect becomes dominant. Therefore, the mechanical stability of Ti-12Mo-xZr (x = 3, 6, 10) increases with the increase of Zr content. The

phenomena are similar with the Sn content on Ti-Nb-Mo based alloys [120], the Ta content on Ti-Nb based alloys [121], and the Sn content on Ti-Nb-Mo based alloys [122]. Thus, the nonlinear mechanical stability of Ti-12Mo-xZr could be explained by the dual effects of Zr addition.

The three alloys present meaningful differences in their yield stress, uniform elongation, and strain-hardenability regarding mechanical behavior. The yield stresses of the three alloys can be described by the sum of several contributions, including mainly the CRSS critical stress of the dominant deformation mechanism (SIM or 332T), Zr solution hardening, and grain-size strengthening. Among them, the grain sizes of the three alloy samples are measured to be around 100 μm, it can be reasonably considered that this parameter provides a similar contribution to the yield stress of the three alloys. Qualitatively, it is reasonable to assume that the CRSS critical stress of SIM should be lower than that of 332T, according to the fault energy order mentioned in the previous section. The contribution of the Zr solution hardening is proportional to the $(\text{Zr at. \%})^{2/3}$, recently proposed by Zhao et al. for the multi-component Ti alloys [123]. When applying the above analysis to the yield stress comparison between Ti-12Mo-3Zr and Ti-12Mo-10Zr, plausible explanation can be suggested that the large increase of yield stress from 520MPa to 740MPa should arise from both strengthening contributions, i.e., increase of the beta phase stability increasing and the Zr solution strengthening from increasing Zr%. When regarding Ti-12Mo-6Zr, it seems that the yield stress strengthening increase is less than expected. Although the Zr% is doubled in atomic percentage, the yield stresses of Ti-12Mo-3Zr to Ti-12Mo-6Zr are increased from 520MPa to only 590MPa. A hypothesis is proposed that the precipitation hardening effect due to the ω_{ath} phase decrease with the increasing Zr content as mentioned before. And the SIM in Ti-12Mo6Zr also could be responsible for the limited yield stress. The SIM, although observed with low area fraction in some grains (figure 6.5), could still be active enough in other grains orientated favorably to SIM, leading to a heterogeneous yielding process. The SIM favored grains could initiate martensitic transformation before the twin nucleation and growth in the 332T favored grains, resulting in an earlier yielding than expected. A similar mechanism has been reported in the TRIP/TWIP Ti-12Mo [23] and Ti-V-Cr-Al [109] alloys.

It is worth noting that the strain-hardening rate is quite different in the three alloys. And the difference of uniform elongation in the three alloys are related to a difference of strain-hardenability, which tends to delay the occurrence of necking [124]. The correspondence between the strain-hardening rates and the observed uniform elongation can be seen with Ti-12Mo-6Zr

alloy, which presents the best elongation associated with the highest strain-hardening rate Ti-12Mo-3Zr and Ti-12Mo-10Zr are both inferior in strain-hardening rates which may lead to earlier strain localization and fracture. The different strain-hardening rates result from different microstructural evolution attributed to their different β phase stability. The microstructural evolution during deformation in Ti-12Mo-xZr alloys indicates different deformation pathways between the two deformation modes (TRIP and TWIP) due to the progressive increase of Zr addition. In other words, the tuning of the deformation mechanisms could be realized by fine-tuning Zr content in the Ti-Mo-Zr alloys. Regarding comparing the strain-hardening behavior among the TWIP alloys, back-stress due to the dislocation pile-ups at boundary/slip band intersections can be considered the critical factor responsible for the kinematic hardening [125]. By TEM investigations, the occurrence of dislocation pile-ups is confirmed near the matrix/332T and matrix/SIM α″ boundaries (shown in figure 6.8 and figure 6.9). Usually, the dislocation pile-ups in these interfaces could cause back-stress fields. And the stress fields provide a long-range strengthening effect throughout the plastic deformation. Qualitatively, the back-stress is usually evaluated to be linearly proportional to the inverse of the mean inter-boundary spacing, i.e., the distance between two adjacent boundaries of the deformation bands (SIM and/or 332T) [126]. Since the thickness of the bands observed in the three alloys is pretty similar, the inverse of the mean inter-boundary spacing is governed by the transformed or twinned fraction of the alloy at a given strain. The kinetics of the nucleation and growth of the deformation bands has been studied by Olson and Cohen [127] for strain-induced martensitic nucleation, and the same model has been adopted by Bouaziz [128] for twinning. The kinetic model has been applied successfully to describe the stress-strain behavior in single TWIP Ti alloys [125]. Indeed, the strain-hardening behavior of Ti-12Mo10Zr is consistent with the literature modeling results [125] since the deformation mechanism operated is single TWIP, compatible with the simple shear band assumption used in Olson and Cohen kinetic model. However, in the case of Ti-12Mo-6Zr with mixed TRIP/TWIP mechanisms, the same kinetic TWIP model is not well supported by the experimental results. After the yield point, the Ti-12Mo-6Zr presents a much higher strain-hardening rate than the other two alloys (figure 6.1). It is thought that the difference in strain-hardening rate could be related to the localized SIM formation in the untwinned β matrix, which is not considered in the current kinetic model. It can be seen from the EBSD and TEM images that short SIM bands are likely to form in the untwinned β matrix between two adjacent twin boundaries.

Their formation could be due to the accommodation needs of the highly localized stress or strain misfits near the twin boundaries and grain boundaries [129]. Similar situations have been reported in Ti-V-Cr-Al alloy [109] and Ti-Mo-W alloy [72]. Then it is quite obvious evidence that these local SIM bands further increase the total volume fraction of deformation products than predicted by Olson and Cohen model, and therefore further reduce the inter-spacing of the deformation-induced boundaries in the β matrix (illustrated schematically in figure 6.12). This special fact in the microstructure evolution combing TRIP and TWIP may be one of the reasons to explain the high strain-hardening rate of Ti-12Mo-6Zr when compared to Ti-12Mo-10Zr. About Ti-12Mo-3Zr, the hardening behavior at early deformation stage ($\varepsilon < 0.05$) is quite similar to that of Ti-12Mo-10Zr. The finding is corroborated by the similar microstructure evolutions observed in the two alloys. It might suggest that Olson and Cohen's kinetic is valid to describe the nucleation and growth of SIM α″ at the early stage of the plastic deformation in TRIP Ti alloys. However, in the late stage, the strain-hardening rate increases rapidly to the level close to the strain-hardening rate of Ti-12Mo6Zr, which means the increasing strain hardening rate can be due to other reasons. The exact mechanism requires further investigation.

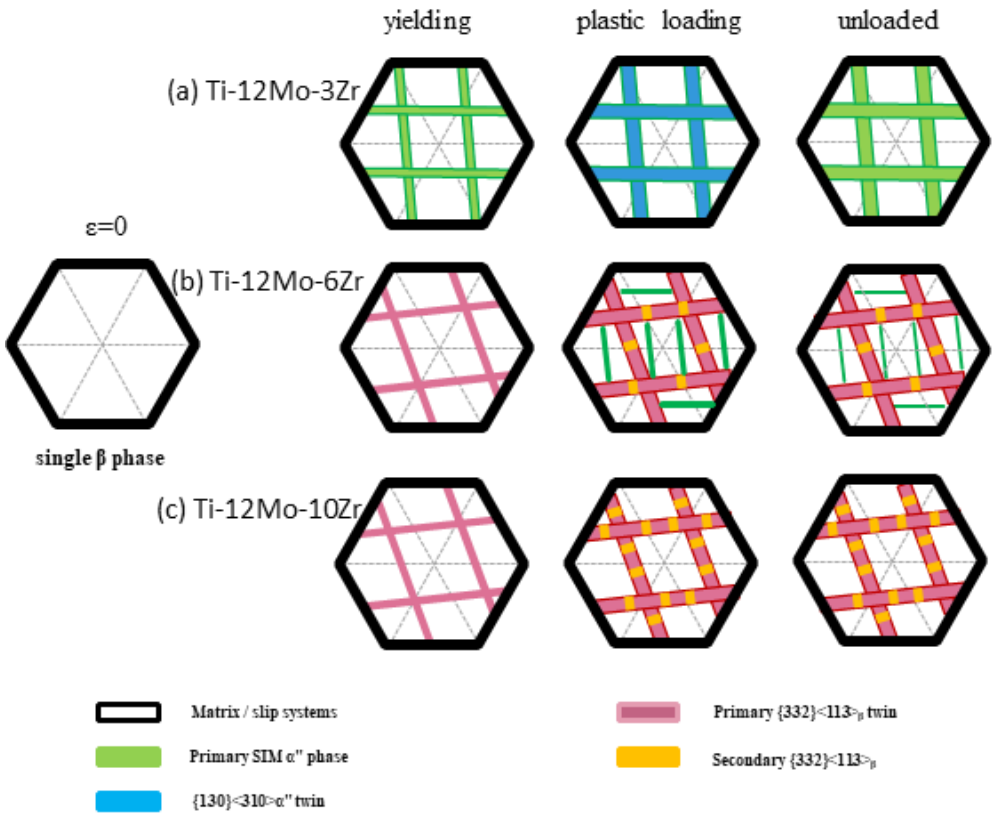

Figure 6.12. Schematic formation sequence of 332T and SIM α″ during loading and unloading process in (a) Ti-12Mo-3Zr; (b) Ti-12Mo-6Zr and (c) Ti-12Mo-10Zr alloys.

6.5 Summary

In this chapter, the influence of Zr element on microstructure evolution, mechanical properties, and deformation mechanism of the Ti-12Mo-xZr (x = 3, 6, 10) alloys are investigated. The following main results are obtained.

1. The transition from TRIP effect to TWIP effect in the Ti-12Mo-xZr alloys can be realized by fine-tuning the addition of the Zr element.

2. All three alloys display excellent strength-ductility. But the yield stress of Ti-12Mo-10Zr alloy, which is much higher than that of Ti-12Mo-6Zr and Ti-12Mo-3Zr, comes from the absence of SIM during deformation and a solid solution of Zr element.

3. Ti-12Mo-6Zr alloys display a higher strain-hardening rate when compared to Ti-12Mo-3Zr and Ti-12Mo-10Zr, which resulted from a mixture of both TRIP and TWIP mechanisms.

4. A real-size stent prototyping by Ti-12Mo-10Zr was successfully fabricated and expanded without fracture, which confirms that the mechanical properties of TRIP/TWIP Ti-12Mo-10Zr is compatible with stent application. However, the FEA results suggested that there still is a risk of fracture during the expansion process of Ti-12Mo-10Zr stent.

They are comparing to L605 alloy, Ti-12Mo-10Zr alloy process higher yield stress, low recoil rate but lower ultimate tensile stress and ductility. These results suggest that as a stent material, the mechanical properties of Ti-12Mo-10Zr stent are better than L605 stent in some aspects, such as the thickness of stent strut and recoil rate. However, both the density and the mass attenuation coefficient of Ti-12Mo-10Zr are much lower than the L605 alloys, limiting the X-ray visibility of the Ti-12Mo-10Zr stent. W is a kind of element with high density and linear attenuation coefficient. Thus, a series of Ti-W-Mo alloys and Ti-W-Mo-Zr alloys were developed by replacing Mo element by W element based on the Ti-Mo-Zr alloys to get high radio-opacity and maintain excellent mechanical properties. The mechanical properties of a novel Ti-W-Mo-Zr alloy and its deformation mechanism will be investigated in chapter 7.

Chapter7 Development of a new quaternary Ti-W-Mo-Zr TWIP alloy for cardiovascular stent application

Introduction

As mentioned in chapter 1, titanium alloys applied in permanent implants, radio-opacity is an important criterion for getting good visibility under X-ray. Ti-Mo and Ti-Mo-Zr-based alloys are reported to possess high strength, excellent ductility, and suitable industrial potential in chapters 5 and 6. However, the radio-opacity of these alloys is low, which limits their visibility under X-ray. W element with high density and linear attenuation coefficient can be regarded as a β-stabilizing element, which is weaker than the Mo element.

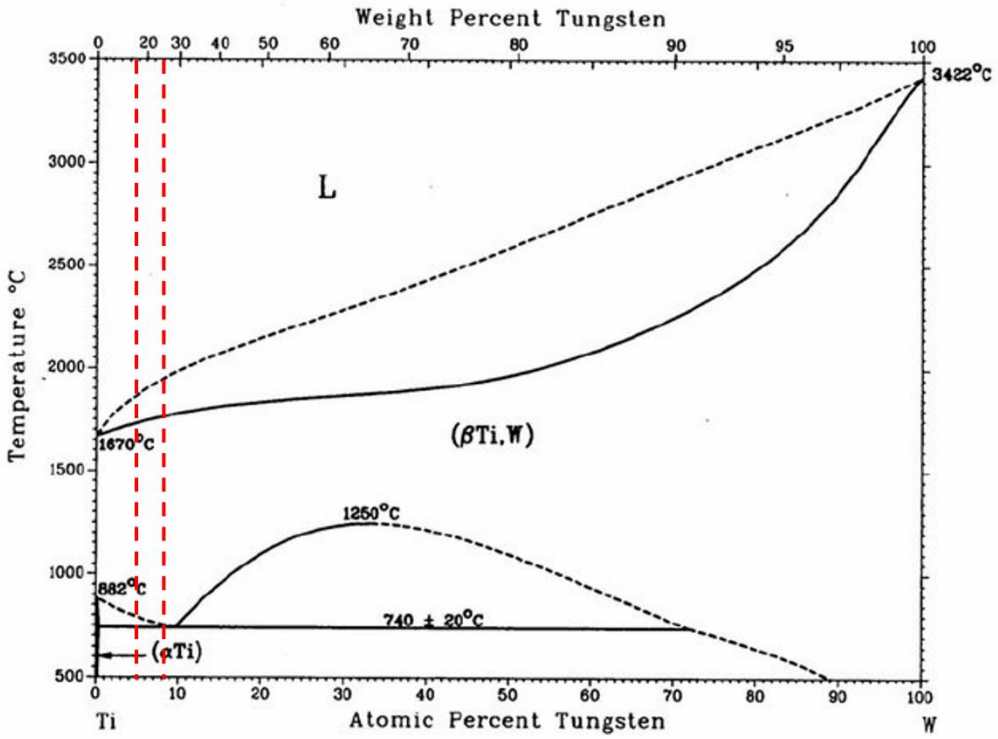

Figure 7.1 Ti-W equilibrium binary phase diagram [138].

Therefore, in this chapter, a series of Ti-W-Mo alloys and Ti-W-Mo-Zr alloys were developed by replacing the Mo element with the W element based on the Ti-Mo-Zr based alloys to get high radio-opacity and maintain excellent mechanical properties in this chapter. The W content of these alloys is at the range of 14wt.% to 28wt.%, marked by the red dashed lines in figure 7.1. As

mentioned above, all these alloys are annealed at 950℃ (over their β transus temperature) for 1.8ks to retain the fully recrystallized β grains and then quenched to room temperature.

Among these alloys, alloy No.1, which exhibits the best combination of strength and ductility, is a Ti-W-Mo-Zr alloy. Its chemical composition is temporarily confidential due to the ongoing patent process. The Ti-W-Mo-Zr alloy mentioned hereafter in the manuscript has the same chemical composition. This chapter focuses on in-situ and out-situ investigations of the deformation mechanisms in metastable β Ti-W-Mo-Zr. The evolution of dislocations and DT at different strain levels are traced by in-situ EBSD (electron backscatter diffraction) during tensile loading and after unloading conditions. The in-situ observations reveal the formation and development of the complex dislocation/332T structure. Based on the results, the macroscopic mechanical properties at room temperature are discussed with the active deformation mechanisms.

7.1 compositions refinement based on previous alloy design

Figure 7.2 shows the 16 novel compositions and mechanical behavior of Ti-W-Mo and Ti-W-Mo-Zr based alloys designed in the thesis. Among them, the Ti-W-Mo-Zr process with a combination of high strength, large high ductility, and improved density (5.7g/cm^3) compared to CP Ti (4.5 g/cm^3), Ti-12Mo (4.84 g/cm^3), and Ti-12Mo-10Zr (5.00 g/cm^3)

Figures 7.3 a and b show true stress – true strain curves and the evolution of the strain-hardening rate. The alloy showed an excellent combination of high stress, large ductility, and high work hardening rate. The yield stress of Ti-W-Mo-Zr alloy approaches 711Mpa (figure 7.3a), which is remarkably high in strain-transformable Ti alloy. Aiming at clarifying the evolution of strain-hardening behavior, the corresponding strain-hardening rate ($d\sigma/d\varepsilon$) curves of the Ti-W-Mo-Zr and reference Ti-12Mo alloys are shown in figure 7.3b. The Ti-W-Mo-Zr alloy shows a non-monotonic strain-hardening rate, similar to those observed in Ti-12Mo alloy [5]. It also can be seen that the Ti-W-Mo-Zr alloy exhibits high values of strain-hardening rate and the value presence stable at about 1700MPa in the range of $\varepsilon = 0.03$-0.15. The high value of strain-hardening rate resulted in a significant uniform elongation (> 32%), as shown in figure 7.3b.

To study the potential of Ti-W-Mo-Zr alloy as a stent material, the specifications of Ti-W-Mo-Zr are carefully analyzed compared to Ti-12Mo-10Zr alloy, and the traditional stent alloy, L605 alloy, and their specifications are listed in table 7.2. Compared Ti-12Mo-10Zr alloys, the Ti-W-Mo-Zr alloy process an improved ultimate tensile stress, ductility, and work hardening rate.

Even compared to traditional L605 alloy, the Ti-W-Mo-Zr alloy also processes reasonable ultimate tensile stress and ductility. FEA simulations are conducted by applying Ti-W-Mo-Zr to analyze fracture resistance by quantifying the maximum stress during the balloon inflation of the stent. Figure 7.2c shows that the maximum stress value is 910MPa, which is lower than the ultimate tensile stress (engineering stress 915MPa) of Ti-W-Mo-Zr alloy, which suggested that Ti-W-Mo-Zr stent could be expanded without fracture. In terms of recoil simulation results of the stent model, the properties of Ti-W-Mo-Zr are better than L605 alloy. Besides, both the central and the distal recoil rates of the Ti-W-Mo-Zr alloy are much lower than those values of the L605 alloy. The simulation results suggest that the Ti-W-Mo-Zr alloy process can meet the requirements of the stent's mechanical properties. The Radio-opacity of the alloy is proportional to the product of density and mass attenuation coefficient ($\rho \times Mc$). Both the density and the mass attenuation coefficient of Ti-W-Mo-Zr are improved compared to Ti-12Mo-10Zr. The radio-opacity is near the L605 alloy, which could get reasonable X-ray visibility Ti-W-Mo-Zr alloys (Table 7.1). The underlying mechanisms are investigated in detail by Synchrotron-based in-situ XRD tensile loading, in-situ EBSD, and TEM techniques.

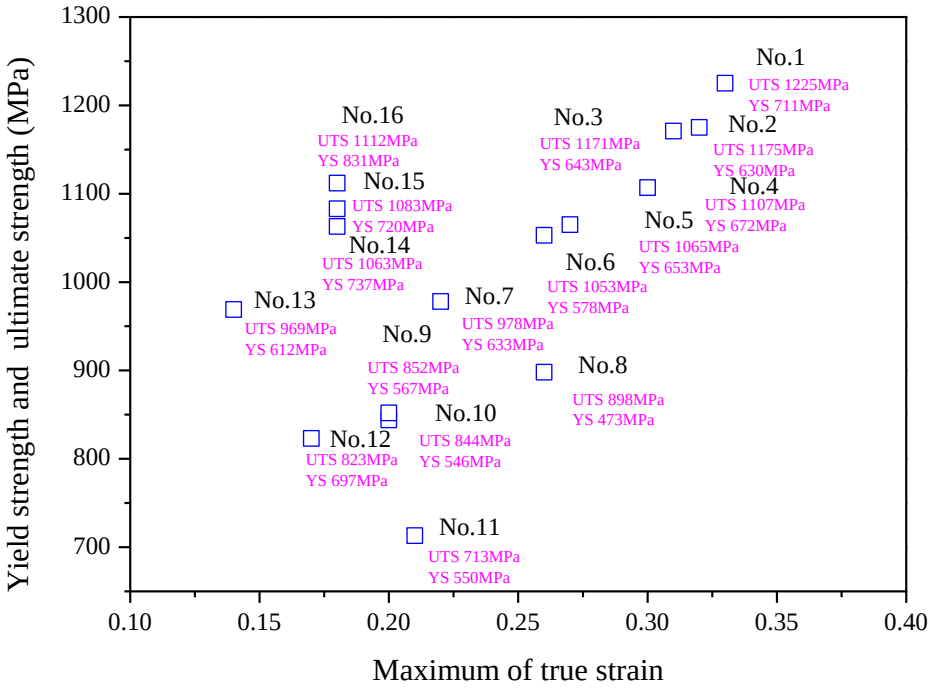

Figure 7.2 The composition of 16 designed Ti-W-Mo and Ti-W-Mo-Zr alloys, as well as their mechanical behavior.

Table 7.1 Specification of Ti-12Mo10Zr, Ti-W-Mo-Zr (mechanical properties obtained from engineering stress-strain curve), and L605 alloy (advantages of mechanical properties among the three alloys are marked in color blue).

Objective: stent strut < 75mm	Properties	L605	Ti-12Mo10Zr	Ti-W-Mo-Zr	Remarks
High radial strength after expansion	High yielding stress (YS)	600 MPa	740 MPa	711 MPa	The YS of Ti-W-Mo-Zr is higher than that of L605 alloy
High fracture resistance during expansion	High ultimate tensile stress (UTS)	1100 MPa	819MPa	915MPa	The UTS of Ti-W-Mo-Zr is higher than that of Ti-12Mo-10Zr but lower than that of L605 alloy
	High ductility	50%	27%	36%	Ti-W-Mo-Zr process improved ductility comparing to Ti-12Mo-10Zr
Low recoil	Reasonable strain hardening rate	2000~2300 MPa	1358MPa	1700MPa	
	High slastic modulus	233 GPa	71GPa	72GPa	
High X-ray visibility	Density, ρ	9.1 g/cm^3	5.0 g/cm^3	5.7 g/cm^3	
	Mass attenuation coefficient, *Mc*	0.99 cm^2/g	0.44 cm^2/g	1.26 cm^2/g	The radio-opacity (proportional to $\rho \times Mc$) of Ti-W-Mo-Zr is much better than that of Ti-12Mo-10Zr but slightly worse than that of L605 alloy

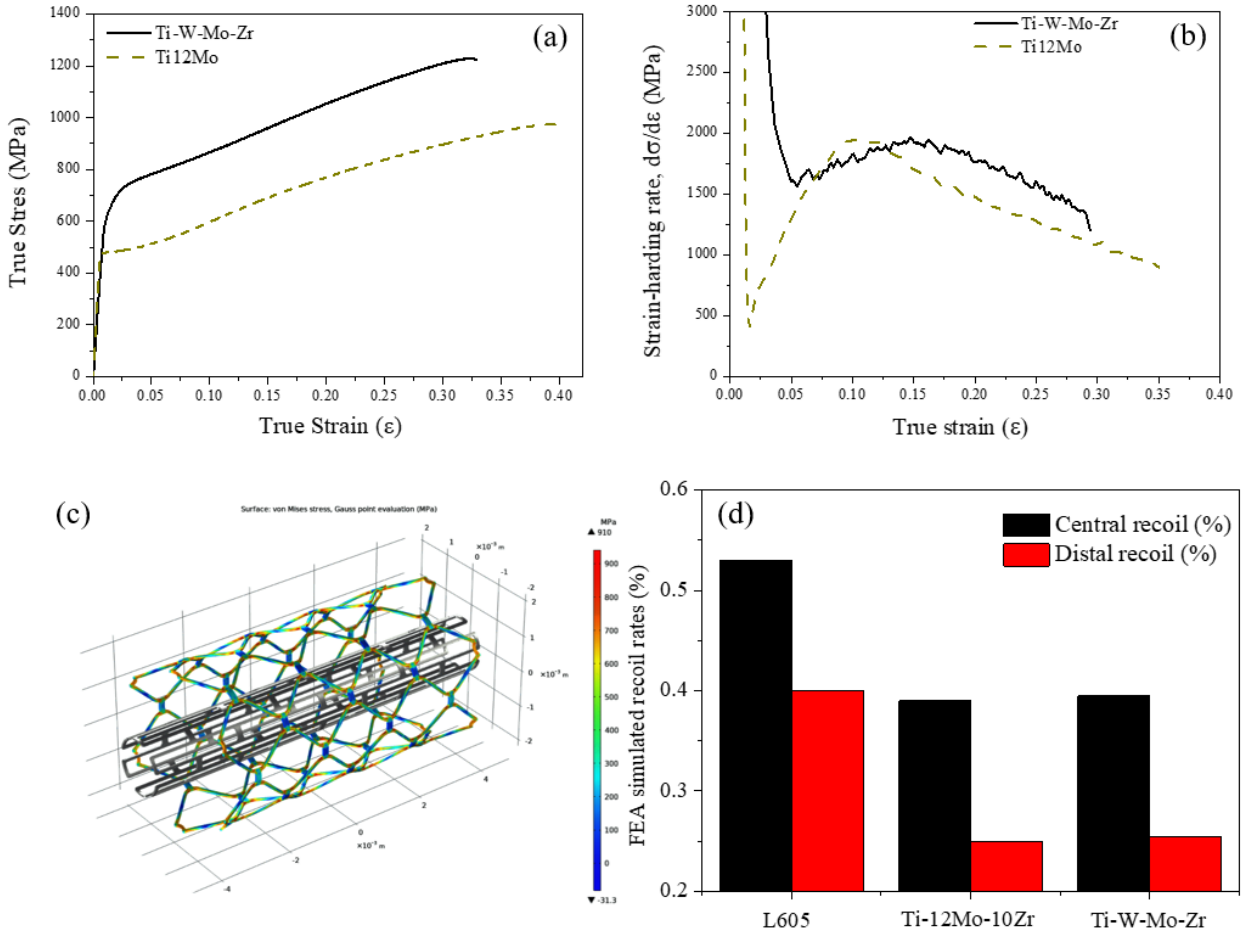

Figure 7.3. (a) True stress – true strain curves of Ti-W-Mo-Zr alloy and reference Ti-12Mo alloy and (b) corresponding strain hardening rates. FEA simulation on expansion and recoil of Ti-W-Mo-Zr alloy: (c) maximum stress in-stent during the balloon inflation. (d) the simulated recoil rates of Ti-W-Mo-Zr alloy and L605 alloy.

7.2 Deformation mechanism in Ti-W-Mo-Zr

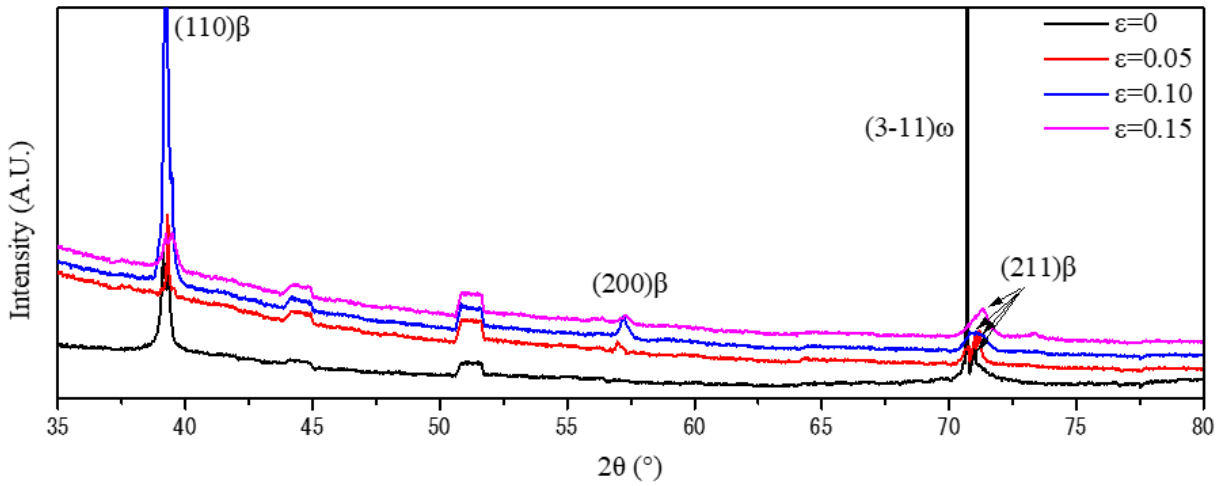

Figure 7.4. Synchrotron-based in-situ XRD tensile loading.

The transformation mechanism during the plastic loading process was further investigated by synchrotron-based in-situ XRD tensile loading in figure 7.4. Only β phase and ω phase are identified in the Ti-W-Mo-Zr alloy without α″ peaks during the whole deformation process (ε from 0 to 0.15), suggesting SIM α″ might not occur during the tensile process. The fitted lattice parameter of the β phase is α = 3.260Å. The peak position of the β phase (2θ: degree) slightly shifts towards higher angles with the increasing strain, suggesting a slight change of the β phase lattice parameter consistent with the applied stress.

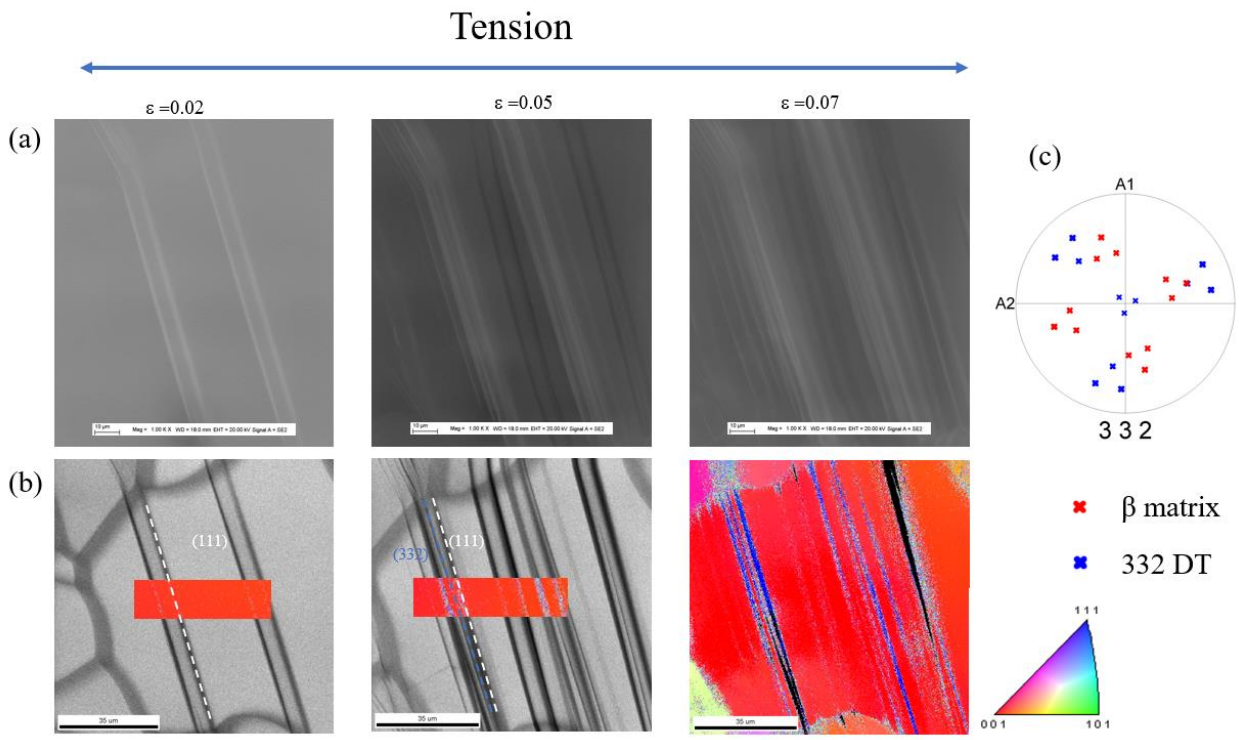

Figure 7.5 SEM and EBSD analysis of the Ti-W-Mo-Zr alloy deformed sample taken from grain A at strain ε = 0.02 (loading), 0.05 (loading), and 0.07 (loading), respectively. (a) SEM images, (b) IPF and IQ maps, and (c) pole figures of β matrix, {332}<113> twinning.

In-situ SEM images and EBSD mapping under tension are performed in the early deformation stage to further clarify the activation and evolution of the deformation microstructure in the Ti-W-Mo-Zr alloy. Figure 7.5 shows the SEM image and EBSD analysis of Ti-W-Mo-Zr at different tension strains taken from the same region. The SEM image at ε = 0.02 in figure 7.5a shows that thin plate-like deformation bands appear in pairs in β matrix grain. At the same time, the orientation of the deformation bands is indexed as the same as that of the β matrix by the IPF map in figure 7.5b. The habit plane of the deformation band, highlighted by the white dotted line in figure 7.5b, corresponds to the (111) trace, which can be identified as a classic dislocation slip plane in BCC alloy [130]. This kind of deformation band structure will be discussed in detail later.

A series of new variants of deformation bands, highlighted by the blue dotted line in figure 7.5b, appears at ε = 0.05 (figure 7.5a and 7.5b). The habit plane trace of these deformation bands can be identified as $(332)_{\beta}$ trace of β matrix. The multiplication and thickening of deformation bands, identified as 332T by stereographic projection (figure 7.5 c), can be observed in the β matrix in the IPF map at ε = 0.07 (figure 7.5a) during tensile loading.

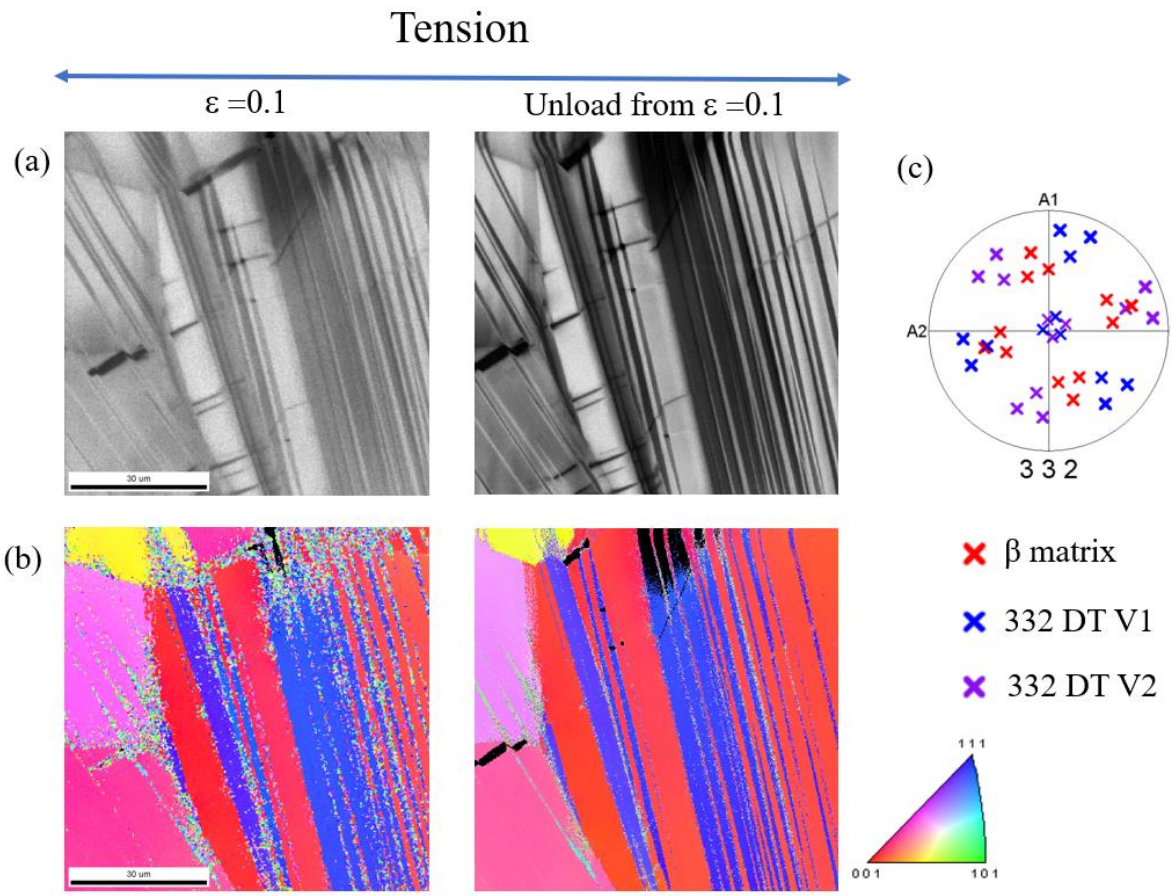

Figure 7.6 EBSD analysis of the Ti-W-Mo-Zr alloy deformed sample taken from the grain B at strain ε = 0.1 (loading) and 0.1 (unloading). (a) IQ maps, (b) IPF maps, and (c) pole figures ofβ matrix, {332}<113> twinning.

Likewise, in-situ EBSD mapping is also performed in another β grain with a similar orientation to grain A as shown in figure 7.6. The IPF maps show two different color contrasts (blue and purple) deformation bands appear in the β grain at strain ε = 0.1 (figure 7.6b). The stereo projection analysis shows these deformation bands can be indexed as two variant 332T relationships to the β matrix. After the unloading process, these 332T bands remain unchanged in their crystal orientations and thicknesses, suggesting that the mechanical twinning between the β matrix and 332T is irreversible.

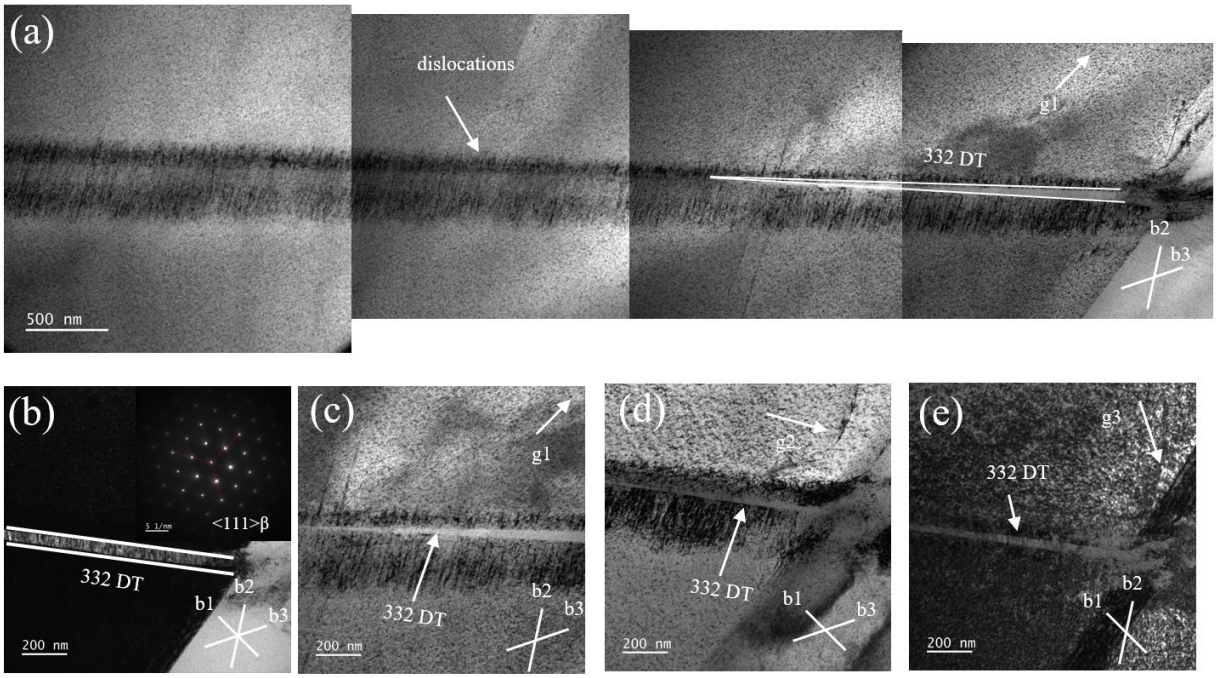

Figure 7.7 TEM micrographs of Ti-W-Mo-Zr alloy at ε = 0.02: (a) BF image of 332 DT nucleated in dislocation band, (b) BF images in $[111]_\beta$ zone axis, (c-e) BF images of the three g conditions around $[111]_\beta$ zone axis.

In order to clarify the activation and the evolution of the deformation bands observed in in-situ EBSD, TEM observations are performed to investigate the deformation microstructure in the sample after ε = 0.02 and ε = 0.1. A dislocation band with a width of about 200nm, composed of a set of parallel dislocations, can be observed in the Ti-W-Mo-Zr alloy at ε = 0.02 (figure 7.7a). A 332T band, with a width of 10nm (figure 7.7b), takes place inside the dislocation band, and the twin interface is perpendicular to these dislocations' lines (figure 7.7a). The Burgers vectors of the dislocation lines are analyzed by using the three $\boldsymbol{g.b} = 0$ extinction conditions around $[111]_\beta$ zone axis (Figure 7.7c-e). The dislocation lines constituting the dislocation band can be attributed to three Burgers vectors $b = a/2\langle 111\rangle$ (labeled by b_1, b_2, and b_3 in Fig. 7.7b). The phenomena suggest that 332T could be formed inside the dislocation band to accommodate the local stress caused by the dislocation slip. Thus, the TEM technique observed a kind of structure of 332T nucleating inside dislocation bands. The deformation bands with (111) habit plane trace followed in EBSD mapping at ε = 0.02 (figure 7.5) also should be attributed to the same structure.

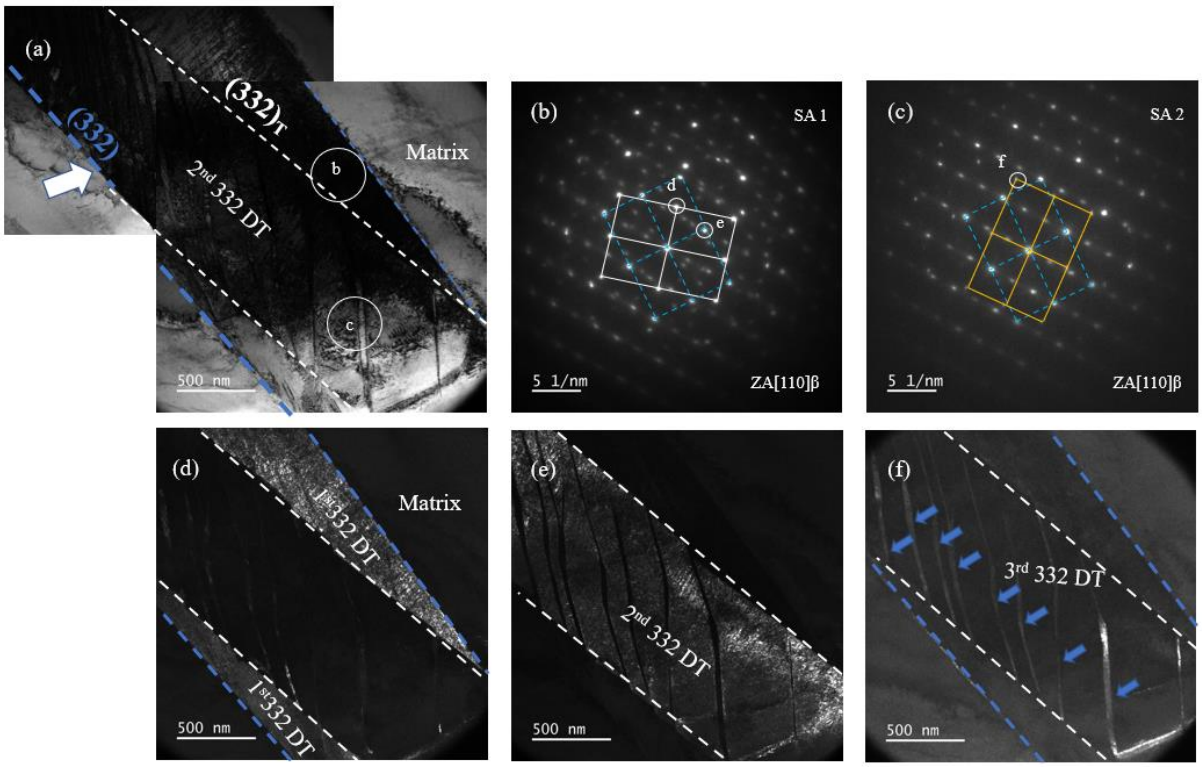

Figure 7.8 TEM images of the hierarchical structure of triple 332 DT in Ti-W-Mo-Zr alloy at ε = 0.1. (a) BF image of triple 332 DT; (b-c) SAED pattern taken from the region indicated by a circle in (a), DF image of 1st (d), 2nd (e), and 3rd (f) 332 DT.

Figure 7.8 shows the TEM investigations of the 332 T and its interface at ε = 0.1. A hierarchical structure of triple 332T can be observed, as shown in figure 7.8. A secondary deformation bands take place inside the primary 332 T band with a width of 1μm, which is identified by SAED (inset of figure 7.8b) as secondary twinning bands in the mode of {332}<113> (2^{nd} 332T). Unlike the thin plate-like 2^{nd} DT inside 332T reported in previous literature [113, 131, 132] and chapter 3, the 2^{nd} 332T replaces most of the volume fraction inside the primary twin as shown in figure 7.8 d and e. The interface trace of 2^{nd} 332T and primary 332T (marked in white dash lines in figure 7.8) can be identified as (332) plane of primary 332T. Additionally, the interface trace between 2^{nd} 332T and the β matrix is observed parallel to the primary 332T and the β matrix, as shown in figure 7.8 (a) (marked by the white arrow). Besides, a set of tertiary 332 T (3^{rd} 332 T) was identified in the 2^{nd} 332 T by TEM following the same crystallographic orientation relationship as the 1^{st} to 2^{nd} 332T (figure 7.8c and f).

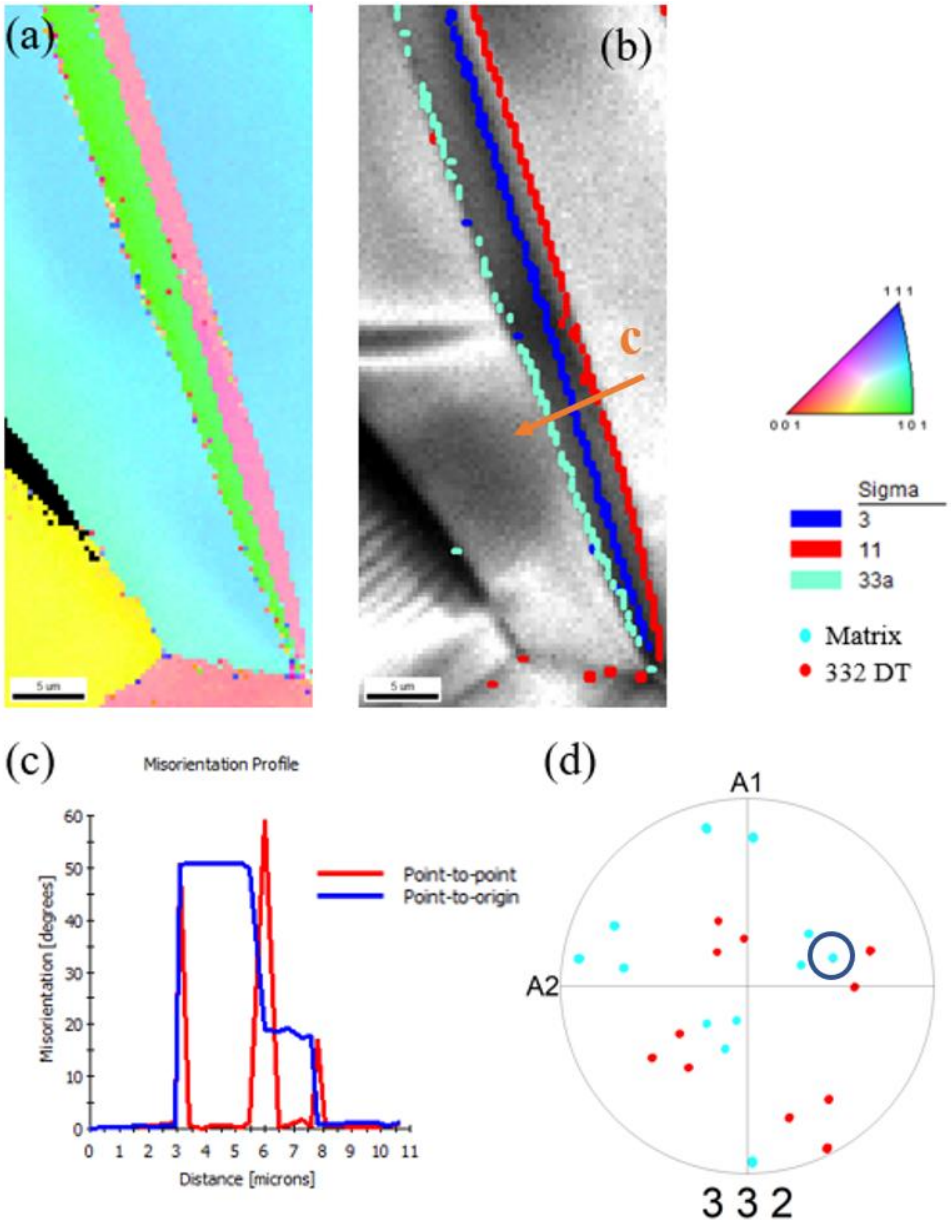

Figure 7.9 EBSD analysis of Ti-W-Mo-Zr alloy at ε = 0.08. (a) IPF map, (b) IQ map, (c) misorientation profiles along the arrows labeled c in IPF may, and the (d)corresponding stereographic projection pole figure.

Figure 7.9 shows the EBSD analysis of Ti-W-Mo-Zr alloy at ε = 0.08. A plate-like band could be observed in the IPF figure (figure 7.9a). The corresponding boundaries of these bands are clear, as shown in the IQ map (figure 7.9b). Interestingly, these deformation bands can identify two different structures: 332 T and 2nd 112T in the 332T, according to the corresponding misorientation of their boundaries (figure 7.9c) and stereographic projection pole figure shown in figure 7.9d [133]. The misorientation profiles of the band along the arrows labeled c in the IQ map

as shown in figure 7.9c. The boundaries between the β matrix and 332 T can be identified as 50.5° Σ 11 corresponding to the twinning plane of {332}<113> twinning system, and the boundary between the 332T and the 2nd 112T (figure 7.9b and c) can be identified as 60°Σ3 corresponding to the classical twinning plane of {112}<111> twinning system [134]. Moreover, the boundaries between the 2nd 112T and the β matrix can be identified as Σ33a with a 20° misorientation angle. Similar bands with the same misorientation of the corresponding boundaries have been observed by Lai et al. in Ti-36Nb-2Ta-3Zr [50].

7.3 Discussions

Based on the in-situ EBSD analysis and ex-situ TEM observation. A global schematic illustration about the deformed microstructure in the early stage of plastic deformation of Ti-W-Mo-Zr is given in figure 7.10. The initial microstructures of the alloy at ST state are the equiaxed β grains. Dislocation slip, 332T the secondary or third deformation products in primary 332T could be activated during the deformation process. As described in figure 7.9, the dislocation slips bands appear at the onset of the plastic regime. 332T could be nucleated inside these dislocation bands, then multiplicate and replace the dislocation band. The 2nd 332T and 3rd 332T can form inside the primary deformation bands with further loading.

Moreover, the 2nd 112T could be activated at the inside boundary of primary 332T. The interface between 2nd 112T and the matrix is identified as a 20° Σ33a boundary, and the interface between matrix and 332T is identified as 55° Σ11. The hierarchical 332T microstructure (primary 332T, 2nd 332T, 3rd 332T, and secondary 112T) keeps stable after unloading.

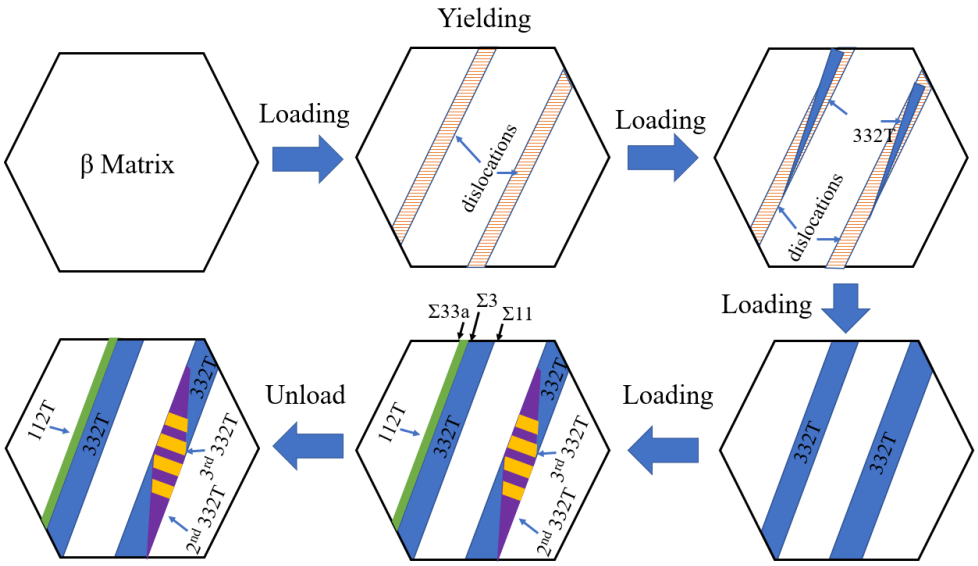

Figure 7.10 Schematic formation sequence of dislocation and deformation twinning during loading and unloading process in Ti-W-Mo-Zr.

It is worth noting that the Ti-W-Mo-Zr alloy process has high yield stress, large ductility, and an excellent work hardening rate (figure 7.3). The excellent mechanical properties have resulted from the deformation products in the alloy during the deformation process. The activations of these deformation products mainly depend on their critical resolved shear stress (CRSS). As mentioned above, dislocation slips are activated at yielding (figure 7.5 and 7.7), and then 332T could be activated inside the dislocation slip bands or nucleated independently. The phenomena are observed in many grains with different orientations in the alloy, which suggests CRSS $_{332T}$ (CRSS for deformation by 332T) $\approx$ CRSS $_{slip}$ (CRSS for deformation by dislocation slip), leading to a combination of deformation modes with dislocation slip and 332T in the alloy. Min et al. [135] found that the deformation mode changes from a 332T to dislocation slip could cause improved yield stress in Ti-10Mo-xFe alloy. Similar effects were also observed in Ti-Mo-Zr based alloys [136]. Thus, the high yield strength of Ti-W-Mo-Zr should be attributed to the activation of dislocation slip at yielding.

Usually, the dislocation slip dominant β Ti alloys generally possess a limited strain-hardening rate [136] [18]. It is worth noting that the strain-hardening rate of Ti-W-Mo-Zr is quite high, even compared to the TRIP/TWIP Ti-12Mo alloy (figure 7.3). The formation of mechanical 332T during deformation leads to an instantaneous increase in strain-hardening, which is probably attributed to both the dynamic reduction of the mean free path for dislocation glide by the

formation of 332T and the mechanical contrast effect of twins/matrix [137]. As shown in figure 7.7, the 332T is activated inside the dislocation slip band. Thus, an intense stress concentration at the 332T/matrix interfaces is hindered by the 332T interface due to dislocation. In the Ti-W-Mo-Zr alloy with a high uniform elongation, an effective accommodation mechanism is necessary to accommodate the large localized stress concentration at the interface of 332T. Figure 7.8 and figure 7.9 show that a hierarchical 332T microstructure (primary 332T, 2nd 332T, 3rd 332T, and 2nd 112T) is observed in the alloy. Hierarchical 332T twinning has been proved as an effectively auto-accommodated mechanism in Ti-Mo based alloy [23, 25]. Therefore, a combination of high strain-hardening rate and the accommodation mechanism of hierarchical 332T twinning microstructure results in the high uniform elongation in Ti-W-Mo-Zr alloy. In brief, the dislocation slip and hierarchical 332T combination deformation modes lead to the combination of high yield stress, excellent work hardening rate, and large ductility in Ti-W-Mo-Zr.

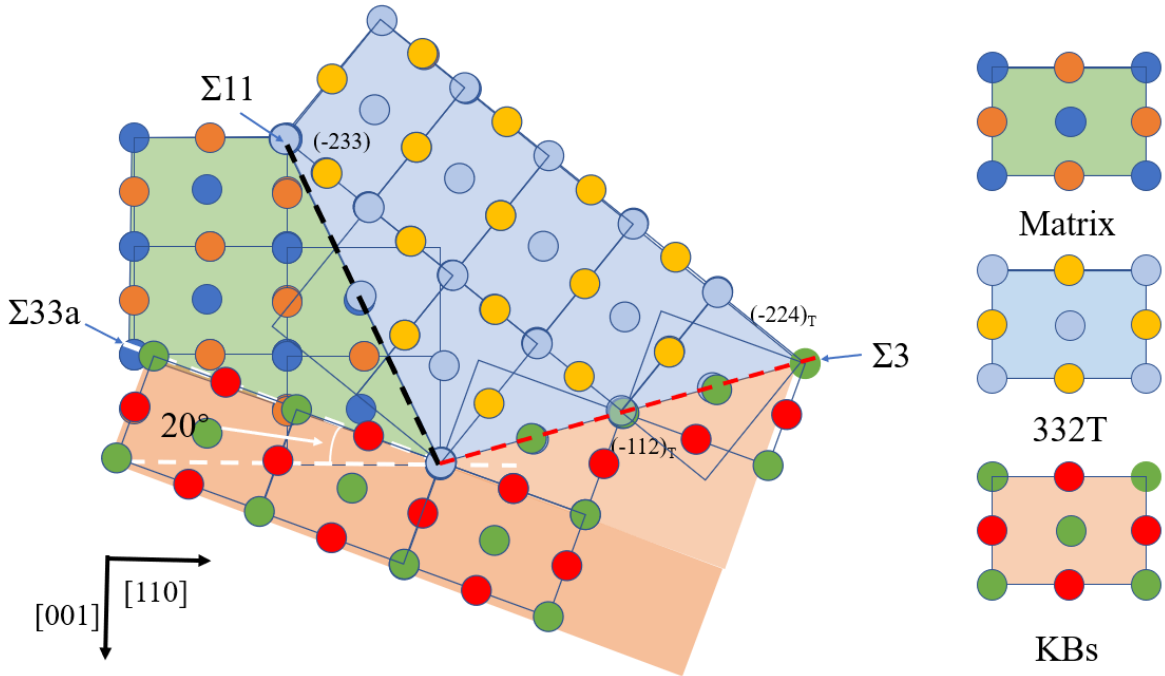

Figure 7.11 atomic model of 332DT and its 2nd 112DT

As seen in the EBSD analysis (figure 7.9), a kind of hierarchical 332T deformation band with 2nd 112T can be observed. Lai et al. [50] also observed a similar composed deformation band

adjacent to 332T, which was identified as β phase by EBSD but identified as α" by TEM, with 59.7° misorientation with the 332T. About 20° misorientation with matrix in Ti-36Nb-22Ta-3Zr. They suggested the deformation band is SIM α" remained in the surface of the sample. As seen in figure 7.7, high densities of straight parallel dislocation can be observed pile-up at the 332T boundary leading to a large local stress. Deformation twinning has been reported as an effective accommodation effect to accommodate the local stress [25]. In addition, according to Mazilova et al. [33], 20° Σ33 interface in pure BCC tungsten can be regarded as a result of reactions between lattice dislocations. As seen in the atomic projection of 2nd 112Tand 332T structure onto $(1\bar{1}0)$ plane (fig. 7.11), the 2nd 112T with Σ33a boundary with a matrix. However, these boundaries (the Σ33a (between 2nd 112T and matrix), Σ11(between 332T and matrix), and Σ3 (between 332T and 2nd 112T)) in the atomic model are inconsistent with their trace, which are observed in EBSD mapping (figure 7.9). The contradiction of atomic model and observed results in EBSD might suggest that the 112T with a 20° Σ33 (Σ33a) boundary of β matrix is formed on the surface of the sample, which might be a result of the local stress or strain misfits near the twin boundaries. The special composite structure might have a new way to get a high ductility β Ti alloy.

7.4 Summary

In this work, a new quaternary β Ti-W-Mo-Zr (wt. %) alloy with a yield stress of 750Mpa and a uniform elongation of 32% was designed and fabricated. To clarify the deformation mechanism of the alloy, the deformation sequence, the microstructural analyses, and the orientation relationships are traced by In-situ SEM, In-situ EBSD, In-situ SXRD, and ex-situ TEM observations. The main results are obtained.

1. Ti-W-Mo-Zr displays high yield stress from the dislocation slip domain deformation mechanism at the yield point.

2. A TWIP effect was observed in Ti-W-Mo-Zr after yielding, which results in a high strain-hardening rate.

3. The excellent strength-ductility in Ti-W-Mo-Zr resulted from the hierarchical 332T structure (primary 332T, 2nd 332T, 3rd 332T, and 2nd 112T).

4. FEA simulations results suggested that the Ti-W-Mo-Zr stent could be expanded without fracture.

Comparing to Ti-12Mo-10Zr alloys, the Ti-W-Mo-Zr process improved yield stress, ultimate tensile stress, ductility, and much better radio-opacity. However, compared with L605 alloy, the Ti-W-Mo-Zr process has reasonable ultimate tensile stress, ductility, and radio-opacity. Besides, the recoil rate (calculated by FEA) of Ti-W-Mo-Zr is similar to that of Ti-12Mo-10Zr alloy, which is much lower than L605 alloy. Therefore, the Ti-W-Mo-Zr has potential in the cardiovascular stent application. The real-size stent prototype has not been prepared yet and will be ready by the end of 2021. The related experiments based on the prototype will begin to be carried out at the end of the year.

Corrosion susceptibility, biocompatibility, and toxicity are very important prosperities to alloys for the cardiovascular stent. Our collaborators are doing this part experiments, and the relevant results will be obtained at the end of 2021.

Chapter 8 General conclusions

The aim of this study is to further investigate the transformation mechanism of Ti-12Mo alloy. Then based on the knowledge, the mechanical properties of Ti-12Mo are continue to be improved via thermomechanical treatment and optimizing of chemical compositions.

In the **Chapter 3**, transformation pathways operating in the β grains of a β-metastable Ti-12Mo alloy for different orientation conditions was carefully investigated via Schmid factor calculation coupled with in-situ SEM and ex-situ TEM observations. In this chapter, we proposed a method to describe and predict the distribution of the primary deformation mechanisms for all the grain orientations in TRIP/TWIP Ti alloys. The proposed method is based on the experimental transformation partition maps and the computation of a series of theoretical transformation partition maps for different combinations of Schmid factor thresholds for 332T and SIM α″. The transformation pathway in Ti12Mo depends on the grain-orientation. The transformation pathways could be partitioned into four orientation domains in the stereographic triangle, which correspond to twin-dominated- or martensite-dominated-deformation or a combination of both or the domain unfavorable for both transformations. The transformation pathways are highly diversified in TRIP/TWIP alloys due to the operations of the two transformations in a cascade manner with respects to the external tensile stress resolved in each grain; to the deformation incompatibility between neighbor grains belonging to different orientation domains; and to the strain-stress misfits at newly formed interfaces by 332T and SIM α″. The transformations are adaptive to the local deformation condition at each grain without a unique pathway. And in this chapter, experimental evidences are highlighted on the unprecedented formation mechanisms of 332T assisted by martensite 130 α″ DT via two different ways.

To further clarify the role of martensitic transformation and its twinning in the deformation process of Ti-12Mo, the SIM α″ transformation with twinning and detwinning evolution was traced by in-situ EBSD mapping observation under tensile loading and unloading conditions in **Chapter 4**. In this part, we found that two types of twinning of the martensite could be activated during the loading process, i.e. 130 α″ DT and 110 α″ DT, both contributing to a large transformation strain along the tensile direction. 130 α″ DT can be widely observed in TRIP/TWIP Ti12Mo alloy because it can provide more strain than 110 α″ DT in most orientations. The detwinning process of martensite during unloading is found to be the major contribution to the

pseudo-elastic recovery since the SIM α″ volume fraction is almost unchanged before and after unloading.

Chapter 5 is dedicated to clarify the ω_{ath}–ω_{iso} transition mechanism as well as its effects on mechanical properties and the transformation pathways in Ti-12Mo alloy. A fixed hardening temperature at 200°C was selected to realize two objectives: a) to clarify the ω_{ath}–ω_{iso} transition by electrical resistivity measurement, synchrotron X-ray diffraction, and in-situ TEM under heating; b) to better understand and control the effects of the maturity degree of ω_{iso} on the deformation mechanisms selection then the overall tensile properties via EBSD statistics and in-situ TEM studies. In the part, we found that after being hardened at 200°C for 60s (ω_{iso} hardened 60s), a considerable increase of yield strength from 659MPa to 865MPa is observed, still retaining the large uniform elongation. After the increasing the ω_{iso} hardening duration, the uniform elongation dramatically decreases to 3.3% after 150s of hardening treatment and completely inhibited after a 300s . The strengthening effect is due to the increasing CRSS of all the SIM, $\{332\}\langle 113\rangle_{\beta}$ twinning, and dislocations with the nucleation and growth of ω_{iso}; the drop of uniform elongation is due to the suppression of SIM and dislocations slip; with the ω_{iso} further growth, the alloy becomes brittle due to the suppression of TRIP/TWIP effects and dislocations slip. This gives us a new way to improve the mechanical properties of metastable β Ti alloys.

In the **Chapter 6**, the influence of Zr element on microstructure evolution, mechanical properties and deformation mechanism of the Ti-12Mo-xZr (x = 3, 6, 10) alloys is investigated by in-situ EBSD and TEM. The yield strength of Ti-12Mo was successfully improved by the addition of Zr elements. The yield strength increased from 490MPa to 740MPa after addition of 10 (wt) %Zr element, and still keep excellent ductility (> 25%). The increase of the yield stress comes from the inhibition of SIM during deformation, as well as a strong solid solution effect of Zr element. In addition, the transition from TRIP effect to TWIP effect in the Ti-12Mo-xZr alloys can be realized by fine-tuning the stability of β phase by adjusting the Zr content. Ti-12Mo-6Zr alloys display a higher strain-hardening rate when compared to Ti-12Mo-3Zr and Ti-12Mo-10Zr, which resulted from a mixture of both TRIP and TWIP mechanisms.

In the **Chapter 7**, a set of Ti-W-Mo-Zr alloys was designed and fabricated based on the Ti-Mo-Zr alloys. Using the W elements to replace Mo element in Ti-12Mo based alloy to increase its density thereby increase its radio-opacity, and fine-tuning the deformation mechanisms by addition of Zr. Through this way, a kind of new quaternary β Ti-W-Mo-Zr with a yield stress of 750MPa

and a uniform elongation of 32% was designed and fabricated. In addition, the density of Ti-W-Mo-Zr (wt%) increased from 4.84g/cm^3 (in Ti12Mo) to 5.70g/cm^3 and an improved radio-opacity is expected. Ti-W-Mo-Zr display a high yield stress, which can be attributed to the dislocation slip domain deformation mechanism at yield point. A TWIP effect was observed after yielding, which results in a high strain-hardening rate, and the excellent strength-ductility resulted from the hierarchical 332T structure (primary 332T, 2nd 332T, 3rd 332T and 2nd 112DT).

In conclusion to this thesis, this study not only contributes to the fundamental understanding of the correspondence between primary and secondary transformation products (SIM and 332T) and the grain orientation as well as the Schmid factor. ω_{iso} precipitation was confirmed to be able to strengthen Ti-12Mo alloy by shifting the TWIP and TRIP effects in the alloy to higher stress levels. Therefore, the mechanical properties of Ti-12Mo alloy could be tailored by controlling the precipitation of this phase, providing a potential new strategy for improving the mechanical properties that could be applied to other β-metastable titanium alloys.

In parallel, the mechanical properties of these alloys could also be improved by optimizing their chemical compositions. We have designed and fabricated a set of Ti-Mo-Zr and Ti-W-Mo-Zr alloys with improved properties that meet the specifications for the manufacture of cardiovascular stents. The excellent mechanical properties could be attributed to the combination of different deformation modes: dislocations, 332T, 112T, and SIM α″. The deformation mechanism could be tuned by β-stabilizing elements, such as W and Mo, and could also be finely tuned by neutral elements such as Zr. Among these alloys, Ti-12Mo-10Zr and Ti-W-Mo-Zr were selected for making full-size stent prototypes and for simulation by FEA calculations. The Ti-12Mo-10Zr stent prototype was successfully fabricated and passed the expansion balloon inflation test without fracture. Although the Ti-W-Mo-Zr prototype is not yet ready, FEA calculations were performed using the characteristics of the Ti-W-Mo-Zr alloy as parameters, and the results suggest that it meets the mechanical requirements of the stent.

Compared with traditional alloys used for stents such as L605 alloy, the mechanical properties of the metastable Ti alloys designed and studied in this thesis are better in some aspects, such as yield strength, recoil rate, for application in cardiovascular stents. The mechanical properties of metastable titanium alloys will also continue to be improved by thermomechanical treatments. In parallel, collaborations are underway to fabricate stent prototypes and the resulting in-vitro/in-vivo biological evaluations. New metastable titanium alloys will continue to be developed by

optimizing chemical compositions based on this PhD work. For example, we could continue to design a set of Ti-W-Zr alloys via substitution Mo by W elements to further increase the radio-opacity based on the Ti-W-Mo-Zr alloy. According to the knowledge of this work, the deformation mechanisms and mechanical properties of these Ti-W-Zr alloys could be fine-tuned by neutral elements such as Zr.

Bibliography

[1] D. Banerjee, J.C. Williams, Perspectives on titanium science and technology, Acta Materialia 61(3) (2013) 844-879.
[2] R.P. Kolli, A. Devaraj, A review of metastable beta titanium alloys, Metals 8(7) (2018) 506.
[3] R.R. Boyer, An overview on the use of titanium in the aerospace industry, Materials Science and Engineering: A 213(1-2) (1996) 103-114.
[4] M. Peters, J. Kumpfert, C.H. Ward, C. Leyens, Titanium alloys for aerospace applications, Advanced engineering materials 5(6) (2003) 419-427.
[5] M. Niinomi, Recent research and development in titanium alloys for biomedical applications and healthcare goods, Science and technology of advanced Materials 4(5) (2003) 445.
[6] M. Niinomi, Recent metallic materials for biomedical applications, Metallurgical and materials transactions A 33(3) (2002) 477-486.
[7] M. Niinomi, Mechanical biocompatibilities of titanium alloys for biomedical applications, Journal of the mechanical behavior of biomedical materials 1(1) (2008) 30-42.
[8] H.J. Rack, J.I. Qazi, Titanium alloys for biomedical applications, Materials Science and Engineering: C 26(8) (2006) 1269-1277.
[9] M. Geetha, A.K. Singh, R. Asokamani, A.K. Gogia, Ti based biomaterials, the ultimate choice for orthopaedic implants–a review, Progress in materials science 54(3) (2009) 397-425.
[10] D. Kuroda, M. Niinomi, M. Morinaga, Y. Kato, T. Yashiro, Design and mechanical properties of new β type titanium alloys for implant materials, Materials Science and Engineering: A 243(1-2) (1998) 244-249.
[11] Y. Li, C. Yang, H. Zhao, S. Qu, X. Li, Y. Li, New developments of Ti-based alloys for biomedical applications, Materials 7(3) (2014) 1709-1800.
[12] R.W. Schutz, H.B. Watkins, Recent developments in titanium alloy application in the energy industry, Materials Science and Engineering: A 243(1-2) (1998) 305-315.
[13] G. Lütjering, J.C. Williams, Titanium, Springer Science & Business Media2007.
[14] C. Leyens, M. Peters, Titanium and titanium alloys: fundamentals and applications, John Wiley & Sons2003.
[15] A.H. Chokshi, A.K. Mukherjee, T.G. Langdon, Superplasticity in advanced materials, Materials Science and Engineering: R: Reports 10(6) (1993) 237-274.
[16] M.J. Lai, T. Li, D. Raabe, ω phase acts as a switch between dislocation channeling and joint twinning-and transformation-induced plasticity in a metastable β titanium alloy, Acta Materialia 151 (2018) 67-77.
[17] W. Chen, S. Cao, W. Kou, J. Zhang, Y. Wang, Y. Zha, Y. Pan, Q. Hu, Q. Sun, J. Sun, Origin of the ductile-to-brittle transition of metastable β-titanium alloys: self-hardening of ω-precipitates, Acta Materialia 170 (2019) 187-204.
[18] F. Sun, J.Y. Zhang, P. Vermaut, D. Choudhuri, T. Alam, S.A. Mantri, P. Svec, T. Gloriant, P.J. Jacques, R. Banerjee, Strengthening strategy for a ductile metastable β-titanium alloy using low-temperature aging, Materials Research Letters 5(8) (2017) 547-553.
[19] B. Champin, D.E. Gelas, Traitements thermiques des alliages de titane, (1983).
[20] S. Banerjee, R. Tewari, G.K. Dey, Omega phase transformation–morphologies and mechanisms: dedicated to Professor Dr. Knut Urban on the occasion of his 65th birthday, Zeitschrift für Metallkunde 97(7) (2006) 963-977.
[21] J. Zhang, F. Sun, Y. Hao, N. Gozdecki, E. Lebrun, P. Vermaut, R. Portier, T. Gloriant, P. Laheurte, F. Prima, Influence of equiatomic Zr/Nb substitution on superelastic behavior of Ti–Nb–Zr alloy, Materials Science and Engineering: A 563 (2013) 78-85.
[22] M.J. Blackburn, J.C. Williams, PHASE TRANSFORMATIONS IN Ti--Mo AND Ti--V ALLOYS, Boeing Scientific Research Labs., Seattle, 1968.
[23] F. Sun, J.Y. Zhang, M. Marteleur, T. Gloriant, P. Vermaut, D. Laillé, P. Castany, C. Curfs, P.J. Jacques, F. Prima, Investigation of early stage deformation mechanisms in a metastable β titanium alloy showing combined twinning-induced plasticity and transformation-induced plasticity effects, Acta Materialia 61(17) (2013) 6406-6417.
[24]K.A. Bywater, J.W. Christian, Martensitic transformations in titanium-tantalum alloys, Philos. Mag. 25(1972) 1249-1273.
[25] J. Zhang, Y. Fu, Y. Wu, B. Qian, Z. Chen, A. Inoue, Y. Wu, Y. Yang, F. Sun, J. Li, F. Prima, Hierarchical {332}<113> twinning in a metastable β Ti-alloy showing tolerance to strain localization, Materials Research Letters 8(7) (2020) 247-253.
[26] H. Qin, J.J. Jonas, Variant selection during secondary and tertiary twinning in pure titanium, Acta Mater 75 (2014) 198-211.

[27] R.P. Kolli, W.J. Joost, S. Ankem, Phase stability and stress-induced transformations in beta titanium alloys, Jom 67(6) (2015) 1273-1280.
[28] A.V. Dobromyslov, V.A. Elkin, Martensitic transformation and metastable β-phase in binary titanium alloys with d-metals of 4-6 periods, Scripta materialia 44(6) (2001) 905-910.
[29] J.Y. Zhang, J.S. Li, Z. Chen, Q.K. Meng, F. Sun, B.L. Shen, Microstructural evolution of a ductile metastable β titanium alloy with combined TRIP/TWIP effects, Journal of Alloys and Compounds 699 (2017) 775-782.
[30] J.S. Bowles, J.K. Mackenzie, The crystallography of martensite transformations I, Acta metallurgica 2(1) (1954) 129-137.
[31] T. Inamura, J.I. Kim, H.Y. Kim, H. Hosoda, K. Wakashima, S. Miyazaki, Composition dependent crystallography of α ″-martensite in Ti–Nb-based β-titanium alloy, Philosophical Magazine 87(23) (2007) 3325-3350.
[32] P. Gaunt, J.W. Christian, The crystallography of the β-α transformation in zirconium and in two titanium-molybdenum alloys, Acta Metallurgica 7(8) (1959) 534-543.
[33] T.I. Mazilova, V.A. Ksenofontov, V.N. Voyevodin, E.V. Sadanov, I.M. Mikhailovskij, Mechanical recrystallization of ultra-strength tungsten nanoneedles, Philosophical magazine letters 91(4) (2011) 304-312.
[34] J.P. Liu, Y.D. Wang, Y.L. Hao, H.L. Wang, Y. Wang, Z.H. Nie, R. Su, D. Wang, Y. Ren, Z.P. Lu, High-energy X-ray diffuse scattering studies on deformation-induced spatially confined martensitic transformations in multifunctional Ti–24Nb–4Zr–8Sn alloy, Acta materialia 81 (2014) 476-486.
[35] E. Bertrand, P. Castany, Y. Yang, E. Menou, T. Gloriant, Deformation twinning in the full-α ″martensitic Ti–25Ta–20Nb shape memory alloy, Acta Materialia 105 (2016) 94-103.
[36] C. Cayron, Complements to Mügge and Friedel's Theory of Twinning, Metals 10(2) (2020) 231.
[37] N. Chen, H. Kou, Z. Wu, F. Qiang, C. Wang, J. Li, J.M. Molina-Aldareguia, Stress-induced α ″martensitic phase transformation and martensitic twinning in a metastable β titanium alloy, Journal of Alloys and Compounds 859 (2021) 157809.
[38] B. Qian, J. Zhang, Y. Fu, F. Sun, Y. Wu, J. Cheng, P. Vermaut, F. Prima, In-situ microstructural investigations of the TRIP-to-TWIP evolution in Ti-Mo-Zr alloys as a function of Zr concentration, Journal of Materials Science & Technology (2021).
[39] A. Bhattacharjee, S. Bhargava, V.K. Varma, S.V. Kamat, A.K. Gogia, Effect of β grain size on stress induced martensitic transformation in β solution treated Ti–10V–2Fe–3Al alloy, Scripta Materialia 53(2) (2005) 195-200.
[40] M.-H. Cai, C.-Y. Lee, Y.-K. Lee, Effect of grain size on tensile properties of fine-grained metastable β titanium alloys fabricated by stress-induced martensite and its reverse transformations, Scripta Materialia 66(8) (2012) 606-609
[41] L. Lilensten, Y. Danard, C. Brozek, S. Mantri, P. Castany, T. Gloriant, P. Vermaut, F. Sun, R. Banerjee, F. Prima, On the heterogeneous nature of deformation in a strain-transformable beta metastable Ti-V-Cr-Al alloy, Acta Materialia 162 (2019) 268-276.
[42] J.W. Christian, S. Mahajan, Deformation twinning, Progress in materials science 39(1-2) (1995) 1-157.
[43] R. Priestner, W.C. Leslie, Nucleation of deformation twins at slip plane intersections in BCC metals, Philosophical Magazine 11(113) (1965) 895-916.
[44] N.A. Boucher, J.W. Christian, The influence of pre-strain on deformation twinning in niobium single crystals, Acta Metallurgica 20(4) (1972) 581-591.
[45] H. Bhadeshia, Geometry of crystals, Institute of Materials London2001.
[46] A.G. Crocker, Twinned martensite, Acta Metallurgica 10(2) (1962) 113-122.
[47] H. Tobe, H.Y. Kim, T. Inamura, H. Hosoda, S. Miyazaki, Origin of {3 3 2} twinning in metastable β-Ti alloys, Acta materialia 64 (2014) 345-355.
[48] T. Kawabata, S. Kawasaki, O. Izumi, Mechanical properties of TiNbTa single crystals at cryogenic temperatures, Acta materialia 46(8) (1998) 2705-2715.
[49] V.S. Litvinov, G.M. Rusakov, Twinning on the {332}< 113> system in unstable β titanium alloys, The Physics of Metals and Metallography 90(SUPPL. 1 0031-918X) (2000).
[50] M.J. Lai, C.C. Tasan, D. Raabe, On the mechanism of {332} twinning in metastable β titanium alloys, Acta Materialia 111 (2016) 173-186.
[51] P. Castany, Y. Yang, E. Bertrand, T. Gloriant, Reversion of a Parent {130}⟨ 310⟩ α″ Martensitic Twinning System at the Origin of {332}⟨ 113⟩ β Twins Observed in Metastable β Titanium Alloys, Physical Review Letters 117(24) (2016) 245501.
[52] J. Zhang, Mechanical Behavior and Microstructural Evolution in Metastable β Ti-Mo Based Alloys with TRIP and TWIP Effects, Université Pierre et Marie Curie-Paris VI, 2014.

[53] P.W. Serruys, P. De Jaegere, F. Kiemeneij, C. Macaya, W. Rutsch, G. Heyndrickx, H. Emanuelsson, J. Marco, V. Legrand, P. Materne, A comparison of balloon-expandable-stent implantation with balloon angioplasty in patients with coronary artery disease, New England Journal of Medicine 331(8) (1994) 489-495.
[54] M.F. Ashby, D. Cebon, Materials selection in mechanical design, Le Journal de Physique IV 3(C7) (1993) C7-1-C7-9.
[55] N. Foin, R.D. Lee, R. Torii, J.L. Guitierrez-Chico, A. Mattesini, S. Nijjer, S. Sen, R. Petraco, J.E. Davies, C. Di Mario, Impact of stent strut design in metallic stents and biodegradable scaffolds, International journal of cardiology 177(3) (2014) 800-808.
[56] P. Poncin, J. Proft, Stent tubing: understanding the desired attributes, 2004, pp. 253-259.
[57] A. Vaicelyte, C. Janssen, M. Le Borgne, B. Grosgogeat, Cobalt–Chromium Dental Alloys: Metal Exposures, Toxicological Risks, CMR Classification, and EU Regulatory Framework, Crystals 10(12) (2020) 1151.
[58] A. Fortier, V. Gullapalli, R.A. Mirshams, Review of biomechanical studies of arteries and their effect on stent performance, Ijc Heart & Vessels 4 (2014) 12-18.
[59] T. Hanawa, Materials for metallic stents, Journal of Artificial Organs 12(2) (2009) 73-79 %@ 1434-7229.
[60] X. Min, X. Chen, S. Emura, K. Tsuchiya, Mechanism of twinning-induced plasticity in β-type Ti–15Mo alloy, Scripta Mater 69(5) (2013) 393-396.
[61] J.H. Hubbell, Photon mass attenuation and energy-absorption coefficients, The International Journal of Applied Radiation and Isotopes 33(11) (1982) 1269-1290.
[62] G. Baysinger, L.I. Berger, R.N. Goldberg, H.V. Kehiaian, K. Kuchitsu, G. Rosenblatt, CRC handbook of chemistry and physics, National Institute of Standards and Technology (2015).
[63] K. Cho, R. Morioka, S. Harjo, T. Kawasaki, H.Y. Yasuda, Study on formation mechanism of {332}< 113> deformation twinning in metastable β-type Ti alloy focusing on stress-induced α" martensite phase, Scripta Materialia 177 (2020) 106-111.
[64] Y. Yang, P. Castany, Y.L. Hao, T. Gloriant, Plastic deformation via hierarchical nano-sized martensitic twinning in the metastable β Ti-24Nb-4Zr-8Sn alloy, Acta Materialia 194 (2020) 27-39.
[65] D.H. Ping, Y. Yamabe-Mitarai, C.Y. Cui, F.X. Yin, M.A. Choudhry, Stress-induced α ″martensitic (110) twinning in β-Ti alloys, Applied Physics Letters 93(15) (2008) 151911.
[66] Y. Yang, P. Castany, E. Bertrand, M. Cornen, J.X. Lin, T. Gloriant, Stress release-induced interfacial twin boundary ω phase formation in a β type Ti-based single crystal displaying stress-induced α" martensitic transformation, Acta Materialia 149 (2018) 97-107.
[67] Y.L. Hao, S.J. Li, S.Y. Sun, C.Y. Zheng, Q.M. Hu, R. Yang, Super-elastic titanium alloy with unstable plastic deformation, Applied Physics Letters 87(9) (2005) 091906.
[68] W.L. Wang, X.L. Wang, W. Mei, J. Sun, Role of grain size in tensile behavior in twinning-induced plasticity β Ti-20V-2Nb-2Zr alloy, Materials Characterization 120 (2016) 263-267.
[69] L.C. Zhang, T. Zhou, S.P. Alpay, M. Aindow, M.H. Wu, Origin of pseudoelastic behavior in Ti–Mo-based alloys, Appl Phys Lett 87(24) (2005) 241909.
[70] R. Davis, H. Flower, D. West, Martensitic transformations in Ti-Mo alloys, J Mater Sci 14(3) (1979) 712-722.
[71] M. Hida, E. Sukedai, C. Henmi, K. Sakaue, H. Terauchi, Stress induced products and ductility due to lattice instability of β phase single crystal of Ti-Mo alloys, Acta Metallurgica 30(8) (1982) 1471-1479.
[72] F. Sun, J.Y. Zhang, M. Marteleur, C. Brozek, E.F. Rauch, M. Veron, P. Vermaut, P.J. Jacques, F. Prima, A new titanium alloy with a combination of high strength, high strain hardening and improved ductility, Scripta Mater 94(0) (2015) 17-20.
[73] C. Brozek, F. Sun, P. Vermaut, Y. Millet, A. Lenain, F. Prima, Development of New Trip/Twip Titanium Alloys Combining High Strength, High Strain Hardening and Improved Ductility, 2016.
[74] J.Y. Zhang, F. Sun, Y.L. Hao, N. Gozdecki, E. Lebrun, P. Vermaut, R. Portier, T. Gloriant, P. Laheurte, F. Prima, Influence of equiatomic Zr/Nb substitution on superelastic behavior of Ti–Nb–Zr alloy, Mater Sci Eng A-struct 563 (2013) 78-85.
[75] M. Abdel-Hady, H. Fuwa, K. Hinoshita, H. Kimura, Y. Shinzato, M. Morinaga, Phase stability change with Zr content in β-type Ti–Nb alloys, Scripta Mater 57(11) (2007) 1000-1003.
[76] Y. Hao, S. Li, S. Sun, R. Yang, Effect of Zr and Sn on Young's modulus and superelasticity of Ti–Nb-based alloys, Mater Sci Eng A-struct 441(1-2) (2006) 112-118.
[77] J. Zhang, J. Li, G. Chen, L. Liu, Z. Chen, Q. Meng, B. Shen, F. Sun, F. Prima, Fabrication and characterization of a novel β metastable Ti-Mo-Zr alloy with large ductility and improved yield strength, Mater Charact 139 (2018) 421-427.
[78] S. Miyazaki, H. Kim, H. Hosoda, Development and characterization of Ni-free Ti-base shape memory and superelastic alloys, Mater Sci Eng A-struct 438-440 (2006) 18-24.

[79] Q. Wang, C. Dong, P.K. Liaw, Structural stabilities of β-Ti alloys studied using a new Mo equivalent derived from [β/(α+ β)] phase-boundary slopes, Metallurgical and Materials Transactions A 46(8) (2015) 3440-3447.
[80] E. Schmid, W. Boas, Plasticity of crystals, (1950).
[81] Q.-J. Chen, S.-Y. Ma, S.-Q. Wang, The Nucleation and the Intrinsic Microstructure Evolution of Martensite from 332⟨ 113⟩ β Twin Boundary in β Titanium: First-Principles Calculations, Metals 9(11) (2019) 1202.
[82] Y.W. Chai, H.Y. Kim, H. Hosoda, S. Miyazaki, Self-accommodation in Ti–Nb shape memory alloys, Acta Materialia 57(14) (2009) 4054-4064.
[83] H.Y. Kim, Y. Ikehara, J.I. Kim, H. Hosoda, S. Miyazaki, Martensitic transformation, shape memory effect and superelasticity of Ti–Nb binary alloys, Acta materialia 54(9) (2006) 2419-2429.
[84] S.A. Mantri, F. Sun, D. Choudhuri, T. Alam, B. Gwalani, F. Prima, R. Banerjee, Deformation Induced Hierarchical twinning Coupled with omega transformation in a Metastable β-ti Alloy, Scientific reports 9(1) (2019) 1-8.
[85] J.W. Christian, The theory of transformations in metals and alloys, Newnes2002.
[86] H.Y. Kim, Y. Ikehara, J.I. Kim, H. Hosoda, S. Miyazaki, Martensitic transformation, shape memory effect and superelasticity of Ti–Nb binary alloys, Acta Mater 54(9) (2006) 2419-2429.
[87] L.A. Girifalco, H. Herman, A model for the growth of Guinier-Preston zones-the vacancy pump, Acta Metallurgica 13(6) (1965) 583-590.
[88] J.F. Xiao, Z.H. Nie, C.W. Tan, G. Zhou, R. Chen, M.R. Li, X.D. Yu, X.C. Zhao, S.X. Hui, W.J. Ye, Effect of reverse β-to-ω transformation on twinning and martensitic transformation in a metastable β titanium alloy, Materials Science and Engineering: A 759 (2019) 680-687.
[89] M. Lai, T. Li, D. Raabe, ω phase acts as a switch between dislocation channeling and joint twinning-and transformation-induced plasticity in a metastable β titanium alloy, Acta Materialia 151 (2018) 67-77.
[90] A. George, R. Divakar, Evidence for spinodal decomposition in Ti-15Mo quenched alloy using transmission electron microscopy, Micron 121 (2019) 43-52.
[91] F. Prima, J. Debuigne, M. Boliveau, D. Ansel, Control of omega phase volume fraction precipitated in a beta titanium alloy: development of an experimental method, Journal of materials science letters 19(24) (2000) 2219-2221.
[92] T. Gloriant, G. Texier, F. Sun, I. Thibon, F. Prima, J.-L. Soubeyroux, Characterization of nanophase precipitation in a metastable β titanium-based alloy by electrical resistivity, dilatometry and neutron diffraction, Scripta Materialia 58(4) (2008) 271-274.
[93] P. Zháňal, P. Harcuba, J. Šmilauerová, J. Stráský, M. Janeček, B. Smola, M. Hájek, Phase Transformations in Ti-15Mo Investigated by in situ Electrical Resistance, Acta Physica Polonica, A. 128(4) (2015).
[94] M. Hájek, Phase Transformations in Ti 15Mo Investigated by in situ Electrical Resistance.
[95] H.L. Fraser, M.A. Imam, Y. Kosaka, H.J. Rack, A. Chatterjee, A. Woodfield, PHASE TRANSFORMATIONS IN BETA-Ti ALLOYS STUDIED BY IN-SITU METHODS, John Wiley & Sons, 2016, p. 437.
[96] P. Zháňal, P. Harcuba, M. Hájek, J. Šmilauerová, J. Veselý, M. Janeček, Characterization of Phase Transitions Occurring in Solution Treated Ti-15Mo during Heating by Thermal Expansion and Electrical Resistance Measurements, Trans Tech Publ, 2017, pp. 2318-2323.
[97] D. De Fontaine, O. Buck, A Monte Carlo simulation of the omega phase transformation, Philosophical Magazine 27(4) (1973) 967-983.
[98] T.S. Kuan, S.L. Sass, The structure of a linear omega-like vacancy defect in Zr-Nb BCC solid solutions, Acta Metallurgica 24(11) (1976) 1053-1059.
[99] D. Schryvers, L.E. Tanner, High resolution electron microscopy observations of athermal omega phase in Ti-Mo alloys, Trans Tech Publ, 1990, pp. 329-334.
[100] E. Sukedai, Y. Kitano, A. Ohnishi, Investigation of initial structures of aged ω-phase crystals in β-titanium alloys using high resolution electron microscopy, Micron 28(4) (1997) 269-277.
[101] E. Sukedai, H. Hashimoto, M. Hida, Fine structure of as-quenched omega-phase of Ti-Mo alloy observed by HREM with image processing, Japanese journal of applied physics 26(6A) (1987) L961.
[102] M.A. Meyers, O. Vöhringer, V.A. Lubarda, The onset of twinning in metals: a constitutive description, Acta materialia 49(19) (2001) 4025-4039.
[103] Q. Yu, Z.-W. Shan, J. Li, X. Huang, L. Xiao, J. Sun, E. Ma, Strong crystal size effect on deformation twinning, Nature 463(7279) (2010) 335-338.
[104] H.Y. Kim, L. Wei, S. Kobayashi, M. Tahara, S. Miyazaki, Nanodomain structure and its effect on abnormal thermal expansion behavior of a Ti–23Nb–2Zr–0.7 Ta–1.2 O alloy, Acta materialia 61(13) (2013) 4874-4886.
[105] Q. Yu, J. Zhang, Y. Jiang, Direct observation of twinning–detwinning–retwinning on magnesium single crystal subjected to strain-controlled cyclic tension–compression in [0 0 0 1] direction, Philosophical magazine letters 91(12) (2011) 757-765.

[106] S.G. Song, G.T. Gray Iii, Structural interpretation of the nucleation and growth of deformation twins in Zr and Ti—II. Tem study of twin morphology and defect reactions during twinning, Acta metallurgica et materialia 43(6) (1995) 2339-2350.
[107] J. Gao, Y. Huang, D. Guan, A.J. Knowles, L. Ma, D. Dye, W.M. Rainforth, Deformation mechanisms in a metastable beta titanium twinning induced plasticity alloy with high yield strength and high strain hardening rate, Acta Mater 152 (2018) 301-314.
[108] L. Ren, W. Xiao, C. Ma, R. Zheng, L. Zhou, Development of a high strength and high ductility near β-Ti alloy with twinning induced plasticity effect, Scripta Mater 156 (2018) 47-50.
[109] L. Lilensten, Y. Danard, C. Brozek, S. Mantri, P. Castany, T. Gloriant, P. Vermaut, F. Sun, R. Banerjee, F. Prima, On the heterogeneous nature of deformation in a strain-transformable beta metastable Ti-V-Cr-Al alloy, Acta Mater 162 (2019) 268-276.
[110] C. Brozek, F. Sun, P. Vermaut, Y. Millet, A. Lenain, D. Embury, P.J. Jacques, F. Prima, A β-titanium alloy with extra high strain-hardening rate: Design and mechanical properties, Scripta Mater 114 (2016) 60-64.
[111] E.L. Pang, E.J. Pickering, S.I. Baik, D.N. Seidman, N.G. Jones, The effect of zirconium on the omega phase in Ti-24Nb-[0–8]Zr (at.%) alloys, Acta Mater 153 (2018) 62-70.
[112] J.Y. Zhang, J.S. Li, Z. Chen, Q.K. Meng, F. Sun, B.L. Shen, Microstructura1 evolution of a ductile metastable β titanium alloy with combined TRIP/TWIP effects, J Alloy Compd 699 (2017) 775-782.
[113] J. Zhang, F. Sun, Z. Chen, Y. Yang, B. Shen, J. Li, F. Prima, Strong and ductile beta Ti–18Zr–13Mo alloy with multimodal twinning, Materials Research Letters 7(6) (2019) 251-257.
[114] P. Castany, Y. Yang, E. Bertrand, T. Gloriant, Reversion of a Parent {130}α" Martensitic Twinning System at the Origin of {332}β Twins Observed in Metastable beta Titanium Alloys, Phys Rev Lett 117(24) (2016).
[115] X. Zhou, X. a Min, S. Emura, K. Tsuchiya, Accommodative {332}< 113> primary and secondary twinning in a slightly deformed β-type Ti-Mo titanium alloy, Materials Science and Engineering: A 684 (2017) 456-465.
[116] Y.L. Hao, S.J. Li, S.Y. Sun, R. Yang, Effect of Zr and Sn on Young's modulus and superelasticity of Ti–Nb-based alloys, Materials Science and Engineering: A 441(1-2) (2006) 112-118.
[117] M. Tane, S. Akita, T. Nakano, K. Hagihara, Y. Umakoshi, M. Niinomi, H. Nakajima, Peculiar elastic behavior of Ti–Nb–Ta–Zr single crystals, Acta Materialia 56(12) (2008) 2856-2863.
[118] Y. Al-Zain, H.Y. Kim, T. Koyano, H. Hosoda, T.H. Nam, S. Miyazaki, Anomalous temperature dependence of the superelastic behavior of Ti–Nb–Mo alloys, Acta Materialia 59(4) (2011) 1464-1473.
[119] Y. Al-Zain, H.Y. Kim, H. Hosoda, T.H. Nam, S. Miyazaki, Shape memory properties of Ti–Nb–Mo biomedical alloys, Acta Materialia 58(12) (2010) 4212-4223.
[120] D.C. Zhang, S. Yang, M. Wei, Y.F. Mao, C.G. Tan, J.G. Lin, Effect of Sn addition on the microstructure and superelasticity in Ti–Nb–Mo–Sn alloys, Journal of the mechanical behavior of biomedical materials 13 (2012) 156-165.
[121] H.Y. Kim, S. Hashimoto, J.I. Kim, T. Inamura, H. Hosoda, S. Miyazaki, Effect of Ta addition on shape memory behavior of Ti–22Nb alloy, Materials Science and Engineering: A 417(1-2) (2006) 120-128.
[122] M.F. Ijaz, H.Y. Kim, H. Hosoda, S. Miyazaki, Effect of Sn addition on stress hysteresis and superelastic properties of a Ti–15Nb–3Mo alloy, Scripta Materialia 72 (2014) 29-32.
[123] G.H. Zhao, X.Z. Liang, B. Kim, P.E.J. Rivera-Díaz-del-Castillo, Modelling strengthening mechanisms in beta-type Ti alloys, Materials Science and Engineering: A 756 (2019) 156-160.
[124] A.K. Ghosh, Tensile instability and necking in materials with strain hardening and strain-rate hardening, Acta Metallurgica 25(12) (1977) 1413-1424.
[125] G.-H. Zhao, X. Xu, D. Dye, P.E.J. Rivera-Díaz-del-Castillo, Microstructural evolution and strain-hardening in TWIP Ti alloys, Acta Materialia 183 (2020) 155-164.
[126] L. Zhu, H. Ruan, X. Li, M. Dao, H. Gao, J. Lu, Modeling grain size dependent optimal twin spacing for achieving ultimate high strength and related high ductility in nanotwinned metals, Acta Materialia 59(14) (2011) 5544-5557.
[127] G.B. Olson, M. Cohen, Kinetics of strain-induced martensitic nucleation, Metallurgical transactions A 6(4) (1975) 791.
[128] O. Bouaziz, N. Guelton, Modelling of TWIP effect on work-hardening, Materials Science and Engineering: A 319 (2001) 246-249.
[129] A. Artemev, Y. Jin, A.G. Khachaturyan, Three-dimensional phase field model and simulation of cubic→ tetragonal martensitic transformation in polycrystals, Philosophical Magazine A 82(6) (2002) 1249-1270.
[130] L.L. Hsiung, On the mechanism of anomalous slip in bcc metals, Materials Science and Engineering: A 528(1) (2010) 329-337.

[131] J. Zhang, Y. Fu, Y. Wu, B. Qian, Z. Chen, A. Inoue, Y. Wu, Y. Yang, F. Sun, J. Li, Hierarchical {332}< 113> twinning in a metastable β Ti-alloy showing tolerance to strain localization, Materials Research Letters 8(7) (2020) 247-253.
[132] X. Min, X. Chen, S. Emura, K. Tsuchiya, Mechanism of twinning-induced plasticity in β-type Ti–15Mo alloy, Scripta Materialia 69(5) (2013) 393-396.
[133] Y. Zheng, W. Zeng, Y. Wang, S. Zhang, Kink deformation in a beta titanium alloy at high strain rate, Materials Science and Engineering: A 702 (2017) 218-224.
[134] E. Bertrand, P. Castany, I. Péron, T. Gloriant, Twinning system selection in a metastable β-titanium alloy by Schmid factor analysis, Scripta materialia 64(12) (2011) 1110-1113.
[135] X.H. Min, S. Emura, T. Nishimura, K. Tsuchiya, K. Tsuzaki, Microstructure, tensile deformation mode and crevice corrosion resistance in Ti–10Mo–xFe alloys, Materials Science and Engineering: A 527(21-22) (2010) 5499-5506.
[136] X.H. Min, K. Tsuzaki, S. Emura, K. Tsuchiya, Enhancement of uniform elongation in high strength Ti–Mo based alloys by combination of deformation modes, Materials Science and Engineering: A 528(13-14) (2011) 4569-4578.
[137] S. Hanada, O. Izumi, Correlation of tensile properties, deformation modes, and phase stability in commercial β-phase titanium alloys, Metallurgical and Materials Transactions A 18(2) (1987) 265-271.

Résumé

En raison de leur remarquable combinaison de propriétés : rapport résistance/poids très élevé, faible densité, excellente résistance à la corrosion et biocompatibilité, l'utilisation du titane et ses alliages n'a fait que croître au cours des dernières décennies dans de nombreux domaines d'application tels que l'industrie aérospatiale, l'industrie biomédicale et de la santé, et l'industrie de l'énergie. Cette combinaison remarquable de propriétés tient essentiellement à la grande variété de transformations de phases que peuvent subir ces alliages. En effet, le titane présente différentes formes allotropiques : une forme hexagonale compacte appelée phase α, une forme cubique centrée appelée phase β et une forme hexagonale appelée phase ω. Chaque forme allotropique n'est stable que sur une plage de température et de pression et les transitions entre ces différentes phases peuvent adopter un caractère displacif ou diffusif selon la vitesse de refroidissement. Si on ajoute à cela l'influence spécifique que peut avoir chaque élément d'alliage sur la stabilité des différentes phases et les transitions entre celles-ci, on comprend alors l'extraordinaire variété de microstructures que peuvent présenter ces alliages.

Les alliages de titane sont ainsi classés en catégories en fonction de la phase majoritaire qu'il contient. On distingue alors les alliages de type α, de type β et les alliages mixtes phase $\alpha+\beta$. Ce sont les principaux alliages qui ont été développés depuis les années 50. La phase ω étant réputée fragilisante, les alliages β métastables prompt à former cette phase lors de traitements thermiques n'ont été que peu étudiés jusqu'à la fin des années 90. En revanche, même si le titane est un élément abondant, son affinité avec l'oxygène rend son exploitation difficile. Son prix reste ainsi encore élevé, ce qui limite son utilisation à des applications à haute valeur ajoutée.

Par rapport aux alliages de titane traditionnels, les alliages de titane β-métastables ont attiré davantage l'attention ces dernières décennies en raison de propriétés spécifiques telles que la superélasticité, l'effet mémoire de forme, le faible module d'Young et une meilleure formabilité à l'état trempé, propriétés particulièrement attractives pour les applications biomédicales. Ces propriétés sont issues d'une transformation martensitique induite sous contrainte qui peut se produire dans la phase β-métastable retenue par trempe. Lorsque cette martensite est thermoélastique et donc réversible, elle procure à l'alliage des propriétés de super-élasticité dans une gamme de déformation allant jusqu'à 3%. Lorsque l'alliage est déformé au delà de cette gamme, la martensite α″ peut se former dans le domaine plastique. Cette martensite induite sous contrainte sera désignée par la suite SIM α″. De façon générale, on parle alors de plasticité induite par transformation de phase ou effet TRIP (TRansformation Induced Plasticity). Un autre phénomène apparaissant au cours de la déformation plastique est le maclage mécanique de type {332}<113> de la phase β, que l'on notera par la suite 332T. Ce maclage tout à fait spécifique à cette famille d'alliage a attiré beaucoup d'attention également ces dernières années. Ce mécanisme de déformation est quant à lui appelé effet TWIP pour TWinning Induced Plasticity. Lorsqu'il est combiné au glissement de dislocations et à l'effet TRIP, il est alors possible d'atteindre des niveaux d'écrouissage élevés procurant à ces alliages des résistances mécaniques associées à des déformations à la rupture particulièrement intéressantes. Ces alliages de type TRIP/TWIP également appelés aujourd'hui «transformables par déformation» présentent une combinaison de propriétés qui leur permet d'être envisagés pour la fabrication de stents cardiovasculaires.

Les stents cardiovasculaires, en tant que dispositifs pour traiter les maladies coronariennes, sont considérés aujourd'hui comme l'une des plus grandes percées médicales du 21e siècle. Depuis l'introduction du premier stent en métal nu (acier inoxydable) dans le domaine clinique en 1994,

plusieurs types d’alliages ont été utilisés comme matériau pour les fabriquer. Le mécanisme de fonctionnement de ces stents est illustré à la figure 1 (a). Ces stents sont utilisés pour contrecarrer la diminution locale du diamètre du vaisseau sténosé en le dilatant mécaniquement, rétablissant ainsi l’écoulement du sang. Pour cela, le métal constitutif du stent doit pouvoir supporter une déformation plastique importante sans risque de rupture pendant la phase d’expansion mais également présenter une limite d’élasticité élevée une fois déformé afin de maintenir le vaisseau ouvert après retrait du ballon en empêchant le vaisseau de se refermer par retour élastique. Pour cela, le métal doit respecter des exigences mécaniques minimales qui sont généralement : une limite d'élasticité d'environ 200 MPa, une résistance à la traction élevée (UTS > 300 MPa) et un allongement plastique homogène suffisant (> 15 %).

Un taux d'écrouissage élevé conduirait à une augmentation souhaitable de la résistance mécanique après la phase d’expansion. Or une résistance mécanique plus élevées permettrait également de concevoir des stents aux parois plus minces, améliorant ainsi leur flexibilité, leur facilité de mise en place et l'accès à des vaisseaux plus petits. L'épaisseur du stent a aussi un impact important sur les blessures et inflammation potentielles : plus un stent est épais plus il peut entraîner un degré d'inflammation et de complication (hyperplasie néointimal) élevé. Les alliages employés pour la fabrication de ces stents doivent également présenter un module d'Young élevé afin de minimiser le recul élastique (< 4%). Outre le comportement mécanique du matériau qui va assurer les performances du stent : flexibilité appropriée, forces radiales développées sur les parois du vaisseau, résistance à la fracture, d’autres propriétés sont requises pour assurer la mise en place du stent et son suivi par imagerie médicale sans risques pour le patient: la radio-opacité pour la radiographie, et des propriétés non ferromagnétiques pour l'imagerie par résonance magnétique (IRM). Pour répondre à ces exigences, des alliages Co-Cr tels que le L605 (Co-20Cr-15W-10Ni)

et le MP35N (Co-Cr-35Ni-10Mo) ont été conçus et sont encore employés aujourd'hui. Cependant, le Co métal est considéré comme une substance cancérigène, mutagène et toxique pour la reproduction (CMR) et sera interdit dans l'UE en tant que matériau d'implantation pour le corps humain après 2025. Par conséquent, il est indispensable de trouver des alliages alternatifs pour la fabrication des stents métalliques.

Le Ti de pureté commerciale (CP Ti) et les alliages de Ti traditionnels n'ont pas été envisagés pour cette application pour plusieurs raisons. Premièrement, les propriétés mécaniques de ces matériaux ne répondent pas aux exigences comme le montre la figure 1 (b). Deuxièmement, leur ductilité est faible par rapport aux alliages Co-Cr, ce qui peut entraîner une fracturation pendant l'expansion du ballon ou plus tard par fatigue. De plus, en tant que métal léger, le CP et le Ti6Al4V ne conviennent pas à l'imagerie par radiographie X en raison de leur faible radio-opacité et ce qui impose le recours à des marqueurs constitués de métaux lourds. Les alliages base titane TRIP/TWIP quant à eux peuvent être des alliages intéressants avec une densité potentiellement améliorée, et un taux d'écrouissage, une ductilité et une résistance mécanique élevés. Certaines études se concentrent sur les alliages TRIP/TWIP à base de Ti-Mo en raison de leur excellent comportement mécanique (comme le montre la figure 1(b) et le tableau 1). En effet, le Mo est reconnu comme biocompatible. Le tableau 1 répertorie les propriétés pertinentes des alliages Ti-Mo, CP Ti, alliages traditionnels α/β et les alliages primaires (tels que l'acier inoxydable et les alliages Co-Cr) utilisés dans les implants permanents. Comme le montre le tableau 1, le Ti12Mo semble être un excellent candidat pour la fabrication de stents, puisqu'il combine résistance mécanique et taux d'écrouissage élevés avec un excellent allongement plastique homogène. Cependant, la limite d'élasticité est relativement faible par rapport aux alliages Co-Cr. Cela

entraînerait la fabrication de stents plus épais ce qui n'est pas recommandé. De plus, par rapport aux alliages Co-Cr, le Ti12Mo qui est de plus faible densité présente une trop faible radio-opacité.

Tableau 1 Propriétés physiques et mécaniques des matériaux sélectionnés fabriqués

	Density (g/cm^3)	Elastic Modulus (GPa)	UTS (MPa)	Yield Strength (MPa)	UTS-Yield (MPa)	Elong. (%)	Elastic Range (%)
Stainless steels							
Fe-18Cr-14Ni-2.5Mo "316LVM"	7.95	193	670	340	330	48	0.17
Fe-21Cr-10Ni-3.5Mn-2.5Mo	7.90	195	740	430	310	35	0.22
Fe-22Cr-13Ni-5Mn	7.88	193	827	448	379	45	0.23
Fe-23Mn-21Cr-1Mo-1N	7.63	190	931	607	324	49	0.32
Cobalt alloys							
Co-20Cr-15W-10Ni "L605"	9.10	243	820-1200	380-780	420-600	35-55	0.16-0.32
Co-20Cr-35Ni-10Mo "MP35N"	8.43	233	930	414	516	45	0.18
Co-20Cr-16Ni-16Fe-7Mo "Pynox"	8.30	221	950	450	500	45	0.20
Titanium alloys							
CP Ti Grade 1	4.50	107	300	200	100	30	0.19
Ti-6Al-4V (alpha/beta)	4.43	105	860	795	65	10	0.72
Ti-6Al-7Nb (alpha/beta)	4.74	106	1000	900	100	12	0.85
Ti-15Mo (beta)	4.95	83	793	655	168	22	0.79
Ti-12Mo (beta)	4.84	82	973	480	493	45	0.41

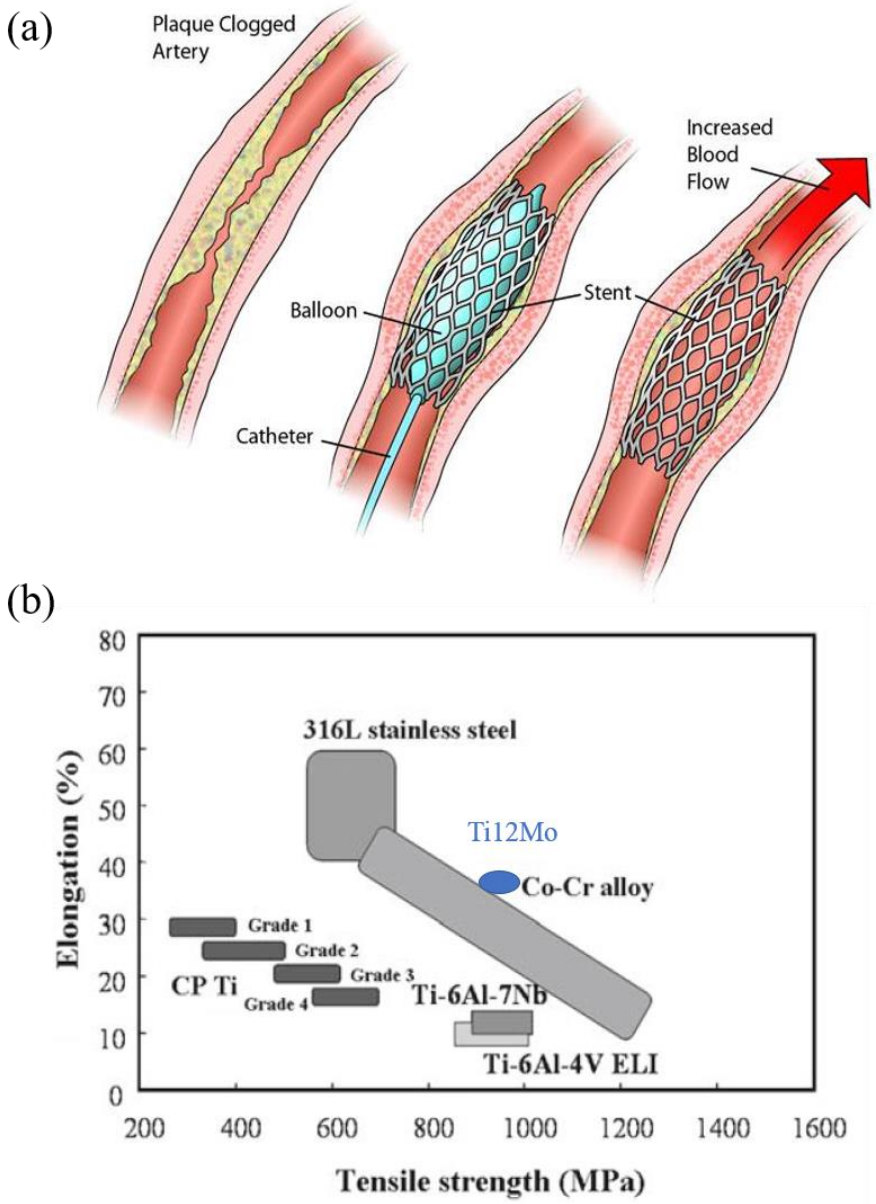

Figure 1 (a) Le mécanisme de fonctionnement du stent extensible à ballonnet, (b) Résistance à la traction et équilibre d'allongement de divers métaux à usage médical.

Le présent manuscrit est structuré en 7 chapitres. Le premier est consacré à l'état de l'art sur les alliages de titane TRIP/TWIP. Le second présente les techniques expérimentales, les logiciels d'analyse et les calculs utilisés pour l'élaboration, la fabrication, le traitement thermique et la caractérisation des alliages étudiés.

L'objectif du chapitre 3 est de montrer que les diverses voies de transformation possibles (systèmes de maclage mécanique, transformation martensitique induite sous contrainte) opérant en début de déformation plastique dans un alliage de Ti β-métastable respectent la loi de Schmid et Boas. Les facteurs de Schmid (SF) calculés ont été couplés aux mécanismes de transformation observés in-situ au MEB et ex-situ au MET. Le Ti-12Mo a été sélectionné pour cette étude car il est considéré comme l'alliage TRIP/TWIP modèle, et bénéficie du plus grand nombre de résultats reportés dans la littérature. Les principaux résultats de ce chapitre sont les suivants :

1. Les voies de transformation dans le Ti-12Mo dépendent de l'orientation des grains. La corrélation avec les facteurs de Schmid calculés a permis d'identifier quatre domaines d'orientation dans le triangle stéréographique, conduisant à des « cartes de partition de transformation » ou TPM pour «Transformation Partition Maps». Comme le montre la figure 2, les quatre domaines d'orientation identifiés correspondent à des domaines d'orientation du grain par rapport à l'axe de traction où les mécanismes de transformation observés sont dominés par le maclage mécanique, par la transformation martensitique sous contrainte, par une combinaison des deux mécanismes, ou par aucun d'eux, l'orientation étant défavorable aux deux mécanismes de transformation.

2. Les voies de transformation sont très diversifiées dans les alliages TRIP/TWIP car les deux modes de transformation peuvent se produire en cascade dans un même grain. Une zone maclée peut se transformer ensuite partiellement ou totalement en martensite. Inversement, une zone transformée en martensite peut ensuite se macler mécaniquement par un maclage $\{130\}\langle 310\rangle_{\alpha''}$ que l'on notera par la suite 130 α″ DT. Les modes de déformation entre grains voisins appartenant à des domaines d'orientation différents peuvent être incompatibles; ou les écarts de contrainte-déformation aux interfaces nouvellement formées par $\{332\}\langle 113\rangle_{\beta}$ et SIMα″ peuvent être trop

importants. Les modes de transformation suivis par le métal s'adaptent donc aux conditions locales sans suivre nécessairement un chemin unique ce qui rend complexe leur étude.

3. Des observations expérimentales in situ ont permis de mettre en évidence des mécanismes de formation de macles {332}<113>$_\beta$ inédit impliquant le maclage mécanique 130 α″ DT de la martensite via deux voies différentes.

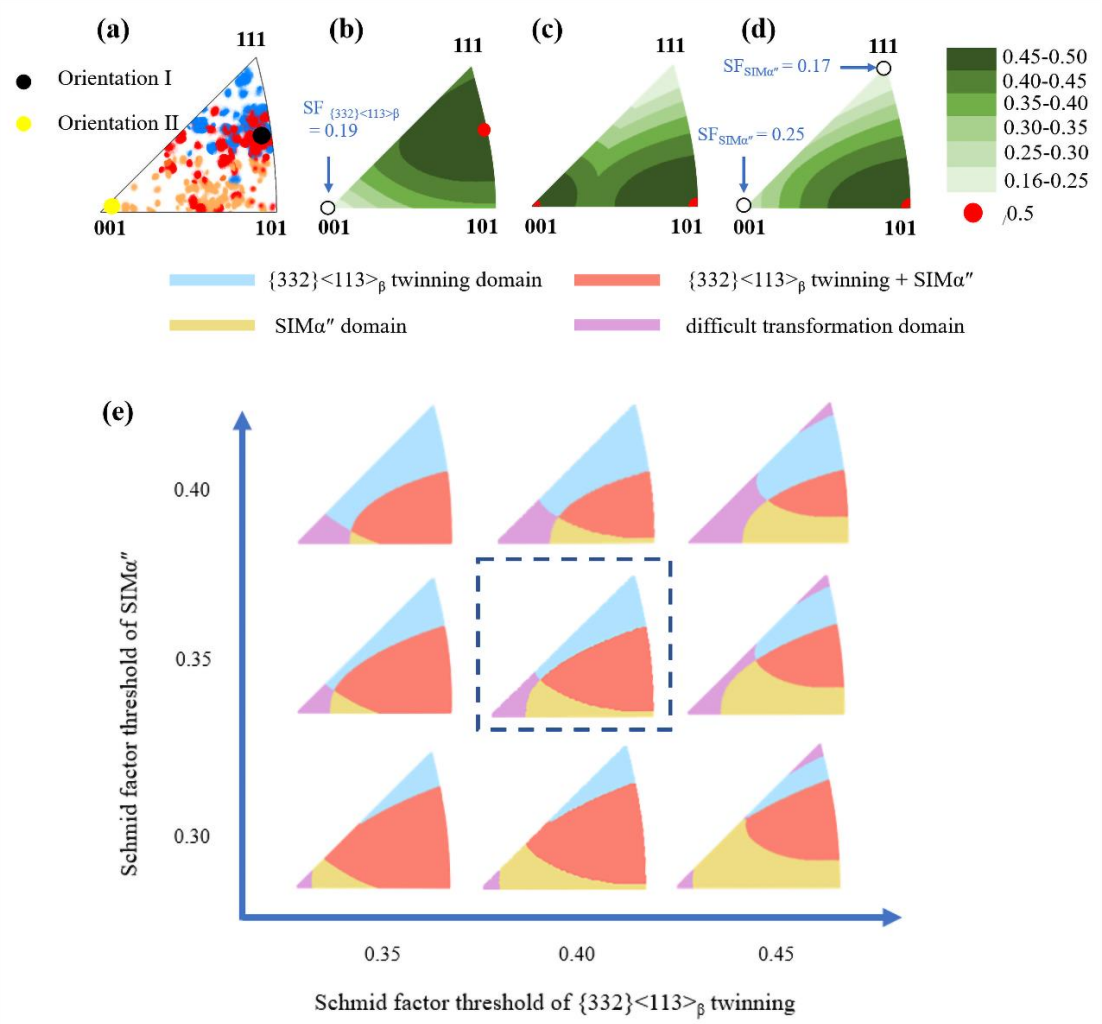

Figure 2: (a) figure de pôle inverse (IPF) expérimentale des produits de déformation primaire identifiés dans un grand nombre de grains de de l'alliage Ti-12Mo par EBSD in-situ sous contrainte de traction (ε = 0,02) ; (b~d) IPF montrant la distribution du SF le plus élevé des différents modes de transformation: 332T (b), SIM α″ toutes variantes cristallographiques confondues (c), de la variante de SIM α″ avec une valeur positive de la

déformation ε_i produite en traction (d) ; (e) Tansformation Partition Maps théoriques : IPF délimitant les 4 domaines d'orientation (une couleur par mode de transformation) et leur évolution en fonction des valeurs seuils des facteurs de Schmid associés à chaque mode de transformation (SIM α″ versus 332T) .

Le chapitre 4 est consacré à l'étude des mécanismes de déformation par maclage mécanique de la martensite induite sous contrainte à l'échelle micrométrique et nanométrique, dans des conditions in-situ. L'étude est ici encore menée sur l'alliage Ti-12Mo. Dans ce chapitre, nous avons soigneusement étudié le mécanisme de maclage via la transformation martensitique induite sous contrainte lors du chargement, et son effet sur le comportement du matériau en déformation. Les principales conclusions, résumées dans la figure 3, sont :

1. La projection sur la direction de traction du taux de déformation produit par le mode de transformation peut être considéré comme un paramètre pertinent pour prédire le système de maclage de la martensite qui sera actif et de sa variante potentielle dans une orientation spécifique.

2. Les observations expérimentales par EBSD combinées aux calculs des déformations produites théoriques des différents modes de transformation ont confirmé que le mode 130 α″ DT est beaucoup plus facile à activer dans l'échantillon de Ti12Mo en raison de sa plus grande déformation de transformation produite comparé au mode de maclage 110 α″ DT pour presque toutes les orientations de sollicitation en traction.

3. Les bandes de martensite α″ primaires qui ont subi un maclage mécanique de type 130 α″ DT ou 110 α″ DT présentent un démaclage partiel au cours de la décharge, qui se traduit par une récupération pseudo-élastique de la déformation.

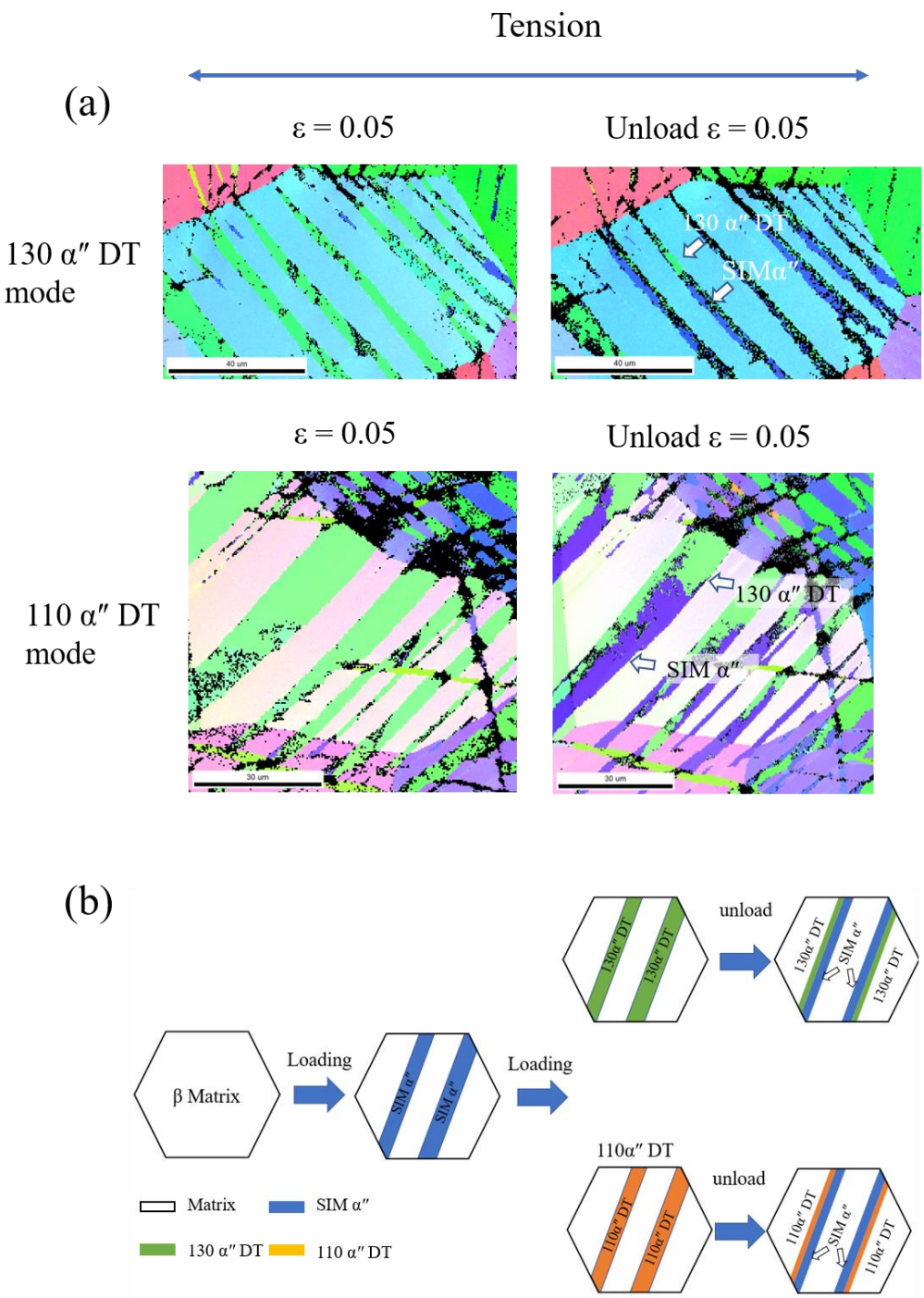

Figure 3 (a) Analyse EBSD des modes de maclage {130}<310> et {110}<110> de la martensite α″ au cours de la déformation plastique; (b) Représentations schématiques des scénarios possibles de maclage et démaclage de la martensite au cours d'un cycle mise en charge - déformation plastique - décharge dans Ti12Mo.

Le chapitre 5 est consacré à l'étude des évolutions structurales subies par l'alliage Ti-12Mo lors de traitements thermiques courts à 200°C et leurs effets sur les propriétés mécaniques. L'objectif est ici double : a) clarifier la transition ω_{ath}-ω_{iso} qui a lieu dans cette gamme de température en réalisant un suivi par des mesures de résistivité électrique, diffraction des rayons X au synchrotron, et par MET in-situ en température; b) mieux comprendre et contrôler les effets de la phase ω_{iso} à différents degrés de maturité sur la sélection des mécanismes de déformation, puis sur les propriétés mécaniques globales en traction via des analyses EBSD et des observations MET dans des conditions de traction in-situ. Les principales conclusions obtenues sont les suivantes :

2. Après avoir été durci (Limite d'élasticité améliorée de 659MPa à 865MPa) à 200°C pendant 60 s, l'allongement uniforme de l'alliage est passé de 29% à 33%. Avec l'augmentation de la durée de traitement, l'allongement plastique uniforme diminue considérablement jusqu'à 3,3% après 150 s et devient nul après un traitement de 300 s.

3. Les trois mécanismes de déformation, SIM α″, 332T et glissement de dislocations, sont progressivement inhibés lorsque le temps de traitement augmente et finalement totalement supprimés au-delà de 150s.

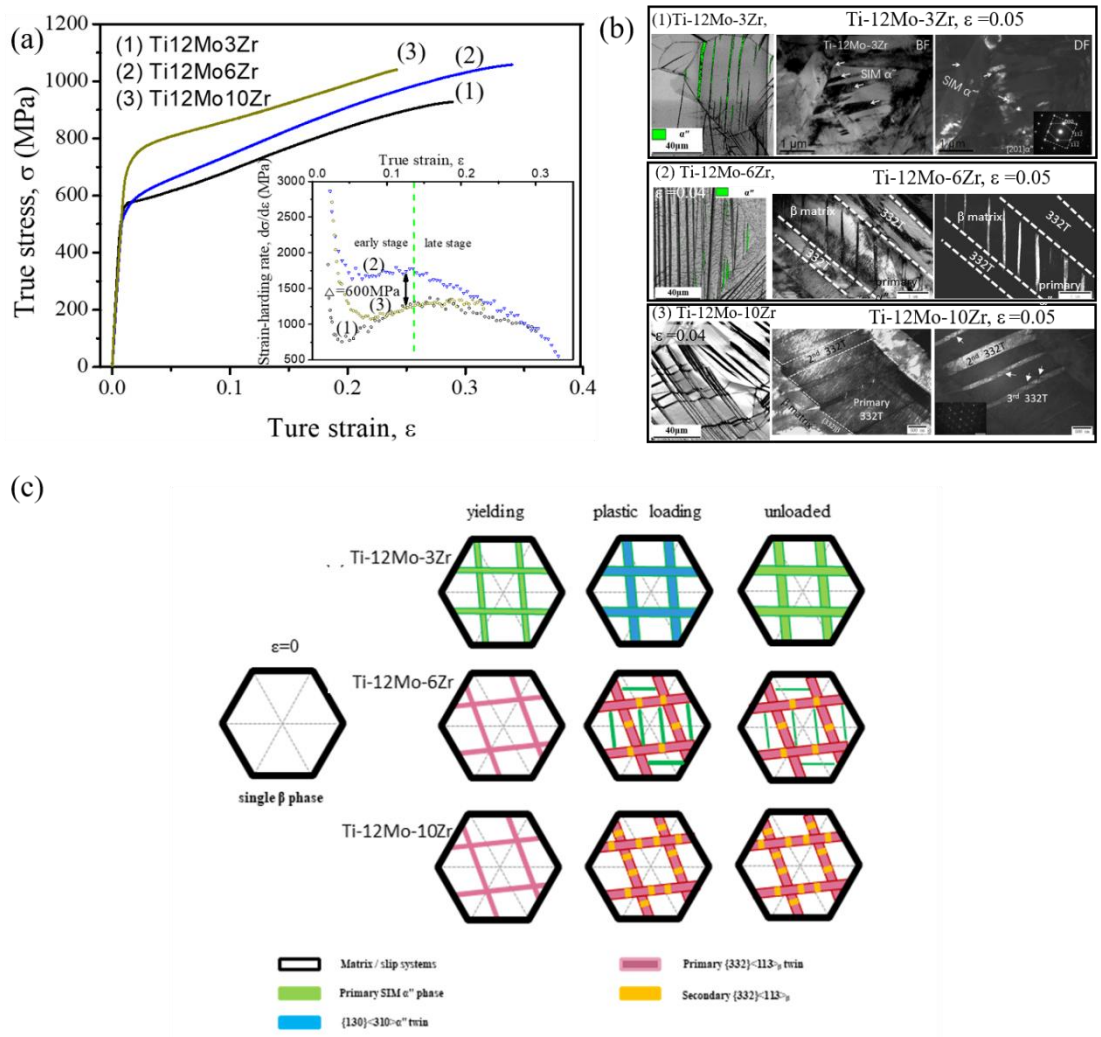

Figure 4 (a) Courbes contrainte - déformation vraies des échantillons Ti-12Mo-xZr (x = 3, 6, 10) trempé et, en médaillon, courbes correspondantes du taux d'écrouissage en fonction de la déformation vraie. (b) microstructures des alliages Ti-12Mo-xZr (x= 3, 6, 10) observées par MEB et MET après une déformation de 0,05 (c) Représentation schématique de la séquence d'activation des mécanismes de déformation 332T et SIMα'', au cours d'un cycle mise en charge - déformation plastique - décharge.

La relativement faible limite d'élasticité du Ti12Mo à l'état trempé imposerait la fabrication de stents plus épais ce qui est problématique. Généralement, l'ajout d'éléments d'alliage est une méthode simple et universelle pour améliorer les propriétés mécaniques des alliages. L'utilisation de Zr pourrait être ici doublement avantageuse puisque cet élément est soluble dans Ti-Mo sur une

large gamme de composition (jusqu'à plusieurs dizaines de pour cent en poids) et impacte la stabilité de la phase β et donc ses mécanismes de déformation de façon modérée. Il est donc envisageable : (1) d'ajuster la stabilité de la phase β et ainsi moduler la contribution des effets TRIP et TWIP à sa déformation plastique ; (2) d'obtenir un durcissement de la phase β par effet de solution solide. L'étude de l'addition de Zr sur le comportement mécanique de l'alliage Ti-12Mo avec notamment une transition d'un comportement mixte TRIP/TWIP vers un comportement uniquement TWIP a fait l'objet du chapitre 6. L'influence de la teneur en Zr sur l'évolution de la microstructure, les propriétés mécaniques et les mécanismes de déformation des alliages Ti-12Mo-xZr (x=3, 6, 10) a été étudiée. Les principaux résultats, résumés dans la figure 4, sont les suivants :

1. Une transition d'un comportement mixte TRIP/TWIP à un comportement uniquement TWIP dans les alliages Ti-12Mo-xZr a effectivement été observée en substituant progressivement le Ti par le Zr.

2. Les trois alliages étudiés présentent une excellente combinaison résistance mécanique-ductilité. La limite d'élasticité de l'alliage Ti-12Mo-10Zr qui est bien supérieure à celle du Ti-12Mo-6Zr et du Ti-12Mo-3Zr, provient d'un durcissement de la phase β par effet de solution solide, mais aussi de l'inhibition de l'effet TRIP.

3. L'alliage Ti-12Mo-6Zr affiche un taux d'écrouissage plus élevé que les alliages Ti-12Mo-3Zr et Ti-12Mo-10Zr, ce qui suggère une interaction plus favorable entre les mécanismes TRIP et TWIP pour cette composition.

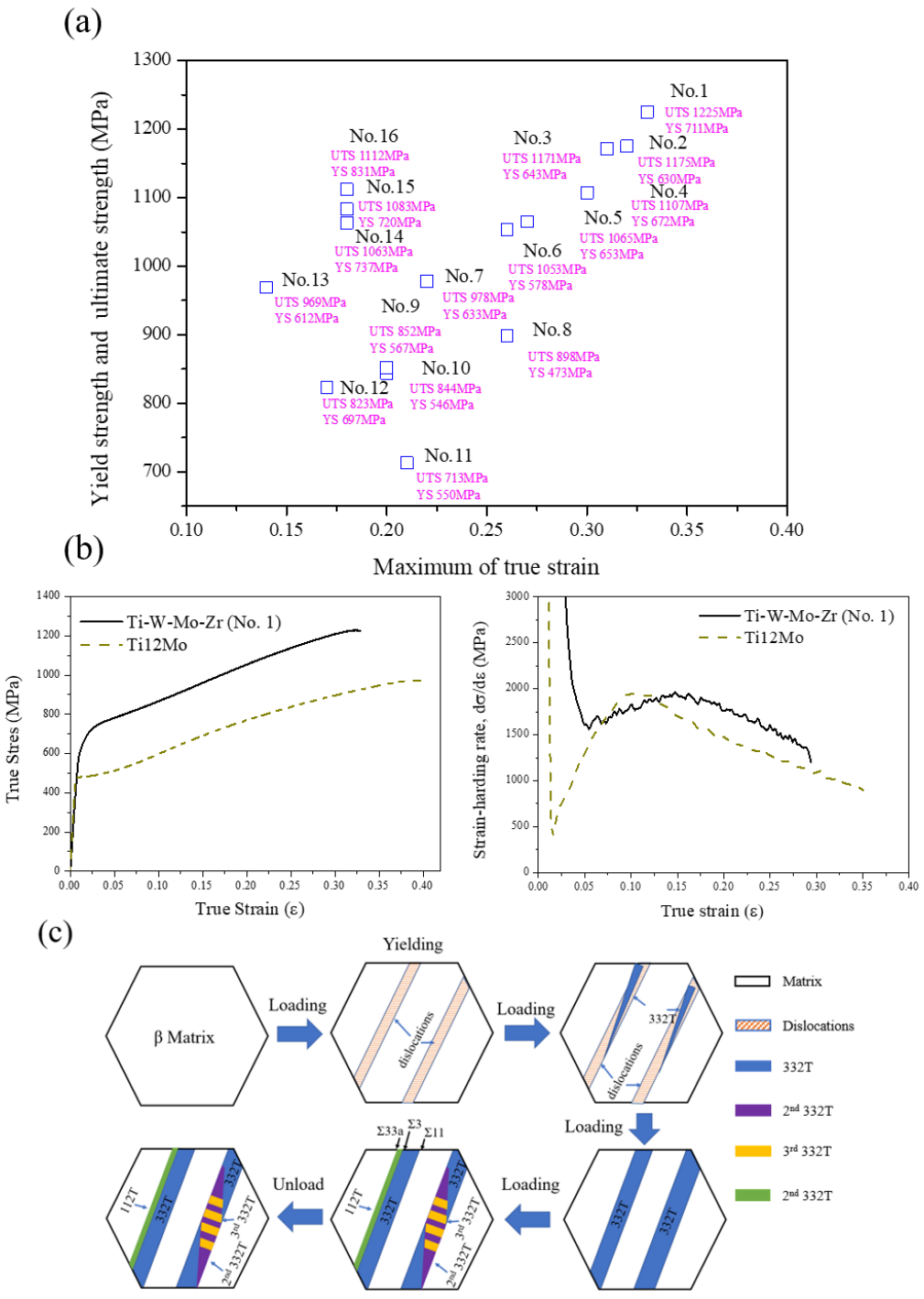

Figure 5 (a) Carte des valeurs maximales des contraintes et déformations vraies obtenues pour les 16 alliages Ti-W-Mo et Ti-W-Mo-Zr étudiés ; (b) Courbes contrainte-déformation vraies –des alliages Ti-W-Mo-Zr et Ti-12Mo, et leurs taux d'écrouissage correspondants. (c) Représentation schématique des scénarios de

déformation plastique au cours d'un cycle mise en charge – décharge observés dans l'alliage Ti-22W-3.5Mo-6.5Zr.

Après avoir amélioré les propriétés mécaniques par l'ajout de Zr, nous avons souhaité améliorer la radio-opacité de nos alliages en substituant partiellement le molybdène par du tungstène. Deux séries d'alliages Ti-W-Mo et Ti-W-Mo-Zr ont été préparées et étudiées. Parmi les 16 alliages envisagés, le No.1 présente la meilleure combinaison résistance mécanique (limite d'élasticité = 760MPa) - ductilité (32%), comme le montre la figure 5b. Sa composition chimique est temporairement confidentielle en raison du processus de brevet en cours. L'alliage Ti-W-Mo-Zr mentionné ci-après dans le manuscrit a la même composition chimique. Une étude plus poussée des mécanismes de déformation par un suivi in-situ au MEB et au MET a donc été réalisée pour cet alliage. Les résultats sont synthétisés figure 5c par une représentation schématique des microstructures de déformation observées aux stades précoces de la déformation plastique du Ti-W-Mo-Zr. La déformation plastique démarre par du glissement de dislocations localisé dans des bandes. Des macles 332T se forment ensuite à l'intérieur de ces bandes, puis se multiplient et s'élargissent pour finalement conquérir l'ensemble de la bande de glissement. La déformation se poursuit avec la formation à l'intérieur des bandes de déformation primaires soit de macles de type 332T secondaires et tertiaires, soit avec la formation de macles de type 112T parallèles au plan de macle de la bande primaire. Les conclusions suivantes sont proposées :

1. Le Ti-W-Mo-Zr présente une limite d'élasticité élevée qui s'explique par un durcissement important par solution solide de la phase β, et une stabilisation de la phase β conduisant à un déclenchement des mécanismes de déformation par transformation à des niveaux de contraintes plus élevés.

2. Un effet TWIP a été observé dans Ti-W-Mo-Zr après plastification par glissement de dislocations localisé dans des bandes, Un effet TWIP a été observé dans Ti-W-Mo-Zr après plastification par glissement de dislocations localisées en bandes, ce qui se traduit par un effet Hall-Petch.

3. L'excellente combinaison résistance mécanique-ductilité de l'alliage Ti-W-Mo-Zr résulte d'une hiérarchie spécifique dans les évènements de déformation avec un glissement plastique localisé suivi de macles 332T primaires puis des macles 332T secondaires et tertiaires ou des macles 112T secondaires.

En conclusion de cette thèse, l'étude contribue à la compréhension fondamentale du mécanisme de déformation de l'alliage Ti12Mo. Les propriétés mécaniques du Ti12Mo ont été confirmées et pourraient être adaptées en contrôlant les précipitations ω_{iso}, ce qui nous donne une nouvelle stratégie pour améliorer les propriétés mécaniques des alliages de titane métastables. En parallèle, les propriétés mécaniques pourraient également être améliorées en optimisant les compositions chimiques. Nous avons conçu et fabriqué un ensemble d'alliages Ti-Mo-Zr et d'alliages Ti-W-Mo-Zr avec une excellente ductilité et une limite d'élasticité élevée, qui ont le potentiel d'être utilisés dans l'application de stent cardiovasculaires. De nouveaux alliages de Ti métastable continueront d'être développés en optimisant les compositions chimiques sur la base des travaux de thèse.

RÉSUMÉ

Ce travail vise à développer une série d'alliages base titane β métastables pour la fabrication de stents cardiovasculaires. L'alliage Ti-12Mo (wt. %) a attiré notre attention en raison de sa grande résistance mécanique, sa grande ductilité et son écrouissage significatif. Afin de mieux comprendre les mécanismes de déformation de l'alliage Ti-12Mo au cours d'un essai de traction, plusieurs études de caractérisation in-situ, telles que la diffraction des électrons rétrodiffusés (EBSD) en traction, la microscopie électronique à transmission (TEM) en traction et en température, des mesures de résistivité électrique en température, etc., combinées par des calculs théoriques ont été employées. Celles-ci nous ont permis d'étudier les diverses séquences d'évolution de la microstructure au cours de la déformation : les transformations induites par la déformation (maclage $\{332\}<113>_{\beta}$ et la transformation martensitique $\beta \rightarrow \alpha''$ induite sous contrainte), le mécanisme de sélection des différents modes de transformation, le processus de maclage de la martensite, le mécanisme de sélection des variantes cristallographiques de la martensite. Par ailleurs, un traitement thermique de durcissement court et à basse température (200°C pendant 60~150s) a été réalisé pour améliorer les propriétés mécaniques en initiant la précipitation de la phase ω_{iso} sans toutefois modifier la composition chimique. La transformation de phase ω et ses effets sur le comportement mécanique et les évolutions de la microstructure de l'alliage ont été soigneusement étudiés et discutés en détail. Deux séries d'alliages métastables transformables par déformation Ti-12Mo-xZr (x=3, 6, 10, wt. %) et Ti-W-Mo-Zr (W =14%~22%, Mo=3%~10%, Zr=0%~6.5%, wt. %) ont été conçues et fabriquées. Leurs propriétés mécaniques et leurs mécanismes de déformation ont été soigneusement étudiés. Parmi eux, les alliages Ti-12Mo-10Zr et Ti-22W-4.5W-6.5Zr combinent une résistance mécanique élevée, un taux d'écrouissage élevé, un excellent allongement plastique uniforme avec une radio-opacité améliorée. Les simulations par éléments finis (FEA) ont été réalisées sur un modèle d'endoprothèse cardiovasculaire en utilisant les caractéristiques des alliages Ti-12Mo-10Zr et Ti-22W-4.5W-6.5Zr, afin d'évaluer leur potentiel pour ce type d'application.

MOTS CLÉS

Alliage de titane, effets TRIP/TWIP, transformation martensitique, ω phase, déformation jumelage, biomatériaux.

ABSTRACT

This work aims to develop a kind of metastable β titanium alloys applied in cardiovascular stent. Ti-12Mo (wt. %) alloy attracted our attention due to its large strength, large ductility and significant work-hardening effect. In order to further understand the deformation mechanism of Ti-12Mo alloy during tensile process, several *in-situ* characterization investigations such as electron backscatter diffraction (EBSD) under tensile load, transmission electron microscopy (TEM) under tensile load and heating, isothermal electrical resistivity measurements, etc., combined with theoretical Schmid factor calculations were carried out. These techniques allowed to investigate in details the diverse pathways (deformation mechanism and microstructure evolution sequence) of the deformation-induced transformations ($\{332\}<113>_{\beta}$ twinning and stress-induced orthorhombic martensite α″), the selection mechanism of the transformation pathways, the martensite mechanical twinning process, the mechanism of martensite variants selection, and the ω phase transformation. Furthermore, short time and low temperature hardening heat treatment (200°C for 60~150s) was performed to improve the mechanical properties through controlling the ω_{iso} phase nucleation without detectable modification of the chemical compositions. ω phase transformations and their effects on the mechanical behaviors and microstructure evolutions were carefully investigated and discussed in detail. A set of strain transformable metastable Ti-12Mo-xZr (wt. %) alloys (x=3, 6, 10, wt. %) and Ti-W-Mo-Zr alloys (W =14%~22%, Mo=3%~10%, Zr=0%~6.5%, wt. %) alloys were designed and fabricated. Their mechanical properties and deformation mechanism were carefully studied. Among them, Ti-12Mo-10Zr and Ti-22W-4.5W-6.5Zr alloys were find to present combinations of high strength, high work-hardening rate, excellent uniform plastic elongation and improved radiocapacity. The finite element analysis (FEA) simulations are applied on the cardiovascular stent model of Ti-12Mo-10Zr and Ti-22W-4.5W-6.5Zr alloys, respectively, to evaluate their potential for cardiovascular stent applications.

KEYWORDS

Titanium alloy, TRIP/TWIP effects, martensite transformation, ω phase, deformation twinning, biomaterials.